Studies on Pt based cathode catalysts for proton exchange membrane fuel cell

Thesis submitted to

Cochin University of Science and Technology

in partial fulfillment of the requirements for
the award of the degree of

Doctor of Philosophy

in

Chemistry

Under the Faculty of Science

by

Abha Bharti
Reg. No. 4940

इसरो ISRO

Propellants, Polymers, Chemicals and Materials Entity
Vikram Sarabhai Space Centre
Indian Space Research Organization
Thiruvananthapuram, Kerala, India-695 022

December 2017

Studies on Pt based cathode catalysts for proton exchange membrane fuel cell

Ph. D. Thesis under the Faculty of Science, Cochin University of Science and Technology

Author:

ABHA BHARTI
Senior Research Fellow
Propellants, Polymers, Chemicals and Materials Entity
Vikram Sarabhai Space Centre
Thiruvananthapuram-695022
E mail: bharti.abha@gmail.com

Research Guide:

Dr. GOURI. C
Scientist/Engineer G
Group Director
Polymers and Special Chemicals Group
Propellants, Polymers, Chemicals and Materials Entity
Vikram Sarabhai Space Centre
Thiruvananthapuram-695022
E mail: gouri.c.k@gmail.com

Propellants, Polymers, Chemicals and Materials Entity
Vikram Sarabhai Space Centre
Thiruvananthapuram- 695 022, INDIA

December 2017

भारत सरकार
अंतरिक्ष विभाग
विक्रम साराभाई अंतरिक्ष केंद्र
तिरुवनंतपुरम - 695022
केरल, भारत
टेलीफोन: **(0471) 256 5689**
फैक्स : **(0471) 256 4203**

Government of India
Department of Space
Vikram Sarabhai Space Centre
Thiruvananthapuram-695 022
Kerala, INDIA
Telephone : (0471) 256 5689
Fax : (0471) 256 4203
+91-9446220454
email: gouri_cheruvally@vssc.gov.in;
gouri.c.k@gmail.com

November 30, 2017

CERTIFICATE

This is to certify that the work embodied in the thesis entitled **"Studies on Pt based cathode catalysts for proton exchange membrane fuel cell",** submitted by Ms. Abha Bharti in partial fulfillment of the requirements for the degree of Doctor of Philosophy in Chemistry to Cochin University of Science and Technology, is an authentic and bonafide record of the original research work carried out by her, under my supervision at Energy Systems Division, Propellants, Polymers, Chemicals and Materials Entity of Vikram Sarabhai Space Centre, Thiruvananthapuram. Further, the results embodied in this thesis, in full or in part, have not been submitted previously for the award of any other degree in any University/Institution. All the relevant corrections and modifications suggested by the audience during the Pre-synopsis Seminar and recommended by the Doctoral Committee have been incorporated in the thesis.

Dr. Gouri. C
(Research Guide)

DECLARATION

I hereby declare that the work presented in this thesis entitled "**Studies on Pt based cathode catalysts for proton exchange membrane fuel cell**" is the outcome of the original research work carried out by me under the guidance of Dr. Gouri. C, Scientist/Engineer G, Group Director, Polymers and Special Chemicals Group, at Energy Systems Division under Propellants, Polymers, Chemicals and Materials Entity of Vikram Sarabhai Space Centre, Thiruvananthapuram. Further the results embodied in this thesis, in full or in part, have not been included in any other thesis/dissertation submitted previously for the award of any degree, diploma, associateship, or any other title, recognition from any University/Institution.

Thiruvananthapuram   **Abha Bharti**
21/12/2017

Dedicated to...

My beloved parents, my adorable brother and my guru, Dr. Gouri. C

ACKNOWLEDGEMENTS

"I stood and looked out to sea,
I said 'Hey Sea, you look at me'.
I have my boat of inspiration, my bravery,
My curiosity and I will conquer thee."

- My PhD; by Marie Lewis

The intellectual voyage of pursuit for my Ph.D. culminates with this thesis. At this juncture, I heartily remember the years of arduous work, illuminating discussions and wonderful company of several people who contributed in numerous ways towards the accomplishment of this study. I would like to take this opportunity to acknowledge and express my sincere gratitude to all of them.

At the outset, I would like to express my deepest gratitude to my research guide, Dr. Gouri. C, Group Director, Polymers and Special Chemicals Group (PSCG), Propellants, Polymers, Chemicals and Materials (PCM) entity, Vikram Sarabhai Space Centre (VSSC). Her valuable guidance, consistent support and relentless optimism have always kept me oriented in the correct direction to achieve my goal. She has always been a source of unwavering encouragement and moral strength. I have learnt many valuable lessons from her, both at scientific and personal level which helped in instilling confidence in me. She has been affectionate and ever ready to help me amidst her busy schedule. I have been extremely lucky, privileged and blessed to have her as my research guide.

I extend my heartfelt thanks to Shri. M. Shaneeth, Head, Fuel Cell Section (FCS) and Smt. T.D. Mercy, Head, Energy Systems Division (ESD) for providing necessary support for conduction of the experiments throughout my research period at FCS/ESD.

I am thankful to Shri. A.S. Kiran Kumar, Chairman, Indian Space Research Organization (ISRO), Department of Space (DOS), Dr. K. Sivan, Director, VSSC, Dr. S.C. Sharma, Deputy Director, PCM entity, VSSC and Dr. S. Aravamuthan, Deputy Director, Management Systems Area (MSA) entity, VSSC for granting

Table of Contents

Table of Contents

List of Figures

List of Figures

List of Tables

Symbols and Abbreviations

[Ox]	Oxidant concentration
[Pt]	Pt loading
[Red]	Reductant concentration
b	Tafel slope
d	Thickness of pellet
E	Potential/Voltage
$E°$	Standard state reversible voltage for the reaction
E_g	Band gap
F	Faraday's constant
F(R)	Kubelka-Munk function
$h\nu$	Energy of light
I	Current
i_d	Disk current
I_D	Intensity ratio of D band
I_G	Intensity ratio of G band
i_r	Ring current
j	Current density (current per unit area)
j_0	Exchange current density
j_k	Kinetic current density
j_l	Limiting current density
k	Rate constant
K_0	Constant associated with the forward or backward reaction
k_b	Rate of the backward (oxidation, anodic) reactions
k_f	Rate of the forward (reduction, cathodic) reactions
$k_{f,b}$	Rate at which species reach the electrode surface and react
L	Average size of metal crystallites
N	Collection efficiency
n	Number of moles of electrons consumed or generated
n_e	Electron-transfer number

Symbols and Abbreviations

p	Partial pressure
Q	Charge
Q_H	Charge for hydrogen desorption after correcting for double layer charge contribution
R	Gas constant
R_{ct}	Charge transfer resistance for oxygen reduction
T	Temperature
T_c	Corrosion time
W_{elec}	Electrical work
α	Charge transfer coefficient
β	FWHM of the diffraction peak
ΔG	Gibbs free energy
$\Delta G°_{rxn}$	Standard state free energy change for the reaction
ΔH	Enthalpy of the reaction
ε	Efficiency
η	Potential drop or over-potential
θ	Diffraction angle in degree
λ	X-ray wavelength of the radiation source (Cu-Kα 1.54 Å)
ρ	Density
σ	Electrical conductivity
2D	Two dimension
ac	Alternating current
ADT	Accelerated Degradation Test
AFC	Alkaline Fuel Cell
AST	Accelerated Stress Test
BET	Brunauer–Emmett–Teller
CA	Chronoamperometry
CB	Carbon black
CCD	Charge coupled device
CCP	Combined Cooling and Power
CH	Conventional heating
CHP	Combined Heat and Power

CL	Catalyst Layer
CNF	Carbon nanofiber
CNT	Carbon nanotube
CP	Carbon paper
CPE	Constant phase element
CSA	Chemical surface area
CTAB	Cetyltrimethylammonium bromide
CTAS	Cetyltrimethylammonium hydrogen sulfate
CV	Cyclic Voltammetry
dc	Direct current
DFT	Density functional theory
DMFC	Direct Methanol Fuel Cell
DOE	US Department of Energy
DRS	Diffuse Reflectance Spectroscopy
EDX	Energy Dispersive X-ray
EIS	Electrochemical Impedance spectroscopy
ESA	Electrochemical surface area
FRA	Frequency response analyzer
FESEM	Field Emission Scanning Electron Microscope
FNBO	First National Bank of Omaha
FT-IR	Fourier transform infrared
FWHM	Full width at half maxima
GA	Graphene aerogel
GC	Glassy carbon
GCM	Graphene cellular monoliths
GD	Galvanic displacement
GDL	Gas Diffusion Layer
GNF	Graphite nanofibers
GNP	Graphene nanoplatelets
GO	Graphene oxide
HB	Hicon Black

Symbols and Abbreviations

HHV	Higher heating value
HOR	Hydrogen Oxidation Reaction
HRTEM	High Resolution Transmission Electron Microscope
IC	Internal Combustion
ICP-AES	Inductively Coupled Plasma- Atomic Emission Spectroscopy
IL	Ionic liquid
ISRO	Indian Space Research Organization
MCFC	Molten Carbonate Fuel Cell
MEA	Membrane electrode assembly
MW	Microwave
MWCNT	Multi-walled carbon nanotube
NC	Nanocluster
ND	Nanodendrite
NLPM	Normal litre per minute
NP	Nanoparticle
OCV	Open circuit voltage
ORR	Oxygen Reduction Reaction
PDDA	Poly(diallyldimethylammonium chloride)
PEM	Proton Exchange Membrane
PEMFC	Proton Exchange Membrane Fuel Cell
PFSA	Perfluorosulfonic acid
PSEPVE	Perfluorosulfonylfluoride ethyl-propyl-vinly ether
PTFE	Polytetrafluoroethylene
rGO	Reduced graphene oxide
RH	Relative humidity
RHE	Reversible Hydrogen Electrode
RRDE	Rotating ring disk electrode
SAED	Selected Area Electron Diffraction
scCO$_2$	Supercritical carbon dioxide
SCD	Supercritical deposition
SDS	Sodium dodecyl sulphate

SHE	Standard Hydrogen Electrode
SMSI	Strong Metal Support Interactions
SOFC	Solid Oxide Fuel Cell
SSA	Specific surface area
SWCNT	Single-walled carbon nanotube
TFE	Tetrafluoroethylene
TGA	Thermogravimetric analysis
TTIP	Titanium (IV) tetraisopropoxide
UPS	Ultra-Violet Photoelectron Spectroscopy
US	United States
XPS	X-ray photoelectron spectroscopy
XRD	X-ray diffraction

Symbols and Abbreviations

Preface

Increasing oil prices, energy security concerns and changing climate have made it necessary for humanity to reduce their dependence on hydrocarbons for energy needs. Alternate energy schemes to ensure clean energy and sustainability are based on several newer technologies. Proton Exchange Membrane Fuel Cell (PEMFC) systems form an important part of future alternate energy schemes and are subjects of intensive research world over. In the emerging energy scenario based on hydrogen, PEMFCs are potential candidates for stationary and transport applications. They can be extensively applied in the various societal as well as ground military applications. The performance of PEMFCs is limited by the sluggish oxygen reduction reaction (ORR) kinetics at the cathode which results in overpotential losses of >0.3 V bringing down the fuel cell efficiency. In addition, decrease in stability of the cathode catalyst over time poses another significant impediment during long term PEMFC operation. Hence, further development and performance enhancement of PEMFCs are highly dependent on significant advances in the field of ORR catalyst materials.

Pt has long been considered as the cathode catalyst for ORR in PEMFCs and still is being widely used as the first option cathodic catalyst over other candidates. However, besides high overpotential, the Pt catalyst has other drawbacks to address like expensive cost, decrease in catalytic activity over a period of repeated usage (e.g. by CO poisoning and by adsorption of oxygen containing species from the electrolyte) as well as short catalytic stability. The other commonly employed carbon supported Pt catalyst (Pt/C) also suffers from significant durability concerns due to carbon corrosion under fuel cell operating conditions. Hence, exploration for an alternative catalyst that is more active and stable than Pt catalyst is of great significance. The further development of the ORR catalyst aims to: (i) curtail the overpotential, (ii) minimize the consumption of expensive Pt, and (iii) increase the catalytic activity and stability. Covering these aspects, promising Pt based cathode catalysts for PEMFC with improved activity and durability are discussed in this thesis that will help wide scale

commercialization of fuel cell. Three classes of PEMFC cathode catalyst *viz.* carbonaceous materials supported Pt, non-carbonaceous (metal-oxide) materials supported Pt and bi-metallic Pt based catalysts are investigated in this study. The investigations include synthesis of the catalyst materials through simple and effective routes followed by their detailed characterization and *in-situ* evaluation as cathode catalyst in working PEMFC.

The thesis is divided into 9 chapters. General introduction to fuel cells focusing in particular on PEMFC and ORR along with the need for developing more efficient cathode catalysts are included in *Chapter 1*. The chapter presents a detailed literature survey on the recent developments in the field of ORR catalysts. This chapter also gives the broad scope and objectives of the present investigation. Details on the chemicals and materials used, experimental procedures adopted for the synthesis of catalysts, and assembly of fuel cell are given in *Chapter 2*. Details of characterization techniques employed including electrochemical techniques are also discussed in this chapter. *Chapter 3* describes the effect of pH of synthesis medium on both physico-chemical and catalytic properties of Pt-TiO$_2$ nano-composite catalysts. In *Chapter 4,* the role of V dopant on TiO$_2$ support characteristics and fuel cell performance are presented. *Chapter 5* focuses on selection of the most suitable reduction condition to obtain high performing Pt/CNT catalysts. *Chapter 6* discusses the comparison and influence of various carbon nano-forms such as carbon black (CB), single-walled carbon nanotube (SWCNT), multi-walled carbon nanotube (MWCNT) and graphene supported Pt catalyst on fuel cell performance. *Chapter 7* describes the influence of anionic surfactant, sodium dodecyl sulphate (SDS) and cationic surfactant cetyltrimethylammonium bromide (CTAB) surfactant on synthesis as well as the physicochemical and catalytic properties of the bi-metallic Pt-Pd/MWCNT catalysts. *Chapter 8* discusses the performance and durability characteristics of two selected cathode catalysts, Pt/V-TiO$_2$ and Pt-Pd/MWCNT. Finally, the important findings and inferences derived from this thesis together with concluding remarks and future scope of work are summarized in *Chapter 9*.

Chapter 1

Introduction

This chapter gives a general introduction to fuel cells focusing in particular on proton exchange membrane fuel cell (PEMFC). Oxygen reduction reaction (ORR) occurring at cathode and its significance in PEMFC performance are discussed in detail along with the need for developing more efficient cathode catalysts. The chapter presents a detailed literature survey on the recent developments in the field of ORR catalysts. Scope and objectives of the present investigation are also included towards the end of this chapter.
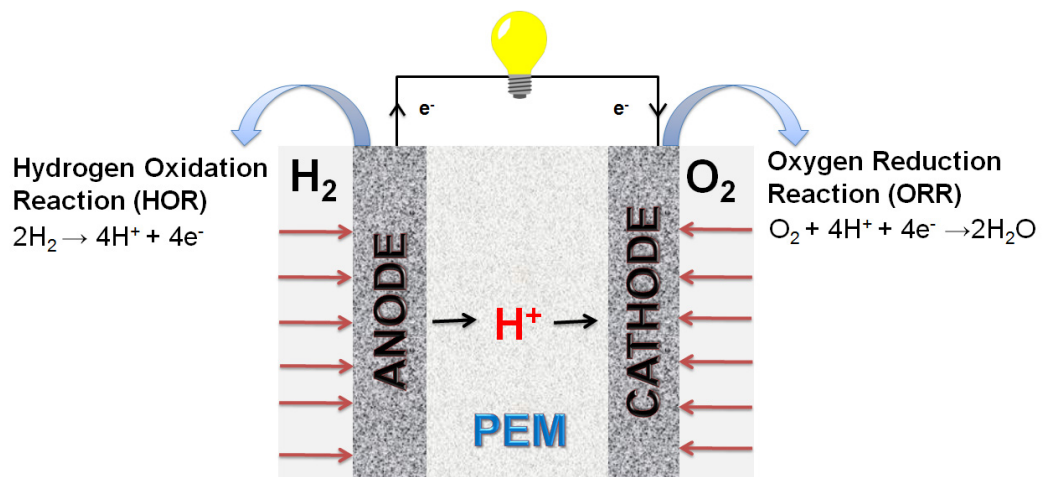
Energy technologies have a central role in social and economic development of mankind at all scales and are thus closely linked to the quality of living at all times. Global energy demand is increasing every day as households, transportation and industries that use these energy sources are constantly on the rise. The vast majority (~90%) of energy use reported world-wide presently is provided by fossil fuels. However, these energy sources are in limited supply and are major contributors towards global warming which causes serious environmental problems like climate changes, melting of ice caps and rising sea levels. Therefore, there is an immediate need to focus on sustainable and renewable energy sources that do not pollute the environment, and at the same time reduce or stop the use of fossil fuels as energy source. Meeting the world's growing demand for new energy sources in a sustainable way will require the deployment of renewable energy systems such as those based on solar and wind energy, in several orders of magnitude more than are in place currently. However, the tapping of energy from the natural renewable energy sources such as the sun and wind pose diurnal and seasonal variability concerns, and hence their utility becomes limited. In this regard, fuel cells operating with hydrogen or hydrogen-rich fuels generating electricity along with water and virtually no pollutant emissions gain immense importance as a potential, sustainable energy system for mankind.

1.1. Fuel cells

Fuel cells are electrochemical devices which convert chemical energy of fuels directly into electrical energy, *i.e.* direct current (dc) electricity. Typically, the process of electricity generation from fuels involves several energy conversion steps comprising of thermal and mechanical energy. Fig. 1.1 summarizes the electricity generation process steps involved in heat engine and fuel cell. In fuel cells, the intermediate steps of producing heat and performing mechanical work (Carnot's cycle), typical of conventional power generations methods, are avoided. Thus, fuel cells are not limited by the thermodynamic limitations of heat engines, and hence, are more efficient. In transportation, hydrogen fuel cell engines operate at an efficiency of upto 65%, compared to 25% for the petrol-driven car engines. When the heat generated in fuel cells is also utilized in combined heat and power (CHP) systems, an

overall efficiency in excess of 85% can be achieved. The fuel cell can thus serve as a quiet, efficient and clean replacement for the internal combustion (IC) engine. The fuel cell concept was first proposed in 1839 by Sir W. R. Grove, who produced water and electricity by supplying hydrogen and oxygen into a sulfuric acid bath in the presence of porous platinum electrodes. The first fuel cell developed by Grove was initially known as "gaseous voltaic battery". Later in 1922, Rideal and Evans coined the more scientific name "fuel cell".
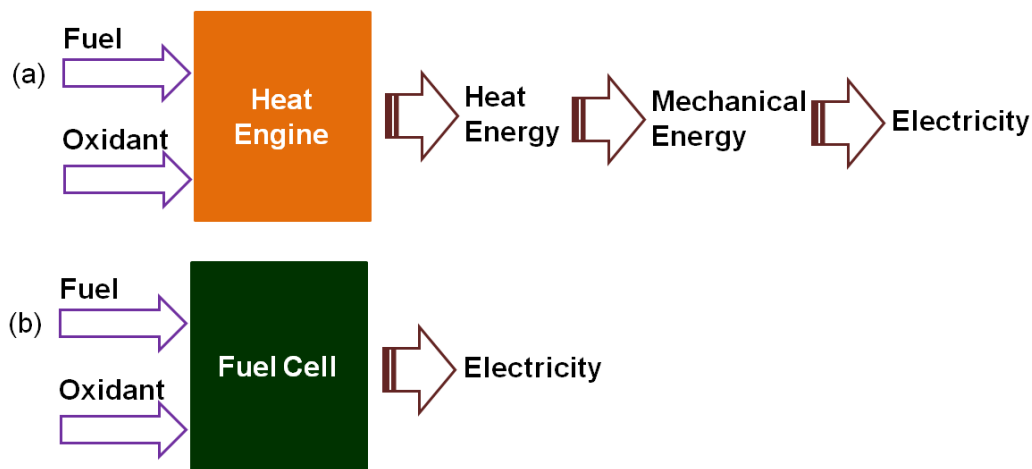
Fig. 1.1. Comparison of electricity generation *via* (a) conventional heat engine, and (b) fuel cell

Fuel cells differ from other electrochemical power sources such as galvanic cells (batteries), mainly as follows:

1. Fuel cells use a supply of gaseous or liquid reactants for the reaction rather than the solid reactants built into the electrodes in batteries.

2. As long as continuous supply of the reactants and continuous elimination of the reaction products are provided, fuel cells can be operated for a longer time without periodic replacement or recharging.

The possible fuel reactants for the current producing reaction are natural types (e.g. natural gas, petroleum products) or products which are derived by fuel processing, such as hydrogen produced by reforming of hydrocarbon fuels or water gas (syngas) generated by treating coal with steam, which gave rise to the name "Fuel Cells" for this type of electrochemical energy source.

1.1.1. Basic principle of fuel cells

The essential components of a fuel cell are its electrodes (anode and cathode) and electrolyte. The fuel and the oxidizing agent are each supplied at the respective electrode. Electrochemical reactions take place at the electrodes so that ions flow through the electrolyte, while the electric current flows in the external circuit and perform work on the load. At the negative electrode (anode), electrons are produced by burning the fuel, and at the positive electrode (cathode), the electrons are used in the reduction of the oxidant, as shown in Fig. 1.2. It is important to create conditions to avoid the direct mixing of the reactants or their supply to the wrong electrodes. In such undesirable cases, the direct chemical interaction of the reactants might happen and yield thermal energy; thus, lowering or stopping the production of electrical energy completely. So, to avoid accidental contact between anode and cathode, an electronically insulating porous separator is often placed into the gap between the electrodes. For the fuel cell to work for longer duration, provisions must be made to realize a continuous supply of reactant to each electrode and continuous withdrawal of reaction products from the electrodes, as well as removal and/or utilization of the heat being evolved.
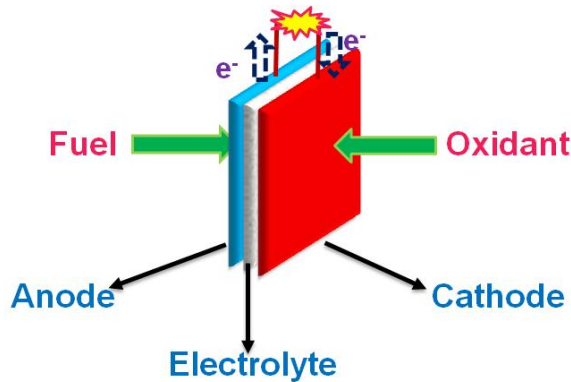
Fig. 1.2. General representation of a fuel cell

1.1.2. Types of fuel cells

There are six major types of fuel cells differentiated from one another on the basis of electrolyte. They are (i) Alkaline fuel cells (AFCs), (ii) Direct methanol fuel cells (DMFCs), (iii) Proton exchange membrane fuel cells (PEMFCs), (iv) Phosphoric acid fuel cells (PAFCs), (v) Molten carbonate fuel cells (MCFCs), and (vi) Solid

oxide fuel cells (SOFCs). Though these six types of fuel cells operate at different temperature regimes, incorporate different materials, and often differ in their fuel tolerance and performance characteristics, they are all based upon the same electrochemical principle [Larminie *et al.* 2003, O'Hayre *et al.* 2016]. Fuel cell produces energy by virtue of two electrochemical reactions occurring separately at the two electrodes, anode and cathode. At the anode, the electrons transferred from the fuel are forced to flow through an external circuit (thus, generating current) and do the useful work before they can complete the reaction by combining with the oxidant at the cathode. The anodic and cathodic electrochemical reactions are spatially separated by an electrolyte which allows ions to flow but not electrons preventing electrical shorting. At a minimum, a fuel cell must possess two electrodes, where the two electrochemical half reactions occur, separated by an electrolyte. Salient features of six types of fuel cells are summarized in Fig. 1.3. A brief description of each type is presented in the following section.

	Anode reaction	Charge carrier	Cathode reaction	Operating temperature
AFC	$2H_2 + 4OH^- \rightarrow 4H_2O + 4e^-$	$\leftarrow OH^- \leftarrow$	$O_2 + 4e^- + 2H_2O \rightarrow 4OH^-$	50-200 °C
DMFC	$CH_3OH + H_2O \rightarrow 6H^+ + 6e^- + CO_2$	$\rightarrow H^+ \rightarrow$	$3/2O_2 + 6H^+ + 6e^- \rightarrow 3H_2O$	20-90 °C
PEMFC	$2H_2 \rightarrow 4H^+ + 4e^-$	$\rightarrow H^+ \rightarrow$	$O_2 + 4H^+ + 4e^- \rightarrow 2H_2O$	30-100 °C
PAFC	$2H_2 \rightarrow 4H^+ + 4e^-$	$\rightarrow H^+ \rightarrow$	$O_2 + 4H^+ + 4e^- \rightarrow 2H_2O$	~220 °C
MCFC	$2H_2 + 2CO_3^{2-} \rightarrow 2H_2O + 2CO_2 + 4e^-$	$\leftarrow CO_3^{2-} \leftarrow$	$O_2 + 2CO_2 + 4e^- \rightarrow 2CO_3^{2-}$	~650 °C
SOFC	$2H_2 + 2O^{2-} \rightarrow 2H_2O + 4e^-$	$\leftarrow O^{2-} \leftarrow$	$O_2 + 4e^- \rightarrow 2O^{2-}$	600-1000 °C
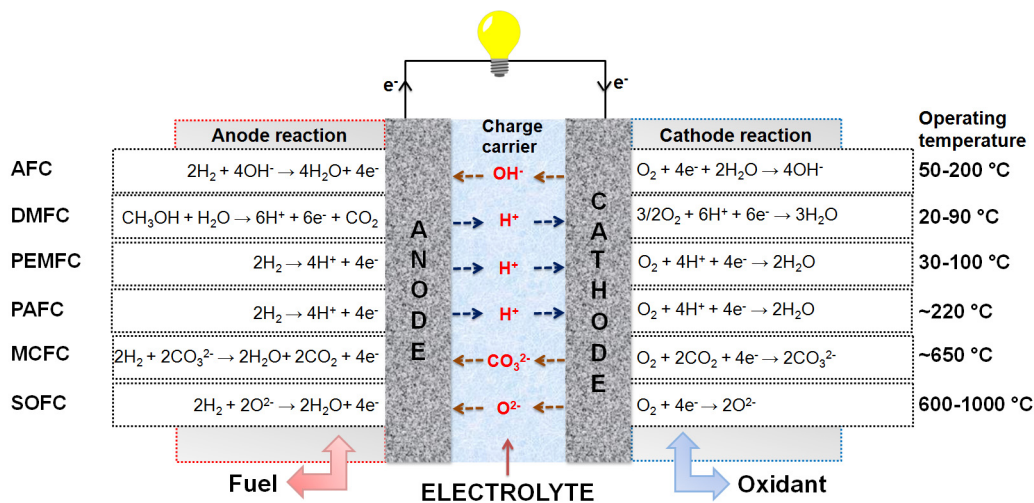
Fig. 1.3. Salient features of different types of fuel cells

(a) Alkaline fuel cell (AFC) uses concentrated KOH (85 wt.%) as electrolyte in fuel cells operated at high temperature (>150 °C), or less concentrated KOH (35 to 50 wt.%) for lower temperature (<120 °C) operation. The electrolyte is retained in a matrix (usually asbestos). A wide range of electro-catalysts can be used (e.g., Ni, Ag, noble metals). Efficiency of this type of fuel cell is about 70%. The AFC was one of the first, modern fuel cells to be developed, beginning in 1960. The application at that

time was to provide on-board electric power for the Apollo space vehicle. The AFC has enjoyed considerable success in the space applications, but its terrestrial application has been challenged by its sensitivity to carbon dioxide.

Advantages: Desirable attributes of the AFC include its excellent performance on hydrogen and oxygen compared to other candidate fuel cells due to its active O_2 electrode kinetics and its flexibility to use a wide range of electro-catalysts.

Limitations: The sensitivity of the electrolyte to CO_2 requires the use of highly pure H_2 as a fuel and CO_2-free oxidant. As a consequence, the use of a reformer would require a highly effective CO and CO_2 removal system.

(b) Direct methanol fuel cell (DMFC) uses a polymer membrane as an electrolyte. The platinum-ruthenium catalyst on the DMFC anode is able to draw the hydrogen from liquid methanol, eliminating the need for a fuel reformer. Therefore, pure methanol can be used as fuel, hence the name. DMFCs operate in the temperature range 20 °C to 90 °C with an efficiency of about 40 to 50%. DMFCs find applications where power requirements are modest, such as mobile electronic devices or chargers and portable power packs.

Advantages: Methanol offers several advantages as a fuel. It is inexpensive, has a relatively high energy density and can be easily transported and stored.

Limitations: A basic problem associated with the operation of DMFC is the gradual penetration of methanol to the oxygen electrode by diffusion, called as methanol cross-over, which has undesirable consequences.

(c) Proton exchange membrane fuel cell (PEMFC) uses a water-based, acidic polymer membrane as its electrolyte, with platinum-based electrodes. PEMFCs operate at relatively low temperatures (< 100 °C) with an efficiency of about 40 to 50%. PEMFC is currently the leading technology for light duty vehicles, materials' handling vehicles, and to a lesser extent for stationary and other applications.

Advantages: PEMFC has a solid electrolyte which provides excellent resistance to gas cross-over. Also, the low operating temperature allows rapid start-up.

Limitations: The low and narrow operating temperature range makes thermal

management difficult, especially at very high current densities. Water management is another significant challenge in PEMFC design, as engineers must ensure a proper balance with enough hydration of the electrolyte and avoid its flooding. In addition, PEMFCs with Pt-based electro-catalysts are quite sensitive to poisoning by trace levels of contaminants including CO, sulfur species and ammonia.

(d) Phosphoric acid fuel cell (PAFC) consists of an anode and a cathode made of finely dispersed platinum catalyst on carbon and a silicon carbide structure that holds the phosphoric acid electrolyte and electro-catalyst in both the anode and cathode. Phosphoric acid, concentrated to 100%, is used as the electrolyte in this fuel cell, which typically operates at 150 °C to 220 °C. Overall efficiency of PAFC can be >80% if the process heat is harnessed for co-generation. This type of fuel cell is used in stationary power generators with output in the 100 kW to 400 kW range to power many commercial premises around the world, and they are also finding application in large vehicles such as buses.

Advantages: PAFCs are much less sensitive to CO than PEMFCs and AFCs: PAFCs tolerate about 1% of CO as a diluent. The operating temperature also provides considerable design flexibility for thermal management. In addition, the waste heat from PAFC can be readily used in most commercial and industrial co-generation applications, and would technically allow the use of a bottoming cycle.

Limitations: Cathode side oxygen reduction is slower than in AFC, and requires the use of a Pt catalyst. Although less complex than for PEMFC, PAFCs still require extensive fuel processing, including typically a water gas shift reactor to achieve good performance. Also, the highly corrosive nature of phosphoric acid requires the use of expensive materials in the stack.

(e) Molten carbonate fuel cell (MCFC) uses a molten carbonate salt suspended in a porous ceramic matrix as the electrolyte. Salts commonly used include lithium carbonate, potassium carbonate and sodium carbonate. The fuel cell operates at 600 °C to 700 °C where the alkali carbonates form a highly conducting molten salt, with the carbonate ions providing ionic conduction. At the high operating temperatures in MCFCs, Ni (anode) and nickel oxide (cathode) are adequate to promote reaction.

Efficiency of MCFC ranges from 60 to 80%. MCFCs are used in large stationary power generation units. Most fuel cell power plants of megawatt capacity use MCFCs, as do large combined heat and power (CHP) and combined cooling and power (CCP) plants. These fuel cells can work at up to 60% efficiency for fuel to electricity conversion, and overall efficiencies can be over 80% in CHP or CCP applications where the process heat is also utilized.

Advantages: The relatively high operating temperature of MCFC allows the use of CO and certain other hydrocarbons. These fuels are feasibly converted to hydrogen within the stack (on special reformer plates) which significantly improves the system efficiency.

Limitations: Disadvantages associated with MCFC units arise from using a liquid electrolyte rather than a solid. The main challenge stems from the very corrosive and mobile electrolyte, which requires use of nickel and high grade stainless steel as the cell hardware. The higher temperature promotes material problems, impacting mechanical stability and stack life. There is also requirement to inject carbon dioxide at the cathode as carbonate ions are consumed in reactions occurring at the anode, this requires additional components in the fuel cell making the fuel cell design quite complex.

(f) Solid oxide fuel cell (SOFC) works at very high temperatures, the highest of all the fuel cell types at around 800 °C to 1000 °C. SOFCs use a solid ceramic electrolyte, such as zirconium oxide stabilized with yttrium oxide, instead of a liquid or membrane. Typically, the anode is $Co-ZrO_2$ or $Ni-ZrO_2$ cermet, and the cathode is Sr-doped $LaMnO_3$. Their high operating temperature means that fuels can be reformed within the fuel cell itself, eliminating the need for external reforming and allowing the units to be used with a variety of hydrocarbon fuels. They are also relatively resistant to small quantities of sulphur in the fuel, compared to other types of fuel cell, and can hence be used with coal gas. Efficiency is about 60% when converting fuel to electricity; if the heat produced is also harnessed, their overall efficiency in converting fuel to energy can be over 80%. SOFCs are used extensively in large and small stationary power generation.

Advantages: Because the electrolyte is solid, the cell can be cast into various shapes, such as tubular, planar, or monolithic. The solid ceramic construction of the unit cell alleviates any corrosion problems in the cell. The solid electrolyte avoids electrolyte movement or flooding in the electrodes. The kinetics of the cell is relatively fast, removing the need for a noble metal catalyst.

Limitations: Due to the high operating temperature, these cells take longer time to start up and reach operating temperature. They must also be constructed of robust, heat-resistant materials, and they must be shielded to prevent heat loss.

1.1.3. Fuel cell applications

Fuel cell applications can be categorized into four broad areas: stationary power generation, power for transportation, portable power generation and military applications [Bagotsky 2012], as shown in Fig. 1.4. The greater efficiency and higher operation temperature of MCFCs and SOFCs make them more amenable to large stationary power generation, where high-grade waste heat can be utilized to heat water or air. Conversely, the lower operating temperature fuel cells like PEMFCs and PAFCs are particularly well suited for transportation applications where the heat is neither usable nor desirable.

Stationary applications: Fuel cells could potentially produce electricity for homes, institutions and industries through stationary power plants. Sizes range from 1 kW to several MW as per the targeted applications. In residential applications, small fuel cell power plants could be installed for the production of both electricity and heat or hot water for the home. Currently, there are a number of companies (e.g. General Motors, AvistaLabsEbara Ballard GE Microgen, Toyota Motor Corporation, UTC Fuel Cells, Teledyne Energy Systems) developing and/or producing residential fuel cells. Similarly, fuel cells are extensively used for commercial applications as well. In 1999, First National Bank of Omaha (FNBO), the nation's largest privately owned bank-installed a 800 kW fuel cell system as the primary power source for its new 200,000 sq.ft. Technology Center's critical loads. Fuel cells are also installed at several breweries and a winery- Sierra Nevada, Kirin, Asahi and Sapporo and Napa Wine Company. Untreated brewery effluent can undergo anaerobic digestion, which breaks

down organic compounds to generate methane, a hydrogen rich fuel. In Sierra Nevada brewery, 1 MW of fuel cells provide 24 x 7 power. It uses both anaerobic digester gas and natural gas from fuel. Fuel cell waste heat generated here is used in anaerobic digester process. The excess electricity is sold to grid and the company enjoys reduced fuel costs between 25 to 40%.
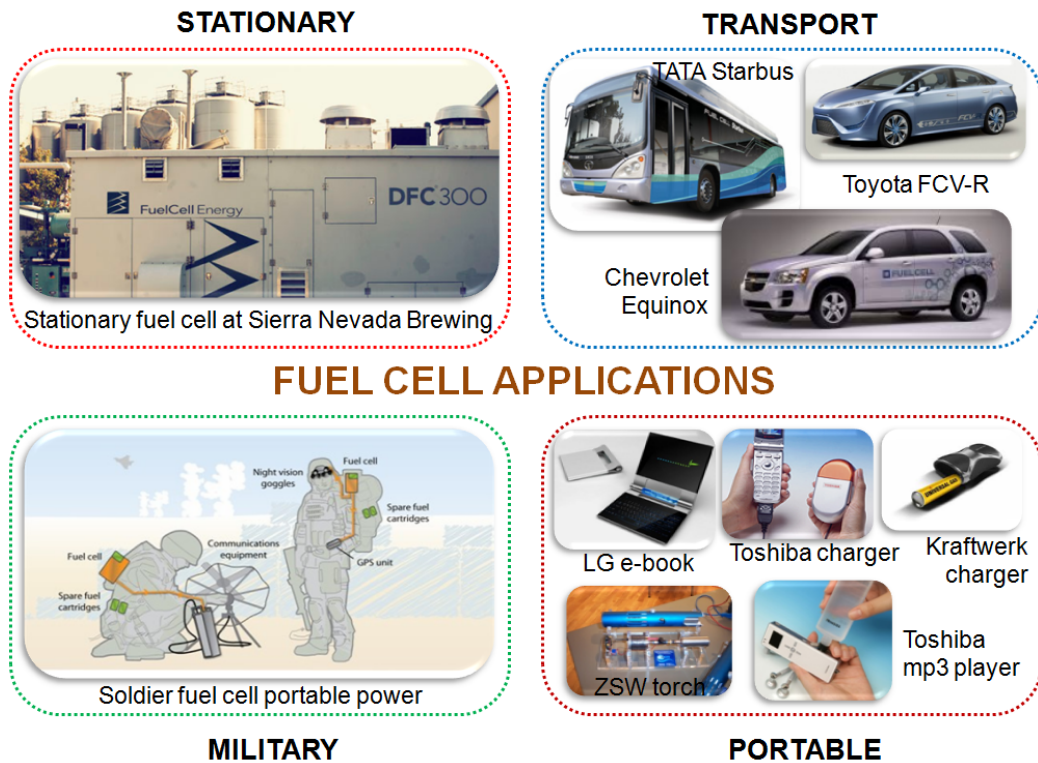
Fig. 1.4. Fuel cell applications

Transportation applications: A key commercial application of fuel cells is to possibly replace the IC engine in transportation applications. Today, all of the major automobile manufacturers and several related companies have demonstrated at least one prototype fuel cell vehicle and many have already been commissioned. General Motors, Toyota and Honda are the leading manufacturers of fuel cell cars and have successfully deployed them. Fuel cell powered buses are also quite popular and have been demonstrated in North and South America, Europe, Asia and Australia. Recently in India, Tata Motors demonstrated H_2 fuel cell powered bus. This hydrogen powered Starbus Fuel Cell bus is a zero-emission mass transport solution, for inter-city commute and has been developed in partnership with Indian Space Research

Organization (ISRO). Fuel cell systems being very much quieter than the diesel engines, fuel cell buses significantly reduce noise pollution as well. In another application, fuel cell forklifts have potential to effectively lower total logistics cost since they require minimal refilling and significantly less maintenance than electric forklifts, whose batteries must be periodically charged, refilled with water, and replaced. Due to the frequent starting and stopping during use, electric forklifts also experience numerous interruptions in current input and output - fuel cells ensure constant power delivery and performance, eliminating the reduction in voltage output that occurs as batteries discharge. Presently, fuel cell powered forklifts are extensively demonstrated at various companies in USA such as FedEx, General Motors and Wal-Mart.

Portable applications: Portable fuel cells are built into, or charge up, products that are designed to be moved. These include portable products (torches, vine trimmers, etc.), small personal electronics (mp3 players, cameras, etc.), large personal electronics (laptops, printers, radios, etc.), education kits and toys. To power this vast range of products, portable fuel cells are being developed in a wide range of sizes, from less than 5 W up to 500 kW. The portable fuel cell applications are mostly based on PEMFC and DMFC. Many companies (Toshiba, Manhattan Scientifics, Smart Fuel Cells and Ballard Power Systems) are developing fuel cell power packs as battery replacement for various consumer electronic devices. Examples are fuel cells packaged into portable devices such as laptops, computers, cellular phones, digital cameras, camcorders, and power tools. Portable devices are seen as employing up to 100 Wh of energy, with supplemental energy available through refueling cartridges.

Military applications: The specific attributes of fuel cells such as low noise/heat signature, faster refueling than recharge rate and long run time/constant power make them highly desirable for military applications. They are widely used in unmanned aerial vehicles (UAV), unmanned ground vehicles (UGV), soldier portable power, defense ground vehicles and forklifts for defense depots. An increasingly important vehicle application is a tactical mode of operation termed silent watch. These units are intended for uninterrupted battlefield observation. To this end, they are equipped with many different electronic devices. An important requirement is the complete absence

of acoustic and infrared emissions, as these would reveal their location. For this reason, a diesel generator cannot be used to power the equipment. Ordinary batteries are not able to provide enough power. Fuel cells are the only possibility as the power supply. One of the few examples where fuel cells are exclusively used for military purposes without its civil analog is that for submarine propulsion. Most recently, the US Army has employed fuel cell powered Chevy Colarado ZH_2 land rover for difficult terrain observation applications.

Since the focus of this research work is PEMFC, subsequent part of this Chapter is limited to discussion pertaining to this type of fuel cell system.

1.2. Proton Exchange Membrane Fuel Cell

PEMFC employs a thin proton conducting polymer membrane as electrolyte, most commonly Nafion®, a perfluorosulfonicacid (PFSA) ionomer. Protons are the ionic charge carrier in a PEMFC membrane. PEMFC operates at a relatively low temperature, <100 °C. The operating environment is kept well hydrated to ensure maximum membrane conductivity. Hydration is achieved by humidifying the inlet reactant gases. In a H_2 - O_2 system, at the anode, hydrogen gas is converted into protons and electrons and the protons pass though the conducting electrolyte. The electrons are forcefully passed through an external circuit to reach the cathode, where it combines with oxygen to complete the electrochemical reaction, producing electricity with water as a by-product.

1.2.1. PEM fuel cell components

The heart of PEMFC is a polymer, proton conducting membrane or proton exchange membrane, PEM. On each side of PEM is a porous electrode. The electrodes must be porous because the reactant gases are fed from the back and must reach the interface between the electrodes and the membrane, where the electrochemical reactions take place in the catalyst layers or, more precisely on the catalyst surface [Barbir 2012]. Technically, the catalyst layer may be a part of the porous electrode or part of the membrane, depending on the manufacturing process. The multilayer assembly of the PEM sandwiched between the two electrodes, anode and cathode is commonly called as membrane electrode assembly (MEA). The MEA

is then placed between the gas flow field plates which are also called as current collector/separator plates. These plates collect and conduct electrical current in both single and multi-cell configuration; whereas, in multi-cell configuration they separate the gases in the adjacent cells. At the same time, in multi-cell configuration, they physically/electrically connect the cathode of one cell to the anode of the adjacent cell, and hence, they are also called the bipolar plates. They provide pathways for flow of reactant gases (so-called flow fields), and also contribute to the cell's structural rigidity.

As shown in Fig. 1.5, the PEMFC consists of the following basic components:

1. Proton exchange membrane (PEM)

2. Catalyst layers (CLs, anode and cathode)

3. Gas diffusion layer (GDL)

4. Bipolar plates

Proton exchange membrane: Typically, the membranes for PEMFCs are made of perfluorosulfonic acid (PFSA) ionomer which is a copolymer of tetrafluoroethylene (TFE) and various perfluorosulfonate monomers [Smitha *et al.* 2005, Zaidi 2009]. They consist of hydrophobic and inert polymer backbone which is sulfonated with hydrophilic acid clusters to provide adequate conductivity. The SO_3H group of PFSA is ionically bonded, so the end of the side chain is SO_3^- ion together with H^+ ion. Because of their ionic nature, the ends of the side chains tend to cluster within the overall structure of the membrane. Although the teflon-like backbone is highly hydrophobic, the sulfonic acid at the end of the side chain is highly hydrophilic. The hydrophilic regions are created around the clusters of the sulphonated side chains and hence this material absorbs relatively large amounts of water. The movement of H^+ ions with the well hydrated regions makes the membrane proton conductive. In order to ensure adequate performance, membrane hydration is essential. However, excess water in the electrodes can result in electrode flooding and lower performance; so, precarious balance must be achieved. The best known membrane material for PEMFC till date is Nafion® made by M/s. Dupont which uses perfluorosulfonylfluoride ethyl-propyl-vinly ether (PSEPVE).

14
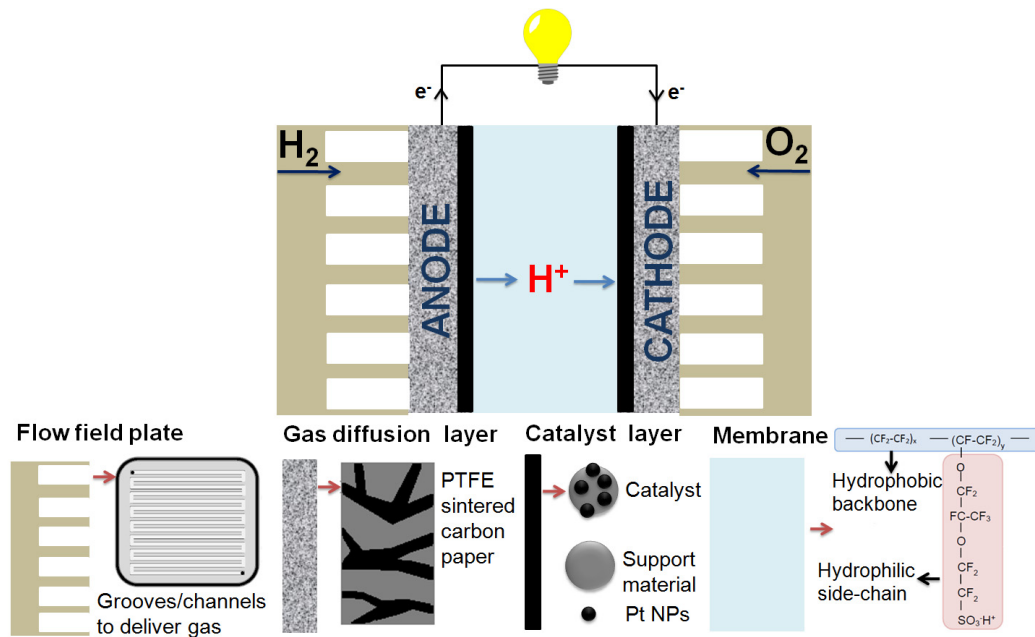
Fig. 1.5. PEM fuel cell components and working principle

Catalyst layers: Catalyst layers (CLs) are porous three dimensional structures in between the membrane and electrically conductive substrate. It must have facile transport of ions, electrons, reactants, and the products with a high electrochemically active surface area, where the reactants, catalyst, proton, and the electron conduction are all available to carry out the electrochemical reaction. The CL typically consists of considerable fraction of ionomer (30-35% by weight) to promote ionic transport to/from the main electrolyte membrane [Passalacqua *et al.* 2001]. The most common catalyst in PEMFCs for both hydrogen oxidation and oxygen reduction reactions is Pt [Lim *et al.* 2009].

Gas diffusion layer: The gas diffusion layer (GDL) consists of a woven carbon cloth or nonwoven carbon held in a carbonized resin binder to provide good electrical conductivity [Lim *et al.* 2004]. The basic carbon fiber in GDL is hydrophilic and thus will spontaneously imbibe liquid water into the porous structure resulting in flooding in PEMFC. Hence, a hydrophobic additive, typically PTFE (Teflon^{TM}) is added to prevent pore blockage and manage internal water distribution in PEMFC. At the GDL surface, the net effect of the PTFE additive and surface roughness is generally a hydrophobic with surface contact angle > 90°. The resulting PTFE-treated GDL structure is actually a mixed hydrophobic-hydrophilic structure with channels

favoring gas-phase and liquid-phase transport, despite the overall hydrophobic surface behavior. GDL also provides mechanical support to the MEA, preventing it from sagging into the flow fields; which otherwise might result in poor catalyst-GDL conductivity, elevated channel pressure drop, catalyst layer damage and local water pooling.

Bipolar plates: In a single-cell configuration (as shown in Fig. 1.5) there are no bipolar plates. The two plates on each side of the MEA may be considered as two halves of a bipolar plate. The full functioning bipolar plates are essential for multi-cell configurations by electrically connecting cathode of one cell to anode of the adjacent cell. The bipolar plates house grooves, or flow channels, which serve to deliver reactant gas to the cell and hence are also called as flow field plates. The primary function of bipolar plates is to connect the cells in series and separate the reactant gases in adjacent cells. They also provide structural support for the stack. In general, two families of materials have been used for PEMFC bipolar plates: graphite-based (including graphite/composite) materials and metallic materials [Barbir 2012]. Where graphite flow plates can be as thin as 2 mm, a stamped metal plate can be almost an order of magnitude thinner, stronger, inexpensive, and much easier to manufacture. The technical difficulties with metal bipolar plates include corrosion and difficulty in scaling up, which results in rapid electrolyte degradation and poor electrical contact resistance.

1.2.2. Basics of PEMFC thermodynamics and electrochemistry

PEMFC operation is based on the following electrochemical reactions happening simultaneously on the anode and the cathode.

Anodic electrochemical pathway (hydrogen oxidation reaction, HOR) can be explained as follows (acidic electrolytes):

$$\frac{1}{2}H_2 + H_2O \rightarrow H_3O^+ + e^-; \; E[H_2/H^+] = 0 \text{ V (Standard Hydrogen Electrode, SHE)} .. \text{(eqn. 1.1)}$$

While the cathodic pathway of oxygen reduction to water (oxygen reduction reaction, ORR) proceeds through a peroxide pathway, the rate quantification of several parallel steps has been investigated and mechanisms have been explained by multi-parallel

pathways [Damjanovic *et al.* 1966]. Following is the overall cathode reaction proposed in an acidic medium:

$$O_2 + 4H^+ + 4e^- \rightarrow 2H_2O; E[O_2/H_2O] = 1.23 \text{ V (SHE)} \ldots\ldots\ldots\ldots \text{ (eqn. 1.2)}$$
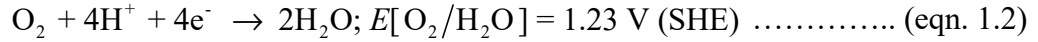
The overall reaction of PEMFC is as follows:

$$H_2 + \frac{1}{2}O_2 \leftrightarrow H_2O; E^0 [H_2/H_2O] = 1.23 \text{ V (SHE)} \ldots\ldots\ldots\ldots\ldots \text{ (eqn. 1.3)}$$
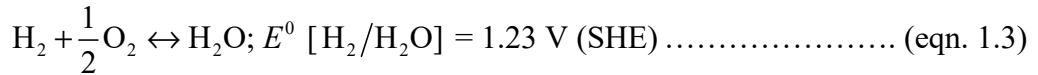
The maximum useful work that can be extracted from fuel cell is *ΔG* (Gibbs free energy) which represents the exploitable energy potential, or work potential of the system. The work carried out by fuel cell *i.e.* electrical work is defined as the work done by the charge Q moving in the field across a voltage E. Hence, electrical work done is:

$$W_{elec} = -\Delta G \ldots\ldots\ldots\ldots\ldots\ldots\ldots\ldots\ldots\ldots\ldots\ldots\ldots \text{ (eqn. 1.4)}$$

$$W_{elec} = Q \times E \ldots\ldots\ldots\ldots\ldots\ldots\ldots\ldots\ldots\ldots\ldots \text{ (eqn. 1.5)}$$

$$Q = n \times F \ldots\ldots\ldots\ldots\ldots\ldots\ldots\ldots\ldots\ldots\ldots\ldots \text{ (eqn. 1.6)}$$

Putting *eqn. 1.5* and *eqn. 1.6* in *eqn. 1.4* gives the following equation;

$$\Delta G = -nFE \ldots\ldots\ldots\ldots\ldots\ldots\ldots\ldots\ldots\ldots\ldots \text{ (eqn. 1.7)}$$

where n is the number of moles of electrons consumed or generated and F is the Faraday's constant (96487 Cmol^{-1} of species).

Thus, the Gibbs free energy change sets the magnitude of the reversible voltage for an electrochemical reaction. The reversible voltage generated by hydrogen-oxygen PEMFC under standard state conditions is thus

$$E^0 = -\Delta G^0_{rxn}/nF \ldots\ldots\ldots\ldots\ldots\ldots\ldots\ldots\ldots\ldots\ldots \text{ (eqn. 1.8)}$$

$$= -237,000 \text{ Jmol}^{-1}/(2 \text{ mol e}^- \text{ mol}^{-1}\text{reactant}^{-1})(96,485 \text{ Cmol}^{-1})$$

$$= +1.23 \text{ V}$$

where $E°$ is the standard state reversible voltage and *ΔG°*$_{rxn}$ is the standard state free energy change for the reaction.

The efficiency of any energy conversion device is defined as the ratio between useful energy output and energy input. In the case of PEMFC, the useful energy output is the electrical energy produced and the energy input is the enthalpy of hydrogen, that is, hydrogen's higher heating value (HHV). Assuming that all of the Gibbs free energy can be converted into electrical energy, the maximum possible efficiency of PEMFC is:

$$\varepsilon = \Delta G / \Delta H \quad \text{... (eqn. 1.9)}$$

$$= 237.34 \text{ kJmol}^{-1} / 286.02 \text{ kJmol}^{-1}$$
$$= 83\%$$

However, the real efficiency of a fuel cell must always be less than the reversible thermodynamic efficiency due to voltage and fuel utilization losses.

Under standard state conditions (room temperature, atmospheric pressure, unit activities of all species), applying thermodynamic principles, the highest voltage achievable from H_2-O_2 fuel cell is 1.23 V. The theoretical electrical potential E for PEMFC with operating pressure and temperature different from standard conditions is given by Nernst equation as follows:

$$E = E^0 - \frac{RT}{2F} \ln \frac{1}{p_{H_2} p_{O_2}^{1/2}} \quad \text{.. (eqn. 1.10)}$$

Where p's are the operating partial pressures of reactants and products in atmospheric units, T the temperature in K, R the gas constant in $Jkg^{-1}K^{-1}$ and F is the Faraday constant in $Cmol^{-1}$.

In operational PEMFC systems, the actual voltage obtained with load is different from the ideal/theoretical voltage from thermodynamics. Typically, the fuel cell suffers a voltage loss of >300 mV during operation. This potential drop or overpotential, η, defined as the difference in the measured potential and the theoretical potential is due to four major irreversibility aspects, namely: activation loss, fuel crossover, ohmic losses and mass transport losses.

$$\eta = E - E^0 \quad \text{... (eqn. 1.11)}$$

The activation losses result from the poor kinetics of reactions occurring at the electrodes and are described by Butler-Volmer equation [Barbir 2012, O'Hayre *et al.* 2016]. For a typical electrochemical reaction comprising of reduction (forward) and oxidation (reverse) process at electrode surface as shown in *eqn. 1.12*, the Butler-Volmer equation is derived from Transition State theory by consideration of kinetics of electrochemical reaction. k_f and k_b are the rates of the forward (reduction, cathodic) and backward (oxidation, anodic) reactions, respectively.

$$[Ox] + ne^- \underset{k_b}{\overset{k_f}{\rightleftharpoons}} [Red] \quad \text{................................…… (eqn. 1.12)}$$

In electrochemical reactions, current is produced by the reactants that reach the surface of the electrode and lose or gain electrons. The magnitude of this current depends on the number of electrons, *n*, the electrode area, the rate at which that species reach the electrode surface and react, $k_{f,b}$, and the reactant concentrations, $[Ox]$ and $[Red]$. The net current is the resultant of current generated from both forward and reverse reactions. The current density, *j*, (current per unit area) is therefore described by the *eqn. 1.13*.

$$j = nFk_f[Ox] - nFk_b[Red] \quad \text{.................................….. (eqn. 1.13)}$$

The rates of forward and backward reactions are given by Arrenhius and Transition State theories (*eqn. 1.14* and *eqn. 1.15*), where, K_0 is a constant associated with the forward or backward reaction, that includes the chemical component of the Gibbs free energy of the transition state. The exponential term refers to the electrical component of the Gibbs free energy of the transition state, where α is the charge transfer coefficient which typically ranges between 0.2 and 0.5 for most electrochemical reactions. α is associated with the electrode material properties and depends on the symmetry of the transition state. The sum of charge transfer coefficients for the oxidation and reduction reactions is equal to unity.

$$k_f = K_{0,f} \exp\left(\frac{-n\alpha F\eta}{RT}\right) Reduction\text{-}cathodic \quad \text{..............… (eqn. 1.14)}$$

$$k_b = K_{0,b} \exp\left(\frac{-n(1-\alpha)F\eta}{RT}\right) \quad Oxidation - anodic \ldots\ldots\ldots \text{(eqn. 1.15)}$$

Putting *eqn. 1.14* and *eqn. 1.15* into *eqn. 1.13* gives *eqn. 1.16*.

$$j = nFK_{0,f}[Ox]\exp\left(\frac{-n\alpha F\eta}{RT}\right) - nFK_{0,b}[Red]\exp\left(\frac{-n(1-\alpha)F\eta}{RT}\right) \ldots \text{(eqn. 1.16)}$$

At equilibrium, over-potential and external current are both zero. In this condition, the exchange current density, j_0, is defined as the current flowing equally in both directions (eqn. *1.17*). The larger the value of j_0, the faster the reaction.

$$j_0 = nFK_{0,f}[Ox] = nFK_{0,b}[Red] \ldots\ldots\ldots\ldots\ldots\ldots\ldots\ldots \text{(eqn.1.17)}$$

After substituting for the exchange current density, the final form of the current density is *eqn. 1.18*, which is called the Butler-Volmer equation.

$$j = j_0\left[\exp\left(\frac{-n\alpha F\eta}{RT}\right) - \exp\left(\frac{n[1-\alpha]F\eta}{RT}\right)\right] \ldots\ldots\ldots\ldots\ldots \text{(eqn. 1.18)}$$

The equation may be simplified by considering the situation far from equilibrium, where the magnitude of the over-potential is large (> 50-100 mV at room temperature). In this situation, the second exponential term in *eqn. 1.18* may be neglected (approximated equal to zero). The Butler-Volmer equation simplifies to *eqn. 1.19*.

$$j = j_0 \exp\left(\frac{-n\alpha F\eta}{RT}\right) \ldots\ldots\ldots\ldots\ldots\ldots\ldots\ldots\ldots\ldots\ldots \text{(eqn. 1.19)}$$

Solving *eqn. 1.19* for η gives *eqn. 1.20*.

$$\eta = -\frac{RT}{\alpha nF}\ln j_0 + \frac{RT}{\alpha nF}\ln j \ldots\ldots\ldots\ldots\ldots\ldots\ldots\ldots\ldots \text{(eqn. 1.20)}$$

The generalization of *eqn. 1.20* in the form of *eqn. 1.21* is known as the Tafel equation, and *b* is called the Tafel slope.

$$\eta = a + b\log j \ldots\ldots\ldots\ldots\ldots\ldots\ldots\ldots\ldots\ldots\ldots\ldots \text{(eqn. 1.21)}$$

It can be seen from the Tafel equation that the over-potential approximates to

straight line when plotted *vs.* the log of current density, *j*, (mAcm^{-2}). The point at which the best fit line intercepts the current density axis corresponds to the exchange current density, *j$_0$* and the charge transfer coefficient and number of electrons transferred in the reaction determines the gradient or Tafel slope. This behavior was observed and reported by Tafel in 1905 and later was demonstrated to have a theoretical basis in the form of Butler-Volmer equation. So, the Butler-Volmer equation basically states that the current produced by an electrochemical reaction increases exponentially with activation over-voltage which represents voltage that is sacrificed to overcome the barrier associated with the electrochemical reaction. Thus, Butler-Volmer equation shows that the generation of more current from the fuel cell occurs at the cost of lost voltage.

Increasing *j$_0$* will result in a decrease of the over-potential from activation loss. *j$_0$* may be increased by increasing the temperature (improving turnover on catalytic sites), increasing the reactant concentration and increasing the pressure (improving site occupancy and increasing theoretical potential as previously described), increasing the surface area (increasing the number of sites), and by using a more effective catalyst (lowering the activation barrier for reaction).

It is the cathodic oxygen reduction reaction (ORR) that is largely responsible for the activation loss observed for hydrogen PEMFCs. This activation loss accounts for the most significant portion of the loss of the cell voltage (> 300 mV) from the theoretical value when compared to fuel crossover, resistive and mass transport losses since these losses can be minimized and controlled by optimizing experimental parameters. For this reason, a key research target is to develop more active catalysts for ORR that has improved durability. Improved activity would enable increased performance or maintain equivalent performance while allowing a decrease in metal loading and therefore cost. In addition, improved durability would extend operational lifetimes.

1.3. Oxygen Reduction Reaction (ORR) and Pt catalyst

Oxygen reduction is an important electrochemical process because of the fact that it plays a central and decisive role in electrochemical energy devices, particularly

in PEMFC. ORR is a multi-electron reaction involving different reaction intermediates, the kinetics and mechanism of which depends on both the electro-catalyst and the electrolyte. In acidic electrolyte, ORR may proceed by two pathways: either by (i) the direct four electron reduction pathway forming water, or by (ii) the indirect two electron reduction pathway generating hydrogen peroxide which may be then electrochemically reduced to water or undergo chemical decomposition.

Direct reduction (4e⁻ pathway)

$$O_2 + 4H^+ + 4e^- \rightarrow 2H_2O; E^0[O_2/H_2O] = 1.23 \text{ V} \quad \text{…....…………..} \quad \text{(eqn. 1.22)}$$
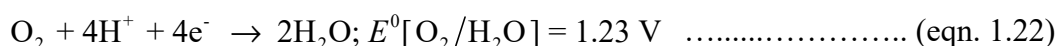
Indirect reduction (2e⁻ pathway)

$$O_2 + 2H^+ + 2e^- \rightarrow H_2O_2; E^0[O_2/H_2O_2] = 0.682 \text{ V} \quad \text{…..…………..} \quad \text{(eqn. 1.23)}$$

followed by further reduction via

$$H_2O_2 + 2H^+ + 2e^- \rightarrow 2H_2O; E^0[H_2O_2/H_2O] = 1.77 \text{ V} \quad \text{…………..} \quad \text{(eqn. 1.24)}$$
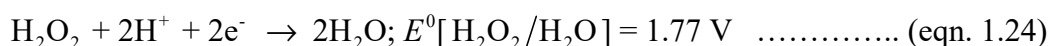
or chemical decomposition via

$$2H_2O_2 \rightarrow 2H_2O + O_2 \quad \text{………………………..} \quad \text{(eqn. 1.25)}$$

Extensive experimental and theoretical studies have been performed and continue to be performed to understand which pathway is followed and the mechanistic steps. In the last two decades, several ORR models for the reaction pathways have been described; however, the exact mechanism is still a subject of much debate. A commonly reported reaction scheme for ORR [Markovic *et al.* 2001] is shown in Fig. 1.6. This simplified reaction scheme is based on the reaction schemes introduced by Wroblowa *et al.* [Wroblowa *et al.* 1976] and Bagotskii *et al.* [Bagotskii *et al.* 1969] and is valid for both acidic and basic environments on all the electrode materials. Based on this scheme, the pre-adsorbed oxygen can be electrochemically reduced either directly to water with the rate constant k_1 (4e⁻) or to H_2O_{2ad} with the rate constant k_2 (2e⁻). The adsorbed peroxide can be electrochemically reduced to water with the rate constant k_3, catalytically (chemically) decomposed on the electrode surface *(k_4)* or desorbed into the bulk of the solution *(k_5)*.

$$O_{2,bulk} \longrightarrow O_{2,ad} \underset{k_4}{\overset{k_2}{\rightleftharpoons}} H_2O_{2,ad} \overset{k_3}{\longrightarrow} H_2O$$

with k_1 arc from $O_{2,ad}$ to H_2O, and k_5 between $H_2O_{2,ad}$ and $H_2O_{2,bulk}$
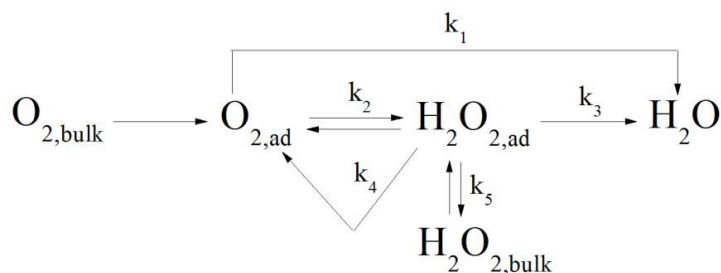
Fig. 1.6. Simplified schematic of the ORR pathway [Markovic *et al.* 2001]

The different reaction pathways depend on different adsorption states of oxygen molecule on metal surface. Three models for oxygen adsorption modes and the corresponding ORR pathways have been proposed [Tarasevich *et al.* 1983, Hamann *et al.* 1998] and are illustrated in Fig. 1.7. The Griffiths model involves edge-wise adsorption of oxygen molecule on metal sites which weakens O-O bond and leads to dissociative adsorption of oxygen molecule. Therefore, four electron reduction to water according to pathway I is favored. In the case of Pauling model, end-on adsorption of oxygen molecule occurs through a single bond to the metal surface resulting in associative pathway *via* superoxide and peroxide species as shown in pathway II. This can lead to the formation of four electron product, H_2O or H_2O_2 *via* two electron reduction. The third mode of binding is described by the bridge mode where oxygen molecule is adsorbed across two metal sites. Similar to pathway I, dissociation of oxygen molecule occur on metal sites and the four electron pathway forming H_2O is favored as shown in pathway III.

In order to obtain maximum efficiency from fuel cell and to avoid the detrimental effects on fuel cell components by peroxide, it is desirable to achieve a four-electron reduction. The oxygen reduction at Pt is characterized under most conditions by a four-electron reduction. Besides, the exchange current densities on Pt are the highest among the noble metals, about 10^{-11}–10^{-9} Acm^{-2} in both acid and alkaline solutions [O'Hayre *et al.* 2016]. Therefore, Pt is the best electro-catalyst for ORR until now. The high activity of Pt towards ORR has also been proven through density functional theory (DFT) modeling. Through the computational screening of different materials, it is possible to rank different materials based on how their surfaces interact with oxygen.

Griffiths model   **Pathway**
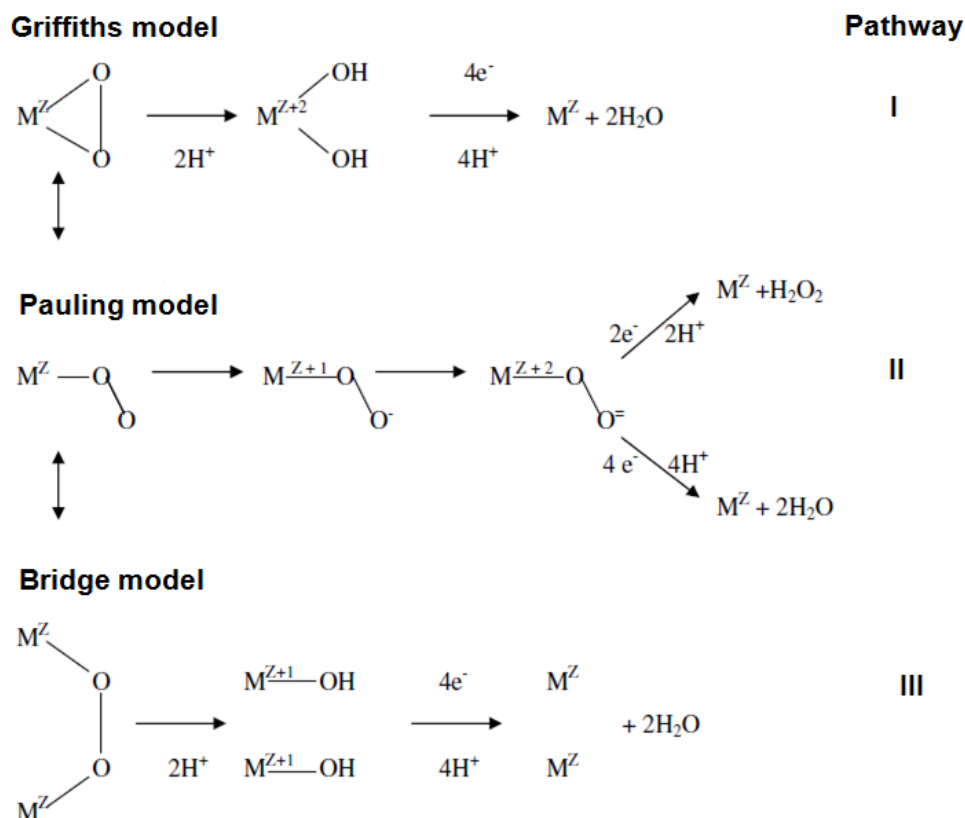
Fig. 1.7. Models for adsorbed oxygen and corresponding reaction pathways for oxygen reduction

Norskov *et al.* [Nørskov *et al.* 2004] generated a ranking of different metal surfaces which was illustrated in the form of a volcano curve (Fig. 1.8), where the oxygen reduction activity is given as a function of the oxygen binding energy. Activation energy for ORR is a function of interaction between metal and adsorbate. Weaker bonding results in larger activation energy for the adsorbate to interact with oxygen while stronger bonding leads to the blockage of active sites by strongly bonded intermediates. So, a good catalyst should be active enough to bond and at the same time noble enough to release the products to have a facile ORR. In the volcano curve, Pt occupies the optimum position among all studied metals demonstrating its superior activity towards ORR. So, from this diagram, the reasoning behind the adoption of Pt as an ideal ORR catalyst becomes evident.

1.3.1. Need for more active ORR catalyst

As mentioned previously, Pt is the most commonly employed ORR catalyst in

PEMFC, but it suffers from certain disadvantages and limitations. The foremost limitation being the fact that Pt is a very expensive precious metal and is in limited global supply. One approach towards reducing the content of Pt in catalysts is to support Pt on high surface area materials. Carbon-based materials have high surface area to disperse the metal grains and in addition, they have high electronic conductivity. This helps in electron transfer during electrochemical reactions and hence participate indirectly in catalytic activity of catalyst . Supporting Pt catalysts on high surface area carbon materials increases the electrochemical surface area (ESA). These are the active sites where actual electrochemical reactions occur and hence, an increase in ESA results in an increase of catalytic activity.
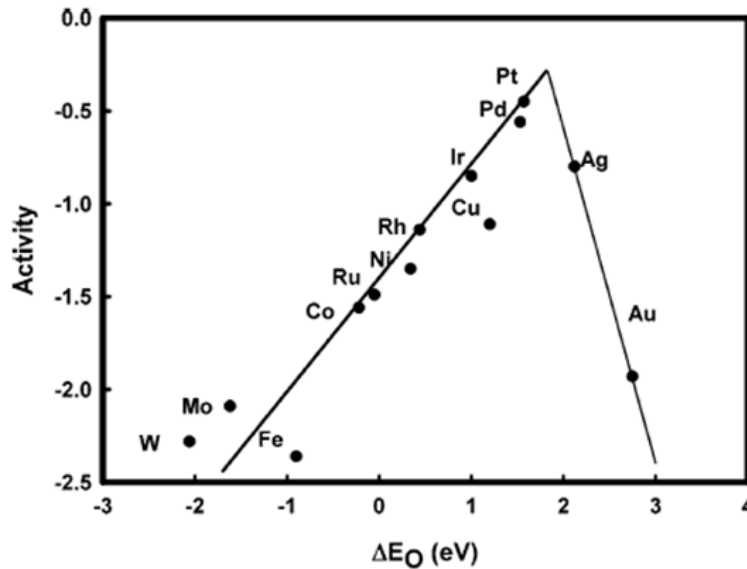
Fig. 1.8. Volcano curve for ORR actvivity on different metals [Nørskov *et al.* 2004]

The durability concerns at the cathode make Pt prone to severe degradation due to harsh operating conditions. The cathode catalyst in PEMFC gets exposed to highly corrosive conditions emanating from the high electrode potential, low pH and high oxygen and water content which deteriorate its catalytic activity. As reported by Couper *et al.*, the problems of finding a good electro-catalyst (and a stable, inert substrate) are compounded by the instability of most materials to corrosion close to the reversible potential for the O_2/H_2O couple [Couper *et al.* 1990]. Corrosion can be accelerated by the presence of trace hydrogen peroxide and the lifetime of candidate catalysts can be reduced by poisoning and sintering. Substrate corrosion is as difficult

to avoid as dissolution of the catalyst. Specifically, carbon support materials are thermodynamically unstable at cathode potentials in PEMFCs. Carbon is lost from the system through oxidation leading to significant losses of carbon over a short period of time. The instability of carbon support affects the loss of platinum surface area following both Pt particle sintering and Pt release from the carbon support [Gruver 1978, McBreen *et al.* 1981, Stonehart 1984]. Therefore, various alternatives to catalyst supports are being searched extensively.

Recently, nanostructured carbon materials with graphitic structure, such as carbon nanotubes (CNTs), carbon nanofibers (CNFs), graphene and their derivatives were investigated as catalyst supports in fuel cells [Antolini 2009]. The higher catalytic activity of the Pt based catalysts supported on these nanostructured carbon supports than that of the same catalysts supported on carbon blacks was ascribed to their unique structure and properties such as high surface area, good electronic conductivity and chemical stability. Tests carried out in PEMFC conditions indicated that these materials can be more durable and can outlast the lifetime of conventional Vulcan XC-72 [Maiyalagan *et al.* 2005, Kongkanand *et al.* 2006, Wang *et al.* 2006]. However, these alternative materials do not prevent carbon oxidation completely; but rather help to decrease the rate of corrosion. Hence, non-carbon materials have also received attention and have been investigated as support materials for catalyst.

Conducting oxides are emerging candidates that are gaining more and more attention as oxidation resistant catalyst supports. In addition to their high stability in fuel cell environment, many metal oxide supports can tune the intrinsic catalytic activity of Pt as well through metal-support interactions. Indeed, it is well known that metal oxides such as RuO_2, SnO_2 and WO_3 enhance the catalytic activity of Pt for methanol and ethanol oxidation [Long *et al.* 2000, Park *et al.* 2003, Jiang *et al.* 2005, Lu *et al.* 2005, Raghuveer *et al.* 2005, Jiang *et al.* 2007]. Also, TiO_2 based catalysts have emerged as a promising class of ORR catalyst supports for PEMFCs [Lee *et al.* 2008, Chhina *et al.* 2009, Cerri *et al.* 2013, Siracusano *et al.* 2013, Takabatake *et al.* 2014]. Additionally, the feasibility of Strong Metal Support Interactions (SMSI) between Pt and TiO_2 brings in newer possibilities for synergistic catalytic activity making this class of support materials more promising [Baker *et al.* 1979, Horsley

1979, Long *et al.* 2013].

Another major disadvantage associated with Pt catalysts is that the dissociative adsorption of oxygen is very slow on Pt and the reduction of adsorbed oxygen atoms takes place in many steps. Also, at potentials >0.8 V, some oxygen species like OH⁻ from electrolyte get adsorbed onto Pt, reducing the number of active sites and thus lower Pt utilization [Mukerjee *et al.* 1995, Lee *et al.* 1998]. These adsorbed OH⁻ species poison the Pt electrode and is one of the main causes of over-potential in the ORR in acid medium [Balbuena *et al.* 2004]. Towards this, Pt alloy (Pt-M, M is a transition metal) catalysts have been found to be promising [Toda *et al.* 1999]. Breaking off of the O-O bond of the oxygen and reduction of the adsorbed atomic oxygen are found to be more facile when Pt is combined with another transition metal [Maghsodi *et al.* 2011]. Based on simple thermodynamic principles, Fernandez *et al.* provided guidelines for the design of binary and multi-component, electro-catalytic materials for the reduction of oxygen, which facilitates easy breakage of the O-O bond of O_2 and reduce adsorbed atomic oxygen [Fernández *et al.* 2005]. Bimetallic Pt-M catalysts (M is a transition metal such as Pd, Ni, Co, Ag, Au, Fe, etc.) have been studied and have shown enhanced ORR electro-catalysis compared to Pt catalyst alone. Moreover, the presence of an alloy element reduces the cost of catalyst as compared to pure Pt catalysts.

In the following sections, an overview of the recent developments made in the field of Pt based cathode catalysts for PEMFC is presented. Particular attention has been given to the electrochemical activity and durability of Pt based ORR catalysts and their influence on fuel cell performance.

1.4. Nano-structured carbon supported, Pt-based catalyst

Carbon blacks (CBs), specifically Vulcan XC-72, are the most commonly used support materials in low temperature fuel cells. These carbon materials offer the advantage of large specific surface area (237 m^2g^{-1} for Vulcan XC-72R [Li *et al.* 2003]), high electrical conductivity (4 Scm^{-1} for Vulcan XC-72R [Li *et al.* 2003]) and easy availability which contributes in the overall cost reduction of fuel cells. Despite these favorable attributes, CB suffers from some serious drawbacks such as the

presence of deep micro-pores which trap the catalyst NPs making them inaccessible to reactants; hence, causing reduction in catalytic activity. Adding to it, the dense networks of pores affects the interaction between Nafion® ionomer and catalyst NPs which in turn results in significant mass transport limitations and lower Pt utilization. CB also suffers from electrochemical oxidation under working PEMFC conditions forming CO_2 at the cathode [Pourbaix 1974]. The oxidation of carbon to CO_2 leads to the loss of catalyst NPs from the support which significantly reduces catalyst active surface area, drastically affecting the performance and operation life-time of PEMFC. The CO_2 formation at the cathode can be generalized by *eqn. 1.26*.

$$C + 2H_2O \rightarrow CO_2 + 4H^+ + 4e^-$$ …………………….…… (eqn. 1.26)

The standard potential for the electrochemical oxidation of carbon to carbon dioxide is 0.207 V *vs*. reversible hydrogen electrode (RHE) at 25 °C [Pourbaix 1974]. Therefore, under typical PEMFC cathode operation conditions, carbon corrosion is not only thermodynamically feasible due to the high potentials (0.6–1.2 V), but also kinetically enhanced by the elevated temperatures (50–90 °C). Further, the carbon corrosion is accelerated at lower pH and higher humidity which are often encountered under working PEMFC conditions.

Recently, nano-structured materials have gathered enormous attention because of their exceptional attributes for catalysis such as high catalytic activity, mechanical and electrical properties which are attained by way of their dimensions. In this context, the role of the nano-structure in carbon supports like carbon nanotubes (CNTs) and graphene has been much emphasized. The main purposes for using nano-structured support based Pt catalysts are to reduce Pt loading through increasing the catalyst utilization, and improving the catalyst activity and total performance. The higher catalytic activity of Pt and Pt-based catalysts supported on CNTs than that of the same catalysts supported on CBs was ascribed to their unique structure and properties such as high surface area, good electronic conductivity and chemical stability [Bessel *et al.* 2001, Steigerwalt *et al.* 2001, Maiyalagan *et al.* 2005, Knupp *et al.* 2008]. Tests carried out in PEMFC conditions indicated that these materials can be more durable and can outperform the lifetime of the most widely used Vulcan XC-72.

CNTs are 2D nanostructures, which are typically tubes formed by rolled up single sheets of hexagonally arranged carbon atoms. They may be single walled (SWCNT) or multi-walled (MWCNT). Depending on the structure, SWCNTs can be conducting, i.e. metallic as well as semi-conducting in nature based upon their tube diameter and helicity [Saito *et al.* 1992]. MWCNTs can have diameters of a few tens of nanometres with a spacing of 0.34 nm between cylindrical walls. CNTs are the most well-known and by far the most widely explored carbon nanostructures for application as catalyst support in fuel cells. Both SWCNTs and MWCNTs have been extensively studied for PEMFC catalyst support applications [Che *et al.* 1998, Long *et al.* 2000, Mawhinney *et al.* 2000, Dudin *et al.* 2010]. Functionalization of CNTs using strong acids like HNO_3, H_2SO_4 are generally carried out to introduce surface oxygen groups such as hydroxyl, carboxyl, carbonyl and sulfate. These surface functional groups function as metal-anchoring sites to facilitate metal nuclei formation and electro-catalyst's deposition and hence helps in better dispersion of catalyst NPs on the CNT support [He *et al.* 2004]. However, this method can damage the structure of CNTs and severely affects its mechanical and electrical properties [Rausch *et al.* 2010]. There are lot of reports [Novikova *et al.* 2017, Du *et al.* 2014, Karthikeyan *et al.* 2015, Gupta *et al.* 2016, Gupta *et al.* 2016, Koh *et al.* 2016, Rosado *et al.* 2016, Yoshii *et al.* 2016, Hussain *et al.* 2017, Schonvogel *et al.* 2017, Zapata-Fernández *et al.* 2017], testifying the applicability of Pt and Pt-M catalysts supported on CNTs as cathode materials in PEMFCs.

Hussain *et al.* reported Pt/MWCNT catalysts prepared using controlled electrochemical deposition from Ar-saturated H_2PtCl_6 solution [Hussain *et al.* 2017]. The electro-deposition parameters (deposition potential and number of pulses) were varied to observe changes in the ORR catalytic activity of Pt/MWCNT catalysts. It was revealed that specific activities of the catalysts decreased with number of pulses and were independent of the deposition potential. Moreover, all Pt/MWCNT catalysts exhibited better ORR activity than the commercial Pt/C catalyst. The Pt/MWCNT cathode catalysts also showed remarkable stability during repetitive potential cycling (5000 cycles) in half cell mode with 0.5 M H_2SO_4 as electrolyte. In the works of Novikova *et al.*

[Novikova *et al.* 2017] Pt NPs supported on different MWCNTs and conventional Vulcan XC-72 were prepared *via* electro-chemical dispersion using ac current. The prepared catalysts were evaluated as ORR catalyst in three-electrode configuration with 0.5 M H_2SO_4 electrolyte. The ORR activity of the MWCNT supported Pt catalysts exceeded that of Vulcan XC-72 supported Pt catalyst. Also, MWCNT supported catalysts exhibited lower loss of ESA ($\leq$ 35%) as compared to 60% ESA loss of Vulcan XC-72 supported Pt catalysts after 10,000 cycles of accelerated potential cycling tests, demonstrating higher durability. The catalyst's performance was also evaluated in single cell PEMFC in H_2 and air configuration at 25 °C with Pt loading of 0.4 $mgcm^{-2}$ and the corresponding polarization and power density curves is shown in Fig. 1.9. Maximum power density of 120 $mWcm^{-2}$ was attained with MWCNT supported Pt cathode catalyst.
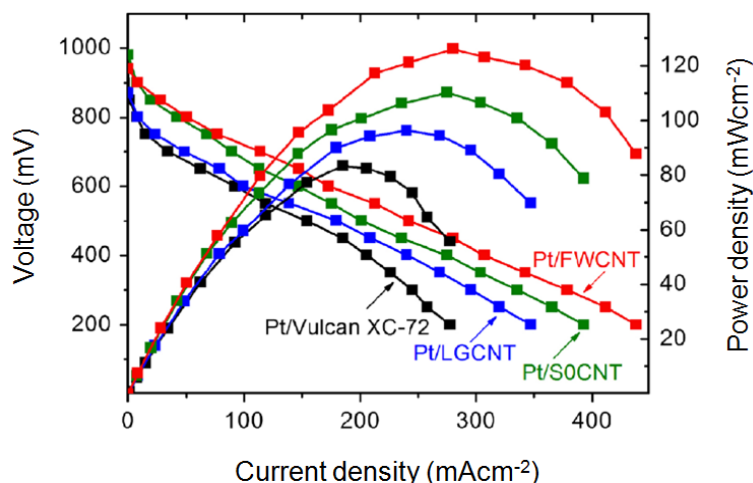
Fig. 1.9. Voltammetric and power characteristics of air–hydrogen MEA with Pt loading of ~ 0.4 $mgcm^{-2}$ at 100% humidity, and 1 atm air pressure [Novikova *et al.* 2017]

Yoshi *et al.* demonstrated highly durable Pt/SWCNT catalyst prepared through magnetron sputtering of Pt NPs dispersed in ionic liquid (IL) [Yoshii *et al.* 2016]. The enhanced performance was attributed to the suppression of carbon corrosion by the IL thin layer that exists between the Pt NPs and carbon support responsible for 75% ESA retention of Pt/SWCNT catalyst even after 15,000 cycles of accelerated degradation tests. The authors also showed

promising results for extension of this material tailoring process for designing durable cathode catalysts for PEMFC systems. Gupta *et al.* studied the effect of pH media during the reduction process on PEMFC performance of Pt/MWCNT catalyst [Gupta *et al.* 2016]. Higher power density was obtained with alkaline medium (156 mWcm^{-2}) prepared catalysts as compared to acidic medium (72 mWcm^{-2}) prepared Pt/MWCNT catalyst (Fig. 1.10). Improved fuel cell performance was attributed to facile formation of smaller Pt NPs and their uniform dispersion onto MWCNT support under alkaline conditions. In another work, Gupta *et al.* investigated the effect of pH and atmospheric gas condition during the synthesis of Pt NPs supported on pristine and purified MWCNTs through ethylene glycol reduction route on ORR catalytic activity [Gupta *et al.* 2016]. The fuel cell performance evaluation of the catalysts revealed better performance with purified CNT supported Pt catalyst prepared under N_2 atmosphere at neutral pH. The purified CNT supported catalyst exhibited 2 times higher power density than pristine CNT supported Pt catalyst under identical conditions. The results demonstrated suitability of the employed synthesis conditions and purified MWCNT to achieve high performing Pt/CNT catalyst for PEMFC applications.
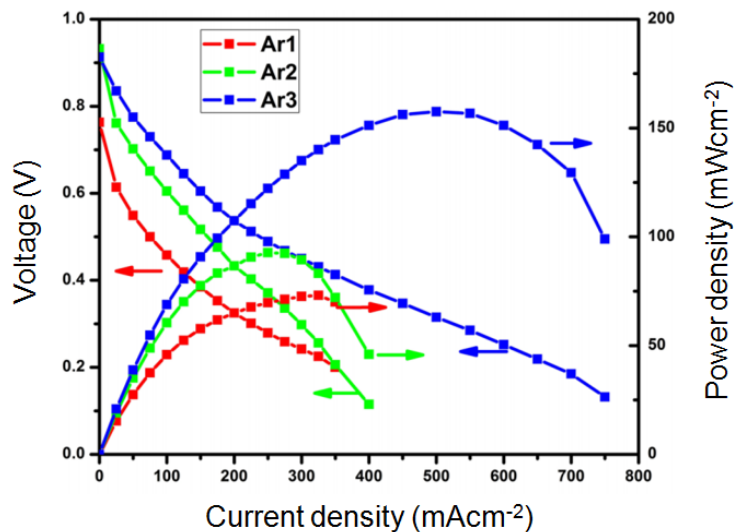
Fig. 1.10. Polarization curves for Pt/MWCNT catalysts Ar1 (pH 2), Ar2 (pH 7), and Ar3 (pH 11) [Gupta *et al.* 2016]

Schonvogel *et al.* investigated the influence of four supports for Pt *viz.* CB, MWCNTs, reduced graphene oxide (rGO) and a nano-composite of indium tin oxide with rGO (ITO-rGO) on durability behavior of the catalysts [Schonvogel *et al.* 2017]. The study showed comparable degradation of the catalysts through ESA and ORR activity loss measurements after 1000 cycles of accelerated stress tests. However, double layer capacitance investigations and formation of HQ/Q species on the carbon surfaces revealed the highest electrochemical stability with MWCNTs. The study demonstrated that MWCNTs meet the stability criteria of low corrosion for PEMFC application. Koh et al. [Koh *et al.* 2016] in their study demonstrated KOH activation of MWCNT as an effective strategy to modify MWCNT surface to achieve high ESA making them more suitable for PEMFC applications as electro-catalytic materials. In another approach to achieve enhanced ORR activity and durability with MWCNT supported Pt catalysts, Karthikeyan *et al.* reported combined chemical modification of MWCNTs with oxygen and nitrogen functionalities and compared the performance with commercial Pt/C catalyst in three-electrode configuration with 0.1 M HClO$_4$ electrolyte [Karthikeyan *et al.* 2015]. The electrochemical studies showed comparable ORR activity of Pt/*f*-MWCNT (259 Ag^{-1}) with Pt/C (252 Ag^{-1}); however, the former catalyst exhibited 30% higher durability after 5000 cycles of accelerated durability tests.

Rosado *et al.* reported bimetallic Pt-Ni supported on MWCNT as ORR catalyst for PEMFC and evaluated their performance in half cell configuration. Results revealed better performance of bimetallic catalysts as compared to commercial catalyst demonstrating Pt-Ni/MWCNT as promising materials for PEMFC applications [Rosado *et al.* 2016]. In the works of Du *et al.* high performing PtNi-MWCNT hybrid catalysts for ORR was prepared through a simple one-pot synthesis in aqueous medium at room temperature without using any organic solvents, templates or growth inducing catalysts [Du *et al.* 2014]. The ORR activity evaluated in half cell mode revealed 4.2 times higher specific area activity of PtNi-MWCNT (1.07 mAcm^{-2}) as compared to commercial Pt/C catalyst (0.24 mAcm^{-2}). PtNi-MWCNT also exhibited 4% higher mass activity

than United States (US) Department of Energy (DOE) mass activity target (0.44 Amg^{-1}) for 2017-2020 establishing its capability as cathode catalyst in PEMFC. Zapata-Fernández *et al.* demonstrated Pt-Pd/MWCNT as a highly promising ORR catalyst for PEMFC through their half cell ORR kinetics investigations [Zapata-Fernández *et al.* 2017]. Pt-Pd/MWCNT catalysts were synthesized *via* simple and fast galvanic displacement (GD) method without the requirement of any surfactants, additive reagent, or post-treatment in the synthesis of bimetallic materials. The effect of Pt concentration and sonication in GD bath on ORR activity was studied in detail. The results indicated favorable effects of sonication of metal NPs dispersion on MWCNT support and among all studied Pt-Pd compositions, $Pt_{10}Pd_{90}$/MWCNT catalyst showed the highest catalytic activity, negligible amount of H_2O_2 generation and 4 electrons transfer for ORR, making a case for the plausible use of this material as a novel alternative catalyst for ORR in PEMFC.

Since its discovery in 2004 by Geim *et al.*, graphene has attracted a lot of interest for further pursuance of research using this wonder material [Novoselov *et al.* 2005]. Graphene is an atomically thin sheet of hexagonally arranged carbon atoms with high electronic conductivity and one having the fastest electron transfer capabilities. The recent advances in graphene nano-electronics have opened a new arena for utilizing these 2D planar structures as support material in PEMFCs. Graphene has aroused interest as prospective support owing to its high electron transfer rate, large surface area and high conductivity [Liu *et al.* 2010, Qu *et al.* 2010]. The 2D planar structure of the carbon sheet allows both the edge planes and basal planes to interact with the catalyst NPs. The rippled but planar sheet structure also provides very high surface area for attaching catalyst NPs. One hopes to employ such 2D sheets as conductive mats to both anchor electro-catalysts and modulate the electrochemical reactions in a controlled manner.

In the work of Hsieh *et al.*, Pt NPs on graphene and its application to fuel cell was presented [Hsieh *et al.* 2013]. In this study, Pt NPs on graphene (PtNPs/GN) were formed from graphite oxide by two routes (one-step and two-step routes). For one-

step route, a fixed weight of graphene oxide (GO) and a variable weight of $H_2PtCl_6 \cdot 6H_2O$ was used with ethylene glycol as the reducing agent. In the two-step route, first the reduction of GO films was done to obtain graphene followed by deposition of Pt particles through ethylene glycol reduction route. The results showed that the Pt particles have smaller size and better distribution on the surface of graphene *via* two-step reduction route. The Pt/graphene nano-composites showed higher electrochemical active surface area (159.48 m^2g^{-1}) and excellent electro-catalytic activity towards the reduction of oxygen. These results obtained were attributed to very high Pt loading and the small size of Pt NPs dispersed uniformly on graphene nano-sheets.

Shao *et al.*, reported graphene nanoplatelets (GNPs), which exhibited the advantages of both single-layer graphene and highly graphitic carbon, as a durable alternative support material for Pt NPs for ORR [Shao *et al.* 2010]. Pt NPs were deposited on poly(diallyldimethylammonium chloride) (PDDA)-coated GNP and CNT. The activity of Pt/GNP towards oxygen reduction was comparable to commercial Etek Pt/C and Pt/CNT catalyst; but, the durability of Pt/GNP was greatly enhanced (2–3 times that of Pt/CNT and Etek Pt/C). These were attributed to the intrinsic high graphitization degree of GNP and the enhanced Pt-carbon interaction in Pt/GNP. Considering the fact that GNP can be easily mass produced from graphite, GNP is a promising, low-cost, and durable electro-catalyst support for oxygen reduction in fuel cells. Daş *et al.* in their study investigated the effectiveness of two synthetic approaches: supercritical carbon dioxide ($scCO_2$) deposition and microwave (MW) irradiation methods to synthesize Pt NPs uniformly dispersed on graphene nanoplatelets (G) as catalyst support [Daş *et al.* 2016]. The study revealed formation of smaller Pt NPs on G through $scCO_2$ deposition route (Pt/G2 1.5-1.6 nm) as compared to MW irradiation route (Pt/G1 3.1-3.4 nm) as shown by transmission electron microscope (TEM) images in Fig. 1.11. Pt/G2 exhibited higher ESA and fuel cell performance as compared to Pt/G1 catalyst. The improved performance of the catalyst prepared *via* $scCO_2$ deposition route was attributed to the decrease in degree of agglomeration of Pt NPs during the reduction process because of the high interaction between adsorbed precursor ions and the graphene surface compared to the

34

MW irradiation method. Pt/G2 also demonstrated higher corrosion resistance with no significant change in Tafel slope after 24 h of accelerated carbon corrosion tests. However, the PEMFC results showed that further improvement in the catalyst properties are needed in order to get better performance when compared to commercial catalyst.
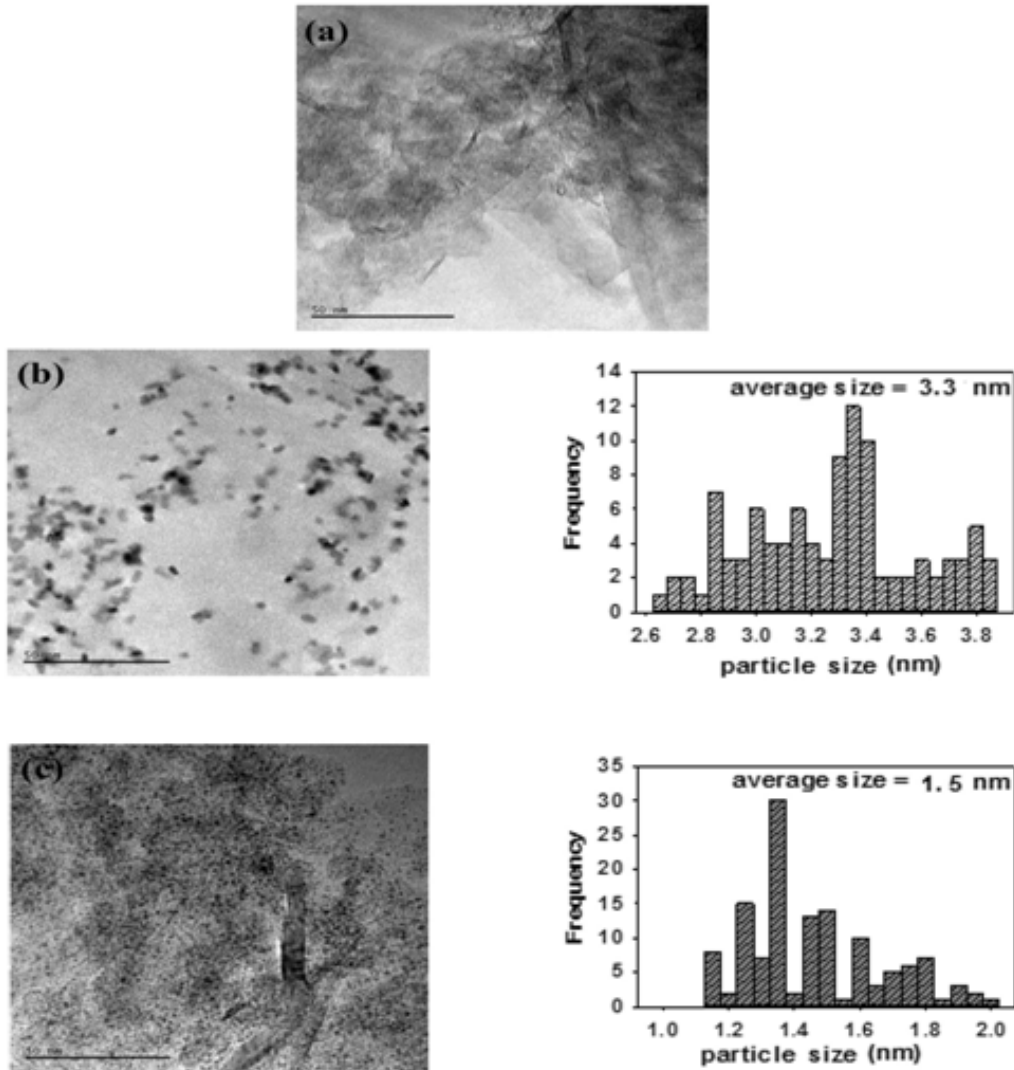
Fig. 1.11. TEM images and Pt particle size histograms of (a) plain graphene nanoplatelets, (b) Pt/G1, and (c) Pt/G2 [Daş *et al.* 2016]

Oztuna *et al.* reported mesoporous graphene aerogel (GA) supported Pt NPs prepared *via* supercritical deposition (SCD) using supercritical CO_2 (scCO_2) as ORR catalyst for PEMFC [Oztuna *et al.* 2017]. The Pt precursor was dissolved in scCO_2 and adsorbed onto GA at 35 °C and 10.7 MPa and was converted to its metal form

under atmospheric pressure at 400 °C, 600 °C and 800 °C. The effects of precursor conversion temperature on the structural properties of the composites and ORR activity were investigated. The results revealed that SCD helped to preserve the textural properties of the GA after the Pt NPs deposition, and Pt/GA converted at 600 °C exhibited an enhanced mass activity of 30.6 mAmg$_{Pt}^{-1}$, outperforming the mass activities reported in the literature for Pt/GA electro-catalysts prepared using conventional routes.

The fast electron transport mechanism offered by graphene can particularly facilitate the ORR to happen quickly and effectively in fuel cells. Nitrogen doped graphene has been shown to yield promising results especially for the sluggish cathodic ORR [Qu *et al.* 2010]. The disorders and defects introduced in the graphene stack due to the incorporation of nitrogen are known to act as anchoring sites for the catalyst NPs [Jafri *et al.* 2010, Jha *et al.* 2011]. Jafri *et al.* used nitrogen doped graphene nano-platelets as Pt NPs support for electro-catalytic studies. Graphene nano-platelets were synthesised by thermal exfoliation of graphitic oxide and further treated in nitrogen plasma to produce nitrogen doped (3 at.%) graphene nano-platelets [Jafri *et al.* 2010]. Pt NPs were dispersed on the support using the sodium borohydride reduction process. MEAs fabricated using Pt/N-G and Pt/G as the ORR catalysts showed a maximum power density of 440 mWcm^{-2} and 390 mWcm^{-2}, respectively. The improved performance of Pt/N-G was attributed to the formation of pentagons and heptagons due to the incorporation of N in the C-backbone leading to increase in the conductivity of neighbouring C atoms. In another work, Jafri *et al.* reported nitrogen doped graphene as support for Pt NPs that were synthesized using hydrothermal method and thermal solid state method using two sources of nitrogen, ammonia and melamine, respectively [Jafri *et al.* 2015]. The synthesized graphene based catalysts were evaluated as ORR catalyst in both half cell and full cell mode. In this work, MWCNT was used as a spacer and fuel cell results demonstrated enhanced performance with nitrogen doped, graphene based Pt catalyst prepared by hydrothermal method. This catalyst exhibited 1.5 times higher power density than commercial Pt/C catalyst (704 mWcm^{-2} *vs*. 460 mWcm^{-2}) establishing it as a promising cathode catalyst for PEMFC.

Zhu *et al.* designed a strongly coupled Pt nanotubes/nitrogen-doped graphene hybrid material, which was fabricated by *in-situ* galvanic replacement method [Zhu *et al.* 2015]. The Pt NTs/NG showed ultrahigh activity and durability towards ORR evaluated in three electrode configuration, in which a 2.7-fold improvement in mass activity was observed at 0.9 V compared to the state-of-art commercial Pt/C catalyst. Accelerated durability tests showed that the Pt NTs/NG catalyst retained 88.9% of its initial activity after the accelerated durability tests. Graphene-supported binary Pt-Co materials have also been explored as ORR catalysts, and the results showed enhanced electro-catalytic performance [Liu *et al.* 2012, Nam *et al.* 2012, Vinayan *et al.* 2013]. The graphene support was thought to have a strong interaction with the bimetallic NPs, thereby enhancing the catalytic activity, stability and decreasing the cost.

1.5. Metal-oxides (non-carbonaceous) supported Pt based catalysts

The use of nano-structured carbon materials have definitely improved the performance of the catalysts used in PEMFCs as they exhibit strong influence on the catalyst durability and behaviour. Unfortunately, carbon corrosion is still prevalent for these systems. Although the undesirable reaction has no doubt been significantly reduced, the complete elimination of carbon corrosion has not yet been achieved. Furthermore, functionalization of the carbon support is generally adopted to improve the anchorage of the catalyst NPs on the support and reduce agglomeration. However, functionalization of the carbon support can make it more susceptible to electrochemical oxidation leading to loss of active surface area. It can also affect the ionomer distribution thereby affecting proton conductivity of the fuel cell electrodes [Maass *et al.* 2008]. Consequently, there is an imperative requirement to explore non-carbonaceous supports to address these issues.

Inorganic metal oxides have been studied to determine whether they can serve as good corrosion-resistant supports. The most often employed metal-oxides as support for Pt for ORR in PEMFC are molybdenum oxides [Elezović *et al.* 2008, Elezovic *et al.* 2009], tungsten oxides [Yan *et al.* 2013, Li *et al.* 2014], tin oxides [Sasaki *et al.* 2014] and titanium oxides [Elezovic *et al.* 2016]. Elezovic *et al.* reported MoO_x based Pt catalyst (MoO_x-PtC) and evaluated their

ORR activity in three electrode configuration [Elezović *et al.* 2008, Elezovic *et al.* 2009]. The study showed higher activity of MoO_x-PtC catalyst as compared to Pt/C catalyst and the enhanced performance was attributed to the formation of favorable interface between the Pt and oxide materials and by spillover due to the surface diffusion of oxygen reaction intermediates. Yan *et al.* demonstrated Pt NPs supported on the C–WO_3 composites (Pt/C–WO_3) as ORR catalyst [Yan *et al.* 2013]. The results revealed that a moderate concentration of WO_3 enhances the catalytic activity of Pt electro-catalysts through promotion effect. The WO_3 based catalysts exhibited 1.8 times higher kinetic mass current density than that of commercial Pt/C catalyst (174.6 $mAmg_{Pt}^{-1}$ *vs.* 98.6 mA mg_{Pt}^{-1}), along with enhanced electrochemical stability. The higher catalytic activity and chemical stability was attributed to the promotion effect of WO_3 nanobars on Pt and the stronger interaction between WO_3 and Pt NPs. Higher ORR activity and stability for tungsten oxide based Pt catalyst was also shown in the studies of Li *et al.*, where sub-stoichiometric tungsten oxide $W_{18}O_{49}$ was used as a support for the Pt catalyst [Li *et al.* 2014]. Pt/$W_{18}O_{49}$ demonstrated higher catalytic activity, anti-poisoning properties and stability than the commercial Pt-black and Pt/C catalysts. X-ray photoelectron spectroscopy (XPS) results revealed a strong metal-support interaction between Pt and the support $W_{18}O_{49}$ (Fig. 1.12). Sasaki *et al.* reported doped SnO_2 as an alternative support material for Pt in PEMFC [Sasaki *et al.* 2014]. MEAs with Pt/doped SnO_2 cathode catalysts were evaluated for long term durability and the results demonstrated very high durability characteristics of these materials even after 60,000 cycles of ageing tests. The authors concluded that the conductive oxides can be promising electro-catalyst supports which could satisfy both cycle durability and suitable catalytic activity for ORR; however, they stressed that further improvement in ORR activities is still desired for their application in PEMFCs.

Among the various metal-oxide supports for Pt, titanium oxide based supports are the most attractive for PEMFC applications. As far as electrochemical oxidation and corrosion resistance are concerned, TiO_2 has an upper

hand as compared to carbon supports [Fovet *et al.* 2001, Sharma *et al.* 2012]. TiO_2 is cost effective, easily available and non-toxic [Leroux *et al.* 2002, Wu *et al.* 2010, Landmann *et al.* 2012]. Moreover, there exists the feasibility of SMSI [Baker *et al.* 1979, Horsley 1979, Vracar *et al.* 1986] between Pt and TiO_2 which brings in newer possibilities for synergistic catalytic activity. Pt-TiO_2 based catalysts have thus emerged as a promising class of ORR catalysts for PEMFCs. On account of the above, this novel class of catalyst has the capability to address the issues of durability and sluggish ORR kinetics in PEMFCs and takes it closer towards commercialization. Unfortunately, replacing carbon with traditional metal-oxides is difficult, due to their electrically insulating properties at temperatures below 200 °C. However, sub-stoichiometric metal oxides, such as reduced oxidation state titania (e.g. Ti_4O_7 and Ebonex), doped tianium oxides, and nano-structured titanium oxide nanotubes, have been proposed as electrically conductive support materials with high corrosion-resistant properties.
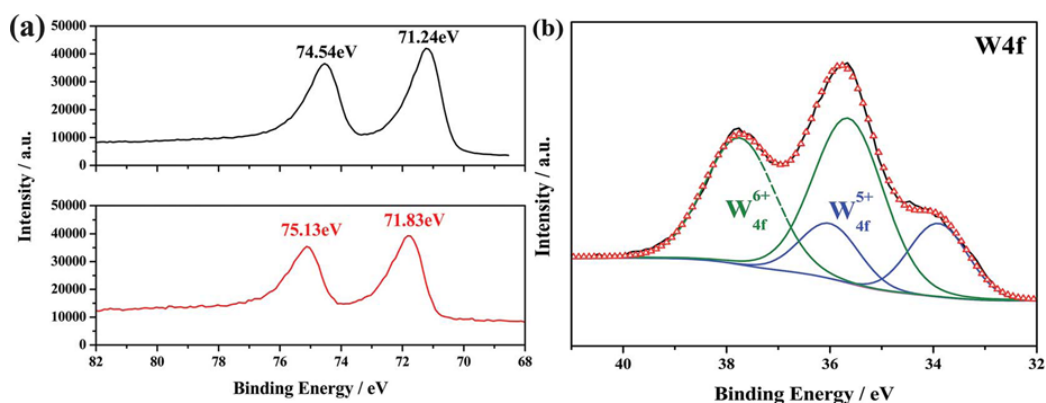
Fig. 1.12. (a) XPS spectra of Pt 4f for Pt/$W_{18}O_{49}$ (red) and Pt-black (black), and (b) W4f spectra for $W_{18}O_{49}$ support [Li *et al.* 2014]

Titania exists in three main crystallographic forms *viz.* anatase, rutile, and brookite. Each structure exhibits different physical properties, which lead to their different applications. It is generally accepted that anatase titania is more efficient as catalyst than rutile titania. Regarding the application in fuel cells, Gustavsson *et al.* investigated thin film of Pt and stoichiometric TiO_2 in a polymer electrolyte electrochemical cell. Individual thin films of Pt and TiO_2 were deposited directly on Nafion® membranes by thermal evaporation [Gustavsson *et al.* 2007]. ORR

polarization plots showed that the presence of a thin TiO_2 layer between Pt and Nafion[®] increases the performance compared to a Pt film deposited directly on Nafion[®]. They attributed this improvement to a better dispersion of Pt on TiO_2 compared to that on Nafion[®] and in addition, substantial proton conduction through the thin TiO_2 layer. Gebauer *et al.* also investigated thin film Pt/TiO_2 catalyst for ORR [Gebauer *et al.* 2016]. The model electrodes were fabricated by cathodic electro-deposition of thin titania film on glassy carbon substrates, which were subsequently decorated by Pt particles. The authors demonstrated conclusive effects of metal particle size and metal-support interaction effects on ORR activity.

Stoichiometric titania (band gap 4.85 eV) is resistive and the presence of Ti^{3+} ions is essential for electronic conductivity. Ti^{3+} ions can either be generated by (i) creating oxygen deficiency by heating TiO_2 in reducing atmosphere (to obtain TiO_x or $Ti_nO_2^{n-1}$) or (ii) introducing dopants. However, sub-stoichoimetric titania when exposed to fuel cell conditions becomes stoichiometric and forms a resistive TiO_2 layer at the three phase reaction interface [Hayden *et al.* 2001, Chen *et al.* 2002]. Among the distinct oxides of Magneli phases of titanium dioxide with the general formula, $Ti_nO_2^{n-1}$, Ti_4O_7 exhibits the highest electrical conductivity exceeding 10^3 S cm^{-1} at room temperature [Bartholomew *et al.* 1969]. Moreover, these oxides show no peaks or waves between 0.0 and 2.0 V *vs.* RHE in 1 M sulphuric acid at 25 °C [Bartholomew *et al.* 1969], indicating high oxidation-resistant characteristics. Due to these conductive and oxidation-resistant properties, $Ti_nO_2^{n-1}$ phases have attracted attention as a possible support for fuel cell catalysts [Krstajic *et al.* 2007]. Commercially available products known as Ebonex® are supplied by Atraverda Ltd. (Sheffield, UK). Ebonex® is an electrically conductive ceramic consisting of several sub-oxides of titanium dioxide, mainly, Ti_4O_7 and Ti_5O_9. Ebonex® has a surface morphology (micro-rough and porous) which impart the desirable properties to it as a substrate for metal layers [Graves *et al.* 1991, He *et al.* 1996].

Ioroi *et al.* prepared Ti_4O_7 supported Pt catalysts (2.5 and 5 wt.%) and compared their activities for both the HOR and the ORR to that of Vulcan XC-72 supported Pt catalyst under PEMFC operation at 80 °C [Ioroi *et al.* 2005]. Tests on Pt-free Ti_4O_7 and Vulcan XC-72 supports showed that the onset potential of the

corrosion current during the positive direction sweep of cyclic voltammetry (CV) was much higher for Ti_4O_7 than for Vulcan XC-72, which indicated that Ti_4O_7 would be quite oxidation resistant under the actual PEMFC operating conditions. PEMFC polarization curves using 5 wt.% Pt/Ti_4O_7 and conventional 20 wt.% Pt/C cathodes indicated that the mass activity of Pt/Ti_4O_7 is lower than that of Pt/C. Compared to the Pt/C cathode, ca. 100 mV voltage loss was observed at 500 $mAcm^{-2}$ for the 5 wt.% Pt/Ti_4O_7 cathode. This was ascribed to the smaller electrochemically active area of Pt/Ti_4O_7 relative to Pt/C, because the Pt particle size deposited on Ti_4O_7 is larger than that of the Pt/C catalyst. However, the specific activities of both catalysts, based on ESA, were very close to each other, indicating that the activity for the ORR of Pt catalyst particles on both Ti_4O_7 and Vulcan XC-72 is nearly the same. Accordingly, the Ti_4O_7 support would be applicable to PEMFC electro-catalysts without degrading the intrinsic catalytic activity of Pt, so that Pt/Ti_4O_7 would be a promising durable catalyst material for PEMFC.

In the work of Huang *et al.*, mesoporous titania was prepared using template assisted route and Pt deposition was done *via* chemical reduction route using sodium borohydride as the reducing agent [Huang *et al.* 2009]. The fuel cell performance of Pt/TiO_2 catalyst was compared with commercial Pt/C catalyst. The electrochemical stability and performance of the Pt/TiO_2 and Pt/C electro-catalysts were examined using an accelerated stress test (AST) protocol. The durability and stability of the electro-catalysts were compared by holding the cell potential at 1.2 V according to the modified AST protocol. In the case of the Pt/TiO_2 electro-catalyst, the polarization losses were similar even after a corrosion time (*Tc*) of 200 h, while the Pt/C showed a significant decrease in performance after *Tc* 50 h due to carbon corrosion and subsequent detachment and agglomeration of catalyst particles (Fig. 1.13). The excellent fuel cell performance of the Pt/TiO_2 catalyst was attributed to the low mass transport limitation in the cathode catalyst layer. The AST results indicated an ultrahigh stability of the Pt/TiO_2 catalysts. The SMSI and corrosion resistance of the TiO_2 support enhanced the stability of the Pt catalysts. This study highlighted the significance of Pt/TiO_2 as an alternative cathode electro-catalyst to improve the reliability and durability of PEMFCs.

Rajalakshmi *et al.* have reported nano-titania for their application as supports at cathode [Rajalakshmi *et al.* 2008]. The titania support was prepared by sol-gel method and Pt deposition was done by impregnating titania powders in chloroplatinic acid solution followed by reduction with 0.1 M sodium borohydride solution and 0.01 M sodium hydroxide solution for controlled reaction. From the fuel cell performance comparison of the electrodes prepared using Pt electrocatalyst supported on carbon and TiO_2, it was shown that the performance for the Pt/TiO_2 up to a current density of 150 $mAcm^{-2}$ was almost the same as with conventional Pt/C catalyst (Fig. 1.14). However, in the ohmic region, the performance is lower by about 100 mV at a current density of 400 $mAcm^{-2}$, showing that the resistance of the MEA is more for TiO_2 based catalyst compared to carbon based catalyst. This may be due to the changed oxidation state of Ti^{2+} to Ti, where there may be a transition from non-stoichiometric oxide to a stoichiometric oxide under the fuel cell environment. In terms of cyclic stability and ESA, Pt/TiO_2 catalysts exhibited upper hand over Pt/C catalysts. The large ESA obtained for the TiO_2 supported Pt catalyst is attributed to the well dispersion of Pt particles on the support material. This study identified that TiO_2 can be used as a support material for fuel cell electrocatalysts due to their thermal stability, electrocatalytic activity and corrosion resistance.
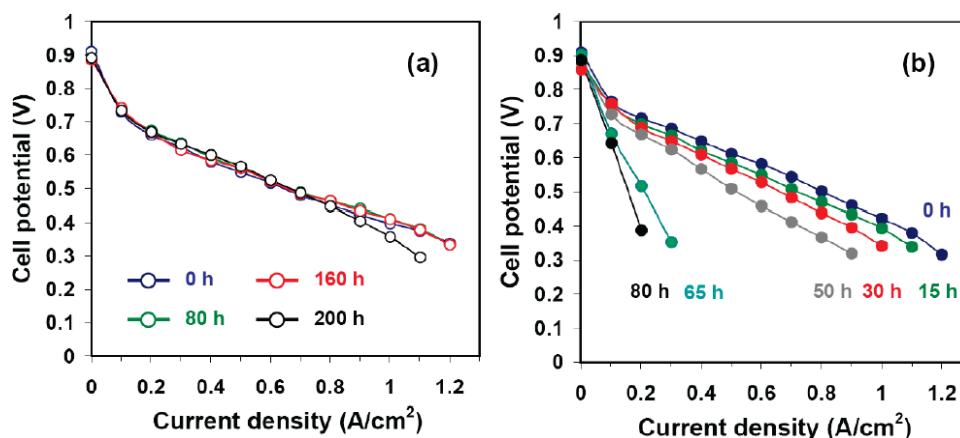
Fig. 1.13. Polarization curves for PEMFCs with (a) Pt/TiO_2 and (b) Pt/C catalysts after the potential was held according to the AST protocol for 0-200 and 0-80 h, respectively [Huang *et al.* 2009]

As discussed previously, the major drawback of titanium oxides for its application as support in low temperature fuel cells is its low electronic conductivity.

42

Hence, increase in electronic conductivity of titania is necessarily required for electrochemical applications. Doping of titania is one of the effective strategies to increase its electronic conductivity. It has been shown that mixtures of NbO_2 and TiO_2 sintered at 1000 °C lead to the formation of an electrically conducting material [Rüdorff *et al.* 1964, Morris *et al.* 2000]. This high temperature synthesis method shows promising results, but it leads to a low surface area material that requires long synthesis time. Because TiO_2 undergoes a phase transition from anatase to the less catalytically active rutile near 700 °C [Arbiol *et al.* 2002], the high temperature synthesis may also reduce some catalytic promotion of methanol oxidation by the support. On this basis, to increase the surface area and avoid the phase transition, a low-temperature synthesis route for $Nb_{0.1}Ti_{0.9}O_2$ *via* a surfactant templating method was proposed by Garcia *et al.* [García *et al.* 2007]. The synthesis method is based on using octadecylamine as a template, and niobium(V)ethoxide and titanium(IV)butoxide as metal precursors. BET surface area of the resulting $Nb_{0.1}Ti_{0.9}O_2$ was 136 m^2g^{-1}, much higher than the value of 1.4 m^2g^{-1} measured for the same compound synthesized at high temperature using the ceramic method [Chen *et al.* 2002].
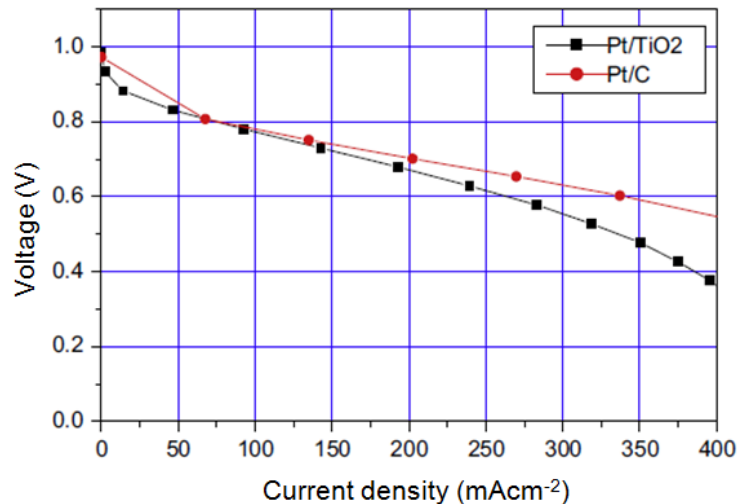
Fig. 1.14. PEMFC performance comparison between Pt/TiO_2 and Pt/C at 60 °C with hydrogen and air at 1 atm [Rajalakshmi *et al.* 2008]

Park *et al.* prepared Nb-doped TiO_2 NPs by means of hydrothermal synthesis [Park *et al.* 2007]. Pt was deposited onto the doped support by chemical reduction

route using $NaBH_4$. In order to compare and evaluate catalyst activity of Nb-TiO_2 supported Pt catalyst, the Vulcan XC-72 carbon supported Pt (40 wt%) catalyst (Pt/Vulcan XC-72) was also prepared by means of the same route as that of Pt/Nb-TiO_2. The Nb-TiO_2 supported Pt catalyst (Pt/Nb-TiO_2) showed the well dispersion of Pt catalysts (3 nm) on the Nb-TiO_2 nanostructure supports (10 nm). The Pt/Nb-TiO_2 also showed much higher reduction current, *i.e.* an excellent catalytic activity for ORR compared with that of carbon supported catalyst. The improved activity of Pt/Nb-TiO_2 for ORR was attributed to the effective dispersion of Pt NPs on Nb-TiO_2 nanosized supports.

In the work of Elezovic' *et al.*, Nb-doped TiO_2 was synthesized through a modified sol–gel route [Elezović *et al.* 2010]. The borohydride reduction method was used to prepare Nb–TiO_2 supported Pt (20 wt. %) catalyst. To test the behaviour of the Nb–TiO_2/Pt as a catalyst for ORR, in comparison with the pure C/Pt, the rotating disk electrode measurements were done in O_2 saturated $HClO_4$ solution, with the sweep rate of 20 mVs^{-1}. These results showed that the onset of O_2 reduction is significantly shifted to the positive potentials (about 80 mV) for Nb–TiO_2/Pt electrode with reference to that obtained with Pt/C. The remarkable ORR activity was explained by higher half-wave potential of 0.88 V (RHE) at Nb–TiO_2/Pt as compared to the 0.70 V (RHE) at Pt/C which indicates its excellent catalytic activity. This enhancement in the activity of Nb–TiO_2/Pt was attributed to both the interactions of Pt NPs with the support and the energy shift of the surface d-states with respect to the Fermi level which changes the surface reactivity.

Kim *et al.* investigated the effect of V, Cr and Nb as dopant for TiO_2 to select the most suitable dopant for TiO_2 to achieve better ORR activity [Kim *et al.* 2016]. This study conducted in half cell mode, reported better ORR activity and durability with Pt/V-TiO_2 compared to Pt/C catalyst, and the enhanced activity was attributed to the compressive strain on introduction of dopant. Hsieh *et al.* reported dual-doped (tungsten or niobium as the cation and nitrogen as the anion) TiO_2 as a more suitable catalyst support with higher electron conductivity than single-doped TiO_2 [Hsieh *et al.* 2017]. The electrochemical results demonstrated that dual-doped TiO_2 based catalysts, Pt/$Ti_{0.9}Nb_{0.1}N_xO_y$ and Pt/$Ti_{0.8}W_{0.2}N_xO_y$ had higher ORR activity than Pt/C

catalyst [Fig. 1.15 (a) and (b)]. $Pt/Ti_{0.9}Nb_{0.1}N_xO_y$ and $Pt/Ti_{0.8}W_{0.2}N_xO_y$ catalysts also exhibited ~3.5 times higher stability than commercial catalyst showing only 22.9 % loss in activity after 30,000 potential cycles [Fig. 1.15 (c), (d), (e) and (f)], a value exceeding the US DOE stability target. The superior activity and durability of dual doping TiO_2 supported catalysts was attributed to enhanced electron conductivity and changes in the electronic state of Pt on the support materials by the dual dopants.
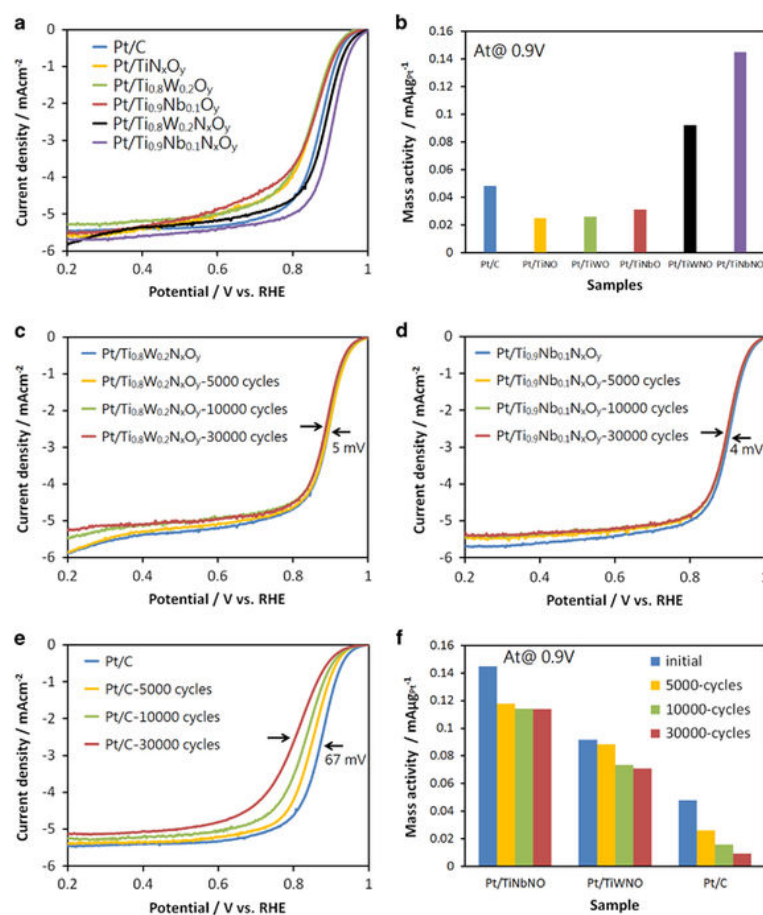
Fig. 1.15. ORR polarization curves of Pt/C, Pt/TiN_xO_y, $Pt/Ti_{0.8}W_{0.2}O_y$, $Pt/Ti_{0.9}Nb_{0.1}O_y$, $Pt/Ti_{0.8}W_{0.2}N_xO_y$ and $Pt/Ti_{0.9}Nb_{0.1}N_xO_y$ catalysts, (b) Mass activity at 0.9 V *vs*. RHE, ORR polarization curves of (c) $Pt/Ti_{0.8}W_{0.2}N_xO_y$, (d) $Pt/Ti_{0.9}Nb_{0.1}N_xO_y$ and (e) Pt/C catalysts before and after 5000, 10000 and 30000 potential cycles, respectively, and (f) Mass activity before and after stability testing at 0.9 V *vs*. RHE [Hsieh *et al.* 2017]

Nano-structured TiO_2 materials, with typical dimension less than 100 nm, have recently emerged which include spheroidal nanocrystallites and NPs together with (more recently synthesized) elongated nano-tubes, nano-sheets, and nano-fibers

[Bavykin *et al.* 2006]. Due to their high stability, high surface area and moderate electrical conductivity, titanium dioxide nano-tubes (TONTs) have been investigated as fuel cell catalyst support [Macak *et al.* 2005, Wang *et al.* 2005, Kang *et al.* 2008, Kang *et al.* 2008]. The nano-tube structure has a variety of advantages as a support for electro-catalysts associated with the specific geometry. The geometry of the arrays affects the dispersion of catalysts, the effective catalyst loading, and easy permeation of reactant species resulting from the highly porous structure, leading to an enhancement of catalytic activity [Bavykin *et al.* 2006]. Manikandan *et al.* investigated TiO$_2$ nano-tubes (TiO$_2$-NT) as support for Pt NPs (Pt/TiO$_2$-NT) for ORR in PEMFC [Manikandan *et al.* 2016]. The TiO$_2$-NT was synthesized *via* anodization method; whereas, Pt NPs deposition was achieved through chemical impregnation method. Pt/TiO$_2$-NT catalyst exhibited superior activity and durability as compared to commercial Pt/C catalyst (12% *vs*. 76% loss in ESA after 10,000 cycles).

1.6. Bi-metallic Pt based catalysts

The slow ORR kinetics on the cathode lead to significantly decreased output power and energy utilization efficiency which remains the major obstacle to commercialization of PEMFC. One of the effective strategies to improve ORR is through the use of Pt alloy catalysts. In the past several decades, significant effort was put into the design and synthesis of Pt nano-structures for PEMFC catalysts to increase their catalytic activity and stability. Research groups worldwide have reported studies such as: (i) simply alloying Pt with the second transition metals [Mukerjee *et al.* 1995, Antolini 2007], (ii) textured Pt-alloys with core–shell structures [Zhang *et al.* 2005, Alayoglu *et al.* 2008], (iii) morphology-controlled large Pt-alloy crystals [Stamenkovic *et al.* 2007], and (iv) elongation of shape-controlled Pt-alloy in at least one dimension [Chen *et al.* 2007, Wang *et al.* 2007]. With Pt alloy catalyst at the cathode, the activity depends on the alloying element as well. The enhancement in electro-catalytic activity in these Pt-M catalysts is attributed to (i) geometric, favorable Pt-Pt interatomic distance [Mukerjee *et al.* 1993, Min *et al.* 2000], (ii) electronic effects, d band vacancy [Stamenkovic *et al.* 2006, Hwang *et al.* 2012], and (iii) adsorption of oxygen containing species from the electrolyte on the alloying element [Stamenković *et al.* 2003, Balbuena *et al.* 2004].

It is well known that the adsorption of O_2 on Pt surface occurs by dual site mode and therefore the nearest neighbor Pt-Pt distance has a key role to play in determining the adsorption behavior of molecular di-oxygen [Min *et al.* 2000]. Lattice contractions observed after alloying Pt results in a more favorable Pt-Pt distance for dissociative adsorption of oxygen while maintaining the favorable Pt electronic properties [Jalan *et al.* 1983, Mukerjee *et al.* 1993].

The enhancement in electro-catalytic activity on alloying Pt with another 3d transition metal can be understood to be due to increase in the 5d vacancies of Pt (Fig. 1.16) [Toda *et al.* 1999]. The increase in the 5d vacancies leads to an increased donation of 2π electrons from O_2 to the surface of Pt. This leads to an increased O_2 adsorption followed by back-donation of electrons from filled Pt 5d orbitals to empty $2\pi^*$ orbitals of O_2. As a result, the bond order of O_2 increases, resulting in weakening of O-O bond and hence, higher catalytic activity. However, there is an optimum content of the second element in the Pt alloys, beyond which the Pt-O bonding becomes stronger and back donation becomes difficult, resulting in lower O_2 reaction rate. When the content of the second element becomes too large, the resulting d vacancy leads to surface oxide formation due to stronger interaction with the adsorbed oxygen and hence, lowering of Pt utilization. It has also been suggested that OH^- species would adsorb at lower potentials onto the more reactive M atoms at the surface and thus, lateral interactions would prevent adsorption of other OH groups on the surface of Pt atoms, which would then be available for ORR [Paulus *et al.* 2002, Malheiro *et al.* 2010].

Mukerjee *et al.* compared the activities of carbon supported, binary Pt alloy and Pt catalysts and found all five of the Pt alloy catalysts showed enhanced activity for ORR and their activities decreased in the order of PtCr/C >PtFe/C >PtMn/C >PtCo/C >PtNi/C [Mukerjee *et al.* 1995]. High activities for PtCr/C, PtFe/C and PtMn/C were also reported by Ralph *et al.* [Ralph *et al.* 2002]. Due to different test conditions and catalyst preparation methods, different activity orders appeared to result. Colón-Mercado *et al.* found that the activities of studied catalysts decreased in the order of PrFe/C >PtCo/C >PtV/C >PtNi/C >Pt/C [Colón-Mercado *et al.* 2006]. Among a series of Pt alloy nano-structured thin film catalysts for ORR, PtNi alloy

was found to be more active than PtCo alloy [Van der Vliet *et al.* 2011]. Huang *et al.* in their breakthrough work reported transition metal doped M-Pt$_3$Ni/C (M= V, Cr, Mn, Mo, Co, W or Re) as a highly promising ORR catalyst for PEMFC [Huang *et al.* 2015]. The Mo-Pt$_3$Ni/C showed the best ORR performance, with a specific activity of 10.3 mAcm^{-2} and mass activity of 6.98 Amg$_{Pt}^{-1}$, which are 81 and 73 fold enhancements compared with the commercial Pt/C catalyst (0.127 mAcm^{-2} and 0.096 Amg$_{Pt}^{-1}$).
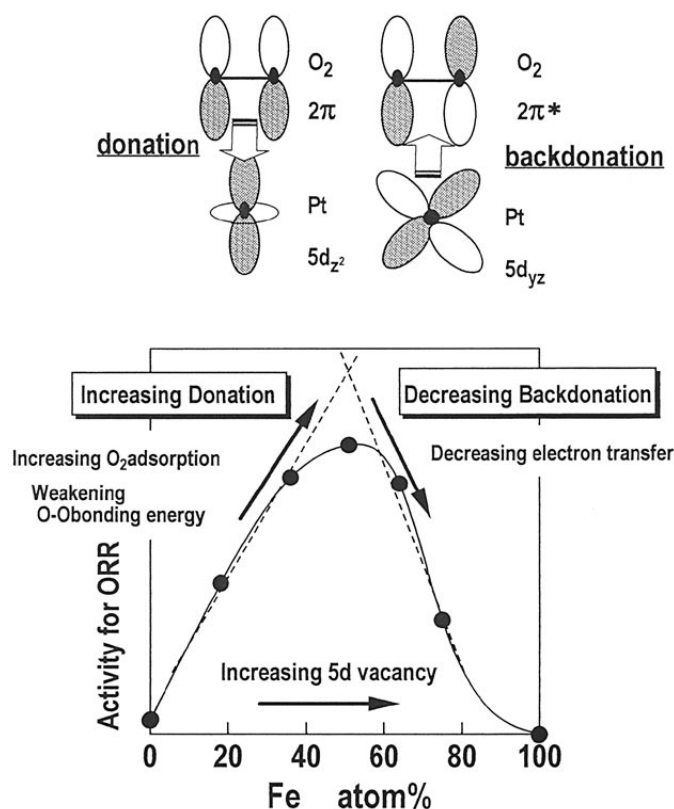
Fig. 1.16. Schematic explanation of the proposed enhancement mechanism of the ORR by alloying Pt with Fe-group metals [Toda *et al.* 1999]

Xiong *et al.* reported Pt-Pd nano-dendrites (NDs) supported on carbon (Pt-Pd NDs/C) as a highly active cathode catalyst for PEMFC [Xiong *et al.* 2017]. Pt-Pd NDs were prepared *via* facile seedless solvo-thermal method using cetyltrimethylammoniumhydrogensulfate (CTAS) as a surfactant and size controlling agent. MEA with Pt-Pd NDs/C catalyst showed 1.5 times higher power density than Pt/C catalyst (1365 mWcm^{-2} *vs.* 904 mWcm^{-2}) making them promising cathode catalyst candidate for PEMFC. In a relatively newer approach, Zhou *et al.* [Zhou *et al.*

2016] prepared graphene cellular monoliths (GCMs) functionalized with bimetallic hollow Pt-M NPs (Pt-M/GCM; M = Ni, Co) *via* sono-chemical reduction and gelatinization process and evaluated them as ORR catalyst in half cell mode. The Pt-M/GCM (M = Ni, Co) catalysts demonstrated 9.4-18.9 fold enhancement in catalytic activity and higher durability towards ORR as compared to commercial Pt/C catalyst.

Besides the alloying metal, the alloy composition also affects the activity enhancement. In the case of a PtCo/C alloy catalyst, a higher activity was observed when the Pt:Co ratio was 3:1, while for a PtNi/C catalyst the optimal Pt:Ni ratio was 1:1 [Colón-Mercado *et al.* 2006]. In another work, urchin like Pt-Ni bimetallic nanostructures showed the best ORR performance with Pt:Ni ratio of 2:1 [Choi *et al.* 2016]. The clear influence of the composition on the catalytic activity for ORR was also observed on a PtFe/C catalyst [Malheiro *et al.* 2009, Malheiro *et al.* 2010]. PtTi/C alloy catalysts were also very sensitive to the Pt:Ti atomic ratio. The peak catalytic activity was obtained for $Pt_{75}Ti_{25}$, showing a two-fold increase in the activity as compared to Pt catalyst, and the activity dropped as the composition shifted away from the optimum Pt:Ti ratio of 3:1 [Ding *et al.* 2008].

The nature of support employed to disperse the bimetallic NPs also affected the ORR catalytic activity and durability of bimetallic Pt catalysts. Lee *et al.* investigated the influence of three carbon nano-forms: defective graphene nanosheets (GNSs), single-walled carbon nanotubes (SWCNTs), and herringbone graphite nanofibres (GNFs) as support for Pd_3Pt_1 bimetallic NPs on their ORR activities [Lee *et al.* 2013]. The best ORR activity and durability was achieved with SWCNTs supported Pt_3Pt_1 catalyst, which was ascribed to metal-support interaction. Limpattayanate *et al.* also investigated effect of supports on Pt-Pd ORR activity [Limpattayanate *et al.* 2014]. In this work three nano-structured supports, Hicon Black (HB), multi-walled carbon nano-tubes (MWCNT, Pt/CNT) and titania (TiO_2) were employed as substrates for Pt-Pd NPs and the performances were compared with commercial Vulcan XC-72 supported Pt-Pd catalyst (Pt-Pd/C) prepared in an identical way. Smaller Pt-Pd particle size and better dispersion was obtained with Vulcan XC-72 supported catalyst. In terms of single cell PEMFC performance, the highest polarization losses and the lowest power density was obtained with TiO_2 supported

catalyst; whereas, the other Pt-Pd catalysts showed comparable performance to Pt-Pd/C catalyst (Fig. 1.17).
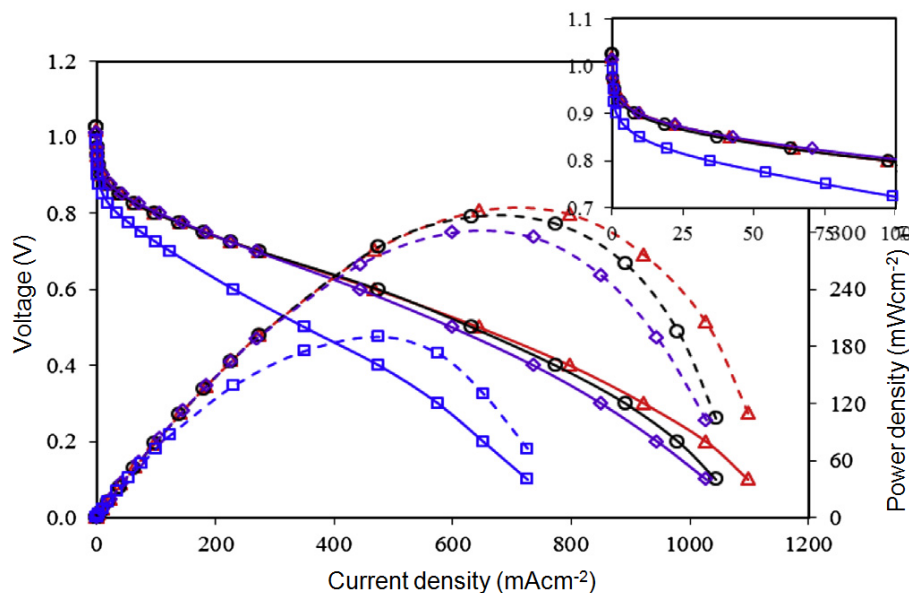
Fig. 1.17. Representative current density-potential curves of the as-prepared Pt-Pd/C (Δ) Pt-Pd/HB (O), Pt-Pd/CNT (◊) and Pt-Pd/TiO$_2$ (□) electrocatalysts in a single H$_2$/O$_2$ PEMFC [Limpattayanate et al. 2014]

Different preparation methods can lead to different chemical and morphological characteristics, and thus, different activities. Xiong *et al.* compared the activities of PtW alloy catalysts prepared by carbonyl, hydrolysis, and reverse micro-emulsion methods, respectively, and found that PtW/C prepared by the carbonyl method exhibited the best platinum mass activity for ORR and a 3.4-fold catalytic enhancement was achieved compared to the benchmark Pt/C catalyst [Xiong *et al.* 2010]. They proposed that a combination of small particle size and uniform particle composition is the key to an active ORR catalyst.

Oxygen adsorption is believed to be the rate-determining step for the ORR [Xiong *et al.* 2005]. An ordered alloy is expected to have a higher oxygen coverage than a disordered alloy on the (100) plane, which is more active than, for example, the (111) plane [Min *et al.* 2000]. In addition, the oxygen reduction activity appears also to be related to the bond strength of adsorbed oxygen. If the bond is too strong, the adsorbed oxygen may be too inactive for further reaction. On the other hand, if the bond is too weak, the amount of adsorbed species could be small, although active

[Xiong *et al.* 2005]. It is believed that the maximum catalytic activity likely results from intermediate bond strengths.

Since the cathode in a fuel cell is exposed to the corrosive environment of the acidic electrolyte and oxygen, metal corrosion, which not only decreases the activity of the cathode catalyst but also lowers the conductivity of the PEM and clogs the pores in GDL [Ralph *et al.* 2002, Yu *et al.* 2005]. Thus, the stability of Pt alloy cathode catalysts remain a challenging problem for the commercialization of PEMFCs [Mayrhofer *et al.* 2009, Dubau *et al.* 2011]. Sode *et al.* found PtZn/C alloy catalysts exhibiting high stability in the acidic environment and could be employed for fuel cell applications [Sode *et al.* 2006]. Yano *et al.* [Yano *et al.* 2008] proposed that uniformity in composition, particle size, as well as a high degree of alloying could contribute to the high stability of Pt alloy catalysts. In order to estimate the leaching tendency of a Pt alloy catalyst, a simple *ex-situ* test, which treats the catalyst in acid, such as H_2SO_4, was proposed by Bonakdarpour *et al.* [Bonakdarpour *et al.* 2006]. Results showed that the acid treatment could simulate the corrosion that occurs in the typical working environment of PEMFCs. By this *ex-situ* test, Pt alloy catalysts can be screened and it offers a convenient way of selecting the more stable ones for further assessment in actual fuel cells.

1.7. Summary

This chapter highlights that ORR catalysis plays a decisive role in PEMFC performance and hence, is of paramount significance. The inherent shortcomings with the state-of-art commercial Pt catalyst such as high cost and loss in catalytic activity and stability with prolonged use have pushed forward the search for alternate, better catalysts. Novel materials in different compositions and configurations have been explored towards this end. Considerable research has been done in the field of both carbonaceous and non-carbonaceous support materials for Pt catalysts. CNTs and titanium oxide have come up as emerging and efficient supports under the two categories of support materials. Pt-alloy/bimetallic systems have also been proposed for further catalytic activity enhancement. The nature of alloying element, composition of the bi-metallic system, the support material as well as the synthetic route employed affect the overall catalytic activity.

Scope and Objectives of the Present Work

The wide scale applications of PEMFCs are limited by the sluggish ORR kinetics resulting in overpotential losses of >300 mV which lead to lower cell performance. The high cost as well as durability issues at the cathode also pose major concerns for their effective commercialization. Many researchers have put an extensive effort over the last few decades in the search for highly efficient catalysts for ORR in PEMFC. However, there is no consensus in literature regarding the most active cathode catalyst candidate for PEMFC and hence, exploration to develop promising ORR catalysts is actively continued now also. PEMFC catalyst consists of two parts, the catalytically active component and the support material. The widely used and most efficient active component has been Pt or bi-metallic Pt. The active component is deposited in the form of metal NPs on the surface of the support material, which should ideally have high surface area, electron conductivity and good corrosion resistance.

Most of the reported studies, which address the activity and durability characteristics of catalysts, present electrochemical results of experiments performed in half cell mode with acidic liquid electrolytes. However, such assessments cannot provide the true representation of the actual performance of the catalyst in a working fuel cell. The activity and durability is influenced not only by the intrinsic catalyst characteristics but also by the nature of the catalyst-electrolyte interface, where the electrochemical reactions occur, which is highly dependent on the fuel cell operating conditions. For a reliable assessment of the performance and durability of the catalyst, it is necessary to evaluate the key performance factors under working full cell mode PEMFC conditions. Thus, *in-situ* electrochemical techniques that can directly characterize the catalyst in the MEA of a PEMFC under operation are the most appropriate methods. These *in-situ* techniques also offer non-destructive, on the spot and quick health assessment of the catalyst, which are significant in the adoption of useful strategies to achieve enhanced fuel cell performance.

Based on these aspects of ORR catalyst, the scope of this research work is to develop promising Pt based cathode catalysts for PEMFC with high activity and

durability that will help wide scale commercialization of fuel cell. The objective of the work is to investigate carbonaceous as well as metal-oxide support materials for Pt and bi-metallic Pt NPs as cathode catalyst. The investigations include synthesis of the catalyst materials through simple and effective routes followed by their detailed characterization and *in-situ* evaluation as cathode catalyst in working PEMFC.

In the metal-oxide support based Pt class of cathode catalyst for PEMFC, TiO_2 has been selected for detailed study, since it is a material of immense importance that can enhance performance of fuel cell and also can impart longer life-time due to its excellent durability characteristics. However, the application of TiO_2 materials in electrochemical systems has been limited by its poor electrical conductivity. In this thesis, two studies are envisaged to improve TiO_2 support characteristics and to achieve enhanced fuel cell performance. In the first study, effect of synthesis medium pH [acidic (pH < 3) and basic (pH > 10)] which strongly affects the hydrolysis and condensation reactions of titanium isopropoxide to form TiO_2 through sol-gel route is proposed to be investigated in detail. This study aims to understand the dependence of ORR catalytic activity on preparation conditions. In the second study, enhancement of electrical conductivity of TiO_2 through doping with transition metal element having d electron configuration suitable for catalysis is planned. Vanadium can be used as a dopant for TiO_2 host lattice and studies will be conducted to understand the influence of doping on support characteristics and ORR catalytic activity of the doped-TiO_2 supported Pt catalysts.

Carbonaceous materials with high surface area, desired pore structure, nano-structured morphology, high corrosion resistance and good electrical conductivity are highly promising as support materials for Pt based catalysts in PEMFC. Carbon class of support materials for Pt has been the most commonly employed supports by virtue of their effective dispersion of metal NPs and the significant reduction in the catalyst cost. In this thesis, two studies have been planned with carbonaceous materials as supports for Pt catalysts. As an initial study, it is planned to perform experiments to select a suitable synthesis method and select the optimum reduction conditions using mixture of $NaBH_4$ and EG as reducing agents to prepare high performing CNT

supported Pt catalyst. Two different heating routes are selected for investigation (1) conventional heating, and (2) MW heating, in order to understand their influence on catalyst performance in PEMFC.

In a carbon-supported metal–catalyst system, carbon support does not function as a mere inert material; it alters the system's Galvani potential, raises the electronic density in the catalyst and lowers the Fermi level. These factors help to accelerate the electron transfer at the electrode–electrolyte interface, thus improving the kinetics of electrode processes. Hence, selection of a suitable carbon support for Pt metal with desirable properties to obtain an active catalyst is vital for achieving enhancement in PEMFC performance. Towards this, in the next part of the study, it is proposed to thoroughly investigate the influence of various carbon nano-forms such as CB, SWCNT, MWCNT and graphene that are typically used as support for Pt catalyst on the ORR activity. It is envisaged that such a study would help in selection of the most suitable support for Pt in order to achieve enhanced fuel cell performance.

The sluggish ORR kinetics occurring at the cathode necessitates a substantially higher Pt metal loading at the cathode compared to the anode and contributes to increasing the cost further. In this regard, bi-metallic Pt-Pd NPs with lower Pt content as catalyst is selected to be explored to improve ORR activity, in the next part of the study. In order to enhance the catalytic activity and stability of Pt based bi-metallic catalysts, the metal NPs need to be dispersed on the support, MWCNT is a suitable one for that. However, for effective utilization of composite properties towards catalysis, the useful retention of MWCNT properties is highly dependent on the disaggregation and uniform dispersion of MWCNTs. Hence, in this study it is also proposed to investigate in detail, the influence of two types of surfactants, anionic SDS and cationic CTAB, on the dispersion characteristics of MWCNTs, metal NPs deposition and subsequently, fuel cell performance. It is envisaged that this study would lead to the selection of suitable surfactant that can assist in effective utilization of composite properties of Pt-Pd/MWCNT catalyst to attain enhanced fuel cell performance.

Another objective of the research work has been to compare the durability and performance characteristics of a few of the screened, in-house catalysts that are synthesized and characterized as a part of this study and to compare the results with that of the commercial Pt/C catalyst. A simple testing protocol comprising of accelerated degradation test (ADT) with potential cycling at 0.2-1.2 V for 6000 cycles in conjunction with a series of electrochemical tests are envisaged to be employed as part of this study to elucidate the performance and understand the degradation behavior of the selected catalysts. This study will lead to the assessment and comparison of practical applicability of the studied catalysts for the overall performance of PEMFC.

Chapter 2

Materials and Methods

This chapter provides details on the chemicals and materials used, experimental procedures adopted for the synthesis of catalysts and assembly of fuel cell. Details of characterization techniques employed including electrochemical techniques are also presented in this chapter.
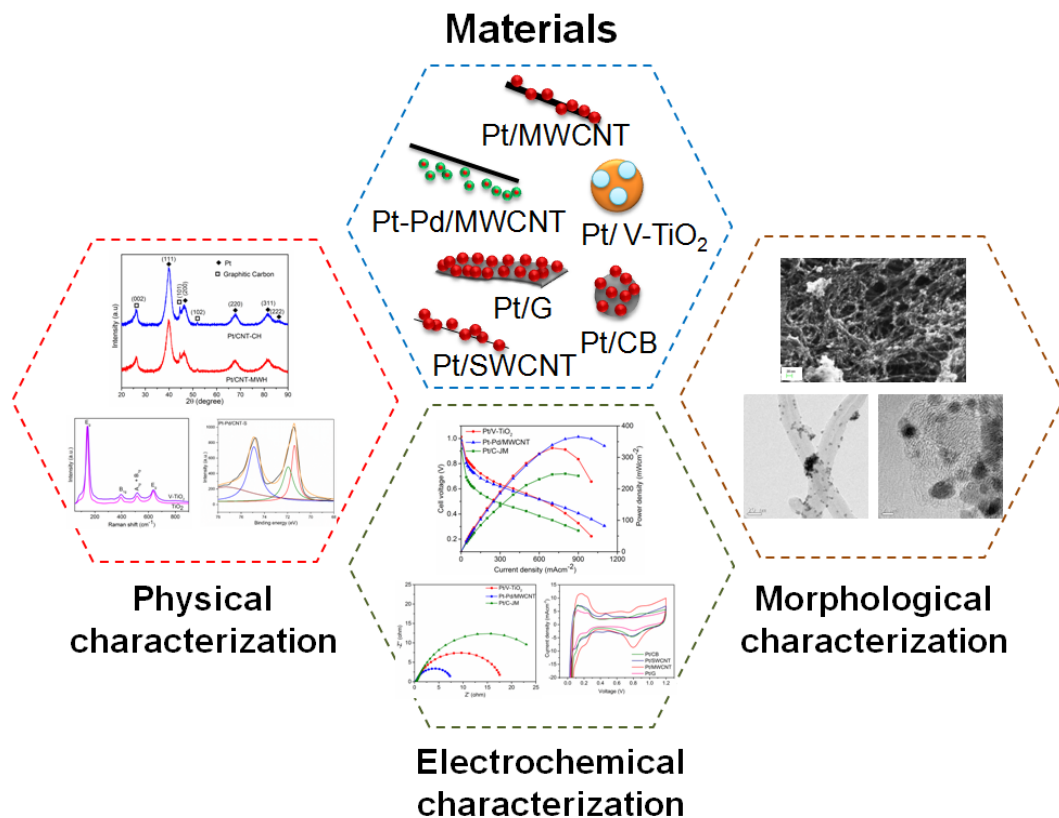
2.1. Chemicals and Materials

The chemicals and materials used in this study for synthesis of different types of Pt based cathode catalysts, preparation of catalyst ink, MEA fabrication and electrochemical characterization are listed in Table 2.1. All the chemicals and reagents used in the experiments were of analytical grade and used without further modification.

Table 2.1. List of chemicals and materials used

Chemicals / Materials	Source
$H_2PtCl_6.6H_2O$ (Purity : 99.95 %)	Alfa Aesar, India
K_2PtCl_6 (Pt-39.6 %)	Alfa Aesar, India
$PdCl_2$ (Pd-59.5 %)	Alfa Aesar, India
Pt powder (Purity: 97.61%, Pt particle size 8.4 nm)	Alfa Aesar, India
Titanium (IV) tetraisopropoxide (Purity : 97%)	Sigma-Aldrich, India
Ammonium metavanadate	Sigma-Aldrich, India
Carbon black (CB, Super P)	Timcal, India
Multi-walled carbon nanotube	Produced in-house [Propellant Fuel Complex (PFC), VSSC]
Single-walled carbon nanotube	SWeNT® CG100-L24, USA
Graphene (XGNP®)	XG Sciences, USA
Sodium dodecyl sulphate (Purity : 99.0 %)	Sigma-Aldrich, India
Cetyltrimethylammonium bromide (Purity : > 98 %)	Sigma-Aldrich, India
$NaBH_4$	Alfa Aesar, India
Ethylene glycol (Purity : 99%)	Sisco Research Laboratory, India
Carbon paper (0.37 mm thickness)	AvCarb, USA
Poly(tetrafluoroethylene) (60.5 % dispersion)	DuPont, USA
Nafion® 5% dispersion	DuPont, USA
Nafion® 115 membrane (0.125 mm thickness, equivalent weight 1100 $gmol^{-1}$)	DuPont, USA

Pt/C (20 wt.% Pt on Vulcan XC-72)	Alfa Aesar, India
HNO₃ (Analytical Reagent)	Nice Analytical Reagents, India
NaOH (Analytical Reagent)	Otto Reagents, India
HCl (Analytical Reagent)	Nice Analytical Reagents, India
Ethanol (Analytical Reagent)	Nice Analytical Reagents, India
Acetone (Analytical Reagent)	Sisco Research Laboratory, India
Isopropyl alcohol (Analytical Reagent)	Supraveni Chemicals, India
Ultra-pure water (18 MΩ cm)	MilliQ, Millipore, India

2.2. Synthesis

2.2.1. Synthesis of Pt-TiO₂ catalysts in acidic and basic medium

Synthesis of Pt-TiO₂ nano-composite catalysts was carried out in both acidic and basic medium *via* sol-gel route. The different formulations are listed in Table 2.2. In a typical procedure, 1 g titanium tetraisopropoxide (TTIP) was dissolved in 10 ml ethanol followed by drop-wise addition of 1M HNO₃ (for pH < 3) or 1M NaOH (for pH > 10) to maintain the required pH. To this, calculated quantity of Pt powder was added to get 1:1, 2:1 and 3:1 atomic ratios of Pt:Ti (Table 2.2), followed by addition of ultra-pure water, in molar ratio of 1:4 (TTIP : H₂O). The resultant gel was aged at room temperature for 24 h and subsequently vacuum dried at 80 °C for 16 h. The powders so obtained were pulverized and subjected to calcination in argon atmosphere at 450 °C for 3 h to form the final product catalyst. The nano-composite catalysts prepared in acidic medium are named as Pt:Ti 1:1-A, Pt:Ti 2:1-A and Pt:Ti 3:1-A; whereas, those prepared in basic medium are named as Pt:Ti 1:1-B, Pt:Ti 2:1-B and Pt:Ti 3:1-B. Pristine TiO₂ samples were also synthesized as above (without the addition of Pt powder) in acidic and basic medium and are named as TiO₂-A and TiO₂-B, respectively.

2.2.2. Synthesis of Pt/TiO₂ and Pt/V-TiO₂ catalysts

2.2.2.1. Synthesis of TiO₂ and V-TiO₂ supports

TiO₂ and V-TiO₂ supports were synthesized using acid-catalyzed sol-gel method. In a typical process, sol was prepared by adding 9.6 g of TTIP in 200 ml of

isopropanol (IPA) followed by drop-wise addition of 1M HNO_3 to maintain the acidic pH (pH < 3) under vigorous stirring at room temperature. To this, ultra-pure water in molar ratio of 1:4 (TTIP: H_2O) was added under continuous stirring. The hydrolysis continued further in acidic medium leading to transparent sol formation, without forming any precipitate. Gelation of the sol was achieved by increasing the temperature to 80 °C. The resultant gel was aged at room temperature for 24 h and subsequently vacuum dried at 80 °C for 16 h. The product so obtained was pulverized and subjected to calcination in argon atmosphere at 450 °C for 3 h to form the undoped TiO_2 support. V doped TiO_2 (V-TiO_2) support was also synthesized in a similar way by addition of NH_4VO_3 as the source of V dopant [x mole%; where x = 1, 5, 10, 15, 20 and 25; as given in Table 2.3, $n_V/(n_v+n_{Ti})$; where n_V is the number of moles of V and n_{Ti} is number of moles of Ti] in TTIP and isopropanol dispersion.

Table 2.2. Different formulations of Pt-TiO_2 nano-composite catalysts

Catalyst	Pt (g)	TTIP (g)
Pt:Ti 1:1-A	0.68	1
Pt:Ti 1:1-B	0.68	1
Pt:Ti 2:1-A	1.37	1
Pt:Ti 2:1-B	1.37	1
Pt:Ti 3:1-A	2.05	1
Pt:Ti 3:1-B	2.05	1

2.2.2.2. Deposition of Pt nano-particles (NPs) on TiO_2 and V-TiO_2 supports

Pt NPs were deposited onto TiO_2 and V-TiO_2 supports (20 wt. % Pt) using a microwave (MW) assisted, modified chemical reduction route. Briefly, 0.7 g of TiO_2 was ultrasonically dispersed in ethanol for 30 min. 0.47 g of $H_2PtCl_6.6H_2O$ was added to this slurry and mixed thoroughly for 30 min. pH of this precursor solution was adjusted to 12 using 1 M NaOH solution. This was followed by the slow addition of the reducing agent mixture [$NaBH_4$ and ethylene glycol (EG) in molar ratio of 1:10] under vigorous stirring for 10 min. The above reaction mixture was subjected to heating in a household MW oven (2450 MHz, 800 W) for 5 alternating cycles of 60 s

ON and 60 s OFF. The suspension thus obtained was cooled to room temperature. Required quantity of 0.2 M HCl was added to bring pH to around 4 which facilitated the deposition of newly formed Pt NPs onto the TiO_2 support. The product was filtered and thoroughly washed with excess of ultra-pure water and acetone and finally vacuum dried at 80 °C for 8 h to get the catalyst, Pt supported on TiO_2, hereafter referred to as Pt/TiO_2. Adopting a similar procedure, the catalyst Pt supported on $V\text{-}TiO_2$ ($Pt/V\text{-}TiO_2$) was also synthesized using $V\text{-}TiO_2$ as the support.

Table 2.3. Different formulations of $V\text{-}TiO_2$ support

Materials	TTIP (g)	NH$_4$VO$_3$ (g)	Concentration of V dopant (mole %)
TiO_2	9.6	0	0
$V(1)\text{-}TiO_2$	9.6	0.04	1
$V(5)\text{-}TiO_2$	9.6	0.21	5
$V(10)\text{-}TiO_2$	9.6	0.44	10
$V(15)\text{-}TiO_2$	9.6	0.70	15
$V(20)\text{-}TiO_2$	9.6	0.99	20
$V(25)\text{-}TiO_2$	9.6	1.32	25

2.2.3. Synthesis of Pt/CNT catalysts through different heating routes

Pt/CNT catalysts were synthesized by a single step, modified chemical reduction route using a mixture of $NaBH_4$ and EG as reducing agent following two different heating routes: (1) conventional heating (designated as Pt/CNT-CH), and (2) MW heating (designated as Pt/CNT-MWH). The combined reducing agent was prepared by mixing $NaBH_4$ and EG (1:10 molar ratio) with constant stirring for 2 h at room temperature. Pt/CNT catalysts were synthesized with 20 wt. % Pt. For this, 0.7 g MWCNT was ultrasonically dispersed in 200 ml ethanol for 30 min and to this slurry, 0.47 g of $H_2PtCl_6.6H_2O$ was added and mixed thoroughly for 30 min. The pH of this precursor solution was adjusted to 12 by dropwise addition of 1 M NaOH solution. This was followed by addition of combined reducing agent under vigorous stirring for 10 min to give the reaction mixture.

For the synthesis of Pt/CNT-CH, the reaction mixture taken in a beaker was stirred for 4 h at 65-70 °C in an oil bath. For the synthesis of Pt/CNT-MWH, the reaction mixture taken in the container was subjected to heating in a household MW oven (2450 MHz, 800 W) for 5 alternating cycles of 60 s ON and 60 s OFF. The suspensions obtained *via* both the routes were cooled to room temperature followed by addition of 0.2 M HCl to reach pH around 4 which facilitated the deposition of newly formed Pt NPs onto the CNT support to form Pt/CNT catalysts. They were filtered and thoroughly washed with excess of ultra-pure water and acetone and finally vacuum dried at 80 °C for 8 h.

2.2.4. Synthesis of Pt on different carbon supports

Pt catalysts (20 wt. % of Pt) supported on four different carbon forms *viz.* carbon black (CB), single-walled carbon nanotube (SWCNT), multi-walled carbon nanotube (MWCNT) and graphene were synthesized by a single step, MW assisted, modified chemical reduction route using a mixture of $NaBH_4$ and EG as reducing agent according to the following procedure. As a typical example, the synthesis of Pt supported on carbon black (Pt/CB) is detailed here. 0.7 g of CB was ultrasonically dispersed in 200 ml ethanol for 30 min. 0.47 g of $H_2PtCl_6.6H_2O$ was added to this slurry and mixed thoroughly for 30 min. pH of this precursor solution was adjusted to 12 using 1 M NaOH solution. This was followed by the slow addition of the reducing agent mixture ($NaBH_4$ and EG in molar ratio of 1:10) under vigorous stirring for 10 min. The above reaction mixture was subjected to heating in a household MW oven (2450 MHz, 800 W) for 5 alternating cycles of 60 s ON and 60 s OFF. The suspension thus obtained was cooled to room temperature. Required quantity of 0.2 M HCl was added to bring pH to around 4 which facilitated the deposition of newly formed Pt NPs onto the CB support. The product was filtered and thoroughly washed with excess of ultra-pure water, acetone and vacuum dried at 80 °C for 8 h to get the catalyst, Pt supported on CB, hereafter referred to as Pt/CB. Similarly, Pt supported on SWCNT (Pt/SWCNT), Pt supported on MWCNT (Pt/MWCNT) and Pt supported on graphene (Pt/G) were also synthesized using SWCNT, MWCNT and graphene respectively, as supports.

2.2.5. Synthesis of Pt-Pd/CNT catalysts

Bi-metallic Pt-Pd catalysts (20 wt. % of Pt-Pd, Pt:Pd atomic ratio 1:1) supported on MWCNT were synthesized in the presence of surfactants (Sodium dodecyl sulphate, SDS or Cetyltrimethylammonium bromide, CTAB) by MW assisted, polyol reduction route using EG as the reducing agent. The procedure adopted for synthesis of Pt-Pd/CNT catalyst in the presence of SDS surfactant (hereafter referred to as Pt-Pd/CNT-S) is detailed here as a typical example. 10.08 g SDS was first dissolved in 100 ml EG (0.35 M SDS). To this, 1.45 g MWCNT was added and ultrasonically dispersed for 60 min to form homogenous slurry. Calculated quantities of K_2PtCl_6 (0.610 g) and $PdCl_2$ (0.222 g) were dissolved in 100 ml EG and this solution was added to the above slurry and mixed thoroughly for 30 min. pH of this precursor solution was adjusted to 12 by addition of 1 M NaOH solution. The above reaction mixture was subjected to heating in a household MW oven (2450 MHz, 800 W) for 5 alternating cycles of 60 s ON and 60 s OFF. The suspension thus obtained was cooled to room temperature. Required quantity of 0.2 M HCl was added to bring pH to around 4 which facilitated the deposition of newly formed Pt-Pd NPs onto the MWCNT support. The product was filtered and thoroughly washed with excess of ultra-pure water and acetone and vacuum dried at 80 °C for 8 h to get the catalyst Pt-Pd/CNT-S. A similar procedure was adopted for the synthesis of Pt-Pd supported on MWCNT in the presence of CTAB surfactant, hereafter referred to as Pt-Pd/CNT-C; wherein CTAB surfactant was used in place of SDS. For comparison, Pt-Pd supported on MWCNT, referred to as Pt-Pd/CNT, was also synthesised by a similar process without the addition of any surfactant.

2.3. Characterization of Materials

2.3.1. Fourier transform infrared (FT-IR) spectroscopy

FT-IR spectroscopy deals with the study of vibrational frequencies originating from the absorption of infrared (IR) radiation by the chemical bonds in matter. It utilizes lower energy IR radiation (10000-100 cm^{-1}) to induce vibrational and rotational excitation of atoms and groups of atoms within a molecule. Because of the variety of symmetry of atomic groups and their differences in atomic masses and electronic structures, the absorption patterns for a specific species will be unique,

which allows for their identification. The resulting spectrum represents the molecular absorption and transmission, creating a molecular fingerprint of the sample. In this work, Perkin Elmer Spectrum GX-A FTIR spectrometer in the wave number range of 4000-400 cm^{-1} was used to record the FT-IR spectra of samples. Samples were pelletized using KBr and subjected to investigation to generate the spectrum. The interferogram was generated by signal averaging of minimum 5 scans at a resolution of 0.5 cm^{-1}. The spectra were recorded in percentage of transmittance against wave number.

2.3.2. X-ray diffraction (XRD)

XRD is one of the most powerful non-destructive techniques used to determine the crystal structure of the powder samples. The determination of crystal structure is based on Bragg's Law ($n\lambda=2d \sin \theta$). This law relates the wavelength (λ) of electromagnetic radiation to the diffraction angle (θ) and the lattice spacing (d) in a crystalline sample. The analysis of peak width (full width at half maximum, FWHM) of XRD pattern provides information on crystallite size. The average crystallite size is calculated using Debye-Scherrer equation for the most intense Bragg's peak as given in *eqn. 2.1*.

$$L = \frac{0.9 \times \lambda}{\beta \cos \theta} \quad \text{... (eqn. 2.1)}$$

where, L is the average size of metal crystallites, λ is X-ray wavelength of the radiation source (Cu-Kα 1.54 Å), θ is the diffraction angle value of diffraction peak, and β is FWHM of the diffraction peak. In this work, XRD patterns were recorded on a Bruker D8 discover diffractometer equipped with a rotating anode and Cu-Kα radiation. The samples were analyzed at step scan of 0.051 and counting time of 5 s step^{-1}.

2.3.3. Raman spectroscopy

Raman spectroscopy is a molecular spectroscopic technique based on inelastic scattering of monochromatic light, usually from a laser source. It is dictated by the change in polarizability of electron cloud present in the molecule. Due to molecular vibrations, scattered light appears at wavelengths higher or lower than the incident

light. The higher and lower frequencies of scattered radiation represent Stokes and anti-Stokes lines, respectively. Plotting the intensities of these "shifted" light *versus* frequency results in a Raman spectrum of the sample. In this work, Raman spectra of materials were recorded using WITec alpha 300R confocal Raman microscope using frequency doubled Nd:YAF laser of excitation wavelength 532 nm.

2.3.4. Field Emission Scanning Electron Microscope (FESEM) and Energy Dispersive X-ray Analysis (EDX)

FESEM is used to obtain the morphology of a surface with the help of highly concentrated electron beam generated from field-emission cathode gun at vacuum condition. The electron beam interacts with the sample and produces signals with various energies that can be used to obtain information about the surface morphology and elemental composition. The ejected electrons pass through a strong electromagnetic field that can render the electron beam narrow even at high electron energy. This leads to an improved spatial resolution and minimized sample charging/damage. The electron beam on hitting the sample emits backscattered, secondary electrons and X-rays. The secondary electrons obtained in this process can give the vital information on surface morphology of the sample; whereas, X-rays can reveal the elemental composition.

EDX offers the possibility to obtain the local elemental composition of the sample during FESEM characterization. When a high energy electron beam (>15 kV) impinges on a sample, X-rays that are characteristic of elements in the sample, are formed as a result of ionization followed by transitions of inner shell electrons. The changes in energy state result in emission of X-rays characteristic of the sample composition. While scanning a sample surface in an electron microscope, the emitted X-rays are analyzed with an energy dispersive X-ray detector and the signals are recorded as elemental mapping in the form of graphs or fluorescence images. In this work, FESEM images and EDX were obtained using Carl Zeiss Supra 55 and Nova nano SEM 450 equipment.

2.3.5. High Resolution Transmission Electron Microscope (HRTEM) and Selected Area Electron Diffraction (SAED)

HRTEM is a powerful characterization tool that can be used to study morphology, crystal structure and elemental composition of nanostructured materials. In principle, an electron source emits a stream of electrons (by thermionic emission with 100-400 kV energy) and with the help of electromagnetic lenses, the electrons are focused into a very thin beam which is transmitted through the specimen. The high energetic beam strikes the specimen and a part of it gets transmitted depending upon the thickness of the coated sample. These transmitted electrons are focused by the objective lens into an image that can be observed using charge coupled device (CCD) camera. In this work, surface morphology of the samples was studied using FEI Tecnai G^2 F30 S-TWIN HRTEM instrument. The HRTEM images were further processed using image processing and analysis software, ImageJ for particle size determination [Abràmoff *et al.* 2004].

SAED is a crystallographic experimental technique that can be performed with HRTEM. SAED is referred to as "selected" because it allows the user to choose the desired part of the specimen (from HRTEM images) to obtain the diffraction pattern and hence helps in understanding the chemical components of the HRTEM images. SAED diffraction patterns are either simple spot patterns corresponding to single-crystal diffraction or ring patterns corresponding to powder diffraction from multiple crystals with a variable orientation. As a diffraction technique, SAED can be used to identify crystal structures and examine crystal defects. It is similar to XRD, but unique in that areas as small as several hundred nanometers in size can be examined; whereas, XRD typically examines areas several centimeters in size.

2.3.6. UV-Visible Diffuse Reflectance Spectroscopy (DRS)

In UV-Visible DRS, diffuse reflection of radiation in the range ultraviolet to visible (190-800 nm) by a sample is measured to understand its optical properties. In this work, changes in the optical properties of TiO_2 support on doping were studied using JASCO UV-Vis NIR V670 spectrometer using $BaSO_4$ as standard.

2.3.7. X-ray photoelectron spectroscopy (XPS)

XPS is a quantitative spectroscopic technique that measures surface elemental composition, chemical states and electronic states of samples. The photoelectric interaction between mono-energetic X-rays and a solid or gaseous sample causes electrons to be ejected from the inner shells of elements with discrete kinetic energies. The electron transition from the inner shells occurs at a specific binding energy (BE) that can uniquely identify the elements present in the sample. The BE values are used to identify the elements present on the surface and their oxidation states. The relative concentrations of elements can be determined from the photoelectron intensities. For quantitative analysis, a curve-fitting process is usually used to determine different atomic percentages. XPS is conducted at ultrahigh vacuum conditions, around 10^{-9} mbar, to avoid the changes in properties of the sample likely to occur at ambient atmospheric pressure. In this work, the surface elemental compositions of the materials were quantified using an Ultra Axis Kratos X-ray Photoelectron Spectrometer (UK) using Al-Kα radiation.

2.3.8. Ultra-Violet Photoelectron Spectroscopy (UPS)

Photoelectron spectroscopy is the most powerful and versatile technique to study the electronic structure of the valence bands in atoms, solids and molecules. UPS is analogous to XPS but the excitation source is a helium discharge source. Depending on the operating conditions of the source, the photon energy can be optimized for He I = 21.2 eV or He II = 44.8 eV which are significantly lower in energy than Al or Mg Kα used in XPS. As with XPS, the BE is related to the measured photoelectron kinetic energy (KE) by the equation; BE = hv - KE where hv is the photon energy (X-ray). The consequence of this lower photon energy is that only the low BE valence electrons may be excited using the He source. In this work, the surface electrical properties of catalysts were studied using Ultra Axis Kratos X-ray Photoelectron Spectrometer (UK) using He lamp source with energy 21.2 eV.

2.3.9. Inductively Coupled Plasma- Atomic Emission Spectroscopy (ICP-AES)

ICP-AES is one of the most versatile methods of inorganic analysis. ICP- AES is an emission spectro-photometric technique, exploiting the fact that excited

electrons emit energy at a given wavelength as they return to ground state after excitation by high temperature Argon Plasma. The fundamental characteristic of this process is that each element emits energy at specific wavelengths peculiar to its atomic character. The intensity of the energy emitted at the chosen wavelength is proportional to the amount (concentration) of that element in the sample being analyzed. Thus, by determining which wavelengths are emitted by a sample and by determining their intensities, the analyst can qualitatively and quantitatively find the elements from the given sample relative to a reference standard. In this work, metal (Pt and Pd) content of the catalysts was estimated using Perkin Elmer Optima 4300-V ICP atomic emission spectrophotometer.

2.3.10. Brunauer–Emmett–Teller (BET) specific surface area

The BET method is based on the physical adsorption of a gas (generally nitrogen) on the surface of the solid and by calculating the amount of adsorbate gas corresponding to a monomolecular layer on the surface. The amount of gas adsorbed at a given pressure allows determining the specific surface area of the material. This method is automated and the amount of gas adsorbed is determined at a number of different relative pressures. A plot of amount of gas adsorbed and the corresponding relative pressure (P/P_0) is called an isotherm. In this work, Quantachrome NOVA 1200e surface area analyzer was employed to determine the specific surface area of samples at the temperature of liquid nitrogen. The nitrogen molecules form monolayer adsorption over these particles at P/P_0 value of 0.03 to 0.5 (extended Langmuir isotherm). Prior to the measurements, all samples were degassed at 100 °C for 24 h. The surface areas were calculated from the linear part of the BET plots.

2.3.11. Electrical conductivity

Four probe technique is very widely used for the measurement of resistivity of conductors and semiconductors. The sample is generally used in the form of a thin wafer. The four probe apparatus consists of four probes arranged linearly in a straight line at equal distance from each other. Electrical current is passed between two of the probes and the voltage created is measured between the other two middle probes. The resistivity can be calculated from the measured values of current and voltage and hence, conductivity of the sample can be obtained. In this work, the electrical

conductivity of the materials was measured by a standard four-probe technique using four probe apparatus supplied by M/s. Scientific Equipment, Roorkee, India. Sample powders were made into pellets of ~10 mm diameter by use of a steel die in a hydraulic press. The electrical conductivity was calculated using Van der Pauw relation, $\sigma = (ln\ 2/\pi d)(I/V)$, where, d is the thickness of the pellet, I is the current and V is the voltage.

2.3.12. Thermogravimetric analysis (TGA)

This technique is used to determine the change in mass of the substance with respect to temperature or time. During the measurements, the sample specimen is subjected to a controlled temperature program in a controlled atmosphere. In this work, TGA of the materials were performed on TA instruments 2960 from 30° to 900 °C in air atmosphere at a heating rate of 10 °Cmin^{-1}. The thermogravimetric profiles are represented as percentage of weight retained against temperature.

2.3.13. Water contact angle

Water contact angle is a measurement used to determine a surface hydrophilic or hydrophobic properties. The ability of a water to spread over a surface without forming individual droplets determines its wettability or hydrophilic characteristics. In contrast to this, a surface that does not allow the water to spread evenly and creates water droplets or beading is considered to be hydrophobic in nature. Data Physics contact angle instruments OCA-15 EC and OCA-20 were used to determine the water wetting nature of the sample surfaces by measuring the static contact angles. Water droplets of 5-10 μl were placed at three different locations on the sample to record the contact angles using the Laplace–Young fitting method. The images of liquid droplets are captured using a CCD camera.

2.4. Sample preparation for electrochemical evaluation
2.4.1. For single cell performance evaluation
2.4.1.1. Preparation of Gas Diffusion Layer (GDL)

At first, 40 ml of PTFE dispersion was thoroughly mixed with 80 ml ultra-pure water using magnetic stirrer to achieve a uniform dispersion which was used for hydrophobization or wet-proofing of carbon paper (CP). For this, first CP was sized into 100 mm x 100 mm pieces. The sized CP was heated in air-oven at 80 °C for 30

min and after cooling down to room temperature, the initial weight (W_i) of the CP was recorded. The sized CP was then dipped into the Teflon solution and kept for 40-50 s. Teflon soaked CP was air-dried under ambient conditions for 12 h followed by heating in air-oven at 120 °C for 1 h. The air-oven dried Teflon soaked CP was further heated in air-furnace at 350 °C for 30 min to give PTFE sintered CP which is called as GDL. After cooling down to room temperature, the final weight (W_f) of the GDL was recorded. This process was repeated until 30-35 % weight gain of PTFE on CP was achieved. The PTFE wt% in CP was calculated as follows:

$$\text{wt. \% of PTFE in CP} = \frac{W_f\text{-}W_i}{W_i} \times 100 \quad \text{.......................... (eqn. 2.2)}$$

2.4.1.2. Treatment of Membrane

Commercial Nafion® 115 membrane was treated with 3% H_2O_2 solution for 1 h at 60 – 70 °C. Finally, treated membrane was washed thoroughly with ultra-pure water and stored in immersed condition in clean trays filled with ultra-pure water.

2.4.1.3. Preparation of Electrode

Catalyst ink preparation- 250 mg of catalyst powder, 2.5 ml of 5% Nafion® dispersion, 0.05 ml of IPA and 2.45 ml of ultra-pure water were mixed and subjected to ultrasonic vibration for 30 min to form a uniform catalyst ink slurry. For the preparation of catalyst ink for anode, commercial Pt/C was used as the catalyst powder; whereas, for the preparation of catalyst ink for cathode, the in-house synthesized catalyst powders as such were used. For performance comparison, catalyst ink for cathode with commercial Pt/C catalyst was also prepared.

Preparation of electrodes (anode and cathode)- Using a small paint brush with smooth bristles (Camlin make), the catalyst ink was applied by hand brushing evenly on one side of the GDL. Catalyst inks prepared earlier with commercial Pt/C and in-house synthesized catalyst powders were hand brushed on GDL to form the anode and the cathode, respectively. Cathode with commercial Pt/C catalyst containing ink was also prepared in an identical manner for performance comparison with the in-house catalysts. To get the desired catalyst loading on electrode, thin coats of ink were subsequently added with drying in air-oven at 80 °C between each brushing. The

electrode was rotated before the addition of subsequent layer to ensure an even coating. Addition continued until the desired loading was reached. The electrodes used in the electrochemical tests were cut from larger areas of catalyst coated GDL. The metal (Pt) loading per cm^2 was calculated as follows:

$$\text{Pt loading (mg}_{Pt}\text{cm}^{-2}) = \frac{W_{G2}\text{-}W_{G1}}{A_G} \times 1000 \times \% \text{ Cat}_G \times \% \text{ Pt}_{cat} \text{ .... (eqn. 2.3)}$$

where, W_{G2} is final weight of the GDL after catalyst ink brushing in g, W_{G1} is initial weight of the GDL before catalyst ink brushing in g, % Cat$_G$ is percentage of catalyst in dried GDL, %Pt$_{cat}$ is percentage of Pt metal content in the catalyst powder and A_G is the geometric area of the GDL.

In this work, a total of 17 types of in-house made catalyst combinations and one commercial catalyst, 20% Pt/C were used for making the cathodes. The anodes remained the same throughout the study: made from commercial 20% Pt/C catalyst. A schematic representation of electrode preparation is shown in Fig. 2.1.
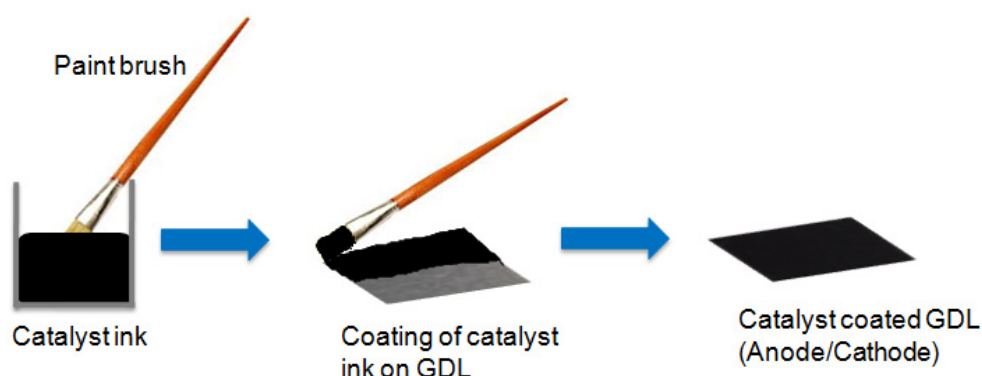
Fig. 2.1. Schematic of electrode preparation

2.4.1.4. Fabrication of Membrane Electrode Assembly (MEA)

MEAs were fabricated by accurately aligning pre-cut anode and cathode electrodes on either side of pre-treated Nafion® 115 membrane as shown in Fig. 2.2 (a). The resultant assembly was placed between two teflon sheets and titanium pressing plates and then hot pressed at 125 °C under a pressure of 80 kgcm^{-2} for 600 s to make MEA with an active geometrical area of 1 cm^2 as shown in Fig. 2.2 (b).

2.4.1.5. Assembly of Single Cell PEMFC

For assembling a single cell PEMFC, MEA was sandwiched between two silicone gaskets for leak proofing followed by a pair of graphite composite bipolar plates with parallel flow field channels and was further placed in between two gold plated, Cu terminal plates and silicone gaskets for electrical insulation from end plates. The preparation of a single cell PEMFC was completed by assembling it with titanium end plates and tie rods. Single cell PEMFC components and cell assembly are shown schematically in Fig. 2.3.
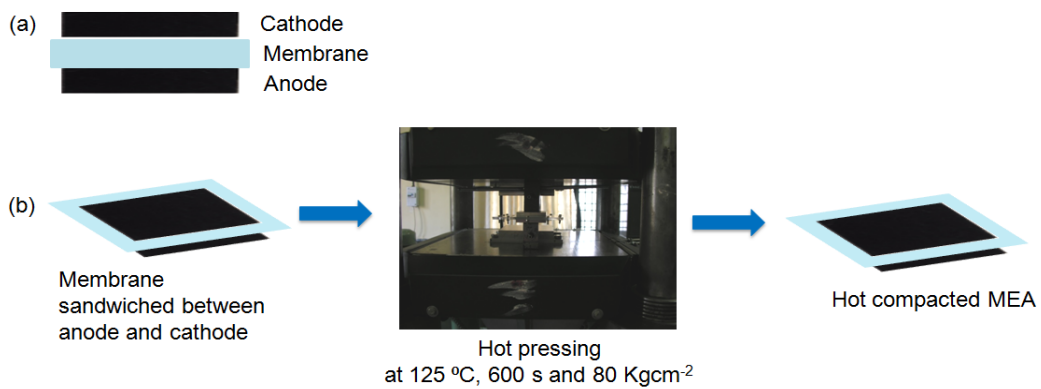
Fig. 2.2. (a) Components of MEA, and (b) Fabrication process of MEA
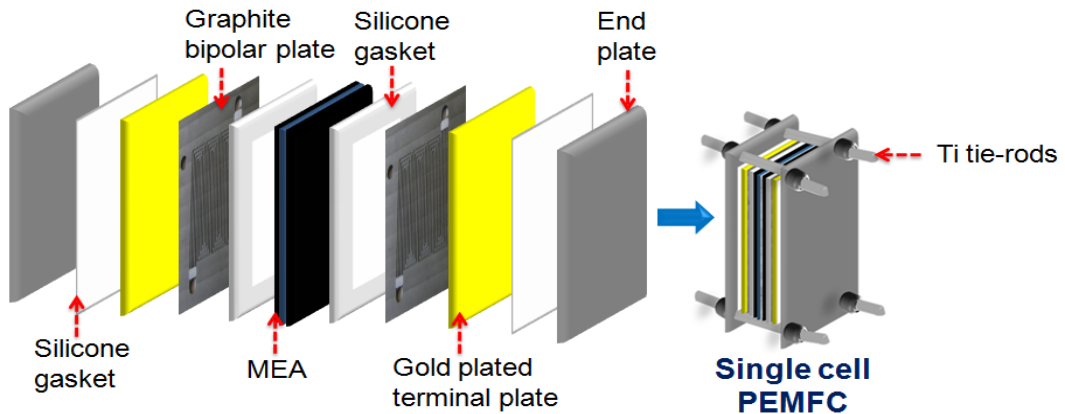
Fig. 2.3. Single cell PEMFC components and assembly

2.4.2. For half-cell performance evaluation

In addition to single cell testing, the catalysts discussed in Chapter 7 were also evaluated in half cell mode using three electrode configuration. The catalyst ink was prepared by dispersing 2 mg of catalyst in 250 µl double

distilled H_2O and 50 μl of Nafion® (5wt.% dispersion) [Ganesh *et al.* 2014]. This mixture was subjected to ultrasonic vibration for 30 min to form catalyst ink and 20 μl of catalyst ink was drop-casted on meticulously polished glassy carbon (GC, disk electrode) of rotating ring disk electrode (RRDE, Pine, geometric area 0.1965 cm^{-2}). This catalyst coated RRDE was allowed to dry at room temperature for 2 h and was used as working electrode for ORR studies. Fig. 2.4 shows the constituents of RRDE.
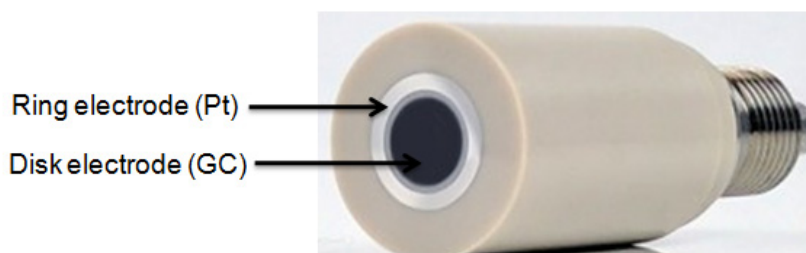
Fig. 2.4. Components of RRDE

2.5. Electrochemical characterization and evaluation

Electrochemical characterization techniques are employed to understand and evaluate the ORR behavior of the catalysts synthesized in this study. Since the in-depth understanding of ORR behavior of different catalyst materials is critical for the development and commercialization of PEMFCs, electrochemical evaluation forms the essential and most important characterization part undertaken in this work. A combination of potential sweep, potential stepping and potential hold experiments have been employed to characterize the materials, to determine active metal areas, catalytic activity and to study catalyst degradation and durability. This work was focused on *in-situ* evaluation of cathode catalysts and hence, all the cathode catalysts were evaluated in a working single cell PEMFC. Nonetheless, in Chapter 7 of this thesis, in addition to single cell testing, half cell evaluation of a few cathode catalysts in liquid electrolyte was also carried out to determine their ORR activities.

2.5.1. Electrochemical testing in single cell PEMFC

The electrochemical evaluation of the synthesized cathode catalysts was done in a working single cell PEMFC. The catalytic activity for ORR has been measured for 1 cm^2 active area MEAs in a single cell PEMFC using Solatron potentiostat and frequency response analyzer (FRA) controlled using commercial software (Corrware and ZPLOT, respectively of M/s. Scribner Associates Inc.). Fig. 2.5 shows the model of potentiostat (1287A) and FRA (1260A) employed in this study. The electrochemical experiments were carried out at room temperature (25 ± 2 °C) with controlled flow of nitrogen or oxygen being passed over the cathode and humidified hydrogen being passed over the anode at 1 atm. The polarization curves were recorded in FuelCon Evaluator-S 70277 test station at 50 °C, 1 atm and with fixed flow rate of 1 NLPM (normal litre per minute) of hydrogen and oxygen gases. The anode side was fed with pure hydrogen humidified to 90% relative humidity (RH), and the cathode side was fed with pure oxygen humidified to 70% RH.
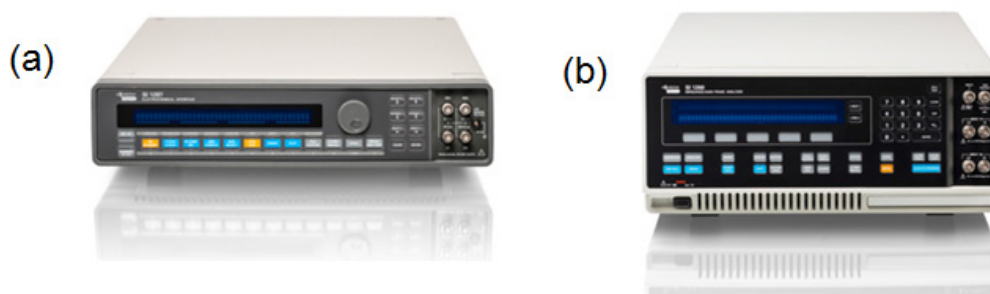
Fig. 2.5. (a) Solatron 1287A Potentiostat/Galvanostat, and (b) Solatron 1260A Impedance Analyzer

2.5.1.1. Pre-test evaluation procedure

Before subjecting the assembled MEA for performance evaluation, a series of pre-test evaluation procedures were carried out to ensure the safety of the test operator and to assess the quality of test results. The commonly followed procedures include visual inspection of the assembly, pressure test, leakage test, electrical isolation test and instrumentation checkout [Wang *et al.* 2011].

Visual inspection: A visual inspection is a simple test to perform and can discover a variety of assembly errors. It is a part of assembly procedure and include confirmation that all fluid lines and cell connecting hardware are securely fastened and all necessary components have been assembled in a proper order. Any errors detected at this stage are rectified before proceeding further.

Pressure test and leakage test: The purpose of pressure and leakage tests is to verify proper hardware sealing, proper gas flow in respective flow field channels, no cross flow of gases and no side leak. These procedures involve closing of the exhaust valve, pressurizing the line with an inert gas, monitoring the gas pressure over a period of time and using soapy water to identify the source of any leaks for repair.

Electrical isolation test: Electrical isolation tests are necessary to verify any electrical short-circuiting in the assembly. In this test, the operator ensures electrical isolation of all tie-rods from flow field plates, the reactant manifolds (end-plates) from the flow field plates, and the flow field plates to ground.

Instrumentation checkout: An instrument checkout is to verify the instrumentation is properly installed, is correctly routed to the data acquisition system, and generates accurate and expected values. Care is taken to ensure that all equipments and instruments used for evaluation are regularly calibrated.

2.5.1.2. Measurement of ORR activity and durability

Measurement of catalytic activity and durability for ORR was conducted to evaluate potential of the prepared catalyst materials as compared to commercial catalyst through the following electrochemical characterization techniques:

2.5.1.2.1. *Cyclic Voltammetry (CV)*

CV is often the first experiment performed in an electro-analytical study. CV is a commonly and frequently used electrochemical analysis in fuel cell research to characterize both qualitatively and quantitatively the performance of a catalyst material. During CV measurement, the potential of working electrode is linearly scanned at a constant potential scan rate. The current resulting from the applied

potential to the working electrode results in the current *vs.* potential plot termed as cyclic voltammogram. Fig. 2.6 shows a typical cyclic voltammogram obtained with a Pt electrode showing hydrogen adsorption/desorption, double charge layer and Pt oxide formation/reduction regions. From the cyclic voltammogram, a number of ORR catalytic parameters can be determined, as detailed below.
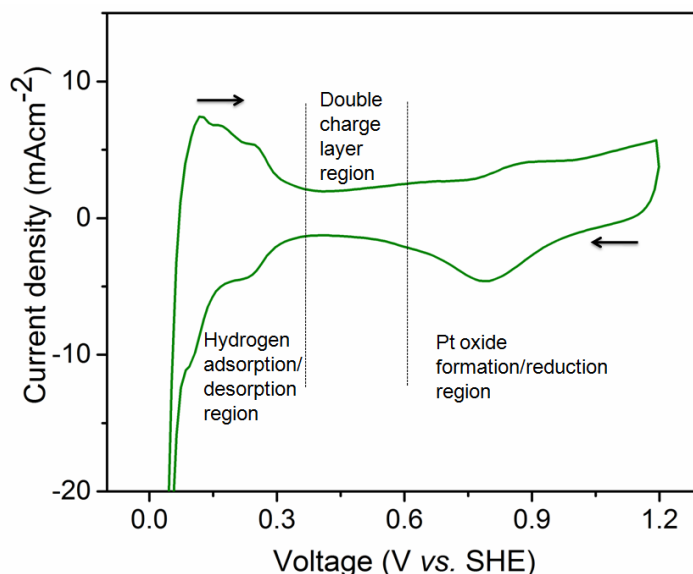
Fig. 2.6. A typical cyclic voltammogram for Pt surface electrode in PEMFC

Analysis of catalytic activity: The activity of the catalyst for ORR can be evaluated by analyzing both the onset potential and the peak current. Higher activity will generate a higher onset potential and a higher peak current.

Determination of Electrochemical active surface area (ESA): The *in-situ* CV technique has been proven to be quite valuable for ascertaining the ESA of electrodes. ESA represents the active sites for catalysis and hence, is one of the most important parameters for evaluating catalyst in MEA. The ESA of an electrode is estimated based on the relationship between the total number of reactive sites and the charge needed to remove a monolayer of adsorbed hydrogen on the electrode as determined from CV measurement. The ESA of the Pt based electrode is calculated using *eqn. 2.3* as given below [Pozio *et al.* 2002]:

$$\text{ESA} = \frac{Q_H}{0.21 \times [Pt]} \quad \dots\dots\dots\dots\dots\dots\dots\dots\dots\dots \text{(eqn. 2.3)}$$

where, Q_H is the charge for hydrogen desorption (mCcm^{-2}) after correcting for double layer charge contribution, $[Pt]$ represents Pt loading (mgcm^{-2}) in the electrode, and 0.21 denotes the charge required to oxidize a monolayer of H_2 on bright Pt surface.

Diagnostics of PEMFC degradation: As a powerful electrochemical tool, CV has been widely employed to determine the ESA change in cathode during durability testing, diagnose degradation mechanisms and explore mitigation strategies for durability. Generally, the % of ESA retained after a pre-defined cycles of durability testing protocol is employed to study the durability of the cathode catalyst.

The CV measurements, pertaining to the studies reported in this dissertation, were performed using a potentiostat and respective voltammograms were obtained by cycling the cathode at 20 mVs^{-1} between 0 to 1.2 V *vs*. Standard Hydrogen Electrode (SHE) with pure nitrogen and pure, humidified H_2 gases fed at cathode and anode compartments, respectively. The potential cycling to clean and activate the electrode surface was carried out until reproducible voltammograms were obtained, and the CVs obtained after reaching a steady state are presented.

2.5.1.2.2. *Electrochemical impedance spectroscopy (EIS)*

Impedance analysis is a very popular and powerful non-destructive *in-situ* investigation method that is commonly employed to investigate charge transfer reactions occurring at the electrode/electrolyte interface, reaction mechanisms and to assess the state of health of the fuel cell. This technique involves applying a low-level alternating current (ac) waveform to the electrochemical system under investigation and measuring the response of the cell to this stimulus. The induced perturbations could be in the form of voltage, monitoring the current response or current drawn from the fuel cell and monitoring the voltage response. The perturbation amount is fixed and this is

superimposed on top of the existing dc voltage or current. The impedance of the cell is obtained by taking the ratio of dc voltage/ac current.

Most commonly, EIS is used to calculate the charge transfer resistance (R_{ct}) for oxygen reduction from Nyquist plots. Nyquist plots are plots between the real and imaginary impedance values of the system under investigation during a frequency sweep. R_{ct} can be determined either by fitting an equivalent circuit comprising of resistors and capacitors to the obtained data [Zhang *et al.* 2006, Du *et al.* 2007] or by measuring the diameter of the kinetic loop [Yang *et al.* 2015] in Nyquist plots representing charge transfer reactions for oxygen reduction. In either of the two cases, a lower R_{ct} value implies faster interfacial oxygen kinetics and hence, better ORR performance of the catalyst. EIS studies are also quite informative in understanding and monitoring the changes in the conductivity of the membrane over a period of time. Similarly, the changes in the activity and durability of the catalyst can also be monitored in a durability testing and reveals the extent and mechanism of degradation.

In this thesis, EIS experiments were performed using FRA by applying ac amplitude of 10 mV over the frequency range 10^{-1} to 10^5 Hz at E_{cell} of 0.9 V with pure, O_2 and humidified H_2 gases fed at cathode and anode, respectively. Additionally, in Chapter 8 of this thesis, the health assessment of catalyst was also carried out using EIS measurements by applying ac amplitude of 10 mV over the frequency range 10^{-1} to 10^5 Hz at dc bias potential of 0.5 V *vs.* SHE with pure, N_2 and humidified H_2 gases fed at cathode and anode, respectively. ZView (Scribner Associates Inc.) or ZSimpWin™ software (Princeton Applied Research) was used to analyse the EIS spectra.

2.5.1.2.3. *Chrono-amperometry (CA)*

CA is most commonly used to study the kinetics of chemical reactions, diffusion, and adsorption processes. In this technique, the current is measured, at a fixed potential, at different times since the start of polarization. The CA experiment can also be used to monitor or detect events and in such a case the selection of polarization potential becomes vital. The current *vs.* time plots can be used to discern catalytic activity of the catalysts. The loss in the

current density over a period of time gives valuable information about stability/durability of the catalyst.

In Chapter 5 and Chapter 6 of this thesis, CA measurements were done at polarization potential of E_{cell} = 0.7 V held over a period of 2.5 h using a potentiostat. In Chapter 4 and Chapter 7, CA measurements were carried out at polarization potential of E_{cell} = 0.90 V, 0.85 V and 0.80 V held over a period of 3600 s. In Chapter 8, CA measurements were carried out at polarization potential of E_{cell} = 0.90 V held over a period of 3600 s. The CA experiments were performed with pure, O_2 and humidified H_2 gases fed at cathode and anode, respectively.

2.5.1.2.4. *Polarization curve*

The polarization curve generation is the standard electrochemical technique for characterizing the performance of fuel cells. Two data collection modes are frequently used in obtaining the polarization curve, conducted by adjusting either the cell voltage or current density and recording the corresponding current density or cell voltage, respectively [Jiang *et al.* 2011]. A typical polarization curve of a cell obtained by collecting the cell voltage as a function of current density is shown in Fig. 2.7. In PEMFC, there are several types of polarization losses during operation condition that result in lower performance [Liebhafsky *et al.* 1968, Larminie *et al.* 2003, O'Hayre *et al.* 2006]. These are detailed as given below.

(i) *Mixed potential at electrodes* – These arise due to unavoidable parasitic reactions that lower the equilibrium electrode potential. One important reason for this loss is the crossover of reactants from one side of electrode to the other through the electrolyte.

(ii) *Activation losses*– These arise predominantly due to kinetics of the electrodes. Activation losses come into play in the initial stage as chemical reaction has not yet begun and activation barrier has to be overcome to drive the reaction to progress. The electrode kinetics is decisive here and an electrode with faster kinetics can easily overcome the activation barrier with minimum

activation losses. The effects of these losses are most pronounced at low current densities (~1 to 200 mAcm^{-2}). In PEMFC, sluggish kinetics of ORR at cathode is a major reason responsible for activation losses amounting upto 500 mV during operating conditions.
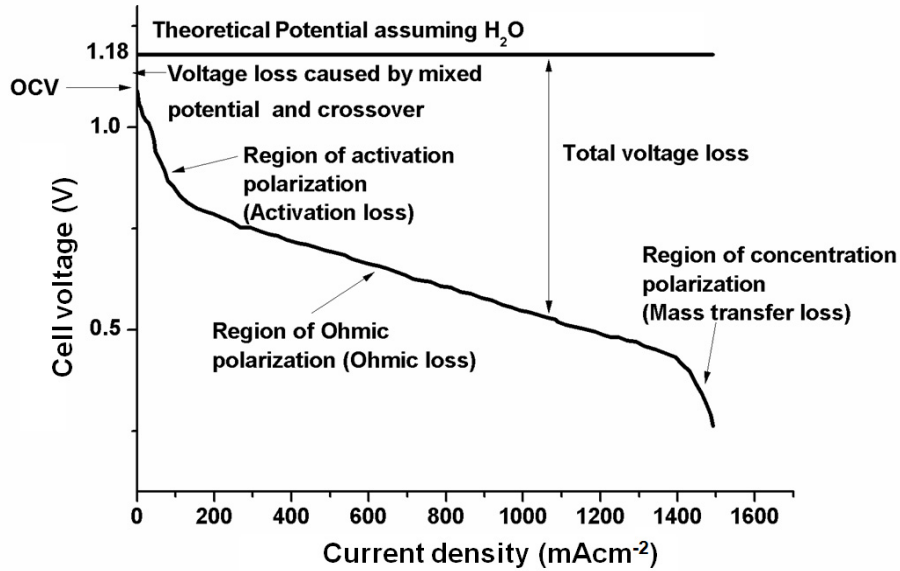
Fig. 2.7. Typical polarization curve of PEMFC [Jiang *et al.* 2011]

(iii) **Ohmic losses** – These kinds of losses arise mainly due to resistance to the flow of charged ions through the electrolyte. Along with this, resistance offered to the flow of electrons in the inter-connects, anode and cathode also contribute to ohmic losses. The effects of these losses are most pronounced at intermediate current densities (~200 to 500 mAcm^{-2}).

(iv) **Mass transport losses** – These losses arise due to concentration differences of the reactant gases. It is the effect of consumption of fuel or oxidant at the respective electrodes at a faster rate than it can be supplied leading to reactant starvation. The effect of these losses are most pronounced at high current densities (>500 mAcm^{-2}).

All these polarization losses contribute in their own way to decide the operational voltage of the cell. The combined contribution of these sources of voltage loss (usually termed as overvoltage or overpotential) causes the cell voltage to decrease with increasing current density.

The data from polarization curve can also be used to calculate the power density of the MEA (cell voltage × current density) and is plotted as a function of current density. From the power density curve, the maximum power density of the fuel cell MEA can be then known. Power density reflects the overall compactness of the fuel cell system; a higher power density indicates that a compact system can be realised with a lower Pt loading. In principle, beside the catalysts, the performance of a fuel cell (polarization curve) is also affected by the quality and property of MEA and the operating conditions, such as temperature, pressure, gas flow rates, etc. Therefore, for accurate comparisons of catalyst performance, it is mandatory to maintain identical cell configuration and testing conditions. Table 2.4 summarizes the cell configuration and testing conditions for single cell PEMFC performance evaluation adopted in this study and Fig. 2.8 presents the photograph of evaluation of single cell PEMFC in test station.

Table 2.4. Typical cell configuration and testing condition of single cell PEMFC

	Anode	Cathode
Catalyst	Pt/C	In-house
Metal loading (mgcm^{-2})*	0.5	0.5
Active area (cm^2)	1	1
Flow field plates	Graphite composite	Graphite composite
Gasket	Silicone	Silicone
Terminal plates	Gold coated Cu plate	Gold coated Cu plate
End plates	Titanium	Titanium
Gases	H$_2$	O$_2$/N$_2$
RH (%) for polarization curve	90	70
Tie-rods	Titanium	
Membrane	Nafion®-115	
Cell temperature (° C)**	25 ± 2	
Gas pressure (atm)	1	

* Chapter 3- 0.8 mgcm^{-2} ; ** Polarization curves- 50 °C
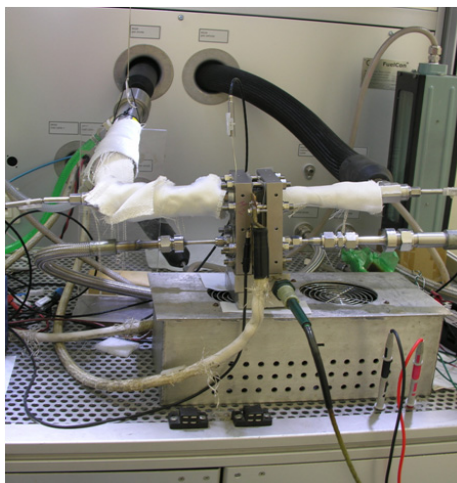
Fig. 2.8. Evaluation of electrochemical performance of single cell PEMFC in test station

Since Pt, the best known catalyst for HOR was used in this study at the anode side, the activation losses due to HOR can be considered to be negligible. Also, HOR kinetics is 6 times faster than ORR making polarization losses due to HOR further negligible. Moreover, while evaluating the ORR catalytic performance of the synthesized catalysts, the anode catalyst was kept the same (Pt/C) with constant Pt loading in all the electrodes used for the studies. Identical cell configuration and testing conditions were employed to have a meaningful comparison. Based on the above considerations, the contributions to the variations in polarization curve from the anode were assumed to be negligible and constant. The variations in cell level performance observed were thus attributed to the characteristics of cathode and, hence, a direct indication of the catalytic activity of the ORR catalysts employed.

Activation over-potential losses which manifest in the polarization curves in the form of lower cell voltage at lower current density region, typically <100 mAcm^{-2}, arise predominantly due to slower kinetics of the reaction at the cathode. Higher cell voltage value implies lower activation over-potential loss [Ahmadi *et al.* 2016], and hence, better ORR catalytic activity. To allow direct comparison between different MEA samples typically the performance values are corrected for mass of Pt on the electrode to give mass activity (mAmg$_{Pt}^{-1}$) or by correction of catalyst ESA to give specific activity

$(mAcm_{Pt}^{-2})$. In this work, mass activities of the catalysts are presented to compare the catalytic activity of the different catalysts. Mass activity is related to catalyst property which defines catalytic activity. Hence, it is obligatory to represent it in the activation region of fuel cell polarization curve where kinetics dominates and the role of catalyst is well represented. Beyond kinetic controlled region (<0.8 V), ohmic and mass transport losses come into picture where fuel cell performance is not just a function of catalyst. Therefore, in this study, mass activity at E_{cell} = 0.9 V, a potential at which reaction kinetics dominate, is presented, which is a direct representation of catalytic activity.

2.5.1.2.5. *Accelerated durability test (ADT)*

ADT is generally employed to evaluate cathode catalyst durability in PEMFC and it provides valuable insights into ORR performance and degradation mechanisms. ADT is typically composed of a fast and suitable aging procedure which is used in conjunction with some measure of performance and/or extent of degradation, such as ESA measurement by CV, being the most common [Hicks *et al.* 2006, Yuan *et al.* 2011, Saleh *et al.* 2012, Ishiguro *et al.* 2016]. In this work, ADT in conjunction with i*n-situ* CV, CA, EIS and fuel cell polarization studies was employed to elucidate the practical performance and understand the degradation behavior of the catalysts and data is presented in Chapter 8.

2.5.2. Electrochemical testing in liquid electrolytes

For electrochemical testing in liquid electrolyte (0.5 M H_2SO_4), a three electrode set-up was used comprising of a working electrode (the electrode where reaction of interest occurs), a counter electrode (the electrode that undergoes charge balancing reaction to that occurring on the working electrode), and a reference electrode (used to define zero volt within the system).

2.5.2.1. Cyclic voltammetry (CV) experiments

Analogous to CV experiments in full cell mode, the CV experiments in half cell configuration can also be used to determine ORR activity and

durability. In Chapter 8 of this dissertation, CVs were performed with an Autolab potentiostat/galvanostat PGSTAT-30 and a standard three-electrode cell at room temperature, employing mercury/mercurous sulphate as the reference electrode, a Pt wire as the counter electrode, and the RRDE with the catalyst layer as the working electrode. All potentials are, however, reported in this dissertation against the reverse hydrogen electrode (RHE). The CV experiments were conducted in N_2 purged 0.5 M H_2SO_4 between 0 and 1.1 V at a scan rate of 50 mVs^{-1}. The potential cycling to clean and activate the electrode surface was carried out until reproducible voltammograms were obtained and the CVs obtained after a steady state has been reached are presented in this study.

2.5.2.2. Rotating ring disk electrode (RRDE) experiments

Rotating disk voltammetry with double working electrodes (ring electrode and disk electrode) is an advanced voltammetric technique used to study the electrode kinetics and reaction mechanism [Lee *et al.* 2008]. RRDE is constructed from a disk of electrode material (e.g. gold, GC or Pt) surrounded by a ring (e.g. Pt, Au.) embedded in a rod of insulating material (e.g. teflon). The electrode is attached to a motor and rotated at a certain frequency. Usually a very slow scan rate (5 or 10 mVs^{-1}) is used while rotating the electrode in order to maintain an electrochemical steady state of electrode and to reduce the charging current to a negligible level. By measuring the current at the ring electrode, information on mechanism of electrochemical reaction occurring at disc electrode surface can be obtained. RRDE experiments are carried out with a bipotentiostat, which allows separate adjustments of disk potential, E_D and ring potential, E_R. In the RRDE technique, the current–potential characteristics of the disc are unaffected by the presence of the ring. There are two significant pieces of information that can be obtained from an ORR curve generated using RRDE. The first is the onset potential. This refers to the first inflexion point on a cathodic sweep ORR curve or the potential at which the O_2 reduction process starts. It is an intrinsic property of the given electro-catalyst. The second piece

of information relates to the pathway that is followed in the reduction of O_2 to H_2O.

In this work, RRDE experiments were conducted with the catalyst coated glassy carbon disk electrode and Pt ring electrode mounted onto an interchangeable RRDE holder (Pine Instruments, USA; Fig. 2.9) and a bipotentiostat (Biologic, VSM300). A Pt wire was used as counter electrode and mercury/mercurous sulphate as reference electrode for the measurements. The polarization curves were recorded at 1600 rpm from 0.2 to 1.2 V *vs.* RHE at a scan rate of 10 mVs^{-1} in O_2 saturated 0.5 M H_2SO_4 and the ring potential was held at 1.4 V vs. RHE.

Fig. 2.9. RRDE instrument and experimental set-up

Chapter 3

Pt-TiO$_2$ catalyst: Effect of pH of synthesis medium

Abstract

Pt-TiO₂ nano-composite materials were explored as cathode catalysts and the results are presented in this chapter. Pt-TiO₂ catalysts in different Pt:Ti atomic ratios (1:1, 2:1 and 3:1) were synthesized in acidic (pH < 3) and basic (pH > 10) medium through sol-gel route. The pH of synthesis medium significantly affected both physico-chemical and catalytic properties of the catalysts. ORR catalytic properties were evaluated *in-situ* for all the synthesized catalysts using single cell PEMFC and the performance was assessed in comparison with that of standard, commercial Pt/C catalyst. Pt-TiO₂ catalysts synthesized in acidic medium performed better than those prepared in basic medium. Among all, Pt:Ti 3:1-A was found to exhibit the best catalytic activity for ORR.
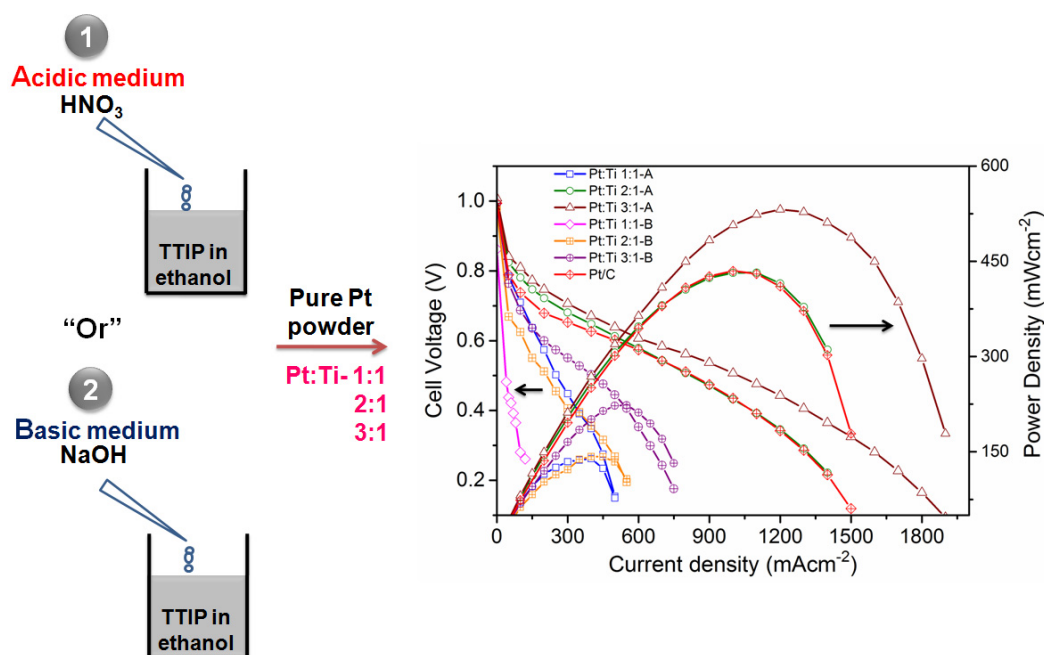
3.1. Introduction

In the emerging energy scenario based on hydrogen fuel, PEMFCs are potential candidates for stationary and transport applications [Gangeri *et al.* 2006, Padmavathi *et al.* 2013, You *et al.* 2016]. Among the various impediments to the successful commercialization of this technology, the sluggish ORR kinetics prevailing at the cathode has been the biggest challenge [Mustain *et al.* 2007]. Due to this, a typical fuel cell experiences an activation loss ≥ 0.3 V [Paulus *et al.* 2002]. This has triggered intense research for a new ORR catalyst system with significantly higher activity and lower activation loss compared to the catalysts in use today.

Alloying of Pt with transition metals is generally attempted to achieve ORR catalytic activity higher than that of state of art Pt/C catalysts [Gasteiger *et al.* 2009, Chandran *et al.* 2014, Mei *et al.* 2015, Divya *et al.* 2016]. However, these alloyed catalysts suffer from leaching of the alloying element into the membrane which undesirably affects the fuel cell performance [Antolini *et al.* 2006]. In addition, alloying generally needs high temperature treatment (> 800 °C) under inert or reducing gas atmosphere, to form homogeneous alloys that are stable in acidic PEMFC environment. Non-alloyed, Pt-MO$_x$ composites (M= Ti, W) have also been investigated for ORR in PEMFC and they have exhibited improved activity than Pt [Shim *et al.* 2001]. Specifically, the discovery of synergistic interactions between Pt and titania (TiO$_2$) which promotes ORR catalytic activity has fuelled many investigations on Pt and titania based catalysts for improved PEMFC performance [Baker *et al.* 1979, Horsley 1979, Beard *et al.* 1986, Long *et al.* 2013]. Huang *et al.* reported similar fuel cell performance for Pt dispersed on mesoporous TiO$_2$ as carbon supported Pt catalyst, but with ~ 12% higher peak power density [Huang *et al.* 2009]. Rajalakshmi *et al.* as well reported Pt-TiO$_2$ catalyst showing comparable performance to Pt/C when operated at 60 °C and 0.8 V [Rajalakshmi *et al.* 2008]. However, due to semi-conducting electrical properties of TiO$_2$, lower fuel cell performance was obtained with Pt-TiO$_2$ catalyst in the ohmic region as compared to Pt/C catalyst. Hence, for the electrochemical applications in fuel cell, the increase in the electronic conductivity of TiO$_2$ is necessarily required.

Increase in electronic conductivity of TiO$_2$ through introduction of dopants such as Nb has been effectively utilized to achieve better fuel cell performance. Elezović *et al.* reported enhanced ORR catalytic activity of Nb doped TiO$_2$ supported Pt with ~6 times higher mass activity at potential of 0.9 V as compared to Pt/C catalyst [Elezović *et al.* 2010]. Conductive non-stoichiometric TiO$_2$ can be prepared by sol-gel technique without the use of any dopants. In the sol-gel technique, the presence of a large number of hydroxyl groups on crystal surface facilitates formation of titanium and oxygen vacancies during annealing process which results in non-stoichiometric and conductive titania [López *et al.* 1999]. The strong dependence of catalytic activity on preparation conditions has been brought out in reports, as they influence the physico-chemical properties of the synthesized materials which can contribute towards ORR catalytic activity [Mukerjee *et al.* 1995, Min *et al.* 2000]. Additionally, mode of preparation also influences electro-catalytic behaviour of TiO$_2$ [Tammeveski *et al.* 1999, Tsujiko *et al.* 2002].

In the studies reported so far [Shim *et al.* 2001, Mentus 2005, Rajalakshmi *et al.* 2008, von Kraemer *et al.* 2008, Huang *et al.* 2009, Bauer *et al.* 2010, Elezović *et al.* 2010, Elezović *et al.* 2010, Cerri *et al.* 2013, Kim *et al.* 2013, Lee *et al.* 2013, Ruiz-Camacho *et al.* 2014, Zhang *et al.* 2015], the role of TiO$_2$ in ORR catalysts has been mainly as support, sometimes with doping to enhance its support characteristics. However, the effect of synthesis conditions, which strongly influence catalyst performance, specifically pH of synthesis medium, on ORR catalytic activity, has not been investigated. Hence, this study was undertaken to understand in detail the effect of pH of synthesis medium on physico-chemical properties and ORR catalytic activity of Pt-TiO$_2$ catalysts.

Pt-TiO$_2$ catalysts in different Pt:Ti atomic ratios (1:1, 2:1 and 3:1) were synthesized in both acidic (pH < 3) and basic (pH > 10) medium through sol-gel route and characterized. For comparison, pristine TiO$_2$ samples were also prepared under similar conditions. ORR catalytic properties were evaluated *in-situ* for all the synthesised catalysts using single cell PEMFC and the performance was assessed in comparison with standard, commercial Pt/C catalyst.

3.2.   Experimental

3.2.1. Materials

Pt-TiO$_2$ nano-composites were synthesized using titanium isopropoxide and Pt powder. HNO$_3$ and NaOH were used to maintain acidic and basic medium, respectively. Ethanol and ultra-pure water were used as solvents. Details of all the above chemicals and materials are furnished in *Chapter 2, Section 2.1*. The materials used for electrode preparation, MEA fabrication and single cell PEMFC assembly remain the same as detailed under *Chapter 2, Section 2.1 and Section 2.4.1*.

3.2.2. Synthesis of Pt-TiO$_2$ nano-composite catalysts

Synthesis of Pt-TiO$_2$ nano-composites and pristine TiO$_2$ samples were carried out in both acidic and basic medium *via* sol-gel route, as detailed in *Chapter 2, Section 2.2.1*.

3.2.3. Characterization

Characterization methods employed include FT-IR, XRD, Raman spectroscopy, ICP-AES, HRTEM, BET specific surface area and four-probe conductivity measurement. The details of all these methods are given in *Chapter 2, Section 2.3*.

3.2.4. Fabrication of MEA and Assembly of single cell PEMFC

MEA for single cell fuel cell was prepared using Nafion$^®$ membrane and catalyst ink coated PTFE sintered carbon paper. The procedures for MEA fabrication and single cell PEMFC assembly are detailed in *Chapter 2, Section 2.4.1.4* and *Section 2.4.1.5*, respectively. The metal (Pt) loading at the anode and cathode in MEA was 0.5 mg$_{Pt}$cm^{-2} and 0.8 mg$_{Pt}$cm^{-2}, respectively.

3.2.5. Evaluation of single cell PEMFC performance

The single cell fuel cell testing was carried out in a fuel cell test station. The polarization curves were recorded at 50 °C, 1 atm and with fixed flow rate of 1 NLPM of hydrogen and oxygen gases. The anode side was fed with pure hydrogen humidified to 90% RH, and the cathode side was fed with pure oxygen humidified to 70% RH.

3.3. Results and Discussion

3.3.1. Synthesis and Characterization of TiO_2 and Pt-TiO_2 nano-composites

The formation of TiO_2 in the synthesized nano-composites was confirmed using FTIR spectra. Fig. 3.1 shows the FT-IR spectra of pristine TiO_2 and Pt-TiO_2 catalysts synthesized in acidic and basic medium. In both medium, pristine TiO_2 and Pt-TiO_2 catalysts have shown peaks around 3400 cm^{-1} and 1620 cm^{-1} corresponding to stretching and bending vibrations of O-H groups, respectively; and peaks around 650 cm^{-1} and 1390 cm^{-1} corresponding to Ti-O and Ti-O-Ti stretching vibrations, respectively. The formation of TiO_2 occurs *via* hydrolysis and condensation of the titanium alkoxides (*eqn. 3.1* and *eqn. 3.2*) [Kallala *et al.* 1992]. The hydrolysis of titanium isopropoxide results in the formation of Ti-OH (*eq. 3.1*) which further undergoes condensation reaction forming an extended Ti-O-Ti network (*eqn. 3.2*). The presence of Ti-O and Ti-O-Ti groups inferred from FTIR spectra confirm the formation of TiO_2 in both pristine TiO_2 and Pt-TiO_2 catalysts. It is also observed that the Ti-O stretching frequency got shifted to a higher wave number in the case of Pt-TiO_2 catalysts (from 570 cm^{-1} to 720 cm^{-1}) which is attributed to the interaction between the local electron density of Pt and TiO_2.

$$Ti\text{-}OR + H_2O \rightarrow TiOH + ROH \quad ………….................. \text{(eqn. 3.1)}$$

$$Ti\text{-}OH + XO\text{-}Ti \rightarrow Ti\text{-}O\text{-}Ti + XOH \quad ……................... \text{(eqn. 3.2)}$$
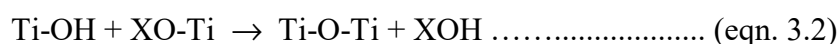
(X = H or alkyl group; R = isopropyl group)

3.3.2. Effect of synthesis medium on physico-chemical properties of pristine TiO_2 and Pt-TiO_2 nano-composite catalysts

Fig. 3.2 (a) shows Raman spectra of pristine TiO_2 and Pt-TiO_2 nano-composite catalysts synthesised in both acidic and basic medium. It was observed that TiO_2-A resulted in the formation of anatase phase; whereas, TiO_2-B led to the formation of amorphous phase. However, the introduction of Pt to TiO_2 has led to the formation of anatase phase in both medium. The anatase TiO_2 phase shows a strong Raman band at around 145 cm^{-1} corresponding to E_g mode and relatively weaker bands at 198 cm^{-1}, 396 cm^{-1}, 517 cm^{-1} and 638 cm^{-1}, which correspond to E_g, B_{1g}, A_{1g} or B_{1g} and E_g

modes, respectively [Ohsaka *et al.* 1978].
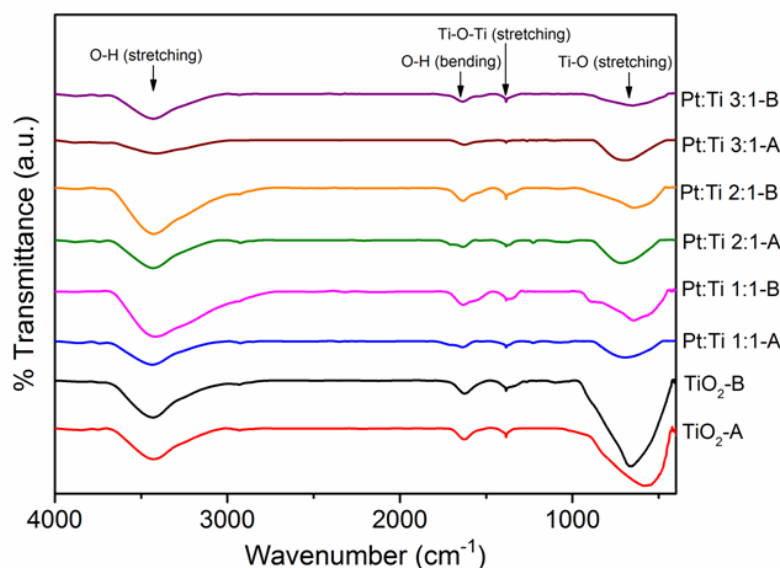
Fig. 3.1. FT-IR spectra of pristine TiO$_2$ and Pt-TiO$_2$ catalysts

The strongest E$_g$ mode at 145 cm^{-1} is attributed to the symmetric stretching vibration of oxygen atoms in O-Ti-O bonds. The B$_{1g}$, A$_{1g}$ mode corresponds to symmetric and anti-symmetric bending vibration of O-Ti-O bonds, respectively. The absence of the conspicuous low frequency E$_g$ mode in pristine TiO$_2$-B and its existence in all the Pt-TiO$_2$ systems indicate that selective anatase phase formation has occurred with the introduction of Pt in these catalysts, in both medium. This suggests a possible interaction between Pt and TiO$_2$ that directs anatase phase formation. Also, a blue shift of the lowest frequency E$_g$ mode (at ~ 145 cm^{-1}) and peak broadening are observed for all Pt-TiO$_2$ catalysts with respect to pristine TiO$_2$-A, as shown in Fig. 3.2 (b) and (c). The peak shift and broadening of anatase TiO$_2$ is attributed to phonon confinement and non-stoichiometric phenomenon [Zhang *et al.* 2000]. Especially, the peak broadening has been attributed to formation of non-stoichiometric titania due to oxygen vacancies [Parker *et al.* 1990]. Stoichiometric titania is highly resistive due to its large band gap (4.5 eV); whereas, the electrons resulting from the electronic disorder introduced by oxygen vacancies impart electrical conductivity in non-stoichiometric titania [Bartholomew *et al.* 1969, Sharma *et al.* 2012]. As it can be seen from Fig. 3.2 (b) and (c), peak broadening is more predominant in the case of catalysts prepared in acidic medium when compared to

95

those prepared in basic medium. This suggests that the Pt-TiO$_2$ catalysts synthesized in acidic medium are more non-stoichiometric than the basic medium catalysts, and hence, are more conductive and are expected to show better catalytic performance in fuel cell.
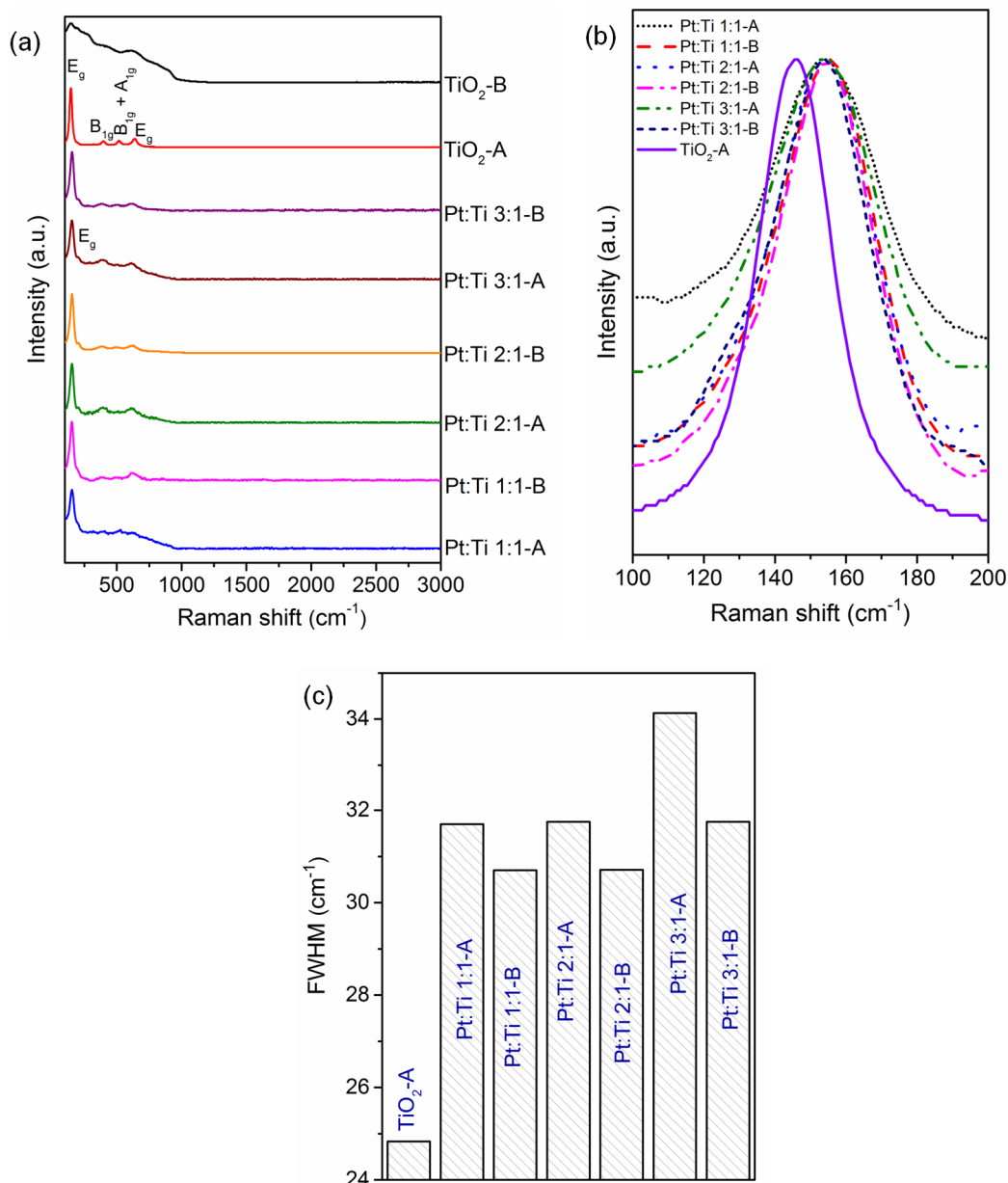
Fig. 3.2. (a) Raman spectra of pristine TiO$_2$ and Pt-TiO$_2$ catalysts; (b) magnified view of the main, low frequency E$_g$ band of anatase TiO$_2$ in TiO$_2$-A and Pt-TiO$_2$ catalysts shown in (a), and (c) FWHM of E$_g$ band of the catalysts shown in (b)

The more non-stoichiometric nature of Pt-TiO$_2$ catalysts synthesized in acidic medium than those in basic medium can also be explained based on titania formation in both medium. As explained earlier (*Section 3.3.1*), the extent of hydrolysis and condensation reactions of titanium isopropoxide (*eqn. 3.1* and *eqn.3.2*) depend on the pH of the medium [Aruna *et al.* 2000]. Under acidic condition, hydrolysis is faster than condensation, leading to the formation of higher concentration of Ti-OH species. The higher rate of hydrolysis under acidic condition can be explained by the protonation of OR groups attached to metal by H$_3$O$^+$, making their charge more positive [Gopal *et al.* 1997]. The metal ions being positively charged repels the OR groups and attach to OH groups, thus promoting hydrolysis and forming more Ti-OH species. Under basic condition, deprotonation of hydroxyl groups occur resulting in increased condensation rates [Simonsen *et al.* 2010] leading to the formation of lesser Ti-OH species. On thermal treatment, the hydroxyl groups present in the samples undergo dehydroxylation producing anionic vacancies, *i.e.* non-stoichiometric titania [López *et al.* 1999]. Thus, the formation of non-stoichiometric, conductive titania is more favored under acidic conditions.

The relationship between pH of synthesis medium and conductivity of the obtained Pt-TiO$_2$ catalysts were further confirmed through electrical conductivity measurements using a four probe conductivity meter and the results are presented in Table 3.1. It is seen that conductivity of the Pt-TiO$_2$ catalysts depends upon synthesis medium pH and Pt content. Increase in electrical conductivity with increase in Pt content was observed for both classes of catalysts; whereas, higher electrical conductivity was obtained in acidic medium prepared catalysts as compared to basic medium prepared catalysts. Additionally, even with the same Pt content, higher conductivity was obtained in acidic medium prepared catalysts signifying the effect of synthesis medium pH on the properties of catalysts.

The XRD spectra of pristine TiO$_2$-A and TiO$_2$-B are compared in Fig. 3.3 (a). TiO$_2$-A shows reflections corresponding to (101), (004), (200), (105), (204), (220), (215) and (312) planes of crystalline anatase phase (JCPDS no. 89-4921) along with a small peak corresponding to brookite phase at $2\theta = 30.8$ °; whereas, pristine TiO$_2$-B exhibits amorphous TiO$_2$ phase. These observations are in agreement with Raman

results discussed earlier. The XRD spectra of Pt powder as such and after calcination under the same conditions as adopted during synthesis are shown in Fig. 3.3 (b). The characteristic fcc Pt reflections corresponding to (111), (200), (220), (311) and (222) planes are obtained (JCPDS no. 89-7382). Fig. 3.3 (c) gives the XRD spectra of the synthesized Pt-TiO$_2$ catalysts. It is seen that all the samples show the characteristic fcc Pt reflections. There was no shift in the position of the characteristic peaks of Pt in these materials, thus confirming the absence of any Pt-Ti alloy formation. Hence, these catalysts system have only two active components present in the form of Pt and anatase TiO$_2$. Besides, the absence of reflections corresponding to TiO$_2$ in Pt-TiO$_2$ catalysts could be due to the low content (< 20 wt.%) of TiO$_2$ or its presence in very fine structures in the catalytic system [Xiong *et al.* 2004] which gets undetected by XRD technique.

Table 3.1. Conductivity, crystallite size and SSA of Pt-TiO$_2$ catalysts

Catalyst	Electrical conductivity (Scm^{-1})	Crystallite size of Pt (nm)	Specific surface area (m^{2}g^{-1})
Pt:Ti 1:1-A	36.04	13.7	53.1
Pt:Ti 1:1-B	0.51	32.7	13.0
Pt:Ti 2:1-A	47.93	18.1	32.1
Pt:Ti 2:1-B	10.88	39.1	14.3
Pt:Ti 3:1-A	72.21	18.0	30.3
Pt:Ti 3:1-B	15.53	27.7	10.5

The XRD results from Fig. 3.3 (b) and (c) were analyzed further to understand the effect of calcination temperature and synthesis medium on the growth of Pt crystallite size in Pt-TiO$_2$ catalysts. The crystallite size of pristine Pt initially was 8.5 nm and after calcination increased to 25.3 nm. Pt crystallite size computed for all Pt-TiO$_2$ catalysts from XRD data are given in Table 3.1. Pt-TiO$_2$-B catalysts exhibited Pt crystallite sizes greater than that of pristine Pt after calcination; whereas, Pt crystallite sizes in Pt-TiO$_2$-A catalysts were less than that of pristine Pt after calcination. This indicates that in acidic medium, crystallite growth of Pt during synthesis process is

hindered, which is not the case in basic medium.
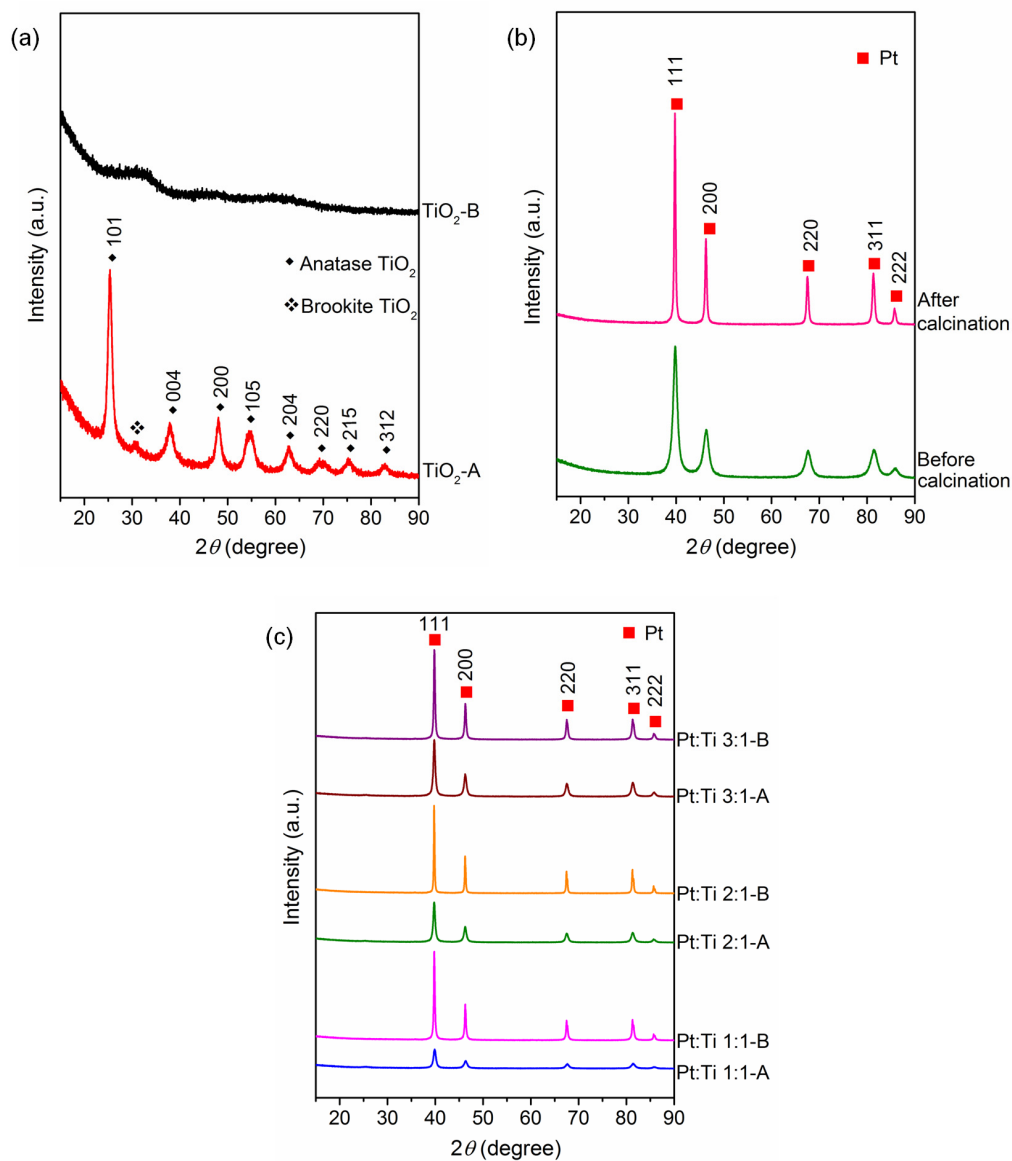
Fig. 3.3. XRD spectra of (a) pristine TiO$_2$, (b) pristine Pt powder before and after calcination, and (c) Pt:Ti catalysts

As discussed previously, in acidic medium the hydrolysis of titanium isopropoxide being faster than condensation, results in the formation of several hydroxyl groups, compared to the situation in basic medium. The presence of surface hydroxyl groups in Ti-OH species helps to provide stronger interaction with Pt during the synthesis process and gives the essential hindrance to crystallite growth on calcination resulting in smaller Pt crystallite size. Thus, the Pt crystallite sizes of Pt-

TiO$_2$-A catalysts are smaller compared to Pt-TiO$_2$-B catalysts. One of the major factors reported to result in loss of catalyst performance during fuel cell operations is increase in Pt crystallite size [Shao *et al.* 2007]. Based on the present study, it can be inferred that the Pt-TiO$_2$ catalysts synthesized in acidic medium with smaller size and resistant to crystallite growth could be expected to perform better with good stability as an ORR catalyst in PEMFC.

The surface morphology of synthesized Pt-TiO$_2$ nano-composites was studied using TEM. Fig. 3.4 and Fig. 3.5 shows TEM images of Pt-TiO$_2$ catalysts and their corresponding SAED patterns, respectively. It can be clearly seen that, Pt NPs are homogeneously distributed on TiO$_2$ substrates (Fig. 3.4). The particle size of Pt in Pt-TiO$_2$-A catalysts is in the range 12-18 nm (Pt:Ti 1:1-A= 12 nm, Pt:Ti 2:1-A= 17 nm and Pt:Ti 3:1-A= 18 nm); whereas, in the case of Pt-TiO$_2$-B catalysts the values are in the range 29-34 nm (Pt:Ti 1:1-B= 29 nm, Pt:Ti 2:1-B= 34 nm and Pt:Ti 3:1-B= 29 nm). These observations match with those obtained from XRD results. The lattice spacing measurements from the SAED patterns of Pt-TiO$_2$ catalysts correspond to Pt and TiO$_2$ reflection planes (Fig. 3.5) which further confirm the presence of Pt and TiO$_2$ as the two active components of the catalyst materials without any alloy formation between them. Diffraction rings with higher intensity are observed for Pt-TiO$_2$-A catalysts compared to Pt-TiO$_2$-B catalysts (Fig. 3.5); this indicates higher crystallinity for Pt-TiO$_2$-A catalysts. For catalyst system based on metal oxides, an increase in ORR catalytic activity is reported with increase in crystallinity of the material [Okada *et al.* 2008]. In a similar way, with higher crystallinity, Pt-TiO$_2$-A catalysts are expected to show better ORR performance in fuel cell. Surface area of the material forms an important attribute for catalysis; better ORR catalytic activity of catalyst with higher surface area is well known. Table 3.1 shows SSA of Pt-TiO$_2$ catalysts. It was found that Pt-TiO$_2$-A catalysts have lower SSA compared to pristine TiO$_2$-A (91.7 m^{2}g^{-1}); whereas, such a trend was not observed in the case of Pt-TiO$_2$-B catalysts in comparison to pristine TiO$_2$-B (11.9 m^{2}g^{-1}). The variation in SSA of TiO$_2$-B and Pt-TiO$_2$-B systems was found to be quite negligible and was within $\pm$ 2.5 m^{2}g^{-1}. However, all the Pt-TiO$_2$-A catalysts have higher SSA as compared to Pt-TiO$_2$-B catalysts. The variations in SSA of Pt-TiO$_2$ catalysts is linked to the strength of

interaction between Pt and titania during the synthesis process [López *et al.* 1999]. Thus, with stronger interaction in acidic medium, smaller crystallites with higher SSA are formed compared to those in basic medium.
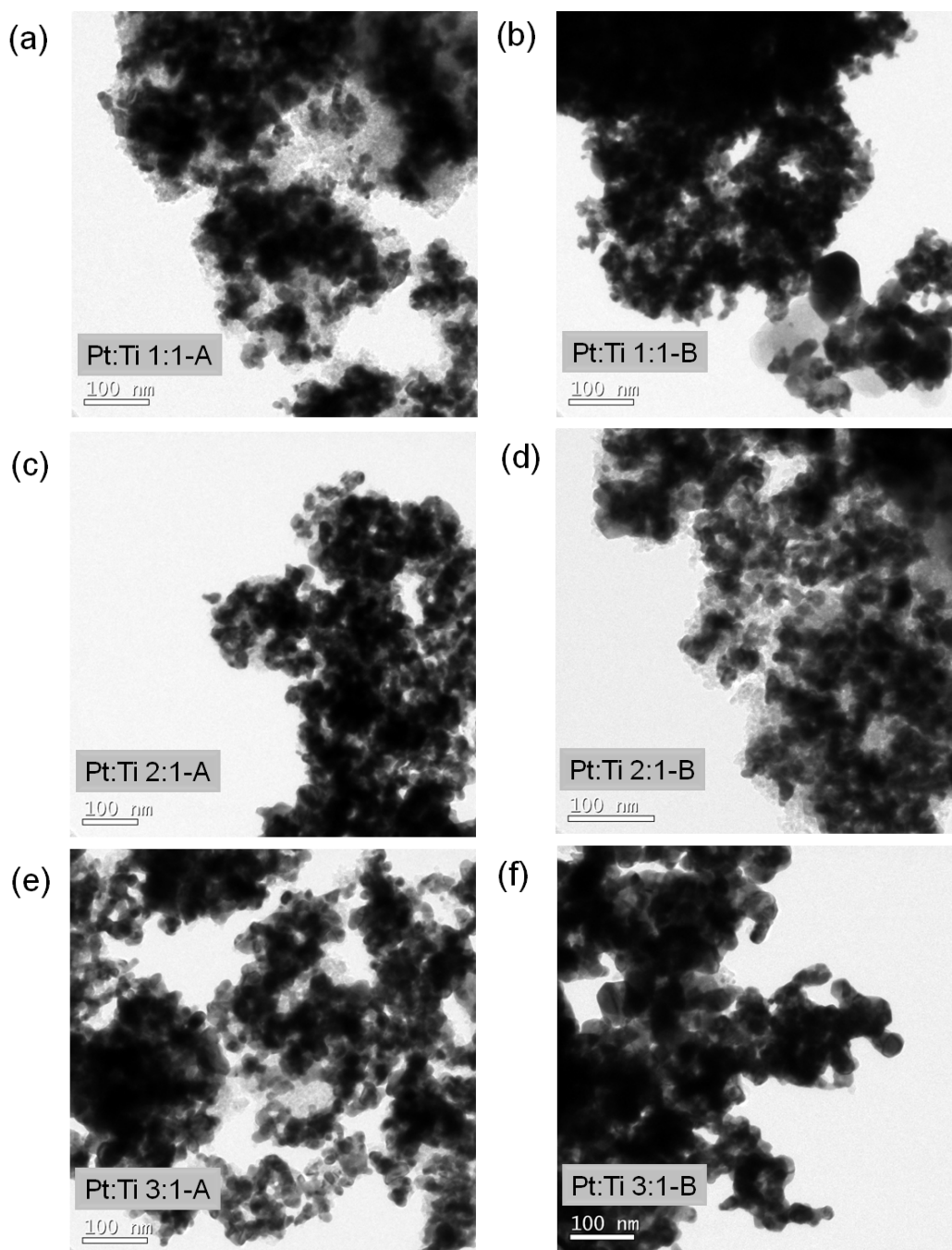
Fig. 3.4. TEM images of (a) Pt:Ti 1:1-A, (b) Pt:Ti 1:1-B, (c) Pt:Ti 2:1-A, (d) Pt:Ti 2:1-B, (e) Pt:Ti 3:1-A, and (f) Pt:Ti 3:1-B catalysts
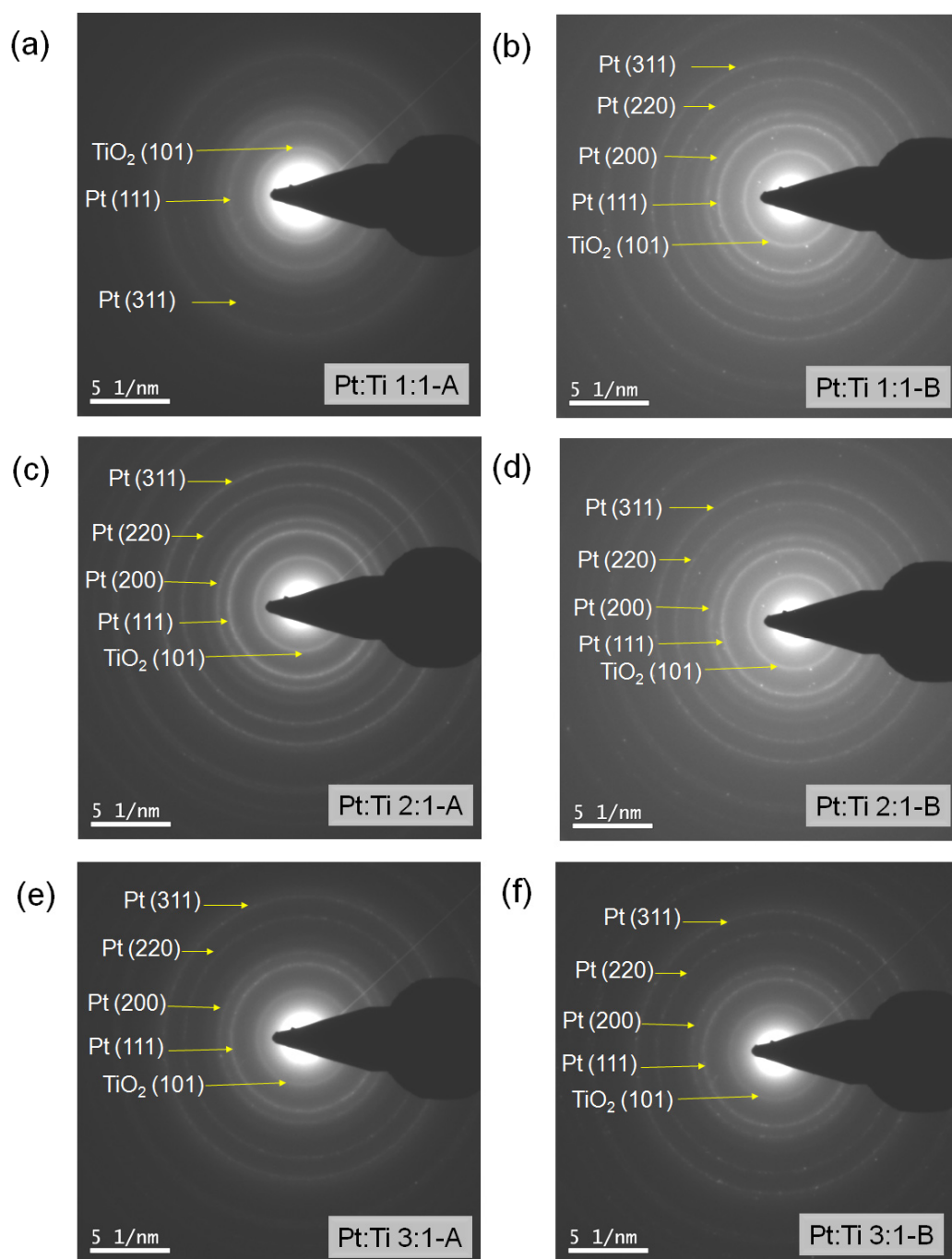
Fig. 3.5. SAED patterns of (a) Pt:Ti 1:1-A, (b) Pt:Ti 1:1-B, (c) Pt:Ti 2:1-A, (d) Pt:Ti 2:1-B, (e) Pt:Ti 3:1-A, and (f) Pt:Ti 3:1-B catalysts

The above studies have confirmed the profound effect of the pH of synthesis medium on the physico-chemical properties of Pt-TiO₂ catalysts. It was seen that Pt-TiO₂ catalysts synthesized in acidic medium had smaller crystallite size, higher SSA, more non-stoichiometric titania with higher electrical conductivity and crystallinity

compared to catalysts prepared in basic medium. It was also observed that the effect of Pt:Ti atomic ratio on properties of synthesized catalysts was of less significance compared to the effect of synthesis medium.

3.3.3. Evaluation of ORR catalytic activity through single cell fuel cell performance

All the synthesized Pt-TiO₂ catalysts were subjected to evaluation of performance as ORR catalyst in PEMFC and were compared with the performance of standard, commercial Pt/C catalyst. Fig. 3.6 shows single cell fuel cell polarization curves of Pt-TiO₂ and Pt/C catalysts, and the derived parameters are given in Table 3.2. Open circuit voltage (OCV) reflects the overall catalytic activity (data given in Table 3.2); a higher OCV indicates potentially lower parasitic reactions. Since all other aspects that contribute to OCV are maintained the same here, cell with Pt:Ti 3:1-A catalyst showed the highest OCV of 1.008 V indicating the best catalytic activity amongst all. The cell voltage at low current density region (typically <100 mAcm^{-2}) gives the direct indication about the activation loss, and hence, the ORR kinetics and catalytic activity. A higher cell voltage value reflects lower activation loss and better ORR catalytic activity. Table 3.2 shows the voltages of cells with Pt-TiO₂ catalysts and commercial Pt/C catalyst at a current density of 50 mAcm^{-2}. Based on this, the cathode catalysts employed follow ORR catalytic activity in the order Pt:Ti 3:1-A > Pt:Ti 2:1-A > Pt/C > Pt:Ti 1:1-A > Pt:Ti 3:1-B > Pt:Ti 2:1-B > Pt:Ti 1:1-B. Both Pt:Ti 3:1-A and Pt:Ti 2:1-A performed better than Pt/C with an operating voltage higher by 52 mV and 35 mV, respectively. All the Pt-TiO₂-B catalysts performed at lower voltages than Pt-TiO₂-A and Pt/C catalysts. Better ORR catalytic activity as evidenced from fuel cell performance is seen with the catalysts synthesized in acidic medium corroborating the Raman, XRD, SSA and SAED results. This can be attributed to the favorable catalytic properties such as smaller Pt crystallite size, higher SSA, more non-stoichiometric titania with higher electrical conductivity and crystallinity obtained for catalysts synthesized in acidic medium.

For Pt-TiO₂-A catalysts with varying Pt:Ti ratios, the order of catalytic activity obtained (3:1 > 2:1 > 1:1) can be explained on the basis of increased local electronic conductivity as a result of increase in Pt content in the catalysts as supported by

electrical conductivity results as well (Table 3.1) [Siracusano *et al.* 2013]. Pt-TiO₂-B catalysts also showed a similar trend with Pt:Ti 3:1-B showing the best ORR performance in fuel cell. Thus, with the highest Pt content, Pt:Ti 3:1 catalysts were found to show the best performance under both categories. However, with the same Pt content in both Pt:Ti 3:1-A and Pt:Ti 3:1-B, the better fuel cell performance of the former catalyst signifies the role of pH of synthesis medium on catalytic activity, which surpasses the effect of Pt:Ti atomic ratio.
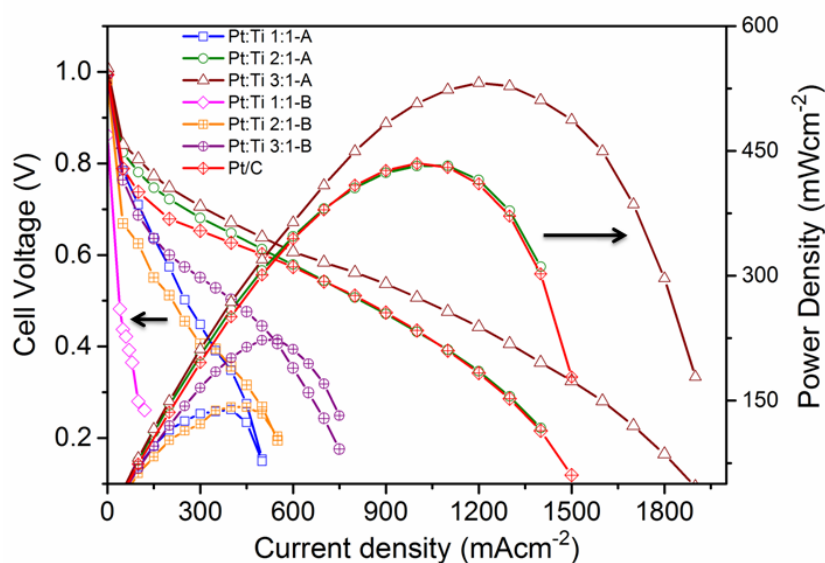
Fig. 3.6. Polarization curves of Pt-TiO₂ and Pt/C catalysts

Fuel cells are usually operated at voltage > 0.65 V to have fuel cell energy conversion efficiency > 55% [Gasteiger *et al.* 2005]. Typically, PEMFCs are operated in the voltage window of 0.7- 0.8 V. Mass activity forms one of the critical aspects of ORR catalysis. In terms of mass activity at cell voltage of 0.9 V, a voltage at which kinetic aspects or activation losses dominate, the ORR catalysts employed follows the order Pt:Ti 3:1-A >Pt:Ti 2:1-A >Pt/C >Pt:Ti 1:1-A>Pt:Ti 3:1-B>Pt:Ti 2:1-B >Pt:Ti 1:1-B. It can be observed that this order is the same as that obtained based on activation loss, as explained earlier. Thus, Pt:Ti 3:1-A showed ~41% higher performance than the standard, commercial Pt/C catalyst, in terms of mass activity. Power density is another important factor that contributes to effective commercialization of PEMFCs. Power density reflects the overall compactness of the fuel cell system; a higher power density indicates that a compact system can be

104

realised with a lower Pt loading. Pt:Ti 3:1-A catalyst showed the highest peak power density of 530 mWcm^{-2} as against 440 mWcm^{-2} of Pt/C catalyst (*i.e.* ~20% higher), both obtained under similar conditions.

Table 3.2. Parameters obtained from single cell fuel cell testing polarization curves

Catalyst	OCV (V*)	Voltage @ 50 mAcm^{-2}** (V*)	Mass activity @ 0.8 V*, (mAmg^{-1}$_{Pt}$)	Maximum Power Density (mWcm^{-2}**)
Pt:Ti 1:1-A	0.996	0.784	29	140
Pt:Ti 2:1-A	1.001	0.824	35	430
Pt:Ti 3:1-A	1.008	0.841	40	530
Pt:Ti 1:1-B	0.862	0.437	-	29
Pt:Ti 2:1-B	0.982	0.669	16	142
Pt:Ti 3:1-B	0.993	0.764	25	223
Pt/C	0.994	0.789	29	440

*absolute cell voltage; **cm^2 values correspond to geometric active area of electrode

Better performance of Pt:Ti 3:1 and 2:1-A catalysts against standard Pt/C catalyst, even with crystallite size 5 times greater than that of Pt/C (Pt:Ti 3:1-A = 18.0 nm, Pt:Ti 2:1-A = 18.1 nm, and Pt/C = 3.4 nm), can be attributed to the favourable catalytic properties obtained under acidic conditions as well as strong synergistic interactions which exist between Pt and TiO₂ [Long *et al.* 2013].

3.4.   Conclusion

Pt-TiO₂ nano-composite catalysts were synthesized in acidic (pH < 3) and basic (pH > 10) medium in three different compositions with Pt:Ti atomic ratio of 1:1, 2:1 and 3:1. The effect of synthesis medium on catalytic properties was ascertained which reflected in fuel cell performance as well. Pt-TiO₂ synthesized in acidic medium exhibited smaller Pt crystallite size, higher SSA, more non-stoichiometric titania with higher conductivity and crystallinity compared to that prepared in basic medium. ORR performance as obtained from fuel cell polarisation curves exhibited activity in the order Pt:Ti 3:1-A > Pt:Ti 2:1-A > Pt:Ti 1:1-A > Pt:Ti 3:1-B > Pt:Ti 2:1-

B > Pt:Ti 1:1-B, with Pt-TiO$_2$-A catalysts showing better performance. In both acidic and basic medium, Pt:Ti atomic ratio of 3:1 was found to show the best performance in their respective classes. With the same Pt content in both Pt:Ti 3:1-A and Pt:Ti 3:1-B, better performance of acidic medium synthesized catalysts highlighted the significance of pH of synthesis medium on ORR catalytic activity. Additionally, Pt:Ti 3:1-A and Pt:Ti 2:1-A with lower activation losses showed better fuel cell performance compared to the standard, commercial Pt/C ORR catalyst. Also, in terms of mass activity at the fuel cell operational voltage of 0.9 V, Pt:Ti 3:1-A and 2:1-A showed better performance than Pt/C catalyst. The better fuel cell performance of Pt:Ti 3:1-A and Pt:Ti 2:1-A, even with Pt crystallite size of almost five times larger than that of commercial Pt/C catalyst, opens up the way to further explore this class of titania supported catalysts to achieve enhanced performance.

Chapter 4

Pt/TiO₂ and Pt/V-TiO₂ catalysts: Prominent effects of V doping

A part of this study has been published:

V-doped TiO₂ supported Pt as a promising oxygen reduction reaction catalyst: Synthesis, characterization and *in-situ* evaluation in proton exchange membrane fuel cell

Abha Bharti [a], Gouri Cheruvally [b,*]

[a] Energy Systems Division, Vikram Sarabhai Space Centre, Thiruvananthapuram 695022, India
[b] Polymers and Special Chemicals Group, Vikram Sarabhai Space Centre, Thiruvananthapuram 695022, India

Abstract

This study deals with the synthesis and characterization of V-doped, TiO_2 supported Pt catalyst (Pt/V-TiO_2) for ORR and its *in-situ* performance investigation in PEMFC. Pt/V-TiO_2 nano-composite catalyst was prepared *via* a facile sol-gel and MW assisted, modified chemical reduction route and its performance was compared with the undoped TiO_2 supported catalyst, Pt/TiO_2 prepared in an identical way. The Pt/V-TiO_2 and Pt/TiO_2 catalysts were employed as cathode catalyst in PEMFC and performance compared with standard Pt/C catalyst. Their comparative studies were conducted with physical and electrochemical techniques. *In-situ* electrochemical characterization studies showed improved ORR catalytic activity of Pt/V-TiO_2 compared to Pt/TiO_2. This study demonstrated Pt/V-TiO_2 nano-composite material as an attractive cathode catalyst candidate for PEMFC.
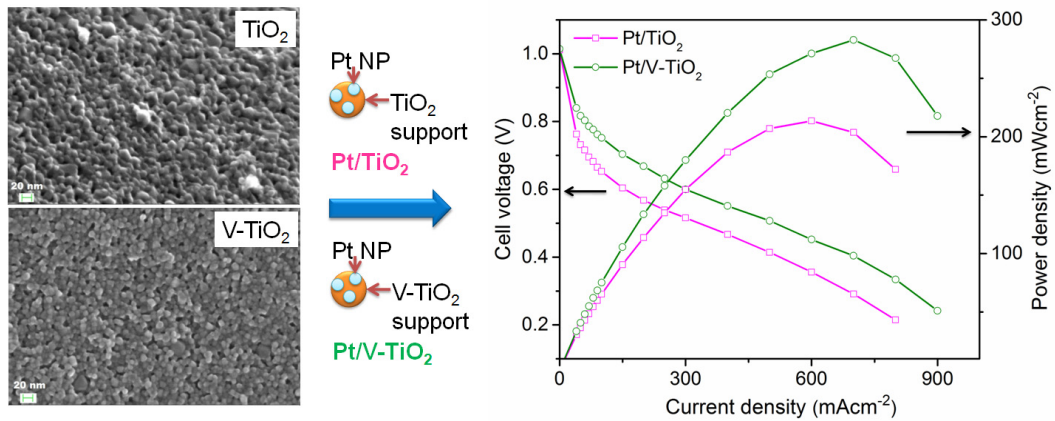
4.1. Introduction

TiO$_2$ based materials have gained attention as attractive supports for Pt catalysts in electrochemical applications because of the lower cost, non-toxicity and high stability in acidic and oxidative environments [Ho *et al.* 2011]. Additionally, TiO$_2$ based materials are well-known for strong metal support interaction (SMSI) which tunes the catalytic properties of supported Pt NPs [Long *et al.* 2013, Kumar *et al.* 2014]. Nevertheless, their low electrical conductivity is a major obstacle to be addressed for their useful application as Pt supports in fuel cells. Consequently, enhancement of electrical conductivity of TiO$_2$ has been explored through doping with transition metal elements having d electron configuration suitable for catalysis [Liu *et al.* 2013, Wang *et al.* 2013, Liu *et al.* 2017] and Niobium (Nb) has been the dopant of choice for many researchers [Elezović *et al.* 2010, Bauer *et al.* 2012, Chevallier *et al.* 2012, Du *et al.* 2013, Liu *et al.* 2014, Shahgaldi *et al.* 2015].

Vanadium (V) is another typical transition metal that has 3d orbitals as Ti atom, and also has ionic radius similar to that of Ti^{4+} ion, making V doping in TiO$_2$ lattice quite facile [Choi *et al.* 1994, Shopova-Gospodinova *et al.* 2012]. Doping with V has been shown to extend the absorption wavelength range of the catalyst into the visible region, increase the number of charge carriers and as a result decrease the resistivity [Klosek *et al.* 2001, Xu *et al.* 2010, Elen *et al.* 2014, Christoforidis *et al.* 2016]. Still, literature scan shows only a single report of V doped TiO$_2$ supported Pt catalyst (Pt/V-TiO$_2$) for ORR in PEMFC [Kim *et al.* 2016]. In this work, V-TiO$_2$ support was synthesized through sol-gel/hydrothermal method and the deposition of Pt NPs onto the support was achieved *via* sodium borohydride reduction. This study, conducted in half cell mode, reported better ORR activity and durability with Pt/V-TiO$_2$ compared to Pt/C catalyst, and the enhanced activity was attributed to compressive strain on introduction of dopant. However, *in-situ* fuel cell performance of Pt/V-TiO$_2$ as ORR/cathode catalyst was not presented in this study. Although half-cell data are supposed to corroborate with full cell performance in theory, often it is not the case in reality. *In-situ* investigations in actual working fuel cell are much more realistic and can give true demonstration of the performance characteristics of the sub-systems. Hence, the need to undertake a detailed study on the physico-chemical

characteristics of Pt/V-TiO$_2$ that make it a potential ORR catalyst and further to evaluate it *in-situ* in PEMFC to validate performance.

The present study investigates electrochemical activity of cathode catalyst Pt/V-TiO$_2$ in PEMFC. Effect of V dopant on physicochemical properties, optical properties and electrical conductivity of the TiO$_2$ support are investigated to understand doping influence on support characteristics. To validate the applicability of Pt/V-TiO$_2$ catalyst, its performance is evaluated through *in-situ* electrochemical investigations in an actual, working PEMFC and the results are compared with undoped TiO$_2$ supported Pt catalyst (Pt/TiO$_2$) under identical conditions. Additionally, the fuel cell performance comparison through polarization and power density curves was done with standard, commercial Pt/C catalyst.

4.2. Experimental
4.2.1. Materials

The raw materials used for synthesis of Pt/TiO$_2$ and Pt/V-TiO$_2$ catalysts were H$_2$PtCl$_6$.6H$_2$O, TTIP, NH$_4$VO$_3$, NaBH$_4$ and EG. HNO$_3$ was used to maintain acidic medium during sol-gel synthesis of the TiO$_2$ and V-TiO$_2$ supports. NaOH was used to maintain the required alkaline medium and HCl was used as a sedimentation promoter during deposition of Pt NPs onto the TiO$_2$ and V-TiO$_2$ supports. Ethanol, acetone and ultra-pure water were used as solvents. Details of all the above chemicals and materials are furnished in *Chapter 2, Section 2.1*. The materials used for electrode preparation, MEA fabrication and single cell PEMFC assembly remain the same as detailed under *Chapter 2, Section 2.1* and *Section 2.4.1*.

4.2.2. Synthesis of Pt/TiO₂ and Pt/V-TiO₂ catalysts
4.2.2.1. Synthesis of TiO₂ and V-TiO₂ supports:

From the earlier study detailed in *Chapter 3*, it was concluded that Pt-TiO$_2$ catalysts synthesized in acidic medium exhibited better fuel cell performance than the catalysts synthesized in basic medium. Hence, in this study, TiO$_2$ and V-TiO$_2$ supports were synthesized using acid-catalyzed sol-gel method. The synthesis procedure is detailed *in Chapter 2, Section 2.2.2.1.*

4.2.2.1.1. Deposition of Pt NPs on TiO₂ and V-TiO₂ supports:

Pt NPs were deposited onto TiO_2 and V-TiO_2 supports (20 wt. % Pt) using a MW assisted, modified chemical reduction route and the process is detailed in *Chapter 2, Section 2.2.2.2.*

4.2.3. Characterization

Characterization methods employed included XRD, Raman spectroscopy, FESEM, HRTEM, ICP-AES, BET specific surface area, four-probe conductivity measurement, UV-Visible Diffuse Reflectance Spectroscopy (DRS), XPS and UPS. The detailed procedures of all these methods are given in *Chapter 2, Section 2.3.*

4.2.4. Fabrication of MEA and Assembly of single cell PEMFC

MEA for single cell fuel cell was prepared using Nafion$^®$ membrane and catalyst ink coated PTFE sintered carbon paper. The procedure for MEA fabrication and single cell assembly is detailed in *Chapter 2, Section 2.4.1.4* and *Section 2.4.1.5*, respectively. The metal (Pt) loading at the electrodes (anode and cathode) in MEA was 0.5 mg$_{Pt}$cm^{-2}.

4.2.5. Electrochemical evaluation

The electrochemical experiments were carried out on a single cell PEMFC at room temperature and atmospheric pressure unless otherwise defined and are detailed in *Chapter 2, Section 2.5.1.* CV experiments were performed by cycling the cathode at 20 mVs^{-1} between 0 to 1.2 V *vs*. SHE. EIS measurements were performed by applying ac amplitude of 10 mV over the frequency range 10^{-1} to 10^5 Hz at cell voltage, E$_{cell}$ of 0.9 V. ZSimpWin™ software (Princeton Applied Research) was used to analyse the EIS spectra. The catalytic activity and stability of the synthesized catalysts towards ORR was evaluated through CA measurements at polarization potential of E$_{cell}$ =0.90 V, 0.85 V and 0.80 V held over a period of 3600 s. All the electrochemical experiments except CV were performed with pure, O₂ and humidified H₂ gases fed at cathode and anode, respectively. For CV experiments, pure N₂ and humidified H₂ gases were fed at cathode and anode compartments, respectively. The polarization curves were recorded at 50 °C, 1 atm and with fixed flow rate of 1 NLPM of hydrogen and oxygen gases. The anode side was fed with pure hydrogen

humidified to 90% RH, and the cathode side was fed with pure oxygen humidified to 70% RH.

4.3. Results and discussion

4.3.1. Selection of optimum concentration of V dopant

For application of TiO_2 materials as support for PEMFC cathode catalyst, enhancement of electronic conductivity is desired in order to achieve favorable support characteristics. Thus, doping of TiO_2 matrix is done to achieve reduction in the band gap which is expected to improve its conductivity. The band gap reduction is a function of both the nature of dopant as well as its concentration in the host matrix. V was chosen as the dopant because it has 3d orbitals as Ti atom, and also has ionic radius similar to that of Ti^{4+} ion, making V doping in TiO_2 lattice quite facile. The effect of dopant concentration on crystal structure, phase formation and optical properties was studied in order to select the most suitable dopant level to achieve superior support characteristics with TiO_2. The dopant concentration was varied as 1, 5, 10, 15, 20 and 25 mole% in the V-doped TiO_2 supports and the properties were evaluated.

The effects of V dopant concentration on the phase structure of the TiO_2 matrix was studied using XRD technique. The XRD patterns of the un-doped TiO_2 and V-doped TiO_2 samples (with various dopant concentrations) annealed at 450 °C are shown in Fig. 4.1. The crystal structure of the TiO_2 mainly consisted of anatase phase and little amount of rutile phase with a dominance of anatase structure. As shown, the peaks at 2θ values of 25.4°, 38.2°, 48.2°, 54.3°, 55.2°, 62.9°, 69.1°, 70.4°, 75.4°, and 83.1° are the diffractions of the (101), (112), (200), (105), (211), (201), (116), (220), (215) and (312) planes of anatase (JCPDS No. 01-084-1286), respectively. The peaks at 2θ values of 27.6°, 36.2°, 41.4°, 44.2°, 56.7°, and 64.2° are the diffractions of the (110), (101), (111), (210), (220) and (310) planes of rutile (JCPDS No. 01-089-4920), respectively. Similar diffraction patterns were obtained with V-doped TiO_2 materials as well. However, the rutile phase was not detected in the XRD patterns for all V doped TiO_2 materials. The intensity of the $(110)_R$ peak relative to that of the $(101)_A$ peak decreased with the increasing V concentration in the TiO_2 samples, indicating that the lattice V ions inhibited the anatase-to-rutile

114

transformation. It has been reported that doping of V within TiO_2 would have a stabilizing effect on the Ti-O bond because the more electropositive V^{4+} and/or V^{5+} will render its electronic concentration to O^{2-} so that it can use this increased concentration of electrons to strengthen the bonding between the less electropositive Ti^{4+} ions [Yang *et al.* 2010, Ren *et al.* 2015]. This stabilization of Ti-O bond will in turn retard the anatase–rutile transformation since this transformation needs the breaking of Ti-O bonds. There is also no discernible or systematic shift in position of XRD lines with increasing extent of V doping. The broad nature of the XRD peaks arising from the nano-crystalline nature of the samples, makes it further difficult to detect a small peak shift, if any. The respective average crystallite sizes as calculated from this peak broadening, with the help of the Debye-Scherrer equation based on anatase (101) diffraction peak, which is the most intense peak of the materials, is presented in Table 4.1.
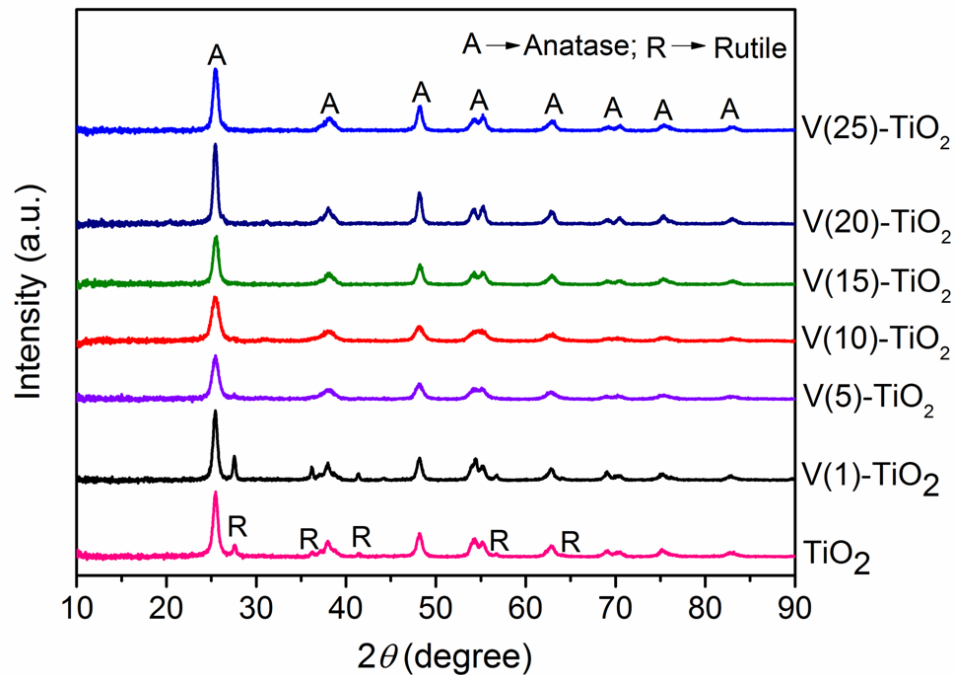
Fig. 4.1. XRD spectra of un-doped TiO_2 and TiO_2 doped with different concentrations of V

It is noteworthy that no obvious diffraction peaks corresponding to vanadium oxides (such as V_2O_5 and/or VO_2) were observed in XRD pattern even at the highest V concentrations. On the basis of this, it can be inferred that either the V ions have

substituted Ti^{4+} ions into the crystal lattice sites of the titania or vanadium oxide, if present, exists in highly dispersed form over the titania surface, which could not be detected by XRD.

Table 4.1. Crystallite size of un-doped TiO_2 and TiO_2 containing different concentration of V dopant

Materials	Crystallite size (nm)	Band gap (eV)
TiO_2	15.2	2.86
V(1)-TiO_2	17.8	1.22
V(5)-TiO_2	10.7	1.05
V(10)-TiO_2	11.9	1.07
V(15)-TiO_2	14.9	1.11
V(20)-TiO_2	20.3	1.38
V(25)-TiO_2	16.0	1.45

However, by means of Raman analysis, it is possible to detect the presence of vanadium oxide, if any, in the high V doping concentration [Schimmoeller *et al.* 2008, Li *et al.* 2009, Jaiswal *et al.* 2012]. Thus, the Raman spectra of un-doped TiO_2 and doped TiO_2 materials with different V dopant content, were taken as shown in Fig. 4.2, and analyzed. The peaks around 148, 399, 517, and 638 cm^{-1} are attributed to anatase phase TiO_2 [Hu *et al.* 2011]. The absence of Raman bands corresponding to the rutile phase of titania (235, 447, and 612 cm^{-1}) again confirms anatase as the dominant TiO_2 phase in the materials concordant with the XRD results [Ohsaka *et al.* 1978]. At the same time, no bands are observed at 285, 703, and 997 cm^{-1} corresponding to V_2O_5 in lower V concentration samples (1,5, 10 and 15 mole%), which unequivocally establish the absence of a separate V_2O_5 phase in these samples. However, when the concentration of V doping increased further (20 and 25 mole%), the Raman spectra showed additional peaks corresponding to V_2O_5 phase. The Raman band located around 997 cm^{-1} arises from the symmetric stretch of V=O groups of V_2O_5 and the bands around 285 and 703 cm^{-1} are characteristic of V-O-V vibrations [Das *et al.* 1993, Khodakov *et al.* 1999]. The Raman band around 100 cm^{-1} is

assigned to TiO_2 lattice vibration [Das *et al.* 1993]. Based on these results, it is postulated that the V dopant forms a solid solution in the anatase TiO_2 lattice till its concentration reached 15 mole%, and beyond that, precipitation of the dopant as vanadium oxides occurs outside the TiO_2 host lattice. Based on this analysis, it is concluded that the upper limit of V dopant concentration to form a solid solution in the TiO_2 lattice is 15 mole%.
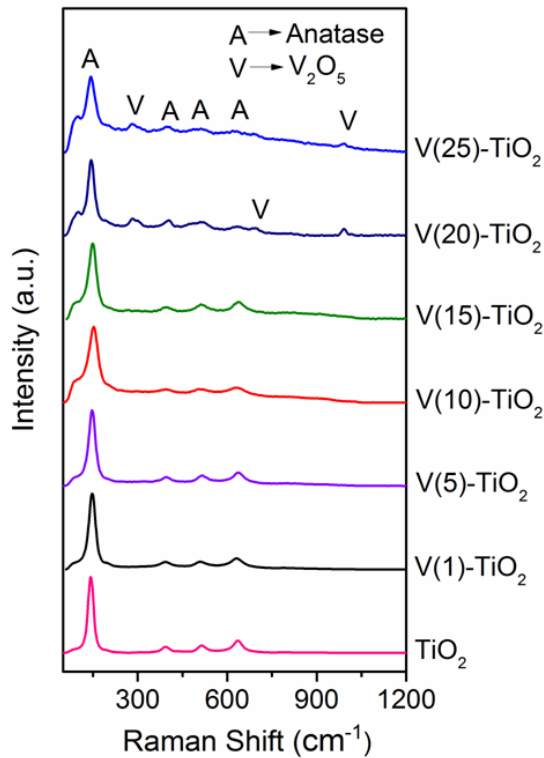
Fig. 4.2. Raman spectra of un-doped TiO_2 and V doped TiO_2 with different concentration of dopant

The effect of V dopant and its different concentration on optical properties of TiO_2 NPs were probed by UV–Visible spectroscopy technique, and Fig. 4.3 (a) shows the absorption spectra obtained. A distinct red shift of the absorption into the visible light region (400 – 700 nm) was observed for all V doped TiO_2 materials which implies a decline of the energy band gap of TiO_2 caused by metal doping in its crystal structure. The absorbance in the visible region for all V doped TiO_2 materials is seen to be higher than un-doped TiO_2 which might be caused by additional impurity states formed in the semiconductor band gap of the material. In the energy band structure of

TiO_2, the top valence band corresponds mainly to O_{2p} states and the conduction band corresponds to Ti_{3d} states. Doping leads to sp–d exchange interactions between the band electrons and the localized d electrons of the dopant [Ganesh *et al.* 2012, Samet *et al.* 2013].

It is also noted that with increase in the concentration of dopant beyond 5 mole%, a significant decrease in absorbance in the visible region is observed indicating broadening of band gap with increase in V concentration. Band gap, E_g can be determined using the following equation.

$$\alpha = \frac{A(h\nu - E_g)^n}{h\nu} \quad \ldots\ldots\ldots\ldots\ldots\ldots\ldots\ldots\ldots\ldots\ldots(\text{eqn. 4.1})$$

where α is absorption coefficient, A is a constant, $h\nu$ is the energy of light and n is a constant depending on the nature of the electron transition [Pankove 1971]. Assuming an indirect band gap ($n = 2$) for TiO_2 [Tang *et al.* 1994], the absorption coefficient α is proportional to Kubelka-Munk function *F(R)*, the band gap E_g can be obtained from the plot of $[F(R)E]^{1/2}$ *vs. h\nu* as the intercept at $[F(R)E]^{1/2} = 0$ of the extrapolated linear part of the plot [Beranek *et al.* 2008] as shown in Fig. 4.3 (b). The band-gap values thus estimated from the Kubelka–Munk function are given in Table 4.1. By doping, a significant decrease in indirect band gap was recorded which is attributed to the electrical transition from the dopant energy level to the conduction band of TiO_2. This reduction in band gap on doping conclusively establishes V as an efficient dopant for TiO_2 matrix. It was also observed that with increase in V concentration from 1 mole% to 5 mole%, a considerable decrease in band gap was observed which remained almost constant till V concentration of 15 mole%. This decrease in band gap with increase in dopant concentration is attributed to many V^{4+}/V^{5+} ions substituting Ti^{4+} at higher doping content [Ren *et al.* 2015, Asgharinezhad *et al.* 2016]. On the contrary, the increase in band gap with further increase in dopant concentration is attributed to Burstein-Moss effect due to the presence of excess charge carriers [Mass *et al.* 2003]. According to Burstein-Moss, at a higher dopant concentration, the band gap increases due to shift of Fermi level to the conduction band and hence occupies some of the

bottom states in the conduction band which now requires higher energy for a transition from valence band to conduction band.
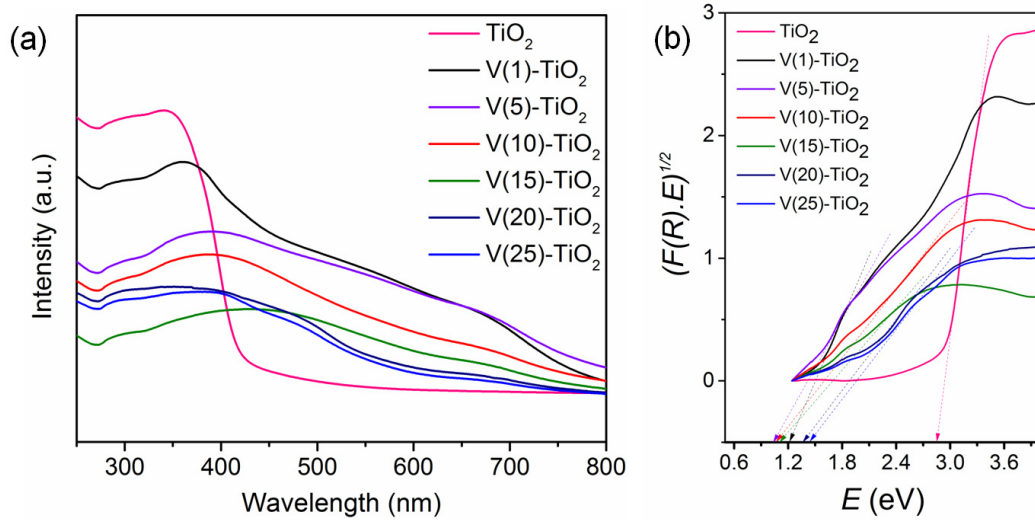
Fig. 4.3. (a) Absorbance spectra, and (b) Band gap determination using $[F(R)E]^{1/2}$ versus E plots for un-doped TiO_2 and V doped TiO_2 materials with different concentration of dopant

Based on the combined results from XRD, Raman and optical analyses, it is inferred that V concentration beyond 15 mole% resulted in the precipitation of V_2O_5 and increase in band gap; whereas, lower concentration of V up to 15 mole% leads to effective incorporation of dopant into host TiO_2 lattice resulting in lowering of band gap. Since no significant change in band gap was observed with increase in V dopant concentration from 5 to 15 mole% (1.05 to 1.11 eV), the composition $V(5)$-TiO_2 with the lowest band gap and low V concentration, was chosen as the support material for Pt catalyst in PEMFC.

The highest reduction in band gap of $V(5)$-TiO_2 is expected to increase the electrical conductivity of the material. $V(5)$-TiO_2 demonstrated 2.4 times higher electrical conductivity than un-doped TiO_2 (5.6 x 10^{-3} Scm^{-1} *vs.* 2.3 x 10^{-3} Scm^{-1}). These results conclusively prove V as an efficient dopant for TiO_2 matrix to realize material with higher conductivity that can function as a potential catalyst support for electrochemical applications. The changes observed in the electrical structure of TiO_2 with V doping further make it highly suitable as support for Pt to achieve better metal-support interaction.

Fig. 4.4 shows the FESEM images of TiO_2 and V(5)-TiO_2 NPs along with EDAX analyses. The images show the formation of near uniform TiO_2 NPs by the synthesis route adopted here. However, relatively larger, corrugated nano-globules were formed in the case of TiO_2; whereas, more uniform, smaller sized and well dispersed nano-spheres were formed in V-TiO_2. This could be due to reduction in crystallite size as a result of the doping process. From EDAX analyses, the V and Ti contents in V-TiO_2 were determined as 2.38 wt.% and 47.06 wt.%, respectively and the remaining corresponding to oxygen content in the TiO_2 matrix. This corresponds to 4.8 mole% of V matching with its feed concentration of 5.0 mole% indicating near complete incorporation of the dopant in TiO_2 lattice.
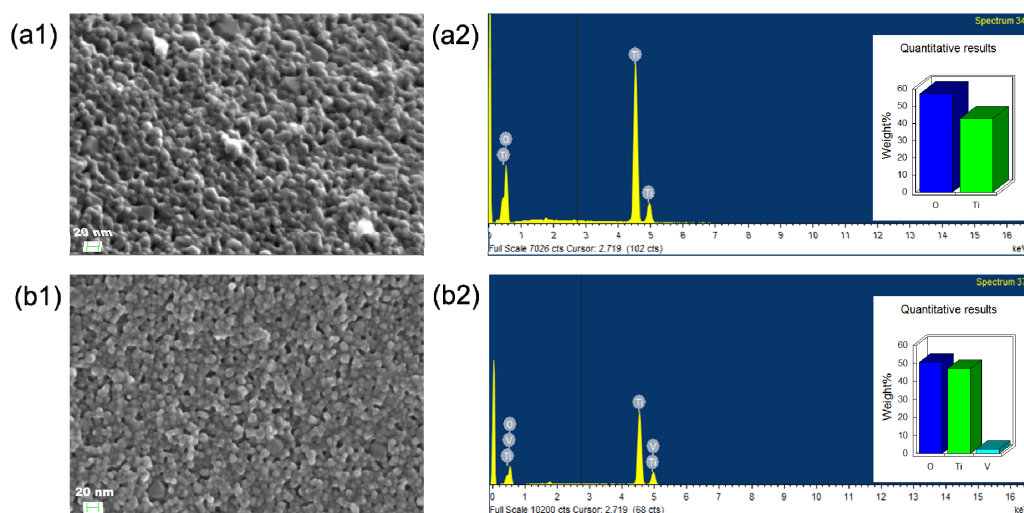
Fig. 4.4. FESEM images and EDAX spectra (a1, a2) of TiO_2 support, and (b1, b2) of V(5)-TiO_2 support

The chemical states of doped V ions in V(5)-TiO_2 was further investigated by XPS analysis. Fig. 4.5 shows the XPS spectra of V(5)-TiO_2 support in the V2p$^{3/2}$ region. All measured binding energies are given to the position of C(1s) core level at 285.0 eV. It is known that the 2p$^{3/2}$ peak position of V species (V^{5+} and V^{4+}) exist with a close binding energy value (515–518 eV) and are easy to overlap [Iketani *et al.* 2004, Ren *et al.* 2015]. However, the peak at higher binding energy is attributed to V^{5+} ions. Therefore, the peak fitted at 522.6 eV can be mainly ascribed to V^{5+}2p$^{3/2}$, whereas that at 519.6 eV was assigned to V^{4+}2p$^{3/2}$. The fitting data demonstrate that V^{5+} and V^{4+} existed in equal concentration in the host TiO_2 lattice. The ionic radius of

both V^{4+} and V^{5+} is very close to that of Ti^{4+}, and hence V^{5+}/V^{4+} can yet be easily substituted for the Ti^{4+} into the TiO_2 crystal lattice. Based on the above analysis, it is evident that the V ions are doped into TiO_2 lattice to substitute Ti^{4+} ions, and form the V-O-Ti bond [Ren *et al.* 2015].
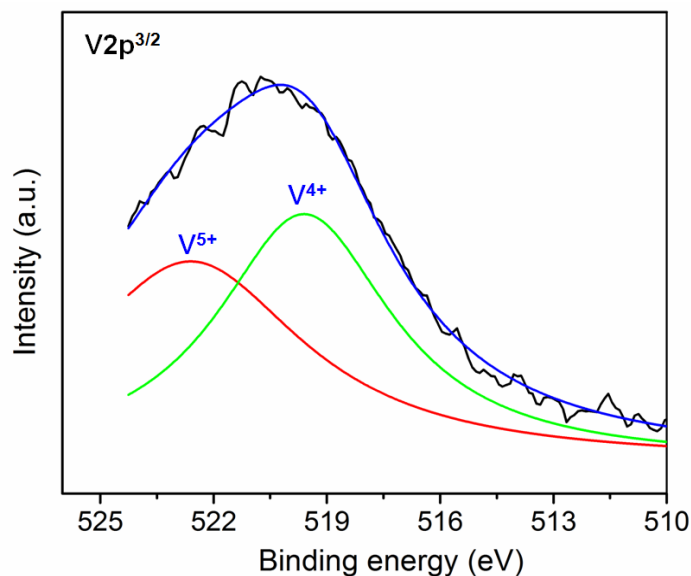
Fig. 4.5. XPS spectra of V(5)-TiO₂ support in the V2p$^{3/2}$ region

4.3.2. Structural and morphological characterization of Pt/TiO₂ and Pt/V-TiO₂ catalysts

Employing TiO_2 and V(5)-TiO_2 as supports, Pt/TiO₂ and Pt/V-TiO₂ nano-composite catalysts, respectively were synthesized *via* MW assisted modified chemical reduction route and their morphology, phase evolution, metal-support interaction and *in-situ* electrochemical properties were studied in detail. The morphology and size of the Pt particles in Pt/TiO₂ and Pt/V-TiO₂ catalysts were examined through TEM and the images are shown in Fig. 4.6. These images clearly revealed the successful deposition of Pt particles onto the TiO_2 based supports. Smaller and well-dispersed Pt particles are formed in Pt/V-TiO₂ compared to those formed in Pt/TiO₂. The mean diameters of the Pt NPs in these supported catalysts were calculated as 5-6 nm for Pt/TiO₂ and 3-4 nm for Pt/V-TiO₂. Lattice structure information of the synthesized TiO_2 supported Pt catalysts was acquired from XRD analysis, as shown in Fig. 4.7. The XRD data revealed the presence of TiO_2 predominantly in the anatase phase along with the residual rutile phase without any

extra reflections from V dopant, suggesting proper doping of V into TiO_2 lattice as discussed previously under *Section 4.3.1*. The characteristic diffraction peaks corresponding to Pt were observed at 2θ values of 39.8°, 46.2°, 67.7° and 81.6° conforming to (111), (200), (222) and (311) planes of an fcc microstructure. The crystallite sizes of Pt in Pt/TiO_2 and Pt/V-TiO_2 catalysts were 5.8 nm and 3.2 nm, respectively in close agreement with TEM results. The smaller crystallite size obtained in the case of Pt/V-TiO_2 can be explained by the presence of favorable, uniform V-TiO_2 nano-spheres for the deposition of Pt NPs as against pristine TiO_2 which exhibited a rough, agglomerated surface for Pt deposition as shown by FESEM images (Fig. 4.4).
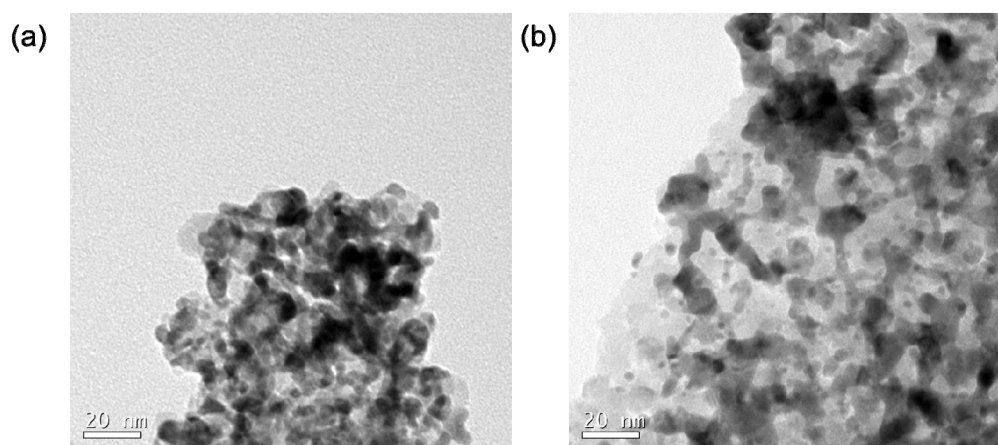
Fig. 4.6. TEM images of (a) Pt/TiO_2, and (b) Pt/V-TiO_2 catalysts
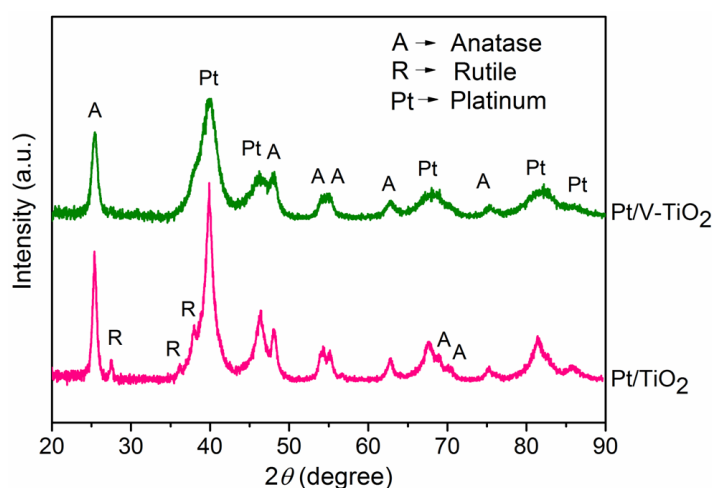
Fig. 4.7. XRD spectra of Pt/TiO_2 and Pt/V- TiO_2 catalysts

UPS was studied to explore the surface electrical properties of Pt in Pt/TiO$_2$ and Pt/V-TiO$_2$ and the results are also compared with commercial Pt/C catalyst to validate electrical interactions between metal and TiO$_2$ based supports. Fig. 4.8 (a) shows UPS spectra for these catalysts.
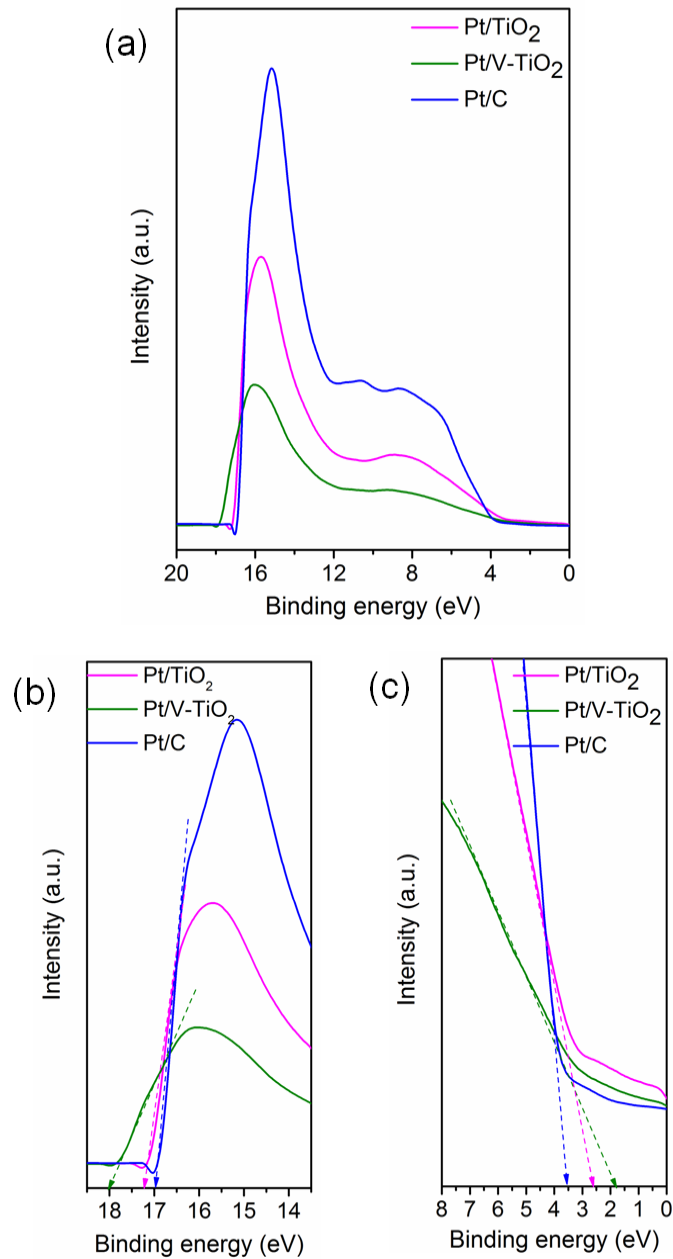
Fig. 4.8. (a) UPS spectra covering the complete binding energy region; (b) and (c) magnified views of the secondary electron cut-off region and valence band edges, respectively of Pt/C, Pt/TiO$_2$, and Pt/V-TiO$_2$ catalysts

It is seen that similar spectral pattern is obtained for all catalysts irrespective of the support employed and the spectra correspond to Pt valence band electrical structures in these catalysts. A broad band around 3-12 eV represents the valence band of Pt which is followed by a sharp and intense high binding energy (> 12 eV) cut-off or secondary edge where the spectrum ends. The electrons responsible for the secondary edge and the sloping up tail before the edge are in-elastically scattered electrons, which were initially emitted from the valence bands states, but lost energy through scattering processes on their way to the sample surface. A significant reduction in the valence band intensity was observed with TiO_2 supported catalysts as compared to the Pt/C catalyst. This reduction indicates considerable electrical transitions between TiO_2 supports and Pt due to hypo-hyper d electron interaction between TiO_2 and Pt. From the UPS spectra, secondary edge energy (E_{SE}) and valence band maximum (E_{VB}) were estimated using the intercept on the abscissa obtained by extrapolating the high and low binding energy edges, respectively to the baseline. Fig. 4.8 (b) and (c) show the zoomed in view of the high and low binding energy edges in the UPS spectra shown in (a). E_{VB} was found to be in the order: Pt/C (3.6 eV) > Pt/TiO_2 (2.7 eV) > Pt/V-TiO_2 (1.9 eV). E_{VB} represents the highest level of occupancy of 5d electrons of Pt and hence can be clearly taken as a representation of 5d band vacancy. Lower value of E_{VB} indicates higher Pt 5d band vacancy and hence lower activation energy for interaction with oxygen during ORR resulting in a facile and faster reaction [Mukerjee *et al.* 1998, Toda *et al.* 1999]. TiO_2 supported catalysts showed lower E_{VB} values compared to Pt/C, suggesting stronger metal-support interactions for these catalysts. Pt/V-TiO_2 showed the lowest E_{VB} and hence is expected to have the strongest synergistic interactions between Pt and support which is favorable for high catalytic activity.

The presence of electronic interactions between metal and support in TiO_2 based catalysts were also shown by the work function (ϕ_{WF}) values of the catalyst. The work-function is given by $\phi_{WF} = h\nu - E_{SE}$, where the first term represents the energy of the photons used to probe the band-structure (He I: 21.2 eV) and the second term is the secondary electron cut-off energy [Farsinezhad *et al.* 2015]. The ϕ_{WF} values were estimated at 4.2 eV, 4.0 eV and 3.3 eV for Pt/C, Pt/TiO_2 and Pt/V-TiO_2

catalysts, respectively. The lowering of the ϕ_{WF} in the case of Pt/TiO$_2$ and Pt/V-TiO$_2$ catalysts with respect to Pt/C catalyst can be explained in terms of the metal-semiconductor contact theory, *i.e.*, Schottky theory. Since ϕ_{WF} of Pt is large, the conduction band electrons of TiO$_2$ support are expected to get transferred to Pt at the interface. Furthermore, because V-based materials are n-type dopants forming a donor level near the edge of the conduction band, the Fermi level of TiO$_2$ in V-TiO$_2$ gets shifted upward which leads to a decrease in ϕ_{WF}. This results in lowering of the Schottky barrier and increasing charge transfer between TiO$_2$ support and Pt. These results are in good agreement with literature reports of favorable synergistic transitions in Pt/TiO$_2$ systems than in Pt/C catalyst [Kim *et al.* 2014, Kim *et al.* 2016]. The metal-support interaction in TiO$_2$ based catalytic systems can improve the electro-catalytic activity and also provide an anchoring effect between metal oxides and the adjacent Pt NPs, contributing to enhanced performance including efficiency and durability.

4.3.3. *In-situ* electrochemical investigations of Pt/TiO₂ and Pt/V-TiO₂ catalysts

The CV curves of the catalysts in a single cell PEMFC configuration are shown in Fig. 4.9 (a). Both samples exhibit typical features of Pt based catalysts with a hydrogen adsorption/desorption region (0 - 0.3 V), a double layer region (0.3 - 0.6 V) and a potential region of Pt oxide formation and reduction (0.6 - 1.2 V). The Pt oxide reduction is favorably modified by the presence of V-TiO$_2$, the onset of the oxide species reduction is shifted to more positive potentials for Pt/V-TiO$_2$ as compared to Pt/TiO$_2$ (Fig. 4.9 (b)). The CV results can be used to estimate the catalytic activity of Pt/V-TiO$_2$ according to the intensities and shift in the oxidation and reduction peaks. Previous reports indicated that a shift to the higher onset potential values of Pt oxide reduction peak is correlated with an improvement in the Pt catalytic activity for ORR [Wu *et al.* 2012]. Additionally, the higher Pt oxide reduction peak current density of Pt/V-TiO$_2$ as compared to Pt/TiO$_2$ also indicated higher activity of the V doped TiO$_2$ supported Pt catalyst [Fig. 4.9 (b)]. The ESA values of the catalysts were obtained by measuring the columbic charge for hydrogen desorption (Q_H) after correcting for double layer charge contribution of the cathodes

as discussed in *Chapter 2*, *Section 2.5.1.2.1*. The ESA was calculated as 58 m^2g^{-1} and 60 m^2g^{-1} for Pt/TiO$_2$ and Pt/V-TiO$_2$, respectively. Although there was only a slight difference in the ESA of Pt/V-TiO$_2$ and Pt/TiO$_2$, there is significant difference in the catalytic activity of the active Pt sites in these catalysts. With higher reduction current density, Pt/V-TiO$_2$ has higher catalytic activity than Pt/TiO$_2$.
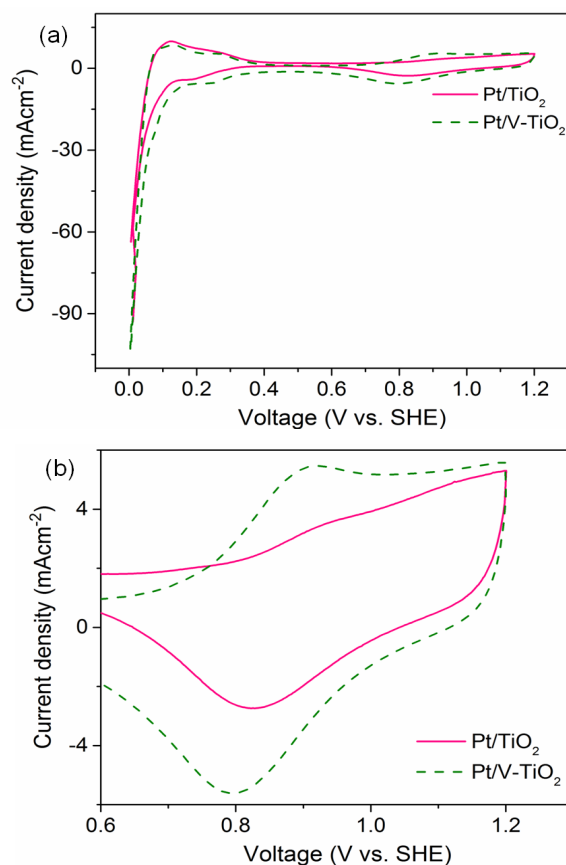
Fig. 4.9. (a) CV curves, and (b) magnified portion of CV in 0.6 V -1.2 V potential range of Pt/TiO₂ and Pt/V-TiO₂ catalysts

EIS is a powerful diagnostic testing method for fuel cells because it is nondestructive and provides very useful information about fuel cell performance. EIS was used to understand the intrinsic behavior of ORR on TiO$_2$ supported Pt catalysts through measurement of the charge-transfer resistance. Fig. 4.10 displays the ac-impedance response of the fuel cell reaction using the catalysts at $E_{cell} = 0.9$ V, a potential at which reaction kinetics dominate. It is to be noted that Nyquist plot is actually the sum of impedances contributed by both the anode and cathode. However, due to the much faster hydrogen oxidation reaction at the anode (higher by 6 orders of

magnitude than that of ORR kinetics), the equivalent anode impedance is negligibly small compared to that of cathode [O'Hayre *et al.* 2016]. Hence, the measured cell impedance can be treated essentially as the cathode impedance. The obtained EIS data were fitted with the circuit shown in the inset of Fig. 4.10, with the circuit elements as follows: R_m is membrane resistance; R_a and R_c are charge transfer resistances for anode and cathode reactions, respectively, and CPE_a and CPE_c are charge transfer related double layer capacitances for the anode and cathode, respectively [Zhang *et al.* 2006]. CPE is constant phase element which is used instead of capacitance to account for inhomogeneity of the electrode surface. The semi-circle or the kinetic loop on the Nyquist plot is ascribed to R_c of the cathode ORR. Lower value of R_c implies faster ORR which results in higher fuel cell performance. The R_c of Pt/TiO₂ is about 5.6 times higher than that of Pt/V-TiO₂. The lower R_c of Pt/V-TiO₂ results from the enhanced interfacial oxygen reduction kinetics promoted by Pt/V-TiO₂ which can be attributed to its higher electrical conductivity as well as stronger metal-support interactions.
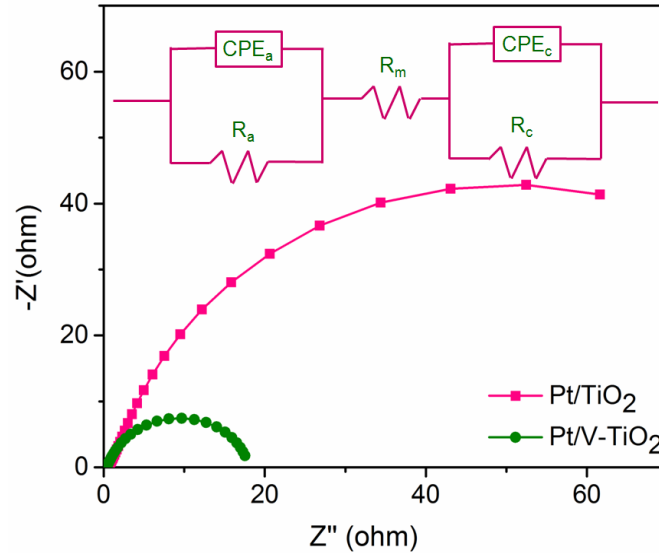
Fig. 4.10. EIS spectra of Pt/TiO₂ and Pt/V-TiO₂;
Inset shows circuit diagram used to fit EIS spectra

The catalytic activity of TiO₂ supported Pt catalysts for ORR was investigated by CA tests and the corresponding data are shown in Fig. 4.11. The polarization potential was carefully chosen to be in activation controlled potential region (0.8 - 0.9

V) where reaction kinetics dominate and hence gives true demonstration of ORR activity. The polarization potentials selected were 0.90 V, 0.85 V and 0.80 V. At each potential, the fuel cell performance was evaluated for over a period of 3600 s with pure O_2 and humidified pure H_2 gases fed at cathode and anode compartments, respectively. The current evolved by an electrochemical reaction is a direct measure of the rate of electrochemical reaction [O'Hayre *et al.* 2016]. Higher current density was obtained with Pt/V-TiO₂ catalyst throughout the measurement at all the studied polarization potentials as compared to Pt/TiO₂ catalyst. This indicates superior ORR catalytic activity of Pt/V-TiO₂ catalyst which is in agreement with CV and EIS results. Table 4.2 summarizes the electrochemical parameters obtained for Pt/TiO₂ and Pt/V-TiO₂ catalysts.
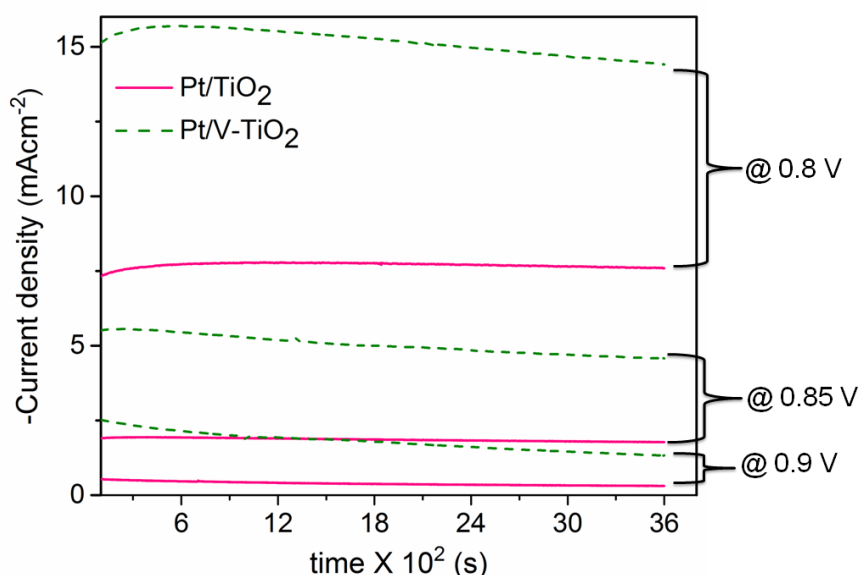
Fig. 4.11. Current *vs*. time curves from CA tests with Pt/TiO₂ and Pt/V-TiO₂ catalysts

4.3.4. Evaluation of performance of Pt/TiO₂ and Pt/V-TiO₂ catalysts through single cell PEMFC polarization curves and comparison with Pt/C catalyst

The performance comparison of Pt/TiO₂, Pt/V-TiO₂ and commercial Pt/C as cathode catalyst in single PEMFC under identical conditions is shown in Fig. 4.12. The high frequency resistance of the MEA with three cathode catalysts *viz.* Pt/TiO₂, Pt/V-TiO₂ and Pt/C was measured before the polarizations tests. The cell resistance from the high frequency intercept was found out to be similar in the case of all the

three MEA (Pt/TiO$_2$: 0.29 Ω, Pt/V-TiO$_2$: 0.26 Ω and Pt/C: 0.23 Ω). The slight difference in the cell resistance between TiO$_2$ based catalysts and Pt/C catalyst can be attributed to electrical conductivity difference of the support materials. TiO$_2$ based materials are semi-conductors and hence shows slightly higher cell resistance with Pt/TiO$_2$ and Pt/V-TiO$_2$ MEA as compared to Pt/C MEA.

Table 4.2. Electrochemical parameters of Pt/TiO$_2$ and Pt/V-TiO$_2$ catalysts

Parameters	Pt/TiO$_2$	Pt/V-TiO$_2$
ESA^x (m^{2}g^{-1})	58	60
R$_c$ ^{y} (Ω)	95	17
j$_{@0.9V,3600s}$^{z}(mAcm^{-2})*	0.3	1.3
j$_{@0.85 V, 3600 s}$^{z} (mAcm^{-2}) *	1.8	4.6
j$_{@0.8 V, 3600 s}$^{z} (mAcm^{-2}) *	7.6	14.4

^{x}from CV; ^{y}from EIS spectra; ^{z}from CA plot; *cm^2 values correspond to geometric active area of electrode
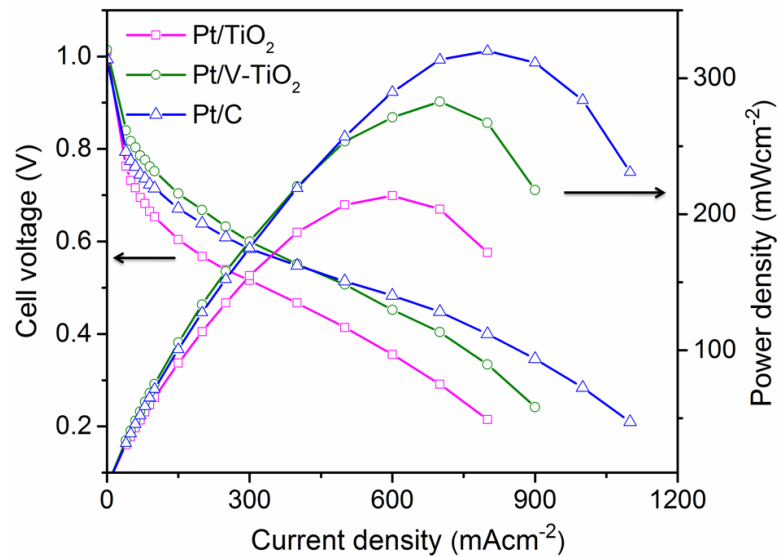
Fig. 4.12. Polarization and power density curves of Pt/TiO$_2$, Pt/V-TiO$_2$ and Pt/C catalysts

In the polarization curves, activation over-potential losses which manifest in the form of lower cell voltage at lower current density region, typically <100 mAcm^{-2}, arise predominantly due to slower kinetics of the reaction at the cathode. The single fuel cell delivers cell voltage 0.817 V, 0.774 V and 0.732 V at current density of 50

$mAcm^{-2}$ with Pt/V-TiO$_2$, Pt/C and Pt/TiO$_2$ catalyst, respectively. Higher cell voltage with Pt/V-TiO$_2$ catalyst implies lower activation over-potential loss and hence, better ORR catalytic activity. However, the lower performance obtained with both the TiO$_2$ based Pt catalysts reflected as lower cell voltage at higher current density (>400 $mAcm^{-2}$) as compared to Pt/C catalyst can be unambiguously attributed to the lower electrical conductivity of TiO$_2$ supports compared to C support. In the higher current density region, ohmic losses are dominant and are reflected in the polarization curves as lower cell voltages. This is also responsible for the lower peak power density achieved with Pt/TiO$_2$ (214 $mWcm^{-2}$) and Pt/V-TiO$_2$ (283 $mWcm^{-2}$) catalysts as compared to Pt/C (320 $mWcm^{-2}$). However, in terms of effective Pt utilization, at the operational voltage of 0.9 V, Pt/V-TiO$_2$ has mass activity of 52 $mAmg_{Pt}^{-1}$, which is almost 1.4 times higher than that of both Pt/TiO$_2$ (36 $mAmg_{Pt}^{-1}$) and Pt/C (38 $mAmg_{Pt}^{-1}$) catalyst. The better performance of Pt/V-TiO$_2$ compared to both Pt/TiO$_2$ and Pt/C catalyst can be attributed to higher electrical conductivity and stronger metal-support interactions between Pt and V-TiO$_2$ support as evidenced by UPS results. These interactions are capable of tuning intrinsic catalytic activity of Pt in terms of d band vacancy, which makes the ORR more facile. These results demonstrate the better prospectus of Pt/V-TiO$_2$ for PEMFC application. Table 4.3 summarizes the parameters obtained from single cell fuel cell testing polarization and power density curves.

Table 4.3. Parameters obtained from single cell fuel cell testing polarization and power density curves of Pt/TiO$_2$, Pt/V-TiO$_2$ and Pt/C catalysts

Parameters	Pt/TiO₂	Pt/V-TiO₂	Pt/C
Voltage, V*@ 50 $mAcm^{-2}$**	0.732	0.817	0.774
Voltage, V*@ 500 $mAcm^{-2}$**	0.414	0.507	0.514
Mass activity @ 0.9 V*, $mAmg_{Pt}^{-1}$	36	52	38
Peak Power density, $mWcm^{-2}$	214	283	320

*absolute cell voltages; **cm^2 values correspond to geometric active area of electrode

4.4. Conclusions

The promising characteristics of V-doped TiO_2 supported Pt NPs as catalyst for ORR reaction in PEMFC is presented in this chapter. Pt catalysts supported on TiO_2 without doping (Pt/TiO_2) and with V-doping (Pt/V-TiO_2) were synthesized by an easy and efficient route combining sol-gel and MW assisted, modified chemical reduction methods. The support materials as well as the catalysts were characterized for structural, physico-chemical and morphological properties. V-TiO_2 showed a higher electrical conductivity than TiO_2 support establishing V as an efficient dopant for electrochemical applications. Both Pt/TiO_2 and Pt/V-TiO_2 were evaluated *in-situ* as ORR/cathode catalyst in PEMFC and performance was compared with the standard Pt/C catalyst. It was found that Pt/V-TiO_2 showed lower polarization losses in activation region than Pt/TiO_2 and Pt/C, exhibiting better ORR performance. The study thus demonstrates V-TiO_2 as a prospective support for Pt catalyst to attain both high cathode performance and durability in PEMFC.

Chapter 5

Pt/CNT catalyst: Synthesis through conventional versus microwave heating routes

A part of the study presented in this chapter has been published:
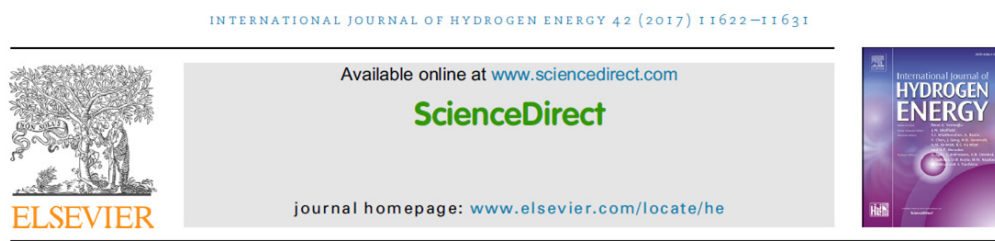
Microwave assisted, facile synthesis of Pt/CNT catalyst for proton exchange membrane fuel cell application

Abha Bharti [a], Gouri Cheruvally [b,*], Shaneeth Muliankeezhu [a]

[a] Energy Systems Division, Vikram Sarabhai Space Centre, Thiruvananthapuram 695022, India
[b] Polymers and Special Chemicals Group, Vikram Sarabhai Space Centre, Thiruvananthapuram 695022, India

Abstract

The studies presented in this Chapter focussed on synthesis of Pt supported on CNT (Pt/CNT) catalyst adopting a single-step, simple and effective modified chemical reduction route using a mixture of $NaBH_4$ and ethylene glycol (EG) as reducing agent. In order to select the most suitable reduction conditions to realize high performing catalyst, heating of the reaction mixture was done following two methods, conventional heating (CH) or microwave heating (MWH). It was found that smaller and well dispersed Pt nanoparticles (NPs) with higher surface area were deposited onto the CNT surface through MW route (Pt/CNT-MWH) as compared to CH route (Pt/CNT-CH). *In-situ* fuel cell studies showed that the cathode with Pt/CNT-MWH showed better performance than the cathodes with Pt/CNT-CH and commercial Pt/C catalysts. This study suggested the viability of MW assisted, metal particle deposition as a simple, yet effective method to prepare high performing Pt/CNT catalyst for ORR in PEMFC.
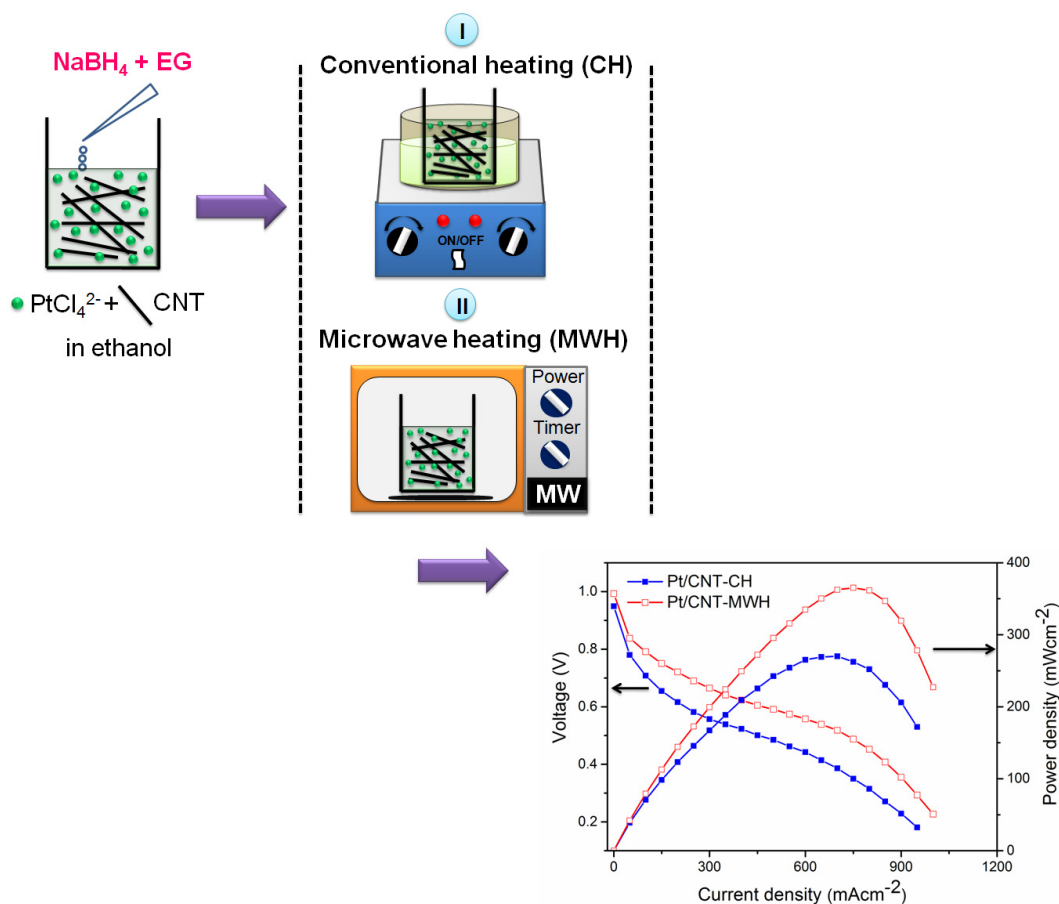
5.1. Introduction

Pt catalysts for fuel cell are commonly prepared *via* chemical reduction route using either NaBH$_4$ [Antolini *et al.* 2007, Pinchuk *et al.* 2012, Wu *et al.* 2012, Celorrio *et al.* 2014] or ethylene glycol (EG) [Hsieh *et al.* 2009, Grolleau *et al.* 2010, Chu *et al.* 2012, Hsieh *et al.* 2013] as the reducing agent. NaBH$_4$ is a strong reducing agent that can perform fast even at room temperature; but, often it does not provide adequate control on the particle size and dispersion of the synthesized metal particles. With EG, smaller particles of metal with good dispersion can be obtained; however, owing to its weak reduction ability, EG requires a higher reaction temperature, generally >120 °C and longer duration (>4 h). The modified chemical reduction route utilizing a mixture of NaBH$_4$ and EG which synergistically combines the stronger reduction ability of NaBH$_4$ and good dispersibility provided by EG, has been shown to be a better method to realize smaller and well dispersed NPs of Pt [Kim *et al.* 2006, Chen *et al.* 2011]. The formation of Pt metal NPs through the modified chemical reduction route is activated by heat and conventional heating (CH) is the most often used method [Chen *et al.* 2011, Yu *et al.* 2012, Ruan *et al.* 2014, Esfahani *et al.* 2015, Pullamsetty *et al.* 2016]. Vulcan XC-72 supported Pt catalysts were prepared for methanol electro-oxidation by using both NaBH$_4$ and EG as reducing agents [Ruan *et al.* 2014]. The complete reduction of Pt salts was assured by conventionally heating the reaction mixture at 100 °C for 4 h. In a similar way, Ag@Pt/MWCNT catalysts were also prepared for ORR in PEMFC [Yu *et al.* 2012]. Methanol tolerant Pt/TiO$_X$-C ORR catalysts were also synthesized through modified chemical reduction method *via* PVP aided CH route; however, complete reduction was ensured by annealing the catalysts further at 400 °C for 4 h under reducing atmosphere [Esfahani *et al.* 2015].

Microwave (MW) heating is another method which is usually preferred in view of its speed, uniformity, simplicity as well as for realization of smaller and well dispersed Pt NPs [Galema 1997]. The effects of MW irradiation on the synthesis of Pt based catalysts have been commonly studied for the EG process [Hsieh *et al.* 2011, Kundu *et al.* 2011, Lebègue *et al.* 2011, Huang *et al.* 2014]. There are only a few reports that deal with the effect of MW irradiation on the particle size, distribution and catalytic activity of Pt NPs prepared by modified chemical reduction route

[Güvenatam *et al.* 2012, El-Deeb *et al.* 2015, Pullamsetty *et al.* 2015, Hameed *et al.* 2016].

The modified chemical reduction method in combination with MW heating has been reported for the synthesis of Pt-TiO$_2$/C and Pt-CeO$_2$/C electro-catalysts for methanol oxidation [Hameed *et al.* 2016]. Pt supported on hollow core mesoporous shell and commercial Vulcan XC-72 carbon with increased Pt loading on carbon support were prepared using additional reducing agents like hydrazine, employing MW method [Güvenatam *et al.* 2012]. Pullamshetty *et. al* reported the synthesis of Pt decorated boron doped graphene catalysts for ORR following various chemical reduction methods such as NaBH$_4$, EG and modified method (both NaBH$_4$ and EG) through CH [Pullamsetty *et al.* 2016] as well as MW assisted heating routes [Pullamsetty *et al.* 2015]. It was shown that the catalyst prepared through modified method exhibited the best catalytic performance following both CH and MW heating routes. However, a one to one comparison of the effect of heating conditions on the catalyst characteristics was not made in this study. In the works of El-Deeb *et. al*, PtCu/CNT catalysts for ORR were prepared through a two-step reduction process using NaBH$_4$ and EG as reducing agents and PVP as a stabilizer that controls the growth of Pt NPs and inhibits agglomeration [El-Deeb *et al.* 2015]. A comparison of heating conditions (CH *vs*. MW) was made in this study which reported the supremacy of MW method over CH.

In comparison to carbon black which is the commonly employed support material for Pt catalyst in PEMFC, CNTs offer better characteristics such as improved corrosion resistance, higher electronic conductivity and higher specific surface area [Serp *et al.* 2003, Shaijumon *et al.* 2006, Wang *et al.* 2006, Golikand *et al.* 2010, Valenzuela-Muñíz *et al.* 2013, Kil *et al.* 2014]. Pt catalysts with smaller particle size and good dispersion throughout their support are reported to exhibit enhanced catalytic activity [Peuckert *et al.* 1986, Kinoshita 1990, Min *et al.* 2000, Roy *et al.* 2013].

The present study aims at developing a high performing Pt/CNT catalyst ensuring the formation of uniformly dispersed metal NPs onto CNT support adopting a single-step, simple, fast and effective synthesis route without the use of any

138

surfactant or stabilizer. Thus, the modified chemical reduction route using a mixture of $NaBH_4$ and EG as reducing agent has been employed. In order to select the most suitable reduction conditions to realize high performing catalyst, heating of the reaction mixture is done following two methods, CH or MW. The synthesized Pt/CNT catalysts were extensively characterized and evaluated *in-situ* as ORR catalyst in PEMFC. A comparison of their performances with the standard, commercial Pt/C fuel cell catalyst is also presented. To the best of our understanding, this is the first time reporting of high performing Pt/CNT catalyst for ORR by a single-step, surfactant-free, MW assisted modified chemical reduction route for PEMFC.

5.2.   Experimental
5.2.1. Materials

The raw materials used for synthesis of Pt/CNT catalysts were $H_2PtCl_6.6H_2O$, CNT (MWCNT, in-house product), $NaBH_4$ and EG. NaOH was used to maintain the required alkaline medium and HCl was used as a sedimentation promoter. Ethanol, acetone and ultra-pure water were used as solvents. Details of all the above chemicals and materials are furnished in *Chapter 2*, *Section 2.1*. The materials used for electrode preparation, MEA fabrication and single cell PEMFC assembly remains the same as detailed under *Chapter 2, Section 2.1 and Section 2.4.1.*

5.2.2. Synthesis of Pt/CNT catalysts

Pt/CNT catalysts were synthesized by a single step, modified chemical reduction route using a mixture of $NaBH_4$ and EG as reducing agent following two different heating routes: (1) conventional heating (designated as Pt/CNT-CH), and (2) MW heating (designated as Pt/CNT-MWH), as detailed in *Chapter 2, Section 2.2.3*.

5.2.3. Characterization

Characterization methods employed include XRD, Raman spectroscopy, TGA, ICP-AES, HRTEM, BET specific surface area and XPS. The details of all these methods are given in *Chapter 2, Section 2.3*.

5.2.4. Fabrication of MEA and assembly of single cell PEMFC

MEA for single cell fuel cell was prepared using Nafion® membrane and catalyst ink coated PTFE sintered carbon paper. The procedures for MEA fabrication

and single cell assembly are detailed in Chapter 2, Section 2.4.1.4 and Section 2.4.1.5, respectively. The metal (Pt) loading at the electrodes (anode and cathode) in MEA was 0.5 $mg_{Pt}cm^{-2}$.

5.2.5. Electrochemical evaluation

The electrochemical experiments were carried out on a single cell PEMFC at room temperature and atmospheric pressure unless otherwise defined and are detailed in *Chapter 2, Section 2.5.1*. CV experiments were performed by cycling the cathode at 20 mVs^{-1} between 0 to 1.2 V *vs*. SHE. EIS measurements were performed by applying ac amplitude of 10 mV over the frequency range 10^{-1} to 10^{5} Hz at cell voltage, E_{cell} of 0.9 V. ZSimpWin™ software (Princeton Applied Research) was used to analyse the EIS spectra. The ORR polarization plot was obtained through potential stair step experiment at a scan rate of 1 mVs^{-1}. The stability of the synthesized catalysts towards ORR was evaluated through CA at polarization potential of $E_{cell} =$ 0.7 V held over a period of 2.5 h. All the electrochemical experiments except CV were performed with pure, O_2 and humidified H_2 gases fed at cathode and anode, respectively. For CV experiments, pure N_2 and humidified H_2 gases were fed at cathode and anode compartments, respectively. The polarization curves were recorded at 50 °C, 1 atm and with fixed flow rate of 1 NLPM of hydrogen and oxygen gases. The anode side was fed with pure hydrogen humidified to 90% RH, and the cathode side was fed with pure oxygen humidified to 70% RH.

5.3.   Results and Discussion
5.3.1.   Effect of heating routes on physico-chemical properties
5.3.1.1. Characterization of Pt/CNT catalysts

The formation of Pt particles onto CNT support in both Pt/CNT-CH and Pt/CNT-MWH catalysts was confirmed through XRD, as shown in Fig. 5.1. Both the catalysts displayed the characteristic patterns for Pt fcc diffraction corresponding to the planes (111), (200), (220), (311) and (222) (JCPDS card no. 01-087-0640). The average crystallite sizes of Pt NPs in Pt/CNT-CH and Pt/CNT-MWH catalysts were 3.8 nm and 2.7 nm, respectively, which are smaller than the reported crystallite size using the reducing agents: $NaBH_4$ (6.0 nm), EG (4.1 nm), and mixture of $NaBH_4$ and EG (4.2 nm) [Güvenatam *et al.* 2012, Vinayan *et al.* 2012]. This establishes the

efficacy of the employed modified chemical reduction route to prepare small-sized Pt NPs dispersed on CNT support. It was also observed that MW assisted route leads to the formation of smaller Pt NPs onto the CNT support than the CH route. This reveals the supremacy of MW assisted route over CH route in attaining smaller Pt NPs onto CNT support through modified chemical reduction route. The corresponding BET specific surface area of Pt/CNT-CH and Pt/CNT-MWH catalysts are found to be 41.4 m^2g^{-1} and 57.9 m^2g^{-1}, respectively.
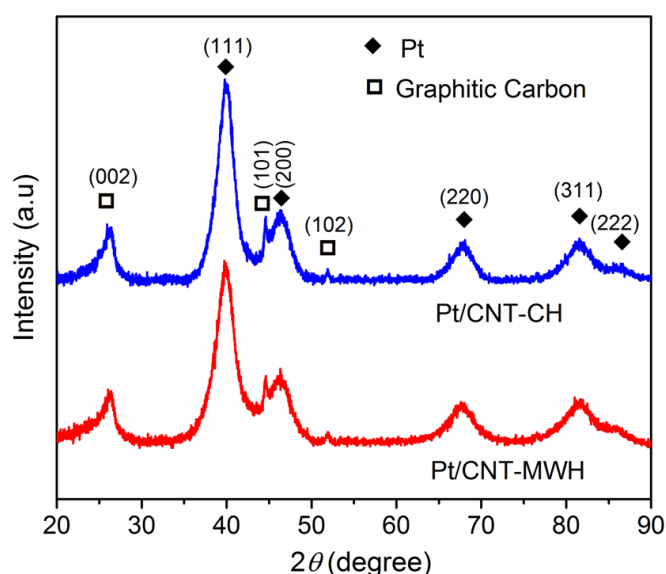
Fig. 5.1. XRD spectra of Pt/CNT-CH and Pt/CNT-MWH catalysts

XRD of both catalysts show the characteristic peaks at 2θ of 26°, 45° and 52° corresponding to planes (002), (101) and (102) of graphitic carbon (JCPDS card no. 00-001-0646) of CNT support. No significant shift is observed in the positions of diffraction peaks. The d_{002} values calculated using Bragg's law from the corresponding (002) diffraction peaks of both catalysts remain the same, 3.39 Å. This value is slightly higher than that of ideal graphite (3.35 Å) resulting from expansion of the (002) planes in the CNT of catalysts [Panomsuwan *et al.* 2016]. This expansion indicates a more disordered structure or lower graphitic ordering in the CNT framework of the synthesized Pt/CNT catalysts. The Pt content in the catalysts evaluated using both ICP-AES method and TGA was found to be about 20 wt.%. Fig. 5.2 shows TGA curves of Pt/CNT-CH and Pt/CNT-MWH catalysts. The materials are stable up to ~400 °C and the peak decomposition temperature range is 420 – 580 °C.

MW heating is seen to slightly accelerate the thermal degradation of the material and the peak decomposition temperature of Pt/CNT-MWH is thus lower than that of Pt/CNT-CH by about 30 °C.
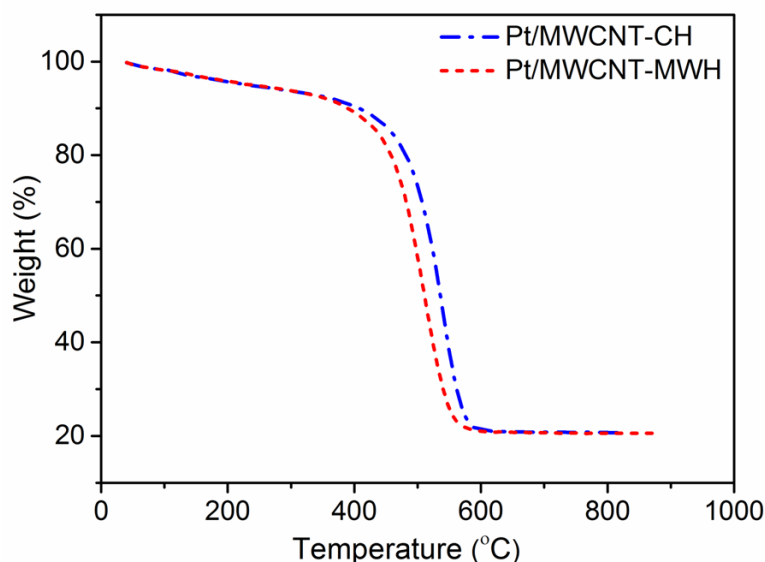
Fig. 5.2. TGA curves of Pt/CNT-CH and Pt/CNT-MWH catalysts

The influence of heating routes on Pt NPs formation and dispersion was further investigated through HRTEM analyses. Fig. 5.3 (a) and (b) present the HRTEM images of Pt/CNT-CH and Pt/CNT-MWH, respectively. It can be seen that the size of Pt NPs deposited *via* MW irradiation route is smaller with narrower particle size distribution compared to that deposited by the CH method. Also, the dispersion of Pt NPs on CNT in Pt/CNT-MWH is more homogenous without much agglomeration. It is well known that Pt NPs with smaller particle size and an even distribution onto the carbon support are key factors for enhancing the electrocatalytic activity and efficiency of the catalyst [Liu *et al.* 2005, Wang *et al.* 2005]. The smaller Pt particle size, homogeneous Pt distribution and higher SSA of Pt/CNT-MWH catalyst can be ascribed to the rapid reduction of metal salts and formation of metal nuclei facilitated by MW. Unlike CH method with an inherent, heterogeneous temperature distribution, the MW irradiation can provide fast and uniform heating of the reaction mixture through dielectric losses [Liu *et al.* 2004]. This accelerated formation of metal nuclei in MW method restricts further growth of the particles

initially formed and hence, produce smaller particles resulting in catalysts with higher SSA.
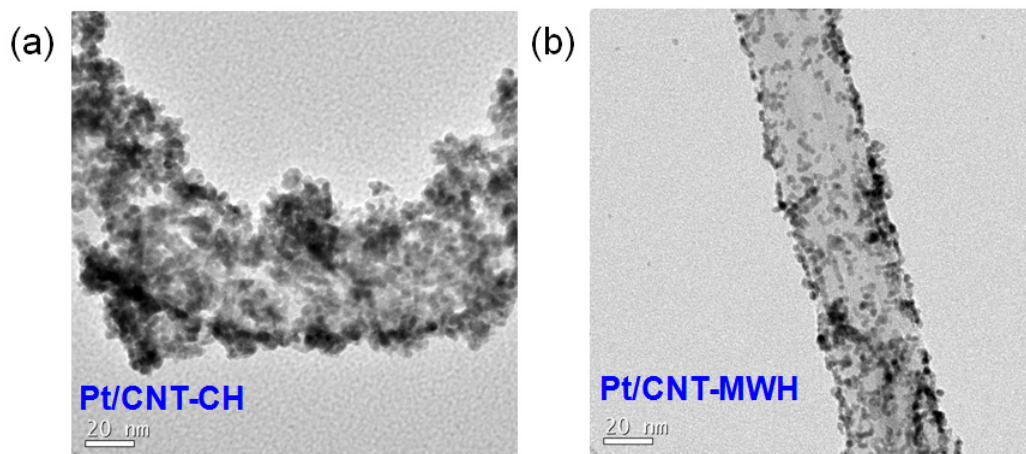
Fig. 5.3. HRTEM images of (a) Pt/CNT-CH, and (b) Pt/CNT-MWH catalysts

5.3.1.2. XPS and Raman analyses of Pt/CNT catalysts

XPS was employed to determine the surface elemental composition of Pt/CNT catalysts. Fig. 5.4 shows the corresponding XPS spectra of C 1s and Pt 4f region of Pt/CNT catalysts. The C 1s spectra (Fig. 5.4 (a)) showed a single intense peak corresponding to alkyl C and sp^2 bonded carbon network (C-C/C=C) at 284.4 eV indicating predominance of sp^2 hybridized graphitic structure in CNT support, in correlation with XRD results. The spectra of $4f_{5/2}$ and $4f_{7/2}$ electrons (Fig. 5.4 (b)) of Pt appeared at 74.6 eV and 71.2 eV, respectively with an asymmetric nature, corresponding to metallic Pt (0) state. Compared to standard metallic Pt (0) state [Venezia et al. 1992] ($4f_{5/2}$ = 74.9 eV and $4f_{7/2}$ = 71.6 eV), both Pt/CNT-CH and Pt/CNT-MWH catalysts showed peak shift to lower binding energies suggesting electron transfers to Pt metal [Khan et al. 2015]. CNTs are π electron density rich materials and hence it can be reasonably assumed that these electrons transferred to Pt were from CNT, evidencing significant interaction between deposited Pt NPs with CNT support. These electronic interactions between CNT support and Pt are considered favourable for both enhancement in catalytic activity as well as improvement in catalyst stability.
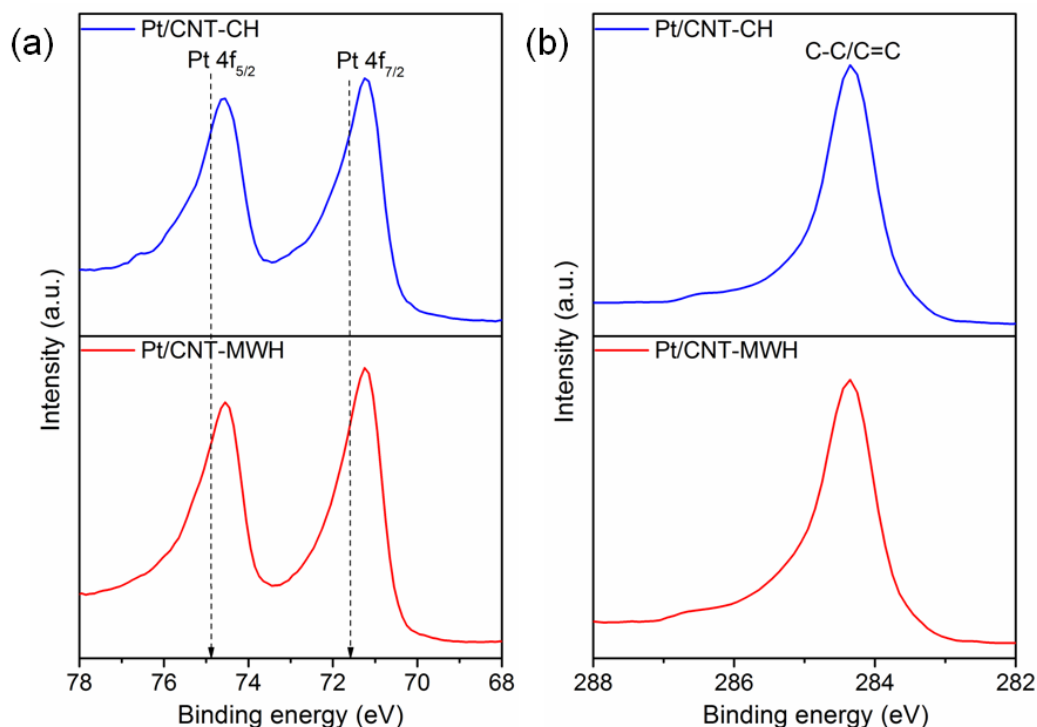
Fig. 5.4. XPS spectra of (a) C 1s and (b) Pt 4f region of Pt/CNT catalysts

Raman spectroscopic analysis is widely used for vivid structural characterization of CNTs. In this study, Raman analysis was employed to understand the effect of Pt deposition through two different heating routes on the structure of CNT. For a meaningful comparison, pristine CNT was also subjected to Raman analysis. Fig. 5.5 (a) shows the Raman spectra of pristine CNT along with Pt/CNT-CH and Pt/CNT-MWH catalysts. Two characteristic peaks at ~1340 cm^{-1} and ~1575 cm^{-1} are seen, which can be assigned respectively to the D and G bands. These D and G bands arise due to disordered (sp^3 bonded sites) and ordered (hexagonal sp^2 sites) carbon structures in CNT, respectively [Barathi *et al.* 2013] and their intensity ratio (I_D/I_G) is often taken as a diagnostic tool to verify the structural perfection of CNTs [Picher *et al.* 2011]. On the deposition of Pt onto CNT, the intensity of D band increases while that of G band decreases in both catalysts as compared to the pristine CNT, as depicted in Fig. 5.5 (a). This clearly demonstrates the occurrence of structural disorder in CNT with Pt deposition, in agreement with XRD results which indicated expansion of (002) planes of CNT. Thus, the deposition of Pt NPs on CNT

causes a disruption in its structure and partially ruin its symmetry, which is manifested by an increase in the intensity of D band [Dobrzańska-Danikiewicz *et al.*].
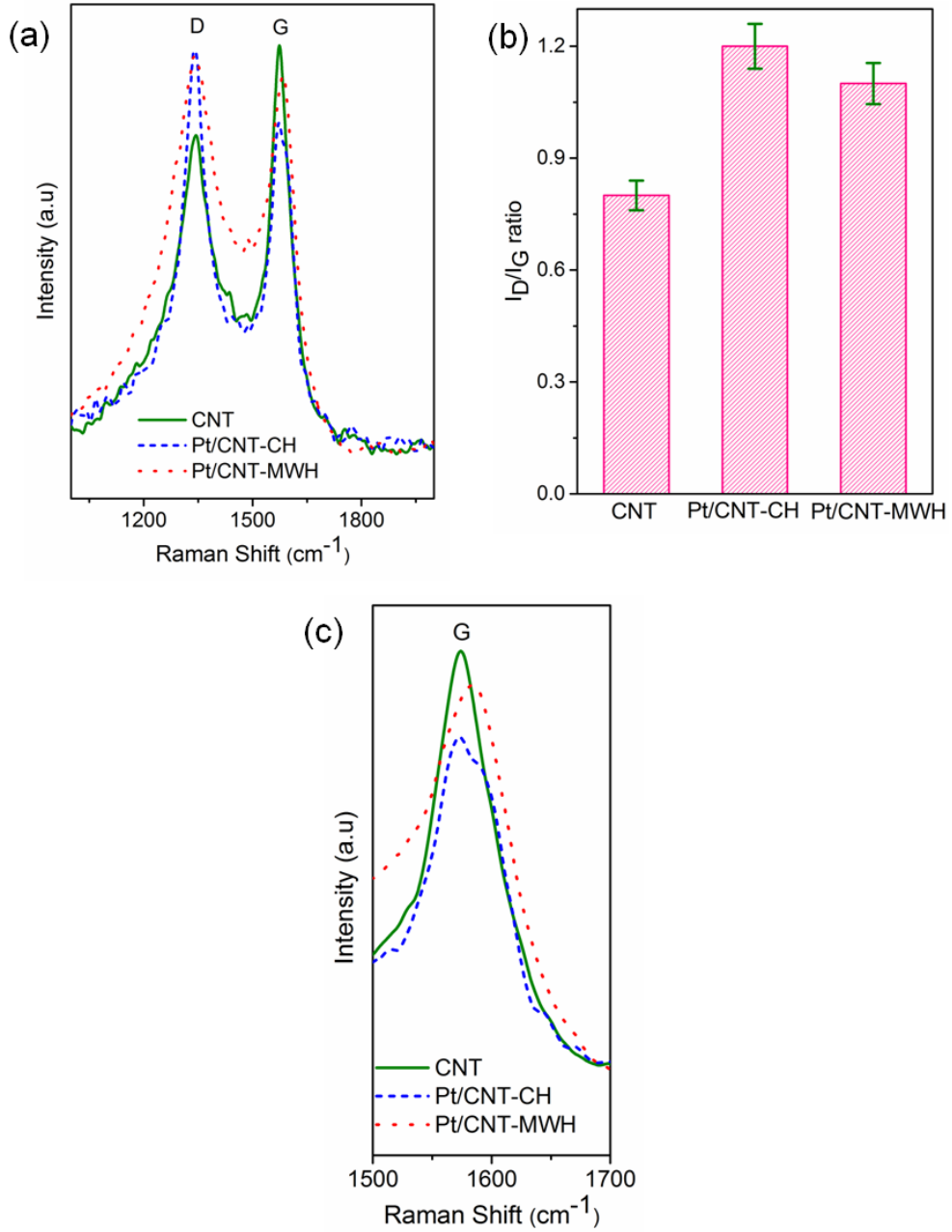
Fig. 5.5. (a) Raman Spectra; (b) I_D/I_G ratio and (c) magnified view of G band of pristine CNT, Pt/CNT-CH and Pt/CNT-MWH catalysts

Similar observations were made from I_D/I_G ratio as well showing increase of structural disorderness of carbon after Pt deposition. Fig. 5.5 (b) presents the comparison of I_D/I_G ratio of Pt/CNT-CH and Pt/CNT-MWH with that of pristine

CNT. Both the catalysts have higher I_D/I_G ratio than that of CNT indicating the formation of large number of defects in the carbonaceous structures during the synthesis of the catalysts with Pt deposition. The deposited Pt particles can exhibit stronger bond with these defect sites in the carbon supports, which are reflected as strong metal-support interactions as evidenced by XPS results.

From Raman spectra, another useful information derived is with respect to the G band position. The spectra between 1500 cm^{-1} and 1700 cm^{-1} is enlarged and shown in Fig. 5.5 (c) to examine the G band position accurately. In the case of pristine CNT, the G band position is at 1574 cm^{-1}. For Pt/CNT-MWH, there is a distinct shift of G band to a higher value by about 11 cm^{-1}, to 1585 cm^{-1}. The G band for Pt/CNT-CH is predominantly at 1574 cm^{-1} with a minor shoulder band at 1585 cm^{-1}. The shift in G band position can be correlated to the formation of defects in the structure of CNT occurring during the synthesis reaction. These defective structures interact strongly with the deposited Pt particles and cause a shift in the characteristic graphitic peak position. CNTs being MW active materials, defect formation *via* MW irradiation is quite feasible, and hence, there is a pronounced shift for G band in Pt/CNT-MWH [Kim *et al.* 2007]. These defect sites introduced onto CNT *via* MW irradiation having stronger interaction with deposited Pt NPs also interrupt further particle growth and thus result in smaller Pt particle size as evident from XRD and HRTEM results.

5.3.2. Effect of heating routes on catalytic activity of Pt/CNT catalysts

The synthesized Pt/CNT catalysts were evaluated *in-situ* as cathode catalyst for ORR in single cell PEMFC. CV and EIS studies were carried out to evaluate ESA and interfacial oxygen kinetics of the catalysts. ORR activities of the catalysts were studied through ORR polarization plot and fuel cell polarization curves. Stability of the catalysts was evaluated through CA studies. Table 5.1 summarizes the results obtained through various electrochemical experiments discussed in detail in the following sub-sections.

5.3.2.1. CV, EIS and ORR polarization studies with Pt/CNT catalysts

Fig. 5.6 (a) shows the CV results of the catalysts in a single cell PEMFC configuration with humidified pure hydrogen and nitrogen gases fed at the anode and

cathode compartments, respectively. The voltammograms showed characteristic features of hydrogen adsorption/desorption processes (0 V < E < 0.3 V) on the catalyst surface implying the Pt character of the catalyst particles. The columbic charge for hydrogen desorption (Q_H) after correcting for double layer charge contribution was used to calculate the ESA of the cathodes as detailed in *Chapter 2, Section 2.2.2.4*. The ESA was calculated to be 48 m^{2}g^{-1} and 70 m^{2}g^{-1} for Pt/CNT-CH and Pt/CNT-MWH, respectively. ESA is largely controlled by the size of Pt NPs dispersed onto the support. The higher ESA of Pt/CNT-MWH is a direct consequence of the smaller Pt particle size attained through MW irradiation. ESA represents effective Pt active sites for ORR where triple phase contact of reactant gas, catalyst and the membrane occurs to carry out the electrochemical reaction leading to more efficient use of metal particles. Hence, with higher ESA, Pt/CNT-MWH might lead to more efficient electro-catalyst reactions and better performance of the PEMFC .

Table 5.1. Electrochemical parameters of Pt/CNT catalysts

Catalyst	ESA* (m^{2}g^{-1})	R$_{ct}$** (Ω)	$j_{@\,0.9\,v}$$^{\#}$ (mAcm^{-2})$^{!!}$	$j_{@1000\,s}$$^{\#\#}$ (mAcm^{-2})$^{!!}$	$j_{@9000\,s}$$^{\#\#}$ (mAcm^{-2})$^{!!}$
Pt/CNT-CH	48	22	1.3	119	113
Pt/CNT-MWH	70	14	3.9	151	142

*from CV; **from EIS spectra; #from ORR polarization plot; ##from chrono-amperometric plot; !!cm^2 values correspond to geometric active area of electrode

Fig. 5.6 (b) displays the ac-impedance response of the cathode using Pt/CNT-CH and Pt/CNT-MWH catalysts at E$_{cell}$ = 0.9 V, a potential at which kinetics dominate. Nyquist plot is actually the sum of impedances contributed by both the anode and cathode. However, due to the much faster hydrogen oxidation reaction at the anode, the equivalent anode impedance is negligibly small compared to that of cathode [O'Hayre *et al.* 2016]. Hence, the measured cell impedance can be treated essentially as the cathode impedance. The obtained EIS data were fitted with the circuit shown in the inset of Fig. 5.6 (b). The circuit elements are the following: R$_c$ is the total ohmic resistance of the cell; R$_{ct}$ is charge transfer resistance; CPE is constant phase element which is used instead of capacitance to account for inhomogeneity of the electrode surface [Du *et al.* 2007]. The high frequency intercept on the real

impedance axis of the Nyquist plot represents R_c of the cell. The R_c values obtained are: 0.28 Ω with Pt/CNT-CH catalyst and 0.20 Ω with Pt/CNT-MWH. The semi-circle or the kinetic loop on the Nyquist plot is ascribed to R_{ct} of the cathode oxygen reduction. R_{ct} values are 22 Ω for Pt/CNT-CH and 14 Ω for Pt/CNT-MWH. The lower R_{ct} of Pt/CNT-MWH indicates improved kinetics of ORR with this catalyst. Smaller Pt NPs with uniform distribution is achieved through MW irradiation leading to higher ESA having more active sites for catalysis and hence, results in improved kinetics in agreement with CV results. Thus, EIS results illustrate better catalytic activity of Pt/CNT-MWH for ORR compared to Pt/CNT-CH.
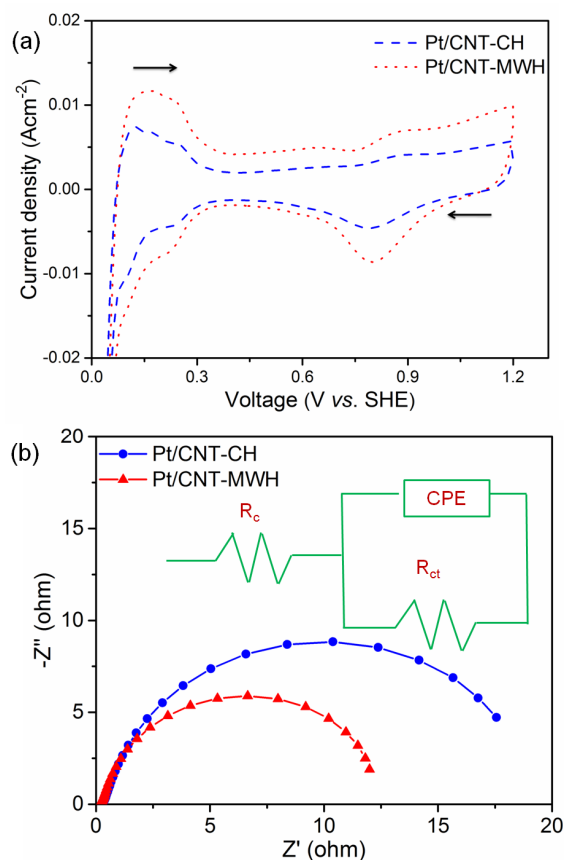
Fig. 5.6. (a) Cyclic voltammograms and (b) EIS spectra of Pt/CNT-CH and Pt/CNT-MWH catalysts recorded at room temperature

Fig. 5.7 (a) shows ORR polarization plots for Pt/CNT catalysts at a scan rate of 1 mVs^{-1} with humidified pure H_2 and O_2 gases fed at anode and cathode compartments, respectively. Current density in the activation controlled region represents the ORR activity of the catalysts. At 0.9 V, where kinetics or activation

losses dominate, Pt/CNT-MWH showed 3 times higher current density than Pt/CNT-CH (3.9 mAcm^{-2} *vs.* 1.3 mAcm^{-2}). As observed from the EIS results, the activity of the Pt/CNT-MWH catalyst is much better than Pt/CNT-CH, which can be attributed to faster interfacial oxygen kinetics of Pt/CNT-MWH with lower R_{ct} as compared to Pt/CNT-CH catalyst.
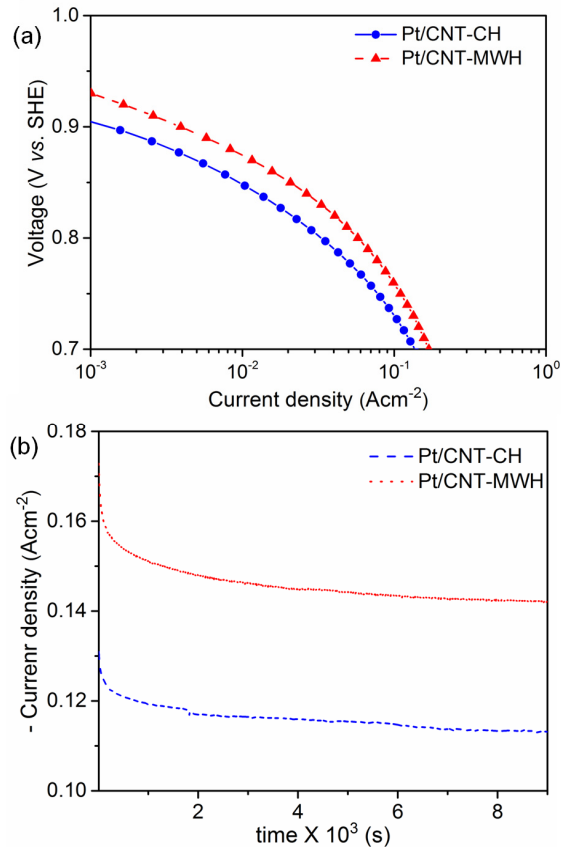
Fig. 5.7. (a) ORR polarization and (b) CA plot of Pt/CNT-CH and Pt/CNT-MWH catalysts

The stability of synthesized Pt/CNT catalysts towards ORR was evaluated through CA measurements at polarization potential of E_{cell} = 0.7 V held over a period of 2.5 h with pure, humidified H_2 and O_2 gases fed at anode and cathode compartments, respectively. Fig. 5.7 (b) shows the evaluation results. Pt/CNT-MWH catalyst exhibited excellent current response throughout the measurement, which was superior to that of Pt/CNT-CH exhibiting better catalytic activity. After the long period of operation (i.e., 9000 s), Pt/CNT-MWH showed 26% higher reduction current than Pt/CNT-CH catalyst, showing higher activity of Pt/CNT-MWH catalyst

with good stability. The current decays gradually with time for both catalysts. However, the deterioration rate of reduction current (c.a. 5-6% overall loss in current density) was very small and similar for both the catalysts; this suggests the good stability of CNT support under the fuel cell operating conditions. The higher initial reduction current value observed for Pt/CNT-MWH compared to Pt/CNT-CH indicates its higher potential with more active sites available for catalysis in agreement with higher ESA obtained from CV results.

5.3.3. Evaluation of performance of Pt/CNT catalysts through single cell PEMFC polarization curves

Since PEMFC performance is the ultimate electrocatalytic activity test for catalysts, the polarization curves of single cell PEMFCs employing Pt/CNT-CH and Pt/CNT-MWH as cathode catalysts were directly investigated and the results are presented in Fig. 5.8 and Table 5.2. For comparison, the polarization curve using commercial Pt/C catalyst at cathode was also generated under identical conditions and is included in Fig. 5.8 (a). Activation over-potential losses which manifest in the polarization curves in the form of lower cell voltage at lower current density region, typically <100 mAcm^{-2}, arise predominantly due to slower kinetics of the reaction at the cathode. The PEMFCs comprising of Pt/CNT-CH, Pt/CNT-MWH and commercial Pt/C cathode catalysts deliver cell voltages of 0.780 V, 0.838 V and 0.774 V, respectively, at a current density of 50 mAcm^{-2}. Higher cell voltage value with Pt/CNT-MWH catalyst implies lower activation over-potential loss [Ahmadi *et al.* 2016], and hence, better ORR catalytic activity. This enhanced fuel cell performance can be attributed to stronger metal-support interaction as evidenced from XPS and Raman results. Additionally, higher ESA and lower R_{ct} achieved through MW route also contribute towards enhancement of fuel cell performance obtained with Pt/CNT-MWH catalyst.

In order to quantify the Pt utilization, mass activity data of the cathodes determined at E_{cell} = 0.9 V are presented in Fig. 5.8 (b). It can be seen that the mass activity of Pt/CNT-MWH is higher by a factor of 2.00 and 1.58 with respect to Pt/CNT-CH and Pt/C catalysts, respectively. Enhancement in the mass activity can be attributed to the smaller particle size as well as better ORR activity achieved *via* MW

irradiation. The peak power densities of 270 mWcm^{-2} and 365 mWcm^{-2} are obtained for Pt/CNT-CH and Pt/CNT-MWH, respectively, while it is 320 mWcm^{-2} for Pt/C catalyst. The power densities obtained for Pt/CNT catalysts in this study are higher than the reported values of Pt/Vulcan Carbon catalysts prepared *via* NaBH$_4$ (245 mWcm^{-2}) and EG-MW routes (230 mWcm^{-2}) [Fang *et al.* 2009]. This reveals the significance of employing the modified chemical reduction route in synthesizing high performing Pt/CNT catalyst. The above results demonstrate the superior performance of Pt/CNT-MWH as an ORR catalyst for fuel cell. This study has thus shown the feasibility to prepare Pt catalyst on MWCNT support that can exhibit high catalytic activity towards ORR for PEMFC application *via* MW assisted, modified chemical reduction route employing a mixture of NaBH$_4$ and EG as the reducing agent.
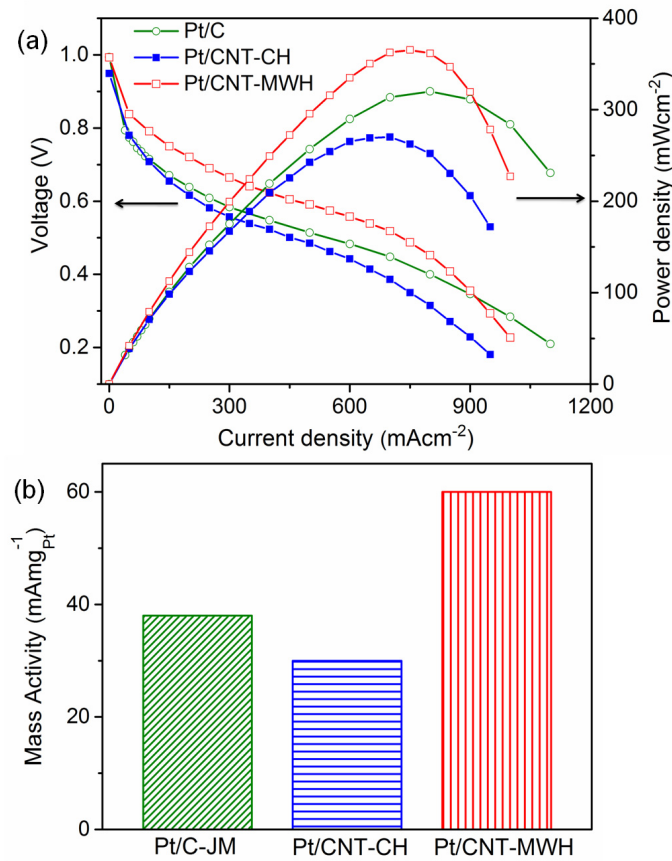
Fig. 5.8. (a) Single cell polarization and power density plots, and (b) mass activity @ E cell =0.9 V of Pt/CNT-CH, Pt/CNT-MWH and commercial Pt/C catalysts derived from (a)

Table 5.2. Parameters obtained from single cell fuel cell testing polarization curves

Catalyst	OCV (V*)	Voltage @ 50 mAcm^{-2}** (V*)	Mass activity @ 0.9 V* (mAmg$_{Pt}^{-1}$)	Maximum Power Density (mWcm^{-2}**)
Pt/C	0.972	0.722	14	270
Pt/CNT-CH	0.993	0.780	30	270
Pt/CNT-MWH	0.949	0.838	60	365

*absolute cell voltage; **cm^2 values correspond to geometric active area of electrode

5.4.   Conclusions

In this study, an approach to synthesize CNT supported Pt NPs catalyst for PEMFC ORR, through a simple and facile, modified chemical reduction route using a mixture of NaBH$_4$ and EG as the reducing agent was investigated. Two different heating methods; CH and MW irradiation were adopted to understand their effect on the properties and catalytic activities of Pt/CNT catalyst. It was found that smaller and well dispersed Pt NPs were deposited onto the CNT surface through MW route (Pt/CNT-MWH) as compared to CH route (Pt/CNT-CH). Additionally, XPS and Raman studies showed the presence of stronger metal support interactions in Pt/CNT-MWH than Pt/CNT-CH catalyst. These results revealed the more suitability of Pt/CNT-MWH as ORR catalyst which was further supported by *in-situ* single PEMFC electrochemical investigations. Cathode with Pt/CNT-MWH showed higher ESA, lower charge transfer resistance, lower activation over-potential loss and higher peak power density compared to the cathode with Pt/CNT-CH and Pt/C. This study revealed that, MW assisted modified chemical reduction route is a very suitable reduction condition to realize high performing catalyst for ORR; which can lead a step forward towards popularising PEMFCs.

Chapter 6

Pt/C catalyst: Influence of various carbon nano-forms as supports

A part of the study presented in this chapter has been published:

Influence of various carbon nano-forms as supports for Pt catalyst on proton exchange membrane fuel cell performance

Abha Bharti [a], Gouri Cheruvally [b, *]

[a] Energy Systems Division, Vikram Sarabhai Space Centre, Thiruvananthapuram 695022, India
[b] Polymers and Special Chemicals Group, Vikram Sarabhai Space Centre, Thiruvananthapuram 695022, India

Abstract

The comparison demonstrating the influence of various carbon nano-forms such as carbon black (CB), single-walled carbon nanotube (SWCNT), multi-walled carbon nanotube (MWCNT) and graphene (G) that can function as support for Pt catalyst are reported in this chapter. The study showed that the different carbon supports do not significantly affect the Pt particle size during synthesis, but leads to generation of different amounts of defective sites in the carbon framework which influenced both the availability of active metal nano-catalysts and metal-support interaction. *In-situ* electrochemical investigations revealed that the different carbon supports influenced both ORR catalytic activity and stability of the catalyst. It was concluded that the MWCNT supported Pt catalyst exhibited the best fuel cell performance among the investigated materials.
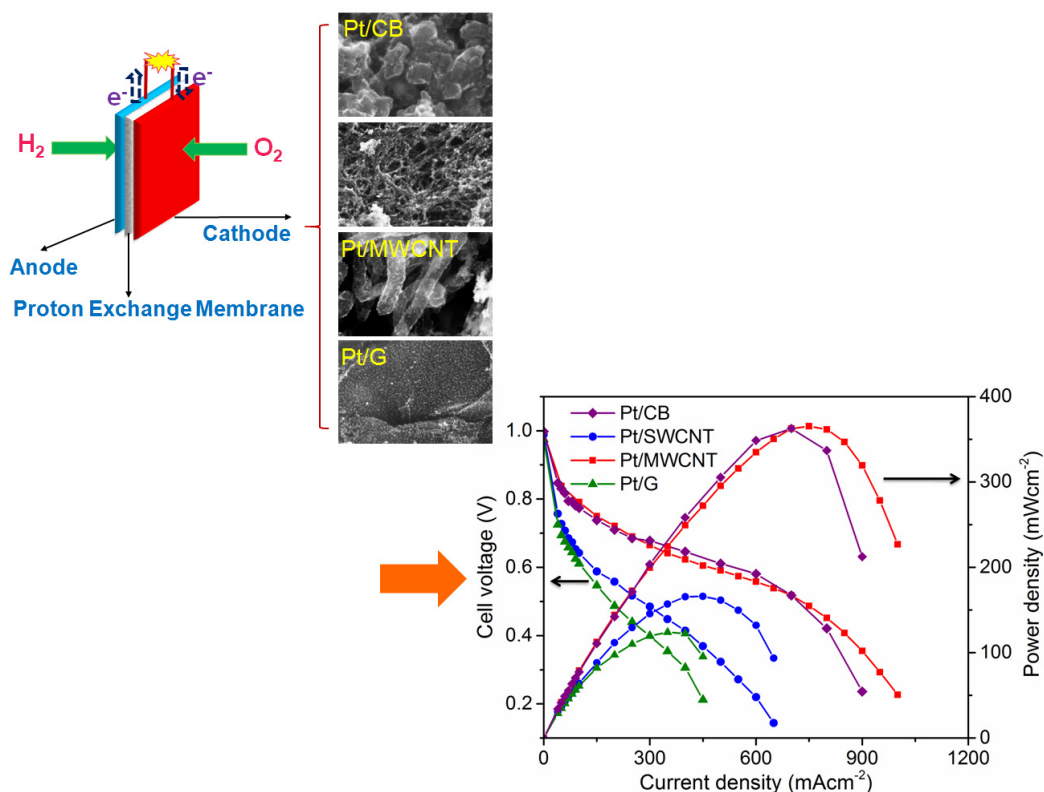
6.1. Introduction

One of the techniques to improve the activity of cathode electrocatalysts and to reduce the content of Pt is to disperse Pt on a conductive support such as carbon [Antolini 2009, Sharma *et al.* 2012]. Carbonaceous materials with high surface area, desired pore structure, nano-structured morphology, high corrosion resistance and good electrical conductivity are highly promising as support materials for electro-catalysts [McCreery 2008]. Carbon supports can strongly influence the particle size of metal as well as its dispersion which are critical parameters in achieving improved activity and stability of the catalysts [Steigerwalt *et al.* 2002, Park *et al.* 2004]. In a carbon-supported metal–catalyst system, carbon support does not function as a mere inert material; it alters the system's Galvani potential, raises the electronic density in the catalyst and lowers the Fermi level. These factors help to accelerate the electron transfer at the electrode–electrolyte interface, thus improving the kinetics of electrode processes. The Pt–carbon support interaction is also beneficial in improving the stability of the electrocatalyst [Vedrine *et al.* 1978, Biloul *et al.* 1990]. In the case of fuel cell catalysts, carbon supports also influence the performance by altering mass transport, catalyst layer electrical conductivity, electrochemically active area and stability of metal NPs during operation [Inoue *et al.* 2008, Salgado *et al.* 2010]. Hence, selection of a suitable carbon support for Pt metal with desirable properties to obtain an active catalyst is vital for achieving enhancement in PEMFC performance.

Among all kinds of carbon supports, carbon black (CB) has been commonly used due to its high mesoporous distribution and graphite-like characteristics [Bezerra *et al.* 2007]. Recently, the non-conventional carbon materials such as carbon nanotubes [De Volder *et al.* 2013, Fujigaya *et al.* 2013] - both single-walled (SWCNT) and multi-walled (MWCNT) - and carbon nanosheets such as graphite based materials [Qu *et al.* 2010, Antolini 2012, Liu *et al.* 2014] have been proposed as Pt supports. Wu and Xu presented a comparison between SWCNT and MWCNT as the carbon support for methanol oxidation reaction (MOR) activity in direct methanol fuel cell (DMFC) and concluded that Pt-SWCNT/Nafion catalyst is superior compared to Pt-MWCNT/Nafion catalyst [Wu *et al.* 2007]. On the contrary, in the works of Carmo *et al.*, the MOR activity was higher for MWCNT supported catalyst

than the SWCNT supported one [Carmo *et al.* 2005]. Lee *et al.* compared the ORR performance of Pd_3Pt_1 catalysts supported on SWCNT, graphene nanosheets (GNS) and graphite nanofibres (GNF) and obtained catalytic activity order as Pd_3Pt_1/GNS> Pd_3Pt_1/SWCNT> Pd_3Pt_1/GNF [Lee *et al.* 2013]. Gamez *et al.* investigated PtPd catalysts supported on Vulcan XC-72R (a form of CB) and on HSAG 300 Lonza (higher surface area graphite) and found that the catalyst supported on Vulcan presented higher active surface area than the other one [Gamez *et al.* 1999]. Conversely, in the works of Wu *et al.*, PtNi catalyst supported on graphene exhibited improved ORR activity than Vulcan-XC-72 [Wu *et al.* 2012]. These studies bring out the significance of carbon as support materials for Pt catalyst in fuel cell and also necessitate the comparison under identical conditions of major classes of carbon supports, *viz*. CB, SWCNT, MWCNT and graphene which are reported to increase the fuel cell performance. Such a comparison would be aimed at studying not only the influence of these supports on catalytic activity but also selection of the most suitable carbon support to achieve enhanced fuel cell performance. To the best of our understanding, there are no reports available comparing the influence of CB, SWCNT, MWCNT and graphene supported Pt on the ORR activity, and hence, on the performance of a working PEMFC.

This study reports the comparison and influence of carbon nano-forms such as CB, SWCNT, MWCNT and graphene that are typically used as cathode catalyst support for Pt catalyst on the ORR activity in PEMFC. To validate the applicability of these carbon supports, performance of the supported catalysts is evaluated through *in-situ* electrochemical investigations in an actual, working PEMFC under identical conditions and the results are compared. Additionally, the fuel cell performance comparison through polarization and power density curves was done with standard, commercial Pt/C catalyst. The study helps in understanding the influence of carbon supports on fuel cell performance and selection of the most suitable carbon supported Pt material to achieve enhanced fuel cell performance.

6.2. Experimental

6.2.1. Materials

The following raw materials were used for the synthesis of Pt catalysts on different carbon supports: $H_2PtCl_6.6H_2O$, CB, SWCNT, MWCNT (in-house product), G, $NaBH_4$, and EG. NaOH was used to maintain the required alkaline medium during synthesis and HCl was used as a sedimentation promoter. Ethanol, acetone and ultra-pure water were used as solvents. Details of all the above chemicals and materials are furnished in *Chapter 2*, *Section 2.1*. The materials used for electrode preparation, MEA fabrication and single cell PEMFC assembly remains the same as detailed under *Chapter 2, Section 2.1* and *Section 2.4.1*.

6.2.2. Synthesis of Pt on different carbon supports

Pt catalysts (20 wt. % of Pt) supported on different carbon supports were synthesized by a single step, microwave assisted, modified chemical reduction route using a mixture of $NaBH_4$ and EG as reducing agents, as detailed in *Chapter 2, Section 2.2.4*.

6.2.3. Characterization

Characterization methods employed include FESEM, HRTEM, XRD, Raman spectroscopy, ICP-AES, HRTEM, BET specific surface area and XPS. The details of all these methods are given in *Chapter 2, Section 2.3*.

6.2.4. Fabrication of MEA and assembly of single cell PEMFC

MEA for single cell fuel cell was prepared using Nafion® membrane and catalyst ink coated PTFE sintered carbon paper. The procedure for MEA fabrication and single cell assembly is detailed in *Chapter 2*, *Section 2.4.1.4 and Section 2.4.1.5*, respectively. The metal (Pt) loading at the electrodes (anode and cathode) in MEA was 0.5 $mg_{Pt}cm^{-2}$.

6.2.5. Electrochemical evaluation

The electrochemical experiments were carried out on a single cell PEMFC at room temperature and atmospheric pressure unless otherwise defined and are detailed in *Chapter 2, Section 2.5.1*. The activity and stability of the synthesized catalysts towards ORR were evaluated through CA measurements at polarization potential of

E_{cell} = 0.7 V held over a period of 2.5 h. CV experiments were performed by cycling the cathode at 20 mVs^{-1} between 0 to 1.2 V *vs*. SHE. EIS measurements were performed by applying ac amplitude of 10 mV over the frequency range 10^{-1} to 10^{5} Hz at cell voltage, E_{cell} of 0.9 V. ZSimpWin™ software (Princeton Applied Research) was used to analyse the EIS spectra. All the electrochemical experiments except CV and EIS were performed with pure, O_2 and humidified H_2 gases fed at cathode and anode, respectively. For CV and EIS experiments, pure, N_2 and humidified H_2 gases were fed at cathode and anode, respectively. The polarization curves were recorded at 50 °C, 1 atm and with fixed flow rate of 1 NLPM of hydrogen and oxygen gases. The anode side was fed with pure hydrogen humidified to 90% RH and the cathode side was fed with pure oxygen humidified to 70% RH.

6.3. Results and discussion
6.3.1. Influence of carbon supports on the physico-chemical properties of the synthesized Pt catalysts

The support characteristics of carbonaceous materials strongly depend on their morphology and dimensionality, which are thus the key factors to their ultimate performance and applications. FESEM technique was employed to study the surface morphology of the supported catalysts; whereas, HRTEM technique was used to understand the nature of dispersion and mean particle size of Pt. Fig. 6.1 shows the FESEM images, HRTEM images and the corresponding SAED patterns of the synthesized catalysts Pt/CB, Pt/SWCNT, Pt/MWCNT and Pt/G. The FESEM images [Fig. 6.1 (a1, b1, c1 and d1)] clearly show the morphologies of the carbon supports, demonstrating nano-clustered, nano-tubular and sheet morphology of CB, CNT (SWCNT and MWCNT) and graphene sheets, respectively. This indicates that the morphologies of the support materials are retained after Pt deposition. From the HRTEM images [Fig. 6.1 (a2, b2, c2 and d2)] the dispersion of Pt nanocatalyst particles onto the carbon supports was revealed. It was observed that in the case of CB and SWCNT support, agglomerated Pt NPs were obtained; whereas, on MWCNT support, uniformly distributed spherical Pt NPs were obtained. On the contrary, in the case of G support, it was found that several Pt NPs coalesce to form Pt nano-clusters (NCs). The lattice spacing measurements from the corresponding SAED patterns of

different carbon supported Pt catalysts exhibit diffraction rings corresponding to Pt and C reflection planes [Fig. 6.1 (a3, b3, c3 and d3)]. Diffraction rings with higher intensity are observed for Pt/G as compared to Pt/CB and Pt/SWCNT and Pt/MWCNT; this indicates higher crystallinity for Pt/G catalyst. From the HRTEM images, the diameters of the deposited Pt NPs in Pt/CB, Pt/SWCNT, Pt/MWCNT and Pt/G catalysts were determined to be 3.7 ± 0.7 nm, 3.5 ± 0.2 nm, 2.6 ± 0.5 nm and 3.2 ± 0.3 nm, respectively.
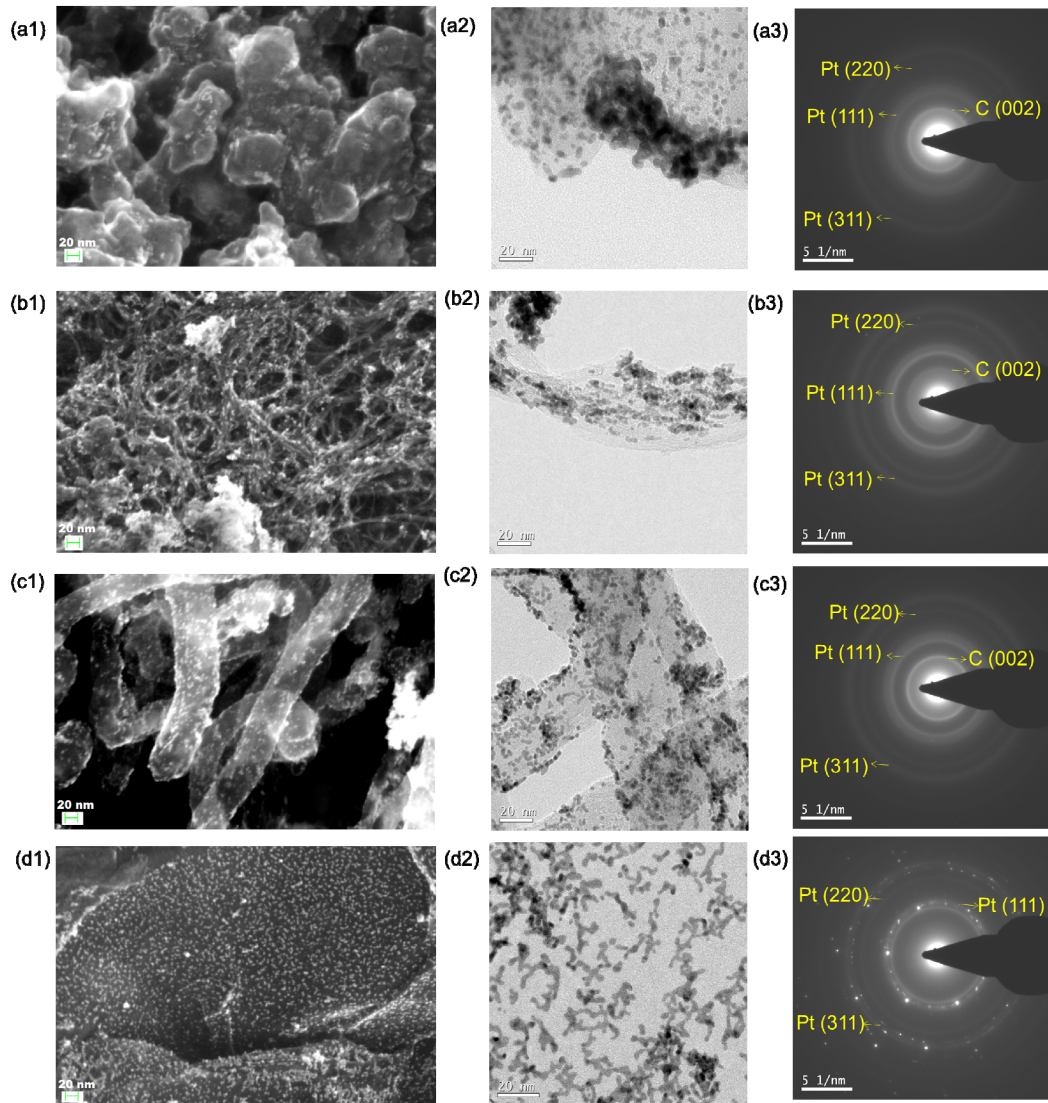
Fig. 6.1. FESEM images, HRTEM images and SAED patterns of Pt/CB (a1, a2 and a3); Pt/SWCNT (b1, b2 and b3); Pt/MWCNT (c1, c2 and c3), and Pt/G (d1, d2 and d3)

The phase composition and crystal structure of the different carbon supported Pt catalysts were further confirmed by XRD analysis, which are shown in Fig. 6.2 (a). For Pt/CB, the characteristic diffraction peaks of Pt were observed at 2θ values of 39.8, 45.5, 67.7 and 81.6 corresponding to (111), (200), (220) and (311) planes of an fcc crystal lattice structure; whereas, the peak at 2θ values of 25.8 corresponds to (002) plane of graphitic carbon from CB support. Similar fcc Pt and graphitic carbon peaks were observed for Pt/SWCNT, Pt/MWCNT and Pt/G catalysts. In the case of Pt/MWCNT, the additional peaks at 2θ value of 44.4 and 51.9 correspond to (101) and (102) planes of graphitic carbon from MWCNT support, respectively. Distinct variations in the line shape of C (002) diffraction peaks were observed among the different carbon supported Pt catalysts. For CB, SWCNT and MWCNT carbon supported Pt catalysts, broadened C (002) peaks were obtained indicating less crystalline or disordered nature of carbon. In the case of graphene supported Pt catalyst, a sharp carbon C (002) diffraction peak at 2θ value of 26.7 was observed due to the highly ordered graphitic structure of the graphene support. The presence of additional C (004) diffraction peak at 2θ value of 54.5 also indicates high crystallinity of the carbon structure in graphene [Kim *et al.* 2003, Shanahan *et al.* 2008]. Similar characteristics of carbon peaks were also obtained in pristine carbon supports (CB, SWCNT, MWCNT and G) as shown in Fig. 6.2 (b), indicating insignificant effect of Pt on phase evolution of carbon after Pt deposition onto the various carbon supports. This indicates that the crystal structures of the support materials are retained after Pt deposition. The XRD results show that the studied CB, SWCNT and MWCNT carbon supports have disordered carbon structure; whereas, graphene support exhibits the most ordered graphitic structure. This is consistent with the SAED patterns of the different carbon supported Pt catalysts wherein the most intense diffraction is obtained for Pt/G catalyst. The average Pt crystallite sizes in these catalysts were calculated based on Pt (111) peak in XRD and were found to be similar irrespective of the different carbon supports used (Pt/CB - 3.0 nm, Pt/SWCNT-3.0 nm, Pt/MWCNT-2.7 nm, and Pt/G - 3.0 nm). The XRD data and calculated particle size from HRTEM images were matching well and indicated that the use of different carbon supports did not significantly influence the size of Pt NPs formed following this synthesis method.

Thus, the efficacy of the synthesis route used to prepare similarly sized Pt NPs dispersed on various carbon supports was established.
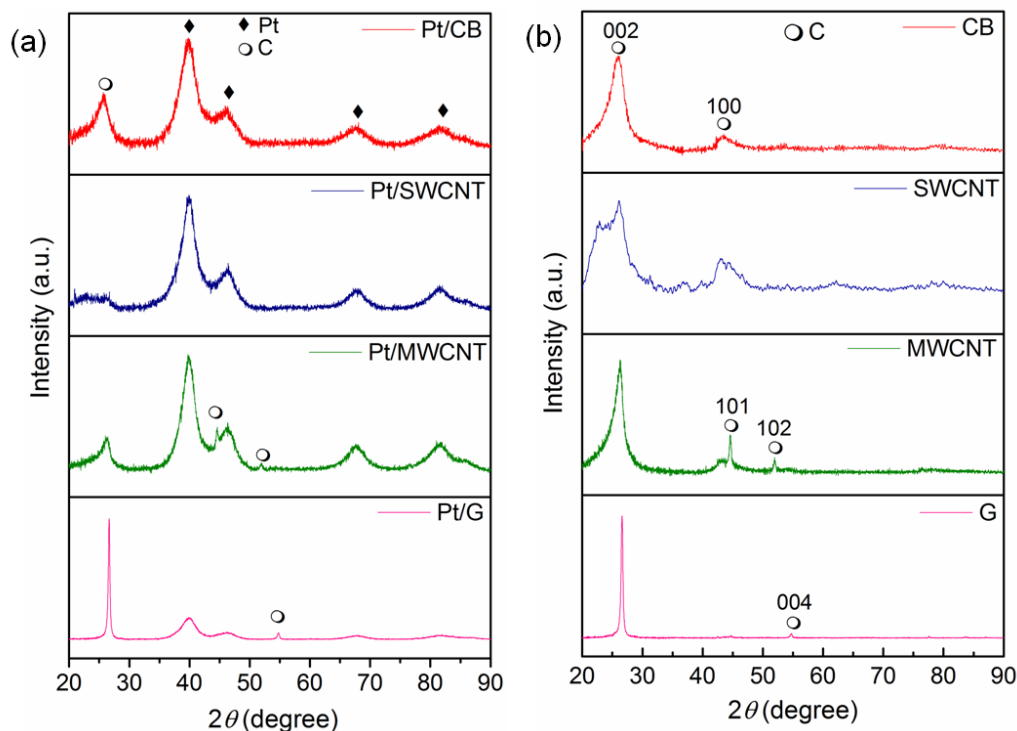
Fig. 6.2. XRD patterns of (a) Pt catalysts supported on different carbon nano-forms, and (b) pristine carbon supports

XPS studies were carried out to understand the interactions between the deposited Pt NPs and the different carbon supports. Fig. 6.3 shows XPS spectra of the Pt 4f peaks of the synthesized catalysts which show the presence of intense Pt $4f_{5/2}$ and Pt $4f_{7/2}$ peaks at binding energies of c.a. 74.5 eV and c.a. 71.2 eV, respectively which correspond to metallic Pt (0) state. As compared to standard Pt (0) peaks [Venezia *et al.* 1992] ($4f_{5/2}$ = 74.9 eV and $4f_{7/2}$ = 71.6 eV), Pt 4f peaks of the Pt catalysts synthesized in the present study were negatively shifted by 0.4 eV, reflecting stronger interactions between Pt and the carbon supports. The lowering of binding energy values of Pt 4f peaks suggests the transfer of electrons to Pt metal [Khan *et al.* 2015]. Since the carbon supports employed in this study are all π-electron rich species, it can be rationally presumed that these electrons that get transferred to Pt originated from the respective carbon supports. This observation gives a strong evidence for the significant metal-support interactions in the studied catalyst systems.

The electronic interaction between Pt and the carbon support is considered to be beneficial for the enhancement of catalytic properties and to improve stability of the electrocatalyst [Vedrine *et al.* 1978, Biloul *et al.* 1990].
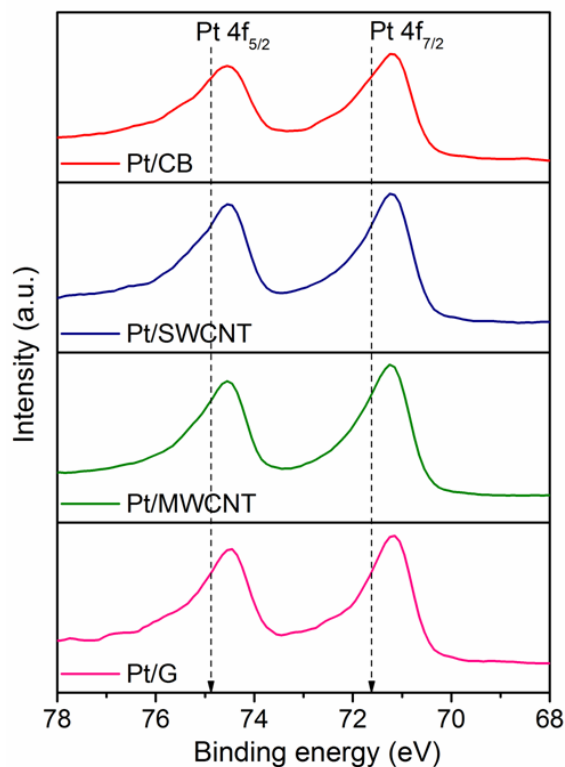
Fig. 6.3. XPS spectra: Pt 4f peaks of Pt catalysts supported on different carbon nano-forms

The structural differences between the different carbon supports were studied using Raman Spectroscopy. Fig. 6.4 (a) shows the Raman spectra of the synthesized Pt catalysts. A broad peak centered around 300 cm^{-1} was observed only for Pt/SWCNT catalyst. This peak corresponds to radial breathing mode (RBM) of carbon, which is the unique Raman active mode of SWCNTs compared to other graphitic carbon systems [Gao *et al.* 2008]. Two characteristic peaks at ~1340 cm^{-1} and ~1575 cm^{-1} are observed for all catalysts, which can be assigned respectively to the D and G bands that arise due to disordered (sp^3 bonded sites) and ordered (hexagonal sp^2 sites) carbon structures. The D bands were dominant for Pt/CB and Pt/MWCNT; whereas, greatly suppressed D bands appeared in Pt/SWCNT and Pt/G catalysts indicating more ordered graphitic structure with lesser defects in the latter

catalysts than the former ones. This observation was further supported by the intensity ratio of D and G bands (I_D/I_G), as depicted in Fig. 6.4 (b), which indicates the amount of defects present in the carbon support. The I_D/I_G order obtained is Pt/MWCNT> Pt/CB > Pt/SWCNT> Pt/G. This illustrates that out of the four carbon supports studied here, MWCNT support has the structure with maximum disorder/defects, and graphene support has the structure with minimum disorder/defects. The Raman analyses results are consistent with the XRD and SAED results.
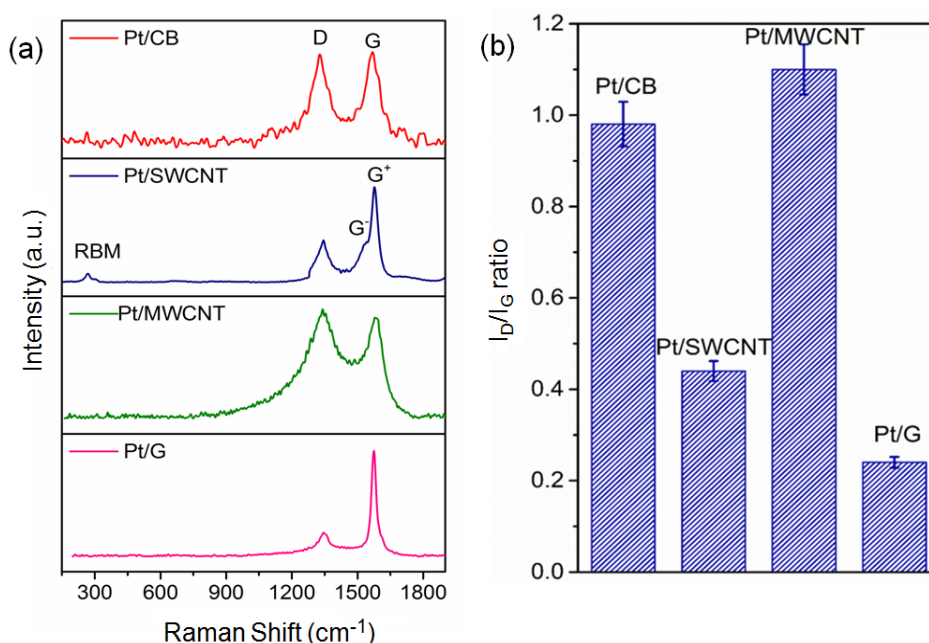
Fig. 6.4. (a) Raman spectra, and (b) I_D/I_G ratio of the Pt catalysts supported on different carbon supports

Among the one-dimensional (1D) graphitic SWCNT and MWCNT carbon supports, significant difference in the line shape of G band was observed. MWCNT supported Pt catalyst showed a single, intense and broad tangential mode G band; whereas, for SWCNT support, splitting of G band into a main peak with a shoulder peak was observed. The peaks at higher wave number and lower wave number are called G^+ and G^-, respectively. These bands arise due to vibrations of carbon atoms along the tube axis (LO phonon mode) or along the circumferential direction (TO phonon mode) of SWCNTs [Dresselhaus *et al.* 2000]. Unlike the other 1D graphitic carbon systems, SWCNTs can be either semiconducting or metallic, and the shape of G-band allows distinguishing between semiconducting and metallic nanotubes

[Herrera *et al.* 2003, Gao *et al.* 2008]. For semiconducting SWCNT, the intensity of G^+ is much stronger than that of G^-. In the case of metallic SWCNT, the G-band can also be fitted by two Lorentzian peaks; but, in contrast to the semiconducting SWCNT, the intensity of G^- is stronger than that of G^+. Based on the above, it is inferred from Raman spectrum of Pt/SWCNT catalyst that Pt is supported on semiconducting SWCNTs (intensity of $G^+ \gg G^-$) and hence, is electrically less conductive than Pt/MWCNT catalyst.

Raman analysis was also employed to understand the effect of Pt deposition on the structure of carbon supports. For a meaningful comparison, pristine carbon support was also subjected to Raman analysis. On the deposition of Pt onto various carbon supports, significant increase in the intensity of D band was observed, as depicted in Fig. 6.5 (a)-(c). This clearly demonstrates the occurrence of structural disorder in carbon supports with Pt deposition. The deposition of Pt NPs on carbon supports causes a disruption in its structure and partially ruins its symmetry, which is manifested by an increase in the intensity of D band. Additionally, a positive shift in G band position was also observed after Pt deposition on the various carbon supports. The shift in G band position can be correlated to the formation of defects in the structure of carbon supports occurring during the synthesis reaction. Carbon materials are MW active and hence, formation of defects/hot spots in the carbon framework is quite feasible during the catalyst synthesis [Zhang *et al.* 2013]. These defective structures interact strongly with the deposited Pt particles and cause a shift in the characteristic graphitic peak position. With the most defective carbon structure in MWCNT support, the possibility for interaction between Pt and the support is the strongest in Pt/MWCNT. This is further corroborated by the observation of a pronounced positive shift in the G band of Pt/MWCNT as compared to the Pt/SWCNT, Pt/G and Pt/CB catalysts [Fig. 6.5. (d)]. Hence, among the various carbon supports studied, MWCNT shows the strongest interaction with Pt, which might also be responsible for the comparatively smaller Pt particle size obtained for Pt/MWCNT catalyst. The Raman spectrum of pristine CB support could not be obtained due to burning of

the CB sample on laser irradiation. Hence, changes in the structure of CB support after Pt deposition could not be assessed. Nevertheless, following the trend of increase in the structural disorder occurring after Pt deposition as observed for the other carbon supports, a similar trend can be rationally assumed for Pt/CB case also.
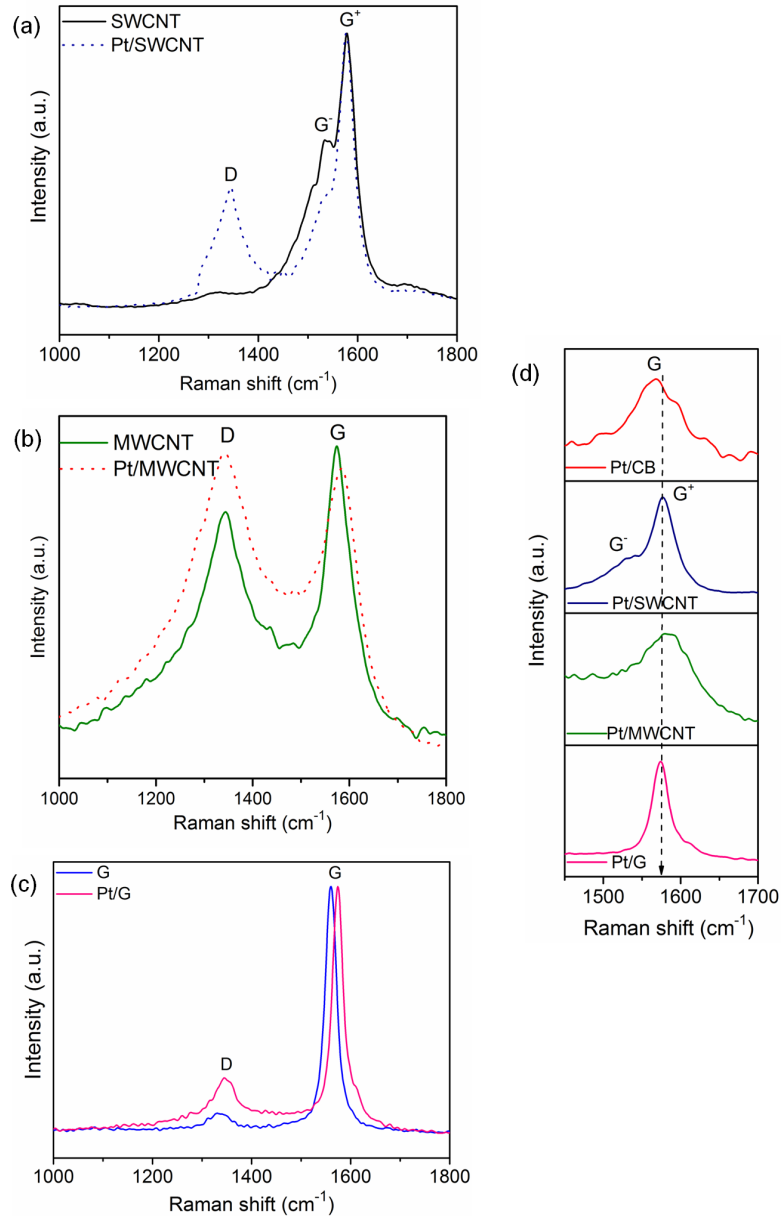
Fig. 6.5. Raman spectra of (a) SWCNT and Pt/SWCNT, (b) MWCNT and Pt/MWCNT, (c) G and Pt/G, and (d) magnified G band Raman spectra of the Pt catalysts supported on different carbon supports

6.3.2. Influence of carbon supports on ORR catalytic activity of Pt
6.3.2.1. CA, CV and EIS studies

The catalytic activity and stability of Pt supported on different carbon nano-forms for ORR were investigated by CA tests and the corresponding curves are shown in Fig. 6.6. The polarization potential was 0.7 V and was held over a period of 2.5 h with humidified pure H_2 and O_2 gases fed at anode and cathode compartments, respectively. It is to be noted that the water management issues in the cell are more prevalent at higher currents which may not be seen at higher voltages and lower currents. Besides, fuel cells are usually operated at voltage >0.65 V to have fuel cell energy conversion efficiencies >55% [Gasteiger *et al.* 2005]. Considering these two important issues of water management and efficiency, cell voltage of 0.7 V was selected to understand the catalytic activity and stability of the different carbon supported Pt cathode catalysts.
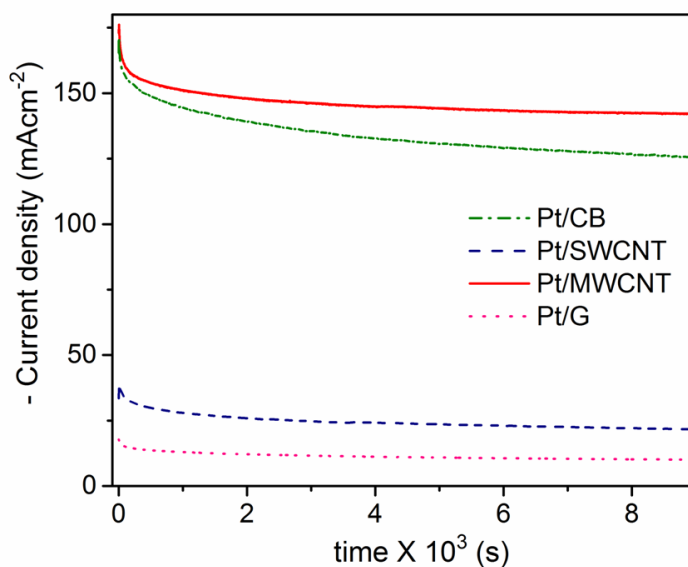
Fig. 6.6. Current *vs.* time curves from CA tests with Pt catalysts supported on different carbon nano-forms at $E_{cell} = 0.7$ V

The current evolved in an electrochemical reaction is a direct measure of the rate of electrochemical reaction [O'Hayre *et al.* 2016]. Different current densities and hence, catalytic activities were obtained with the different carbon supported Pt catalysts signifying the varying influence of the supports on the catalytic activity. At the end of 9000 s, the current density (catalytic activity) of Pt catalysts supported on

different carbon nano-forms follows the order: Pt/MWCNT > Pt/CB > Pt/SWCNT > Pt/G. As shown in Fig. 6.6, the initial current density of Pt/MWCNT catalyst was slightly higher than that of Pt/CB and significantly higher than that of Pt/SWCNT and Pt/G. After an initial decrease, the current densities slowly got stabilized over the experimental period. At the end of 9000 s, the current density of Pt/MWCNT was 1.1, 6.5 and 14.2 times higher than that of Pt/CB, Pt/SWCNT and Pt/G, respectively. Pt/MWCNT showed only 6% loss in current density after the experiment, compared to 13%, 21% and 23% loss exhibited by Pt/CB, Pt/SWCNT and Pt/G catalysts, respectively. These results imply that Pt/MWCNT catalyst exhibits higher catalytic activity and better stability for ORR compared to the other carbon supported catalysts.

Fig. 6.7 shows CV results of the catalysts in a single cell PEMFC configuration with humidified pure H_2 and N_2 gases fed at the anode and cathode compartments, respectively. The curves obtained show the typical features of Pt based catalysts with a hydrogen adsorption/desorption region (0 V to 0.3 V), a double layer region (0.3 V to 0.6 V) and a potential region of Pt oxide formation and reduction (0.6 V to 1.2 V). For Pt/SWCNT, the pair of peaks at 0.50 V and 0.45 V correspond to the reversible redox reaction of oxygen-containing functional groups [Lee *et al.* 2013].
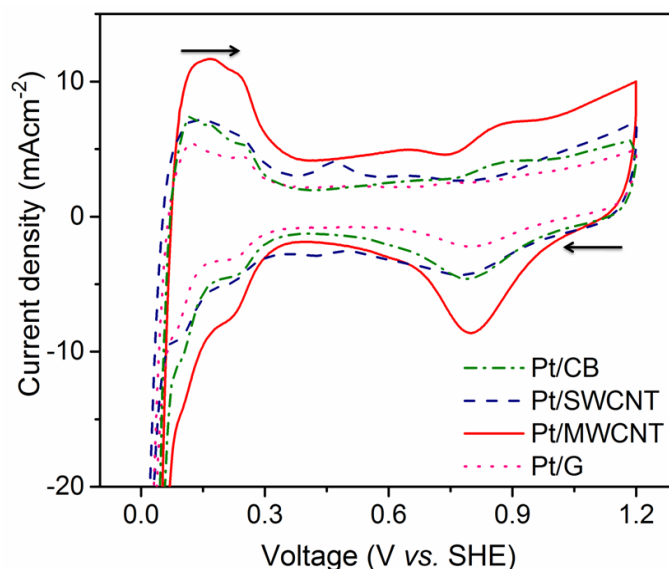
Fig. 6.7. CV diagrams of Pt catalysts supported on different carbon nano-forms at scan rate of 20 mVs^{-1}

The ESA of the catalysts were obtained by measuring the columbic charge for hydrogen desorption (Q_H) after correcting for double layer charge contribution of the cathodes as detailed in *Chapter 2, Section 2.2.2.4*. The ESA was calculated to be 42 m^2g^{-1}, 31 m^2g^{-1}, 66 m^2g^{-1} and 22 m^2g^{-1} for Pt/CB, Pt/SWCNT, Pt/MWCNT and Pt/G, respectively. The ESA is mainly controlled by two factors: (i) the size of Pt NPs dispersed onto the support, and (ii) Pt utilization which is relevant to Pt NPs in contact with the Nafion® membrane [Park *et al.* 2011]. Since the sizes of the Pt NPs are not influenced by the carbon supports and remain similar as shown earlier by XRD results and HRTEM images, the difference in ESA obtained for the different catalysts can be attributed to the Pt utilization efficiency of each catalyst. The Pt utilization efficiency can be calculated using the following equations [Song *et al.* 2011]:

$$\text{Pt utilization \%} = \frac{ESA}{CSA} \times 100 \qquad \text{(eqn. 6.1)}$$

$$CSA = \frac{6 \times 10^4}{\rho \times L} \qquad \text{(eqn. 6.2)}$$

where, *CSA* is chemical surface area (m^2g^{-1}), ρ is the density of the Pt metal (21.4 gcm^{-2}) and *L* is the Pt crystallite size from XRD in Å. The calculated values of Pt utilization efficiency was in the order Pt/MWCNT (63%) > Pt/CB (45%) > Pt/SWCNT (33%) > Pt/G (23%). Thus, the Pt utilization efficiency of MWCNT supported catalyst was 1.4, 1.9 and 2.7 times higher than those of CB, SWCNT and G supported catalysts, respectively. A higher Pt utilization efficiency represents more number of three-phase boundaries (TPB) in the structure where actual catalysis occurs and hence, more number of effective Pt active sites for ORR [Okamoto *et al.* 2009]. The I_D/I_G order of Pt/MWCNT> Pt/CB> Pt/SWCNT> Pt/G is seen to match well with that of Pt utilization efficiency illustrating that the formation of more disordered/defect structures in carbon support is conducive for enhancement in ESA and Pt utilization efficiency. Hence, I_D/I_G ratio can also be taken as an indirect measure of efficient dispersion of Pt NPs onto the carbon support. Therefore, with the least imperfect carbon structure, Pt/G catalyst exhibited the lowest ESA and Pt utilization efficiency; whereas, with the most defective structure, Pt/MWCNT catalyst

displayed the highest ESA and Pt utilization efficiency. These results are in good agreement with the CA test findings confirming that with higher ESA and Pt utilization efficiency, Pt/MWCNT has higher ORR catalytic activity in PEMFC. Table 6.1 summarizes the electrochemical parameters acquired from chrono-amperometric and CV measurements of the different carbon supported Pt catalysts.

Table 6.1. Electrochemical parameters of Pt catalysts with different carbon supports

Catalyst	ESA^a (m^2g^{-1})	$j_{@1000\,s}^{\ b}$ $(mAcm^{-2})^*$	$j_{@9000\,s}^{\ b}$ $(mAcm^{-2})^*$	j loss (%)	Pt utilization (%)
Pt/CB	42	145	126	13	45
Pt/SWCNT	31	28	22	21	33
Pt/MWCNT	66	151	142	6	63
Pt/G	22	13	10	23	23

[a] from CV; [b] from chrono-amperometric plot; * cm^2 values correspond to geometric active area of electrode

EIS studies were carried out to understand the influence of different carbon supported catalysts on the intrinsic behavior of ORR. Fig. 6.8 displays the ac-impedance response of the fuel cell reaction using the catalysts at E_{cell} = 0.9 V, a potential at which reaction kinetics dominate. The obtained EIS data were fitted with the circuit shown in the inset of Fig. 6.8, with the circuit elements as follows: R_m is membrane resistance; R_a and R_c are charge transfer resistances for anode and cathode reactions, respectively, and CPE_a and CPE_c are charge transfer related double layer capacitances for the anode and cathode, respectively [Zhang *et al.* 2006]. CPE is constant phase element which is used instead of capacitance to account for inhomogeneity of the electrode surface. Its impedance is equal to $Z_{CPE} = [Y_o\,(j\omega)^n]^{-1}$, where Y_o is the frequency independent parameter or CPE constant, ω is the angular frequency, and n is the CPE power [Rončević *et al.* 2014]. It is to be noted that this Nyquist plot is actually the sum of impedances contributed by both the anode and cathode. However, due to the much faster hydrogen oxidation reaction at the anode (higher by 6 orders of magnitude than that of ORR kinetics), the equivalent anode impedance is negligibly small compared to that of cathode [O'Hayre *et al.* 2016].

Hence, the measured cell impedance can be treated essentially as the cathode impedance. The equivalent circuit parameters of the cathode with different carbon supported Pt catalysts are summarized in Table 6.2. The semi-circle or the kinetic loop on the Nyquist plot is ascribed to R_c of the cathode ORR. Lower value of R_c implies faster ORR which results in higher fuel cell performance. Coherent with CA and CV results, the influence of supports on ORR catalytic activity was also evidenced with different values of R_c obtained with different supports. The R_c follows the order Pt/G > Pt/SWCNT > Pt/CB > Pt/MWCNT. The R_c of Pt/CB, Pt/SWCNT and Pt/G catalysts are c.a. 1.6, 3.3 and 4.3 times higher than that of Pt/MWCNT. This results from the enhanced interfacial oxygen reduction kinetics promoted by Pt/MWCNT. This can be attributed to higher ESA and Pt utilization efficiency obtained with Pt/MWCNT catalyst compared to the other systems. Thus, it is inferred that, more TPBs, *i.e.* Pt NPs covered by thin ionomer film through which oxygen can diffuse, are formed with MWCNT support in the catalyst layer and are available for ORR. Based on the results obtained, it can also be reasonably predicted that the different carbon supports influence the ORR activity through availability of these TPBs on the catalyst surface.
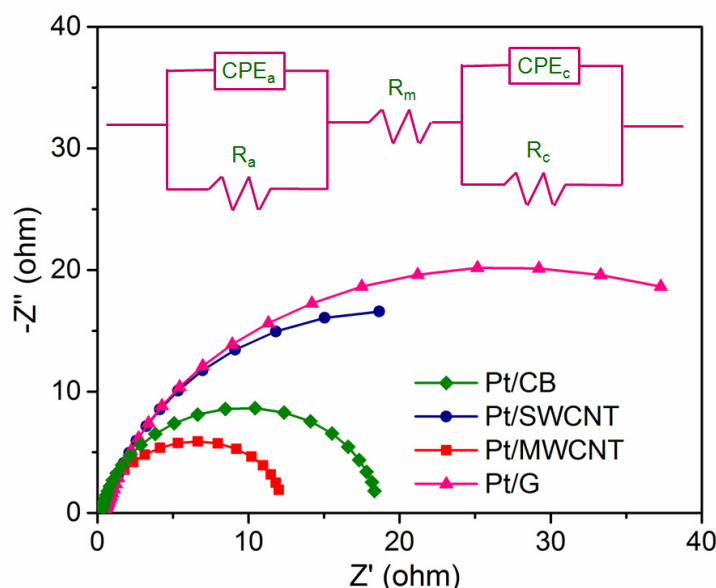
Fig. 6.8. Nyquist plots of Pt catalysts supported on different carbon nano-forms at E_{cell} = 0.9 V

Table 6.2. Equivalent circuit parameters of PEMFC with Pt catalysts supported on different carbon nano-forms

Catalyst	R_m (Ω)	CPE_c-Y_o (F)	CPE_c-n (F)	R_c (Ω)	Error fit R_c (%)
Pt/CB	0.18	0.01	0.96	18.3	1
Pt/SWCNT	0.21	0.04	0.90	39.1	3
Pt/MWCNT	0.18	0.03	0.99	11.7	3
Pt/G	0.23	0.02	0.87	50.2	2

6.3.3. Evaluation of performance of synthesized Pt catalysts through single cell PEMFC polarization curves

It is well known that at low temperature, the catalysts have a dominating effect on the performance of the fuel cell. Hence, it is often the most practical, yet powerful, method to compare the performances of catalysts at relatively low temperatures to estimate their catalytic activity. The synthesized Pt catalysts were evaluated at the cathode side in a lab-made PEMFC, working at 50 °C and atmospheric pressure, in order to study the influence of different carbon supports on catalyst performance. For comparison, the polarization curve using commercial Pt/C catalyst at cathode was also generated under identical conditions. The anode was set as standard using commercial Pt/C catalyst which has Pt supported on Vulcan XC-72, a class of CB support. Since all the prepared electrodes contained the same Pt loading, the data obtained could be utilized for a one-to-one comparison. Fig. 6.9 (a) shows polarization and power density curves of the synthesized catalysts along with commercial catalyst. Activation over-potential losses which manifest in the polarization curves in the form of lower cell voltage at lower current density region, typically <100 mAcm^{-2}, arise predominantly due to slower kinetics of the reaction at the cathode. The PEMFCs comprising of Pt/CB, Pt/SWCNT, Pt/MWCNT, Pt/G and commercial Pt/C cathode catalysts deliver cell voltages of 0.830 V, 0.757 V, 0.838 V, 0.694 V and 0.774 V, respectively, at a current density of 50 mAcm^{-2} (Fig. 6.9 (b)). The highest cell voltage value with Pt/MWCNT catalyst implies lower activation over-potential loss, and hence, better ORR catalytic activity for this system compared to others. This

enhanced fuel cell performance can be attributed to stronger metal-support interaction, higher ESA, Pt utilization efficiency and faster interfacial oxygen kinetics as supported by CV and EIS results. It is also to be noted that, the trend in ORR catalytic activity of CB, SWCNT, MWCNT and G supported catalysts in terms of higher voltage in activation region follows the same order (Pt/MWCNT> Pt/CB> Pt/SWCNT> Pt/G) as of Pt utilization efficiency and R_c, further confirming the influence of carbon supports on ORR catalytic activity through creation of TPBs.
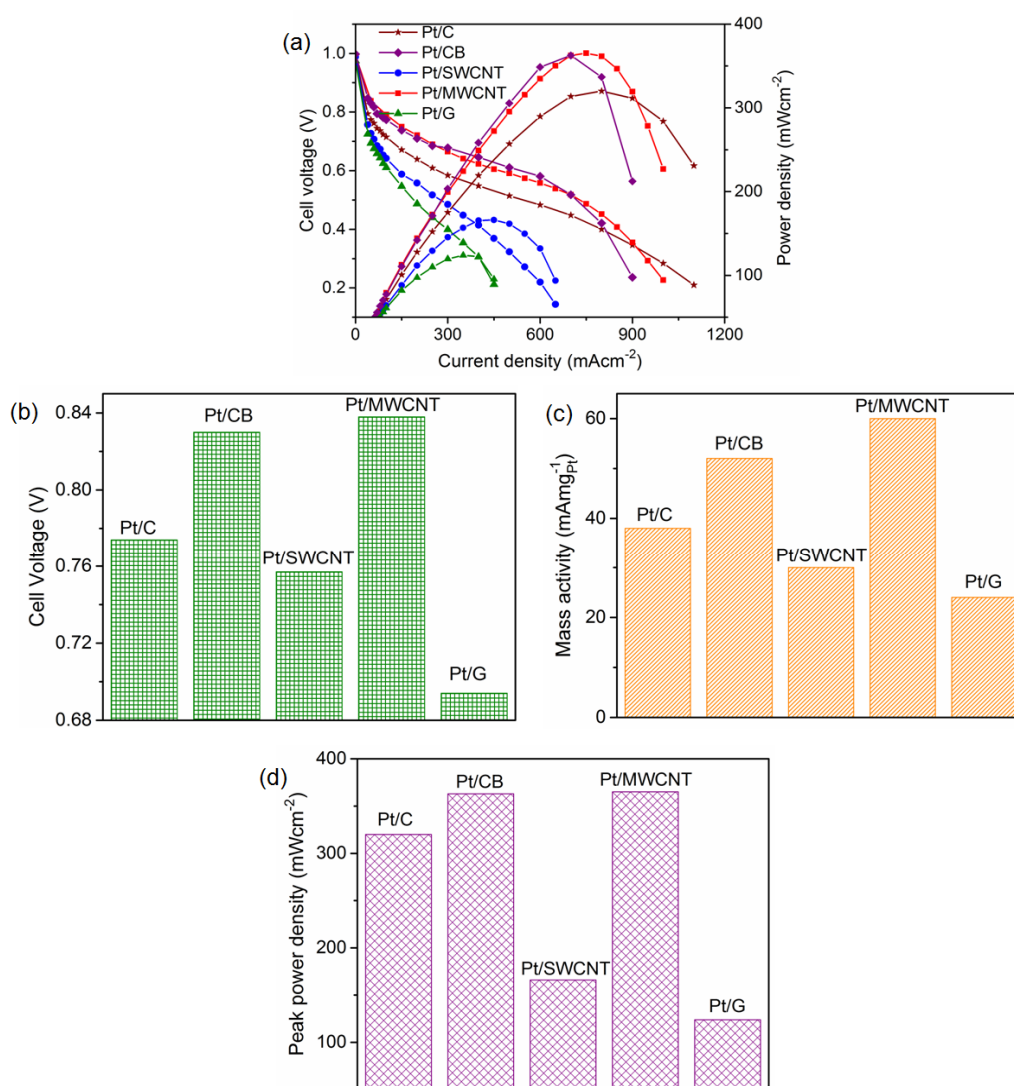
Fig. 6.9 (a) Polarization and power density curves, (b) cell voltage @ 50 mAcm^{-2}, (c) mass activity at E_{cell} = 0.9 V, and (c) power density bar plots of Pt/CB, Pt/SWCNT, Pt/MWCNT, and Pt/G catalysts

In order to quantify the Pt utilization, mass activity data of the cathodes determined at E_{cell} = 0.9 V are presented in Fig. 6.9 (c). Mass activity is related to catalyst property which defines catalytic activity. Hence, it is obligatory to represent mass activity in the activation region of fuel cell polarization curve where kinetics dominates and role of catalyst is well represented. Beyond kinetic controlled region (<0.8 V), ohmic and mass transport losses comes into picture where fuel cell performance is not just a function of catalyst. Therefore, mass activity at E_{cell} = 0.9 V, a potential at which reaction kinetics dominate is generally presented which is a direct representation of catalytic activity. From Fig. 6.9 (c), it can be seen that the mass activity of different carbon supported catalysts also follows the same order as of Pt utilization efficiency establishing once again that the differences in performances of the different catalysts can be attributed to the influence of carbon supports in the favourable formation of TPBs, which are the active catalytic sites where triple phase contact of reactant gas, catalyst and the membrane occurs to carry out the electrochemical reaction leading to more efficient use of metal particles. As discussed previously, with the most defective structure, highest Pt utilization efficiency and lowest R_c, MWCNT supported catalyst illustrates the formation of more TPBs than the other studied carbon supported catalysts. The mass activity of MWCNT supported catalyst is higher by a factor of 1.15, 2 and 2.5 with respect to CB, SWCNT and G supported catalysts, respectively. Also, the mass activity of Pt/MWCNT was higher by a factor of 1.58 than the commercial Pt/C catalyst. This enhancement in the mass activity can be attributed to better ORR activity due to stronger metal-support interactions in Pt/MWCNT than the commercial catalyst as shown by XPS results (Fig. 6.10). Moreover, Pt utilization expressed through peak power density (Fig. 6.9 (d)), achieves maximum for fuel cell with MWCNT supported catalyst operating as the cathode catalyst. The Pt/MWCNT catalyst gave Pt utilization amounting to 730 Wg^{-1}, when calculated with respect to the cathode Pt loading. In comparison to the commercial Pt/C catalyst, this presents a 35% higher Pt utilization. The above results demonstrate the superior performance of MWCNT supported Pt catalyst as an ORR catalyst for fuel cell. Furthermore, this study has shown that the carbon supports influence ORR activity of Pt catalyst and hence, overall fuel cell performance through

TPBs which are reflected in terms of effective Pt utilization. Table 6.3 summarizes the parameters obtained from single cell fuel cell testing polarization curves.
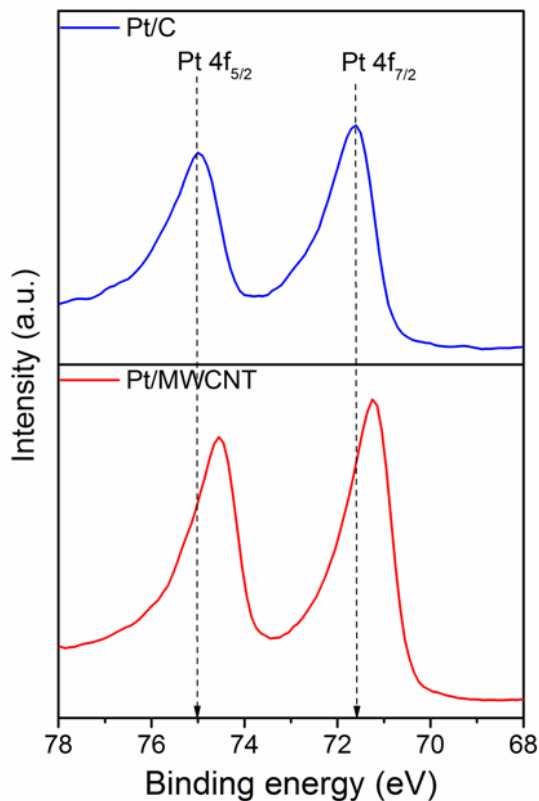
Fig. 6.10 XPS spectra: Pt 4f peaks of Pt/C-JM and Pt/MWCNT catalysts

Table 6.3 Parameters obtained from single cell fuel cell testing polarization curves of different carbon supported Pt catalysts

Catalyst	Voltage @ 50 mAcm^{-2}** (V*)	Mass activity @ 0.9 V* (mAmg$_{Pt}^{-1}$)	Peak Power Density (Wg$_{Pt}^{-1}$)
Pt/CB	0.830	52	726
Pt/SWCNT	0.757	30	332
Pt/MWCNT	0.838	60	730
Pt/G	0.694	24	248
Pt/C	0.722	28	540

* absolute cell voltages; **cm^2 values correspond to geometric active area of electrode

6.4. Conclusions

Pt catalysts supported on CB, SWCNT, MWCNT and G carbon supports were synthesized in order to study the influence of supports on the physico-chemical properties and performance as ORR catalyst in PEMFC. It was observed that different carbon supports did not much affect the Pt particle size during synthesis and Pt particle size was controlled by the synthesis method adopted. Additionally, different carbon supports have different amount of defective sites in the carbon framework which affect the availability of active metal nanocatalysts as well as influence metal-support interaction as evidenced by XPS and Raman results. The influence of different carbon supports on the activity and stability of ORR catalysts in working fuel cell condition was conclusively established through chrono-amperometric, CV and EIS studies. The decisive influence of the different carbon supports on PEMFC performances was proved through fuel cell polarization and power density curves. It was also concluded that the MWCNT supported Pt catalyst exhibited the highest mass activity, stability, Pt utilization efficiency and lower overpotential loss for the ORR among the investigated carbon supports. The high ORR activity along with good stability exhibited by Pt/MWCNT catalyst suggests that this system is an economically viable, potential candidate to be employed as a cathode catalyst in PEMFC. Additionally, Pt/MWCNT catalyst exhibited better fuel cell performance in terms of higher voltage, mass activity and peak power density than the commercial Pt/C catalyst establishing its capability as ORR catalyst in PEMFC.

Chapter 7

Pt-Pd/MWCNT catalyst: Prominent effects of surfactant assisted synthesis

Abstract

This study explored the performance of bi-metallic (Pt-Pd) catalysts supported on MWCNT (Pt-Pd/MWCNT). Pt-Pd/MWCNT catalysts were prepared through MW assisted, polyol route in presence of surfactants SDS (Pt-Pd/CNT-S) or CTAB (Pt-Pd/CNT-C) and their performances were compared with Pt-Pd/CNT prepared in an identical way without any surfactant. The influence of surfactant on synthesis as well as the physico-chemical and catalytic properties of the catalysts was discussed. The study showed that the presence of surfactant did not affect the Pt-Pd alloy NP composition or size during the synthesis; rather they affected the disaggregation of CNT support which in turn controlled the uniformity of Pt-Pd NPs dispersion onto the support. *In-situ* fuel cell investigation demonstrated that Pt-Pd/CNT-S catalyst favorably enhanced the cell performance; whereas CTAB aided Pt-Pd/CNT-C catalyst lowered the performance.
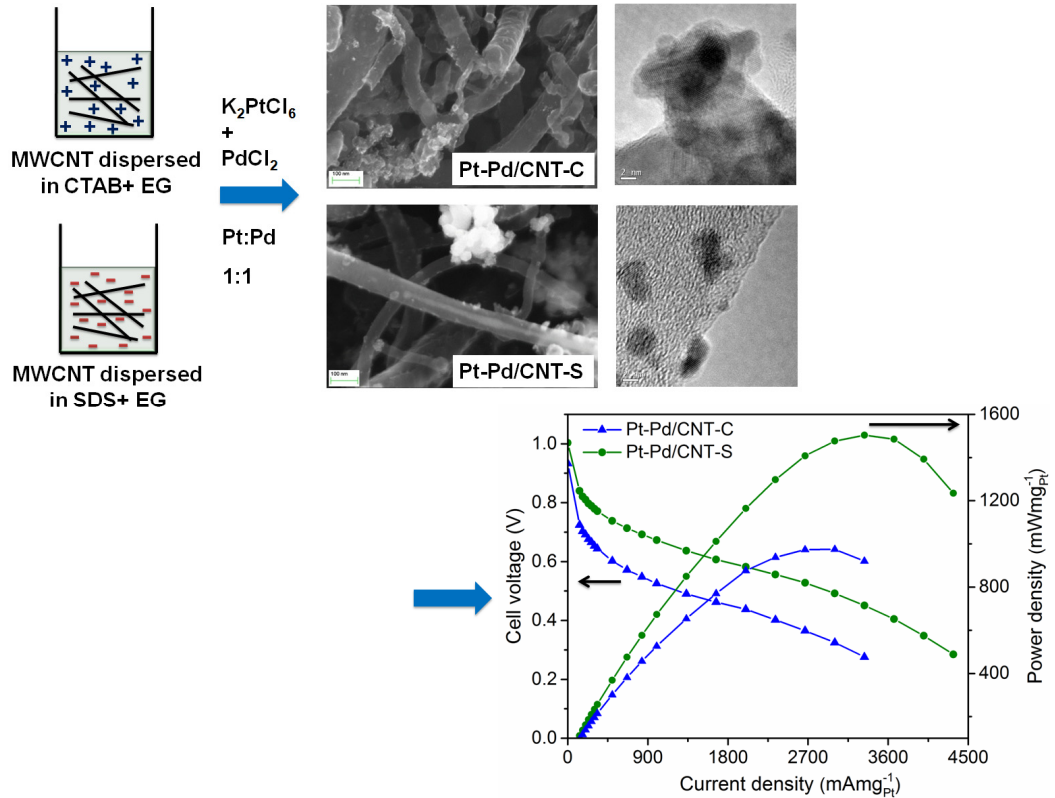
7.1. Introduction

The sluggish ORR kinetics occurring at the cathode necessitates a substantially higher Pt metal loading at the cathode compared to the anode, and contributes to increase in the cost of fuel cell [Debe 2012, Shao *et al.* 2016]. The useful strategies that can address these limitations are to increase the ORR activity as well as to alloy pure Pt with a second metallic element M (M= transition metal) [Jung *et al.* 2014, Wang *et al.* 2015, Lv *et al.* 2016, Chen *et al.* 2017]. Pd has attracted considerable attention as a highly suitable transition metal to alloy with Pt due to their similar face centered cubic structure, good miscibility and a negligible lattice mismatch (of only 0.77 %), which favor facile formation of bi-metallic Pt-Pd nanostructures [Cai *et al.* 2014, Chen *et al.* 2015, Zhang *et al.* 2016]. Besides, the cost of Pd is much lower compared to Pt (about one-third only).

It is essential to disperse the metal NPs on proper supports in order to enhance the catalytic activity and stability of Pt based bi-metallic catalysts [Zhang *et al.* 2014, Du *et al.* 2016]. MWCNT with excellent electronic conductivity, corrosion resistance and presence of inherent defective structures is a highly suitable carbonaceous support that can facilitate the nucleation, growth and dispersion of metal NPs for producing functional hybrid nanostructures which would not only maximize the availability of the active catalytic sites but also aid in mass transport of reactants to the active sites [Stamatin *et al.* 2015]. In a composite structure comprising of metal NPs on MWCNT, the useful retention of MWCNT properties is highly dependent on the disaggregation and uniform dispersion of MWCNTs which allows effective utilization of composite properties towards catalysis [Vaisman *et al.* 2006, Zhang *et al.* 2006, Li *et al.* 2014]. A major obstacle towards realization of such a highly desirable NP/MWCNT composite is the aggregation of MWCNTs into bundles because of the van der Waal's forces which resist proper dispersion of MWCNTs in most aqueous media [Duan *et al.* 2011]. Both covalent and non-covalent approaches are made use of for dispersing CNTs in the reaction media [Rausch *et al.* 2010, Bai *et al.* 2011]. In the covalent chemical approach, the

CNTs are functionalized by introducing polar groups that lead to better dispersibility in aqueous environments. However, this method can damage the structure of CNTs. Also, the increase in dispersibility occurs at the expense of mechanical and electrical properties [Rausch *et al.* 2010]. In the non-covalent method, physical adsorption of a suitable surfactant is used to overcome the van der Waal's interaction of CNTs and to improve their dispersibility. In this case, the chemical structure of the CNTs remains unchanged and the dispersed CNTs are stabilized by the electrostatic repulsion and/or steric hindrance of the micelles formed around them. The non-covalent approach is particularly attractive because of the possibility of adsorbing various groups onto CNT surface without affecting π system of the tube lattice and retention of the nanotube structure and property [Tasis *et al.* 2006]. Surfactants are generally used for the non-covalent modification of CNTs due to their easy availability, low cost and relatively simple experimental procedure [Wang 2009, Tkalya *et al.* 2012].

The aim of this work is to synthesize the composite, bi-metallic Pt-Pd catalyst supported on MWCNT, *via* surfactant assisted route and to study the influence of surfactants on physico-chemical properties and ORR activity of the catalyst. Two types of surfactants, the anionic SDS and cationic CTAB are used to disperse MWCNT in the aqueous phase. The dispersing ability of the surfactant in synthesizing the nano-composite (Pt-Pd/CNT) catalysts and their resultant physico-chemical and morphological characteristics are studied in comparison with that of the catalyst synthesized without any surfactant. Besides, ORR activities of the catalysts are investigated in detail in both half cell and working single cell PEMFC. To the best of our understanding, this is the first time reporting on the prominent role played by the nature of surfactant on the synthesis of MWCNT supported bi-metallic Pt-Pd catalyst and its ORR activity in PEMFC.

7.2. Experimental

7.2.1. Materials

The following raw materials were used for the synthesis of Pt-Pd catalysts on MWCNT support: K_2PtCl_6, $PdCl_2$, MWCNT (in-house product), SDS, CTAB, and EG. NaOH was used to maintain the required alkaline medium during synthesis and HCl was used as a sedimentation promoter. Ethanol, acetone and ultra-pure water were used as solvents. The materials used for electrode preparation for half cell and full cell studies, MEA fabrication and single cell PEMFC assembly remains the same as detailed under *Chapter 2, Section 2.1*, *Section 2.4.1* and *Section 2.4.2*.

7.2.2. Synthesis of Pt-Pd/CNT catalysts

Pt-Pd alloy catalysts (20 wt. % of Pt-Pd, Pt:Pd atomic ratio 1:1) supported on MWCNT were synthesized in the presence of surfactants (SDS or CTAB) by MW assisted, polyol reduction route using EG as the reducing agent, as detailed in *Chapter 2, Section 2.2.5.*

7.2.3. Materials Characterization

Characterization methods employed include FESEM, HRTEM, XRD, ICP-AES, HRTEM, BET specific surface area and XPS. The details of all these methods are given in *Chapter 2, Section 2.3.*

7.2.4. Half-cell studies

The half-cell test was conducted using RRDE set-up as detailed in *Chapter 2, Section 2.5.2*. For CV studies, the electrolyte (0.5 M H_2SO_4) was purged with pure N_2 in order to remove all the dissolved oxygen. In contrast, for LSV, the O_2 saturated electrolyte was used for ORR studies. Potentials of electrochemical studies done using different reference electrodes are presented with reference to RHE. The RRDE experiments of catalysts were performed by sweeping the potential between 0.2 and 1.1 V at the scan rate of 10 mVs^{-1} and the ring potential was held at 1.4 V vs. RHE.

7.2.5.   Full cell studies
7.2.5.1. Fabrication of MEA and assembly of single cell PEMFC

MEA for single cell fuel cell was prepared using Nafion® membrane and catalyst ink coated PTFE sintered carbon paper. The procedure for MEA fabrication and single cell assembly is detailed in *Chapter 2, Section 2.4.1.4* and *Section 2.4.1.5*, respectively. The metal (Pt) loading at the electrodes (anode and cathode) in MEA was 0.5 $mg_{Pt}cm^{-2}$.

7.2.5.2. Electrochemical evaluation

The electrochemical experiments were carried out on a single cell PEMFC at room temperature and atmospheric pressure unless otherwise defined and are detailed in *Chapter 2, Section 2.5.1*. CV experiments were performed by cycling the cathode at 20 mVs^{-1} between 0 to 1.2 V *vs*. SHE. The activity of the catalysts towards ORR was evaluated through CA measurements at polarization potential of E_{cell} = 0.80 V, 0.85 V and 0.90 V. At each potential, the fuel cell performance was evaluated for over a period of 3600 s. EIS measurements were performed by applying ac amplitude of 10 mV over the frequency range 10^{-1} to 10^{5} Hz at cell voltage, E_{cell} of 0.80 V, 0.85 V and 0.90 V. ZView software (Scribner Associates Inc.) was used to determine diameter of the semi-circle loop in Nyquist plot. All the electrochemical experiments except CV and EIS were performed with pure, O_2 and humidified H_2 gases fed at cathode and anode, respectively. For CV and EIS experiments, pure, N_2 and humidified H_2 gases were fed at cathode and anode, respectively. The polarization curves were recorded at 50 °C, 1 atm and with fixed flow rate of 1 NLPM of hydrogen and oxygen gases in a fuel cell test station (FuelCon Evaluator-S 70277). The anode side was fed with pure hydrogen humidified to 90% RH, and the cathode side was fed with pure oxygen humidified to 70% RH.

7.3. Results and discussion

7.3.1. Influence of surfactant on the physico-chemical properties of Pt-Pd catalysts

Surfactants are known to play a crucial role in influencing the orientation of the reactants in a reaction mixture and thus affect the kinetics of the overall reaction as well as the properties of the synthesized material. In this study, Pt-Pd/CNT catalysts were synthesized in the absence of surfactant as well as in the presence of CTAB and SDS surfactants. Fig. 7.1 depicts the XRD patterns obtained for Pt-Pd/CNT, Pt-Pd/CNT-C and Pt-Pd/CNT-S catalysts. The diffraction peaks of Pt-Pd/CNT catalysts at 2θ values of 40.1, 46.5, 68.0 and 81.9 are attributed to (111), (200), (220) and (311) planes of the fcc crystal structure of bi-metallic Pt-Pd, respectively (JCPDS No. 03-065-6418). The diffractions peaks at 2θ values of 26.3, 44.6 and 51.9 correspond to (002), (101) and (102) planes, respectively of graphitic carbon (JCPDS No. 00-001-0640). The presence of these peaks suggests that MWCNT support in the material has a predominant graphitic structure [Winjobi *et al.* 2010]. Similar fcc Pt-Pd and graphitic carbon peaks were observed for Pt-Pd/CNT-C and Pt-Pd/CNT-S catalysts also. This indicates that MWCNT structure is preserved during the synthesis of catalysts in the presence of surfactants also. Table 7.1 summarizes the lattice parameters, crystallite size and SSA of Pt-Pd based catalysts. The lattice parameter remained constant for all the three catalysts, the value (3.8925 Å) was between that of pure fcc Pt (3.9161 Å) and pure fcc Pd (3.8823 Å), reflecting incorporation of Pt and Pd atoms in fcc structure forming bi-metallic Pt-Pd system. Characteristic peaks of oxides of Pt or Pd were not detected in the XRD patterns; however, this observation cannot be taken as a conclusive evidence for their absence because they might be present in very small particle sizes undetectable in XRD or can be in amorphous form. The average Pt-Pd crystallite sizes in these catalysts were found to be similar irrespective of the surfactants used (values in Table 7.1) indicating no significant contribution of surfactant towards the size of Pt-Pd NPs formed.
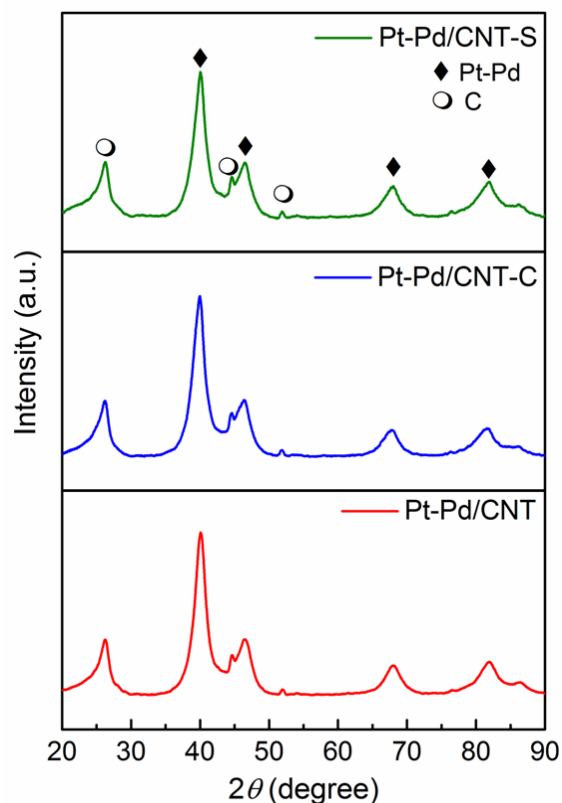
Fig. 7.1. XRD patterns of Pt-Pd based catalysts

Table 7.1. Lattice parameters, crystallite size and SSA of Pt-Pd based catalysts

	Pt-Pd/CNT	Pt-Pd/CNT-C	Pt-Pd/CNT-S
Lattice parameter, Å	3.8925	3.8925	3.8925
Pt-Pd crystallite size, nm	4.0	4.0	3.9
SSA, m^2g^{-1}	50.8	22.5	50.7

The influence of surfactant on surface morphology and dispersion of Pt-Pd/CNT based catalysts was studied through electron microscopy techniques. Fig. 7.2 shows the FESEM images, HRTEM images and the corresponding SAED patterns of the catalysts. The FESEM images [Fig. 7.2 (a1, b1, and c1)] clearly show the tubular nature of the CNT support indicating that the morphology of the support material is retained after Pt-Pd deposition in all the cases. FESEM images also reveal that the presence of surfactants significantly affected the dispersion/aggregation of CNTs during the synthesis of Pt-Pd NPs.

With CTAB surfactant, aggregated nanotubes were observed in Pt-Pd/CNT-C; whereas, well dispersed and de-bundled CNT network was observed with SDS surfactant in Pt-Pd/CNT-S almost comparable to that of Pt-Pd/CNT catalyst without any surfactant. Thus, SDS serves as a good disperser for CNT while CTAB adversely affects its dispersion leading to formation of aggregates which would result in lower catalyst surface area. BET SSA values of the Pt-Pd based catalysts are given in Table 7.1. Lower SSA was obtained with Pt-Pd/CNT-C catalyst (<50% of the other two catalysts) supporting the conclusion made from FESEM studies.

The HRTEM images [Fig. 7.2 (a2, b2, and c2)] clearly reveal the nature of dispersion of Pt-Pd NPs onto the CNT support. In the case of Pt-Pd/CNT-C, non-uniformly dispersed and agglomerated spherical Pt-Pd NPs were obtained; whereas, uniformly distributed spherical Pt-Pd NPs were obtained in the case of Pt-Pd/CNT-S as well as Pt-Pd/CNT. The corresponding SAED patterns [Fig. 7.2 (a3, b3, and c3)] reveal that the Pt-Pd catalysts exhibit features of the (111), (200), (220), and (311) planes of fcc microstructure and (002) plane of graphitic carbon from CNT support in concordance with XRD analyses detailed earlier. The lattice spacing of (111) planes from the corresponding SAED patterns of Pt-Pd/CNT, Pt-Pd/CNT-C and Pt-Pd/CNT-S is calculated to be the same and equals 0.221 nm approaching pure Pt spacing of 0.228 nm, compared to that for Pd, 0.240 nm [Guo *et al.* 2007]. This finding indicates that the synthesized Pt-Pd/CNT catalysts have Pt-Pd NPs with Pt rich shell structure [Lee *et al.* 2010]. The lattice spacing measurements from the FFT patterns of the corresponding high magnification HRTEM images of Pt-Pd catalysts as shown in Fig. 7.3 also revealed the formation of Pt rich shell structure in Pt-Pd NPs. From the HRTEM images, the diameters of the Pt-Pd NPs in the catalysts were assessed to be nearly the same, in the range 3.3 to 4.1 nm. The XRD and calculated diameter results indicated that the use of SDS or CTAB surfactant during the synthesis did not affect bi-metallic Pt-Pd composition or size of NPs; rather they influenced the aggregation of CNT supports which in turn decides the dispersion of Pt-Pd NPs onto the CNT support.
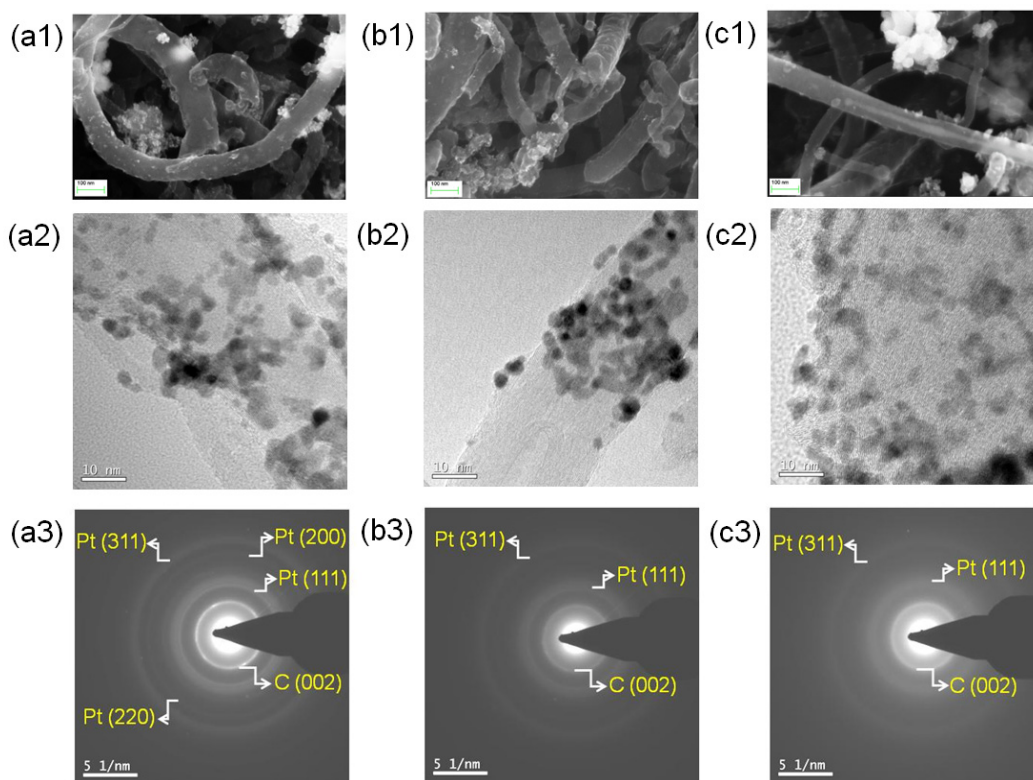
Fig. 7.2. FESEM images (a1, b1 and c1), HRTEM images (a2, b2 and c2), and the corresponding SAED patterns (a3, b3 and c3) of Pt-Pd/CNT, Pt-Pd/CNT-C and Pt-Pd/CNT-S catalysts
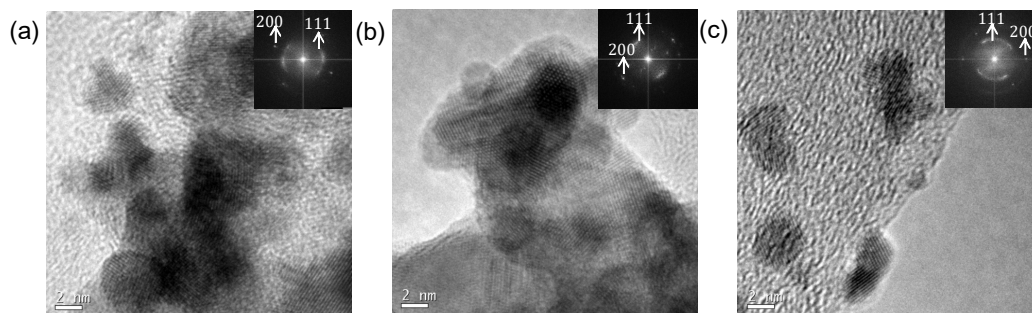
Fig. 7.3. High magnification HRTEM images of (a) Pt-Pd/CNT; (b) Pt-Pd/CNT-C and (c) Pt-Pd/CNT-S catalyst. Inset shows the corresponding FFT pattern

The composition and surface oxidation states of Pt-Pd NPs were analyzed by XPS measurements. Fig. 7.4 shows the corresponding XPS spectra of Pt 4f, Pd 3d, and C 1s, and Table 7.2 summarizes the results obtained from XPS and ICP-AES analyses. According to their elemental components, the atomic ratio of Pt to Pd is 1:1, which is concordant with the ICP-AES analysis.

190

The Pt and Pd wt.% from ICP-AES analysis corresponds to Pt:Pd atomic ratio of c.a. 1:1 in Pt-Pd/CNT, Pt-Pd/CNT-C and Pt-Pd/CNT-S catalysts, matching with the feed value, indicating complete reaction of Pt and Pd precursors to form bi-metallic Pt-Pd NPs.
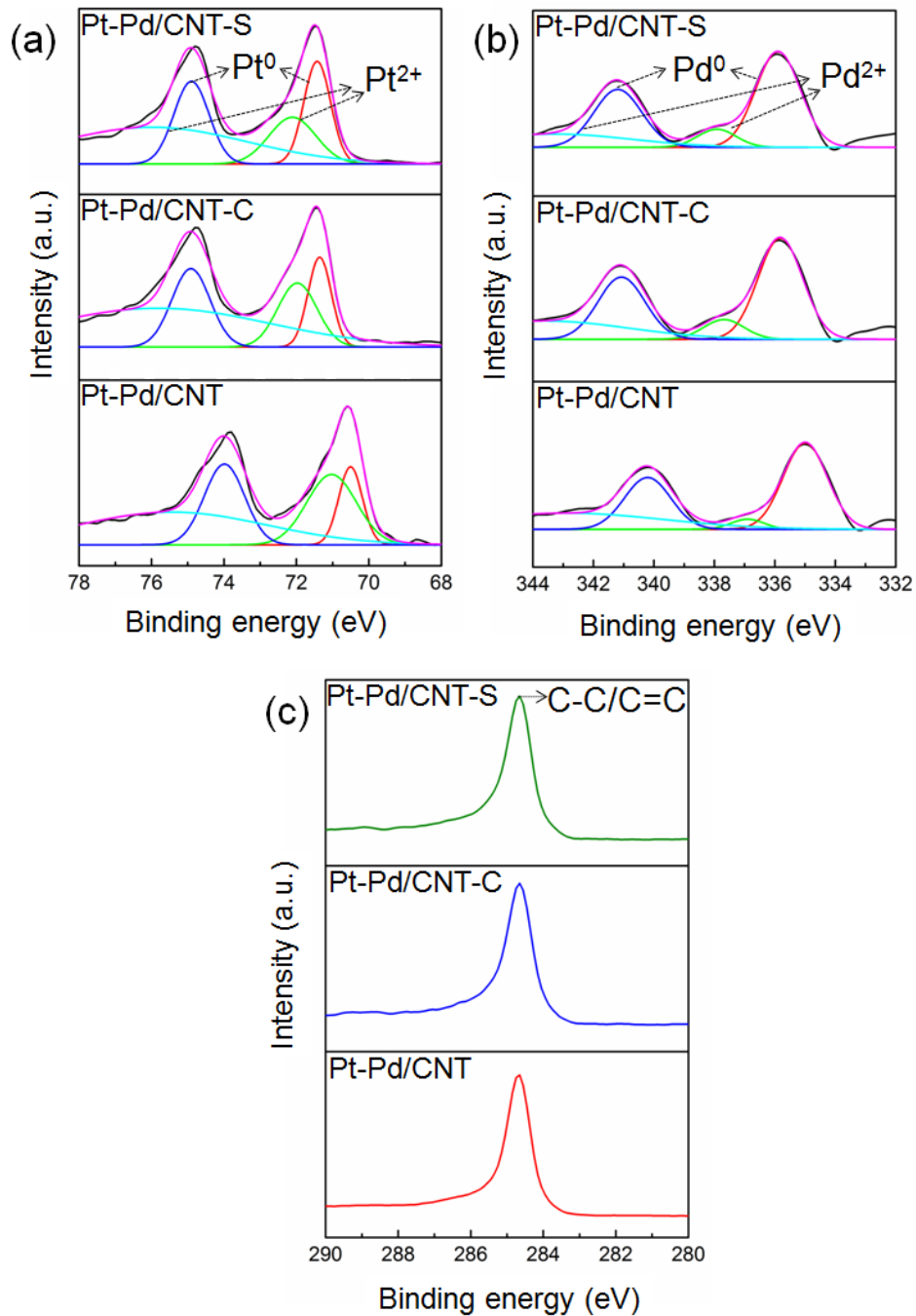
Fig. 7.4. XPS spectra (a) Pt 4f; (b) Pd 3d, and (c) C-1s of Pt-Pd based catalysts

Table 7.2. Summary of XPS and ICP-AES analyses

		Pt-Pd/CNT	Pt-Pd/CNT-C	Pt-Pd/CNT-S
Binding energy of species, eV (from XPS)	Pt^0	70.5	71.4	71.4
		74.0	74.9	74.9
	Pt^{2+}	71.0	72.0	72.1
		75.4	75.8	76.0
	Pd^0	335.0	335.8	335.9
		340.2	341.1	341.2
	Pd^{2+}	336.9	337.7	337.9
		342.9	343.6	343.3
	C-C/C=C	284.7	284.7	284.7
Metal wt. % (from ICP-AES)	Pt	12.2	12.2	12.4
	Pd	7.4	7.5	7.2

The Pt 4f and Pt 3d peaks consist of two pairs of doublets for Pt-Pd/CNT, as shown in Fig. 7.4 (a) and (b). The two main peaks at 70.5 eV (Pt $4f_{7/2}$) and 74.0 eV (Pt $4f_{5/2}$) correspond to metallic Pt (Pt^0); whereas, the other two peaks at 71.0 and 75.4 eV are attributed to Pt^{2+} in the form of platinum oxide such as $Pt(OH)_2$ and/or PtO [Li *et al.* 2014]. As to the spectrum of Pd 3d, two main peaks at 335.0 and 340.2 eV are assigned to Pd $3d_{5/2}$ and Pd $3d_{3/2}$ of metallic Pd (Pd^0), respectively; whereas, the other two minor peaks at 336.9 and 342.9 eV are attributed to Pd^{2+} in the form of PdO and/or PdO_2 species [Duan *et al.* 2015]. The presence of Pt^{2+} and Pd^{2+} can be ascribed to incomplete reduction of Pt and Pd precursors during MW heating as well as the easy oxidation of Pt and Pd NPs formed at the surface to their oxides under ambient conditions [Hsieh *et al.* 2011, Li *et al.* 2014]. Pt 4f and Pd 3d peaks obtained for Pt-Pd/CNT-C and Pt-Pd/CNT-S catalysts are similar.

It is noticed that the binding energies of Pt 4f in all the catalysts are negatively shifted as compared to that of pure Pt NPs [Venezia *et al.* 1992] suggesting modification of Pt electronic properties due to comprehensive strain

and electronic coupling between Pt and Pd [Nilekar *et al.* 2007, Khan *et al.* 2015]. The shift to lower binding energy means downshift of d-band center, which leads to weaker interactions between the adsorbate (oxygen) and the substrate (catalyst) resulting in lower activation energy barrier which is conducive for better ORR activities [Zheng *et al.* 2014]. C 1s spectra of all the Pt-Pd catalysts [Fig. 7.4 (c)] show a single main peak at 284.7 eV attributed to alkyl C and sp^2 bonded carbon network (C-C/C=C) indicating predominance of sp^2 hybridized graphitic structure in CNT support, in agreement with XRD results. It is noteworthy that Pt 4f and Pd 3d peaks of Pt-Pd/CNT-C and Pt-Pd/CNT-S are positively shifted as compared to Pt-Pd/CNT catalyst reflecting stronger interactions between Pt and Pd in these catalysts [Cui *et al.* 2011]. This positive shift in binding energies can be ascribed to the effect of surfactants. Significant electrostatic interactions are prevalent in surfactant aided systems (Pt-Pd/CNT-C and Pt-Pd/CNT-C), presenting a larger driving force for the deposition of charged ionic Pt and Pd species onto CNT leading to better interaction between Pt and Pd as compared to Pt-Pd/CNT without any surfactant.

7.3.2. Proposed mechanism for the formation of Pt-Pd NPs on CNT *via* SDS and CTAB assisted synthesis

Based on the earlier discussion on the influence of surfactants on physico-chemical, structural and morphological properties of the Pt-Pd based catalysts, the possible formation mechanism of Pt-Pd/CNT-C and Pt-Pd/CNT-S catalysts in the presence of CTAB and SDS surfactants, respectively, is proposed as given in Fig. 7.5. Since the concentration of CTAB and SDS employed here (350 mM) are above their critical micelle concentration of 90 mM and 80 mM, respectively [Rausch *et al.* 2010], the adsorption of surfactant molecules or micelles onto CNTs are expected to occur which can result in good dispersibility of CNTs. This was true in the case of SDS assisted route which favorably disaggregates CNT bundles and forms uniform dispersion of Pt-Pd NPs on them. On the contrary, in CTAB assisted route, aggregated CNTs

are formed resulting in less-uniformly dispersed and more agglomerated Pt-Pd NPs.
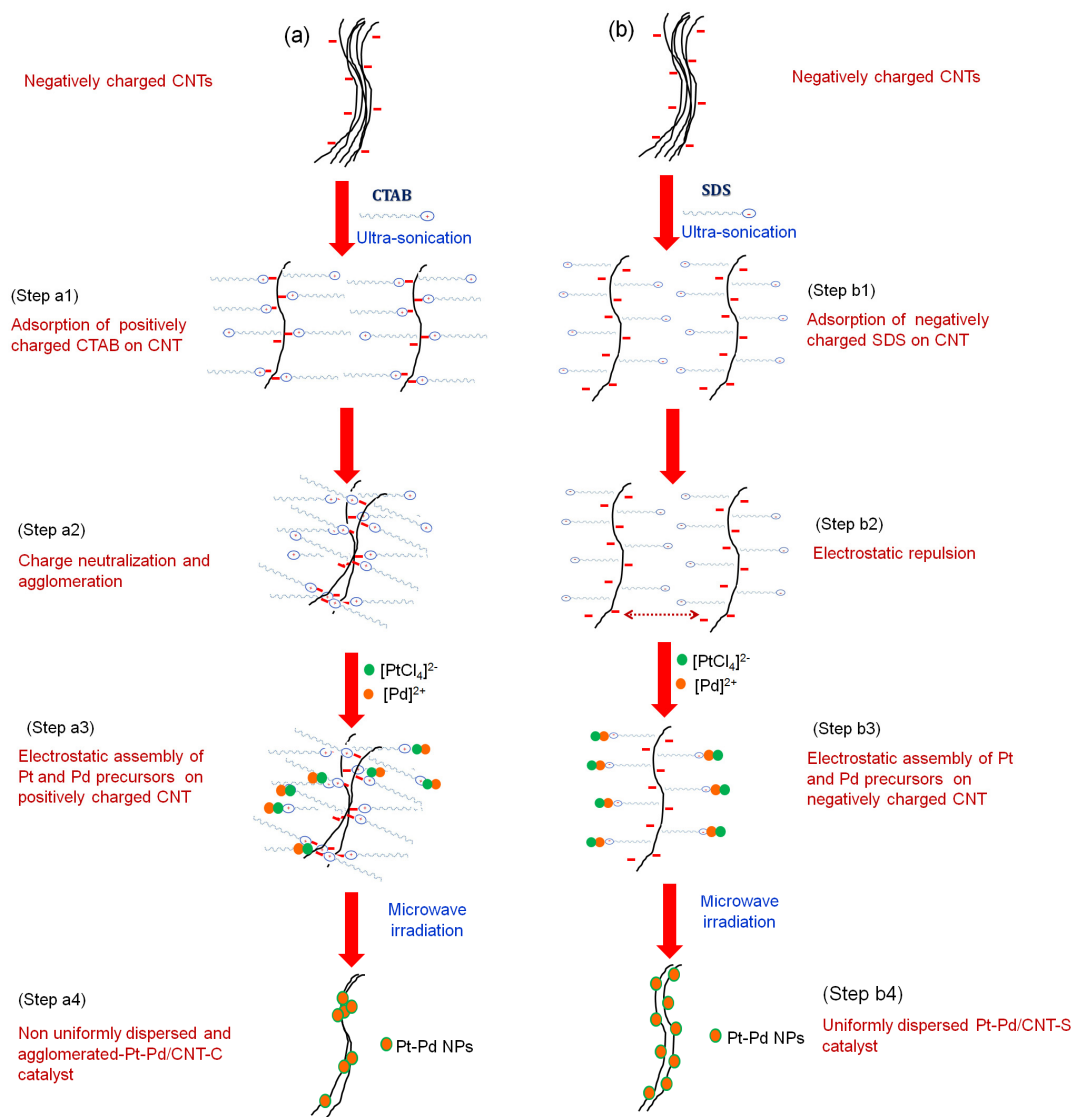
Fig. 7.5. Schematic showing possible reaction mechanism for formation of (a) Pt-Pd/CNT-C with CTAB surfactant, and (b) Pt-Pd/CNT-S with SDS surfactant

The changes observed in dispersion behavior of CNT with CTAB and SDS can be explained as follows: initial ultrasonication provides a high local shear to the CNT bundles separating them and allowing the adsorption of CTAB and SDS surfactant molecules on them (Step a1 and b1). As the individual CNTs move relative to the bundle through Brownian motion, the surfactant continues to get adsorbed along the length of CNT until a complete

separation occurs. However, in the case of CTAB (cationic surfactant) assisted route, when the positively charged CTAB micelle makes contact with negatively charged CNTs, ''charge neutralization'' and ''bridging flocculation'' [Myers 1990] occur which result in aggregation of individual CNTs (Step a2) which is also evidenced from FESEM image [Fig. 7.2 (b1)] and lower BET SSA (Table 7.1). These aggregated CNTs with weak positive charges lead to the electrostatic interaction driven self assembly of the negatively charged $[PtCl_4]^{2-}$ precursors followed by the assembly of positively charged Pd^{2+} precursors on the CTAB micelle's surface (Step a3). Subsequently, MW assisted polyol reduction results in the formation of non-uniformly dispersed and agglomerated Pt-Pd NPs (Step a4) as observed from HRTEM image [Fig. 7.2 (b2)]. On the other hand, in the presence of anionic surfactant SDS, the hydrophobic chain of the surfactant interacts with the sidewall of the nanotubes through hydrophobic interaction and thereby anchor the surfactant molecules onto the CNTs, leaving the hydrophilic head groups protruding into the solution (Step b1) [Duan *et al.* 2011]. The hydrophilicity of the head groups and their mutual electrostatic repulsion result in dis-aggregation of CNT bundles (Step b2) as evidenced from FESEM images [Fig. 7.2 (c1)] with higher SSA than Pt-Pd/CNT-C (Table 7.1). More importantly, the adsorption of the surfactant onto the CNTs leads to distribution of electronic charges at the tube surface making electrostatic assembly of Pd^{2+} and $[PtCl_4]^{2-}$ precursors (Step b3) very facile and the subsequent MW irradiation results in uniformly dispersed Pt-Pd NPs (Step b4) as evidenced from HRTEM image [Fig. 7.2 (c2)]. The prevalence of these electrostatic interactions in surfactant aided systems (Pt-Pd/CNT-C and Pt-Pd/CNT-S) makes assimilation of Pt and Pd onto CNT surface more facile presenting a highly favorable situation for synergistic interactions between the two metals as compared to surfactant-free system (Pt-Pd/CNT). This is reflected in terms of the positively shifted Pt 4f binding energies of Pt-Pd/CNT-C and Pt-Pd/CNT-S as compared to Pt-Pd/CNT (XPS results, Table 7.2).

It is to be noted that, in the present system with Pd^{2+} and $[PtCl_4]^{2-}$ precursors, standard reduction potential (E^0) is higher for Pd^{2+} ions (E^0 [Pd^{2+}] =

0.83 V *vs*. SHE) than that of Pt^{2+} ions (E^0 $[PtCl_4]^{2-}$ = 0.73 V *vs*. SHE). Therefore, the reduction of Pd^{2+} ions preferentially occurs first to form Pd metal seeds on the CNT substrate and serve as *in-situ* seeds for subsequent deposition of Pt resulting in Pt-Pd bimetallic NPs with Pt rich surface and Pd rich core. This corroborates with the lattice spacing measurements from the corresponding SAED and FFT patterns of Pt-Pd catalysts [Fig. 7.2 (b3 and c3); Fig. 7.3].

7.3.3. Catalytic activity of Pt-Pd/CNT based catalysts towards ORR
7.3.3.1. Electrochemical evaluation in half cell

The electrochemical properties of the synthesized catalysts were first studied using CV experiments. Fig. 7.6 shows the comparative CV curves which exhibited well-defined characteristic peaks for hydrogen desorption and adsorption, metal oxide formation and reduction. Generally, the columbic charge for hydrogen adsorption-desorption is used for calculation of ESA of Pt based catalyst [Lim *et al.* 2009]. With Pd based systems, such estimation is not feasible because of Pd-hydrogen complex formation [Lee *et al.* 2010]. Nonetheless, in this study, all the synthesized Pt-Pd catalysts showed Pt rich shell surface as supported by SAED and FFT analyses (Fig. 7.2 and Fig. 7.3). Additionally, to confirm the presence of Pt rich surface, the CV curves of the synthesized catalysts were also compared with Pt/CNT catalysts synthesized using the same procedure. Similar shape for CV curves (Fig. 7.6) in hydrogen reaction region was obtained for all the catalysts and Pt/CNT indicates that the surface of Pt-Pd NPs is rich in Pt atoms. Hence, the CV characteristics of Pt-Pd catalysts can be plausibly attributed to their active, Pt rich surface. The ESA was calculated by measuring the charge collected in the hydrogen desorption region after applying double-layer correction and assuming a value of 210 $mCcm^{-2}$ for the adsorption of a hydrogen monolayer. Based on mass of Pt in the catalyst, ESA of Pt-Pd/CNT-S (161 $m^2g_{Pt}^{-1}$) is determined to be higher than that of Pt-Pd/CNT (129 $m^2g_{Pt}^{-1}$) and Pt-Pd/CNT-C (44 $m^2g_{Pt}^{-1}$); which is a direct consequence of the better dispersion of metal NPs on CNT with SDS surfactant and agglomeration in case of Pt-Pd/CNT-C with CTAB surfactant.

Better dispersion of metal NPs induces more active areas for hydrogen adsorption-desorption reaction increasing the ESA. It implies that there are more active sites available for catalysis with Pt-Pd/CNT-S compared to the other two.
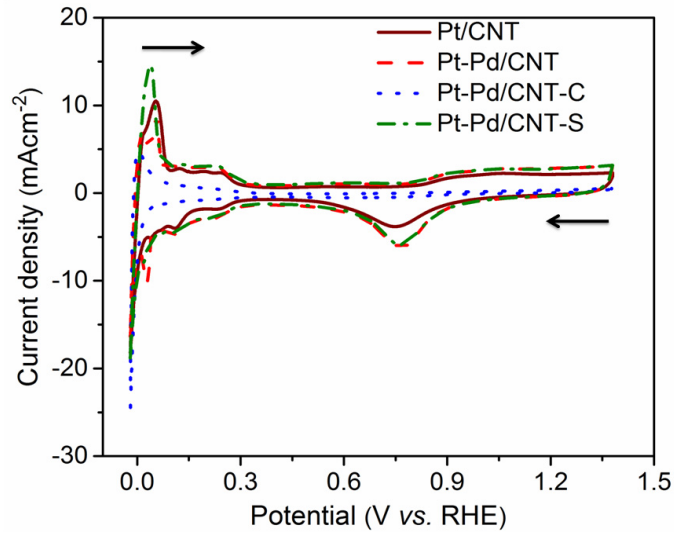
Fig. 7.6. CV curves of Pt-Pd based catalysts in nitrogen purged 0.5 M H_2SO_4 at scan rate of 50 mVs^{-1}

To determine the ORR kinetics of the Pt-Pd based catalysts, RRDE was used to obtain the polarization curves at a scan rate of 10 mVs^{-1} in oxygen saturated 0.5 M H_2SO_4. The rotating speed of the RRDE electrode was set to 1600 rpm. Fig. 7.7 shows RRDE linear sweep voltammograms for the O_2 reduction catalyzed by Pt-Pd based catalysts and the derived electrochemical parameters are summarized in Table 7.3. The ORR polarization curves depict kinetics controlled region ranging between 0.95-0.85 V, the mixed kinetics-diffusion controlled region between 0.85- 0.50 V, and the diffusion-limited current region below 0.5 V. As the net disk kinetic current (j_k) is directly proportional to the ORR activity, the j_k values per unit area at 0.9 V allow a comparison of the oxygen reduction activity of the catalysts. Accordingly, the j_k at 0.9 V was obtained as per the Koutecky-Levich equation. This equation is valid for a first order process with respect to the diffusion species, and is expressed by *eqn. 7.1* [Tamizhmani *et al.* 1996, Moreira *et al.* 2004, Thanasilp *et al.* 2011]:

$$j_k = \frac{j_l \times j}{j_l - j} \quad \text{...(eqn. 7.1)}$$

where j_l is the limiting current and j is the experimental current at 0.9 V. The j_k values of the catalysts are listed in Table 7.3. Pt-Pd/CNT-S catalysts demonstrated better ORR activity both in terms of onset potential and j_k. The ORR onset potential (at -0.1 mAcm^{-2}) for Pt-Pd/CNT-S shifts to more positive value (1.14 V) with higher j_k of 0.55 mAcm^{-2} as compared to Pt-Pd/CNT (1.06 V, 0.38 mAcm^{-2}) and Pt-Pd/CNT-C (1.03 V, 0.31 mAcm^{-2}). The higher activity of Pt-Pd/CNT-S catalyst is ascribed to the formation of smaller and well dispersed Pt-Pd metal-particles on CNT support through SDS assisted route, which results in the higher active surface area of the catalysts. This result is consistent with the CV results above.

Using the RRDE results shown in Fig. 7.7, the electron-transfer number (n_e) was calculated using the following equation [Lee *et al.* 2013]:

$$n_e = 4 - \left(\frac{2i_r}{i_d \times N} \right) \quad \text{...................................(eqn. 7.2)}$$

where i_r is the ring current, i_d is the disk current, and N is the collection efficiency. N of the ring was determined by performing RRDE measurements in $[Fe(CN)_6]^{4-/3-}$ redox medium and was found to be 0.312 [Anandha Ganesh *et al.* 2017]. The number of electrons transferred (Table 7.3) during ORR process for all the Pt-Pd based catalysts was very close to 4 indicating that all the catalysts undergo ORR efficiently through 4 e$^-$ process resulting in water as the major product. Consequently, the % of H$_2$O produced during oxygen reduction process can be estimated using the following equation [Lee *et al.* 2013]:

$$\%H_2O = \frac{N\left(\frac{i_d}{i_r}\right) - 1}{N\left(\frac{i_d}{i_r}\right) + 1} \quad \text{...................................(eqn. 7.3)}$$

The % H_2O values for Pt-Pd/CNT, Pt-Pd/CNT-C and Pt-Pd/CNT-S catalysts were 97.5%, 96.4% and 95.9% (Table 7.3), respectively, confirming the progress of ORR on all the catalysts through 4 e[-] pathway forming H_2O as follows:

$$O_2 + 4H^+ + 4e^- \rightarrow H_2O \quad \dots\dots\dots\dots\dots\dots\dots\dots\dots(eqn.\ 7.4)$$
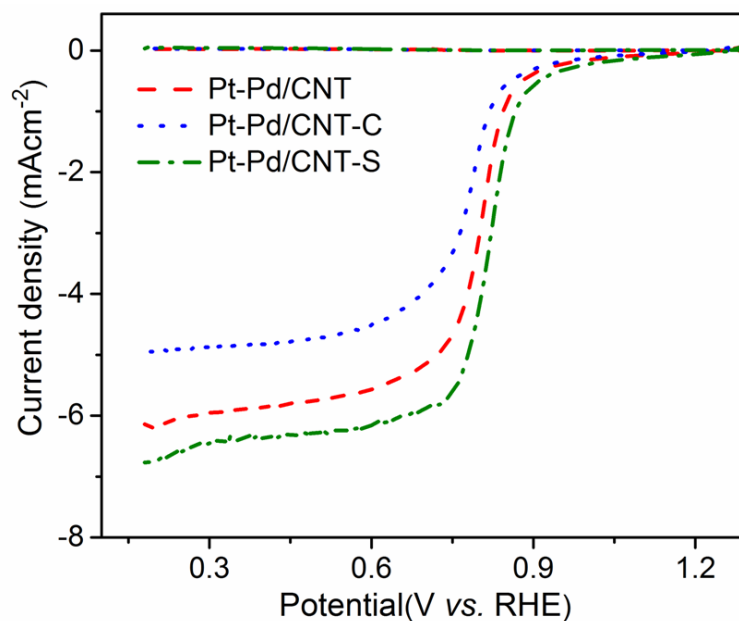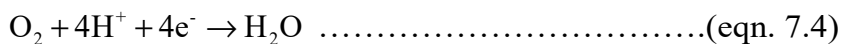
Fig. 7.7. LSV curves obtained using RRDE measurements for Pt-Pd catalysts in an O_2 saturated 0.5 M H_2SO_4 electrolyte. Scan rate of 10 mVs[-1] and electrode rotating speed of 1600 rpm

Table 7.3. Electrochemical parameters derived from half cell studies

	Pt-Pd/CNT	Pt-Pd/CNT-C	Pt-Pd/CNT-S
ESA[a], $m^2g_{Pt}^{-1}$	161	129	44
E_{onset}[b], V vs. RHE	1.06	1.03	1.14
j_k[b], mAcm[-2]	0.38	0.31	0.55
n_e[b]	3.97	3.96	3.96
%H_2O[b]	97.5	96.4	95.9

[a]From CV; [b]From RRDE

7.3.3.2. Electrochemical evaluation in full cell

The half cell studies demonstrated Pt-Pd based catalysts as promising candidates for ORR in PEMFC. All the catalysts proceeded through 4e⁻ oxygen reduction process producing water exhibiting their capability for application as cathode catalyst in PEMFC. Among all the studied catalyst systems, SDS assisted Pt-Pd/CNT-S catalyst showed the best ORR activity. All the Pt-Pd based catalysts were also evaluated *in-situ* in a working single cell fuel cell to validate the half cell studies and demonstrate the applicability of catalysts for PEMFC applications.

7.3.3.2.1. CV, EIS and CA studies

CV measurements were also conducted in full cell mode to investigate the possible electrochemical reactions and activity of the synthesized catalysts. Fig. 7.8 shows the CV curves which exhibited three characteristic electrochemical regions typical of a Pt active surface catalyst [Pozio *et al.* 2002]. These are: (i) adsorption–desorption region of hydrogen (0.0 to 0.3 V), (ii) double layer formation region (0.3–0.6 V), and (iii) metal-oxide formation and reduction region (0.6–1.2 V). Similar to the calculation in half cell studies as discussed in Section 7.3.3.1, ESA was found out to be 110 $m^2g_{Pt}^{-1}$, 83 $m^2g_{Pt}^{-1}$ and 29 $m^2g_{Pt}^{-1}$ for Pt-Pd/CNT-S, Pt-Pd/CNT and Pt-Pd/CNT-C, respectively. It is to be noted that the ESA obtained with catalysts in half cell mode is higher than that obtained in full cell mode. The higher ESA in half cell mode is attributed to the testing under flooded conditions where more sites are accessible for electrochemical reactions unlike in full cell where the electrochemical reactions are restricted to electrode-electrolyte interface. The ranking of catalysts based on ESA (Pd/CNT-S> Pt-Pd/CNT> Pt-Pd/CNT-C) follows the same order as with CV in half cell studies confirming the influence of surfactants on dispersion of metal NPs onto support which is reflected in ESA values.

The catalytic activity of Pt-Pd based catalysts towards ORR was evaluated through CA measurements in the activation controlled potential region (0.80 - 0.90 V) where reaction kinetics dominate and hence, gives true

demonstration of ORR activity. Fig. 7.9 shows the corresponding current density *vs.* time curves of the catalysts. At all the studied polarization potentials (0.80, 0.85 and 0.90 V), reduction current follows the order: Pt-Pd/CNT-C< Pt-Pd/CNT< Pt-Pd/CNT-S throughout the measurements, [Fig. 7.9 (a)-(c)]. This order matches with the availability of active sites in these catalysts and is in line with CV results.
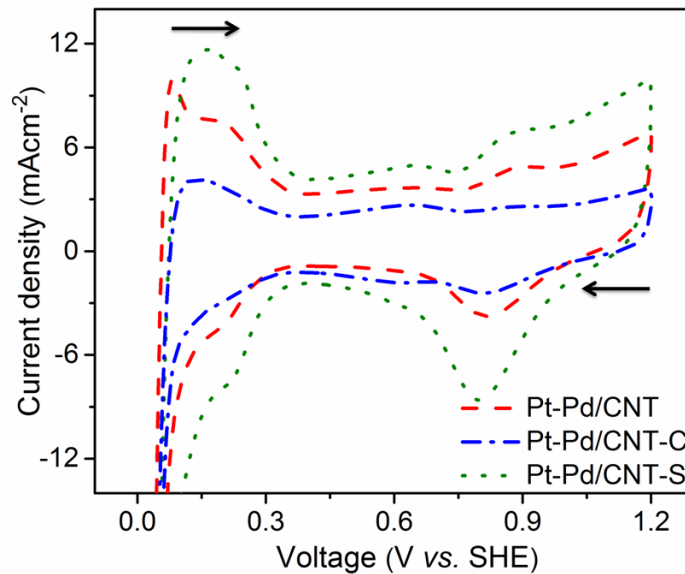
Fig. 7.8. CV curves of Pt-Pd based catalysts at scan rate of 20 mVs^{-1} in single cell PEMFC with pure N_2 and humidified H_2 gas fed at cathode and anode compartments, respectively

After a long period of operation (i.e., 3600 s), Pt-Pd/CNT-S performed significantly better with a much higher current density compared to other catalysts; thus demonstrating higher activity and stability of Pt-Pd/CNT-S catalyst [Fig. 7.9 (d)]. It is also observed that the reduction current density increases with decrease in polarization potential, which follows the general trend and is due to the increase in electrochemical kinetics of ORR with potential losses in the activation controlled region as per the Tafel equation [O'Hayre *et al.* 2016].
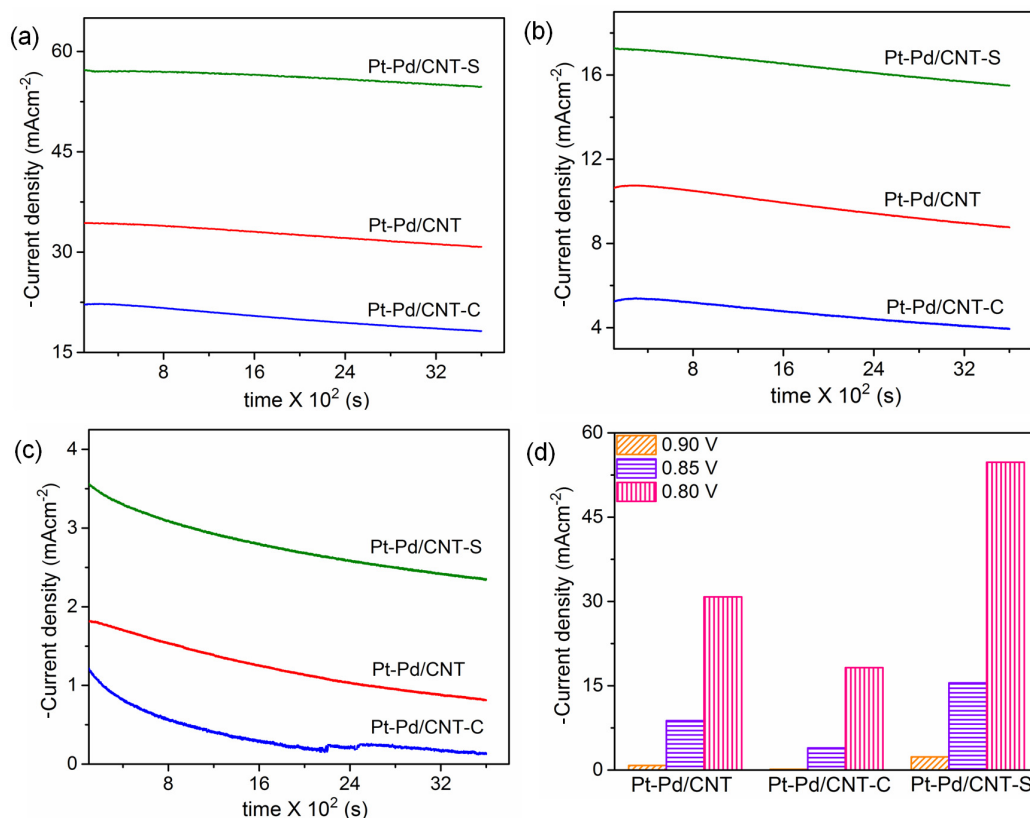
Fig. 7.9. Current density *vs*. time plots of Pt-Pd based catalysts at (a) 0.80 V; (b) 0.85 V; and (c) 0.90 V; and (d) comparison of reduction current densities of the catalysts after 3600 s in single cell PEMFC

EIS analysis was further used to understand the electrochemical behavior of the Pt-Pd based catalysts towards ORR. EIS measurements were also carried out in the activation potential controlled region (0.8 V- 0.9 V) to have a better understanding of ORR kinetics and the results are presented in Fig. 7.10. The Nyquist plots for all the catalysts in the studied potential regime show a single semi-circle arc indicating dominance of interfacial oxygen kinetics of the ORR at the cathode of fuel cell. The impedance spectra here basically consist of two parts: (i) the intersection in the real axis in the high-frequency region, and (ii) a single depressed semicircle. The high frequency intercept is attributed to total ohmic resistance, R_s of single cell; whereas, the diameter of the semi-circle is ascribed to the charge transfer resistance, R_c of cathode oxygen reduction [Tang *et al.* 2011].
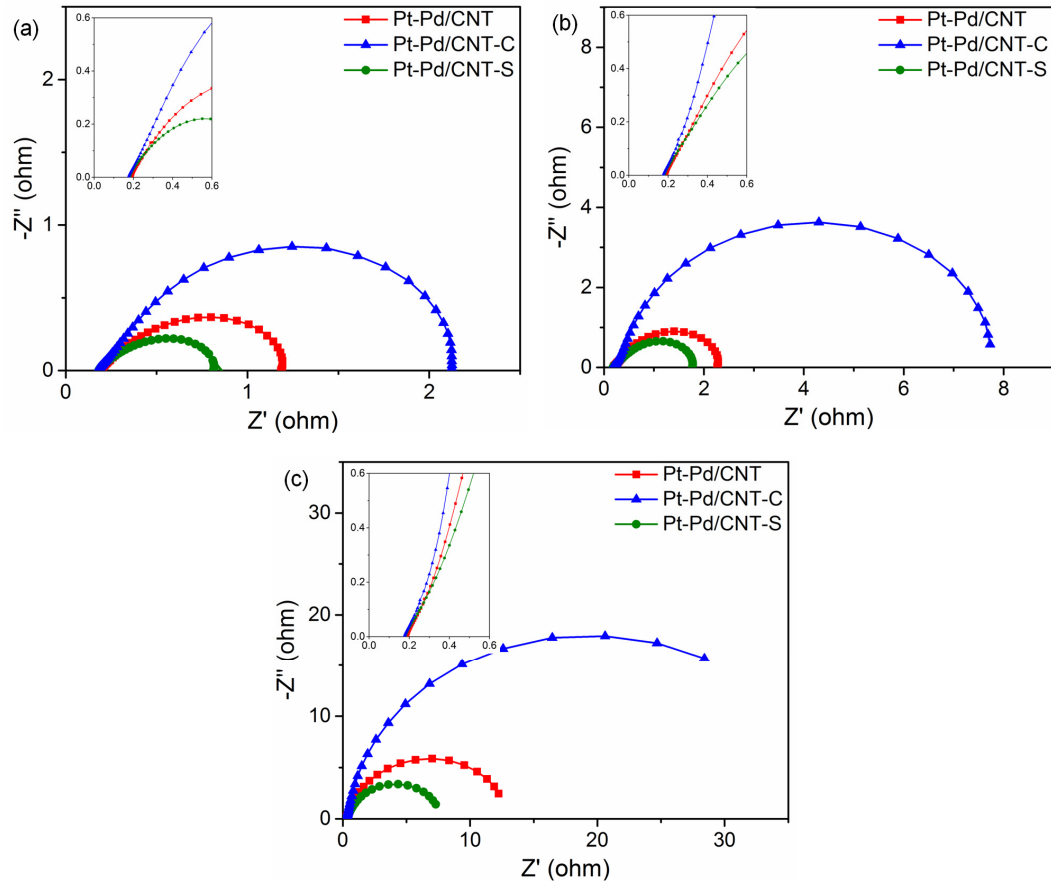
Fig. 7.10. Nyquist plots of Pt-Pd based catalysts at E_{cell} of (a) 0.80 V; (b) 0.85 V, and (c) 0.90 V in single cell PEMFC. Insets in figures show zoomed-in view of high frequency region

It can be seen from Fig. 7.10 that R_s of the cells did not change much with the catalysts suggesting insignificant effect of catalysts on total ohmic resistance of the fuel cell. However, R_c changes significantly for the different Pt-Pd based catalysts. R_c is an important parameter, since it can give a direct correlation with the ORR activity; a lower value denotes higher catalytic activity. R_c, estimated from diameter of semi-circle follows the decreasing order: Pt-Pd/CNT-C > Pt-Pd/CNT > Pt-Pd/CNT-S indicating the increasing order of catalytic activity for ORR in line with CV and CA results. It was also observed that R_s values do not change much with decrease in cell potential from 0.9 V to 0.8 V, while R_c decreases (or the interfacial oxygen kinetics increases) with decrease in potential. The lowering of potential in the activation region increases the current density which enhances the electrochemical kinetics of

ORR leading to smaller charge transfer resistance for oxygen reduction [Xie *et al.* 2004]. Based on the electrochemical results, it can be inferred that Pt-Pd/CNT-S catalyst prepared through SDS route favorably enhances the ORR catalytic activity due to effective disaggregation of CNTs followed by uniform dispersion of Pt-Pd NPs which results in higher ESA, reduction current density and lower R_c. On the contrary, Pt-Pd/CNT-C catalyst prepared through CTAB route results in inferior ORR catalytic performance due to agglomeration of metal NPs on the aggregated CNTs, culminating in lower ESA, reduction in current density and higher R_c. Table 7.4 summarizes the electrochemical results obtained for the three catalysts through *in-situ* investigations in single cell PEMFC.

Table 7.4. Electrochemical parameters of Pt-Pd based catalysts obtained from single cell PEMFC *in-situ* evaluation

		Pt-Pd/CNT	Pt-Pd/CNT-C	Pt-Pd/CNT-S
ESA^x, $m^2mg_{Pt}^{-1}$		83	29	110
j^y, $mAcm^{-2**}$	$0.90\ V^*$	0.81	0.13	2.34
	$0.85\ V^*$	8.77	3.93	15.5
	$0.80\ V^*$	30.79	18.21	54.75
R_s^z, Ω	$0.90\ V^*$	0.19	0.18	0.18
	$0.85\ V^*$	0.19	0.18	0.17
	$0.80\ V^*$	0.19	0.17	0.18
R_c^z, Ω	$0.90\ V^*$	12.7	38.4	7.5
	$0.85\ V^*$	2.1	7.6	1.6
	$0.80\ V^*$	1.1	1.9	0.6

[x]from CV; [y]from chronoamperometric plot; [z]from EIS spectra; [*]absolute cell voltages; [**]cm^2 values correspond to geometric active area of electrode

7.3.3.2.2. *Evaluation of performance of Pt-Pd catalysts through single cell PEMFC polarization curves*

Polarization curve is the most important and ultimate characteristic of a fuel cell which demonstrate the ORR activity of cathode catalyst in terms of unit cell performance. The synthesized Pt-Pd catalysts were evaluated as

cathode catalysts in single PEMFC. For comparison, the polarization curve using commercial Pt/C catalyst at cathode was also generated under identical conditions. The polarization and power density curves of each single cell with the Pt-Pd based catalysts along with commercial Pt/C catalyst are shown in Fig. 7.11 and the corresponding results are presented in Table 7.5.
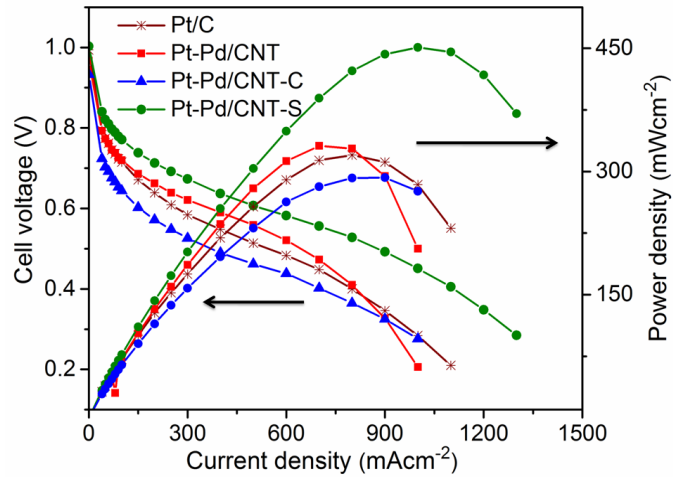
Fig. 7.11. Polarization and power density curves of Pt-Pd based and Pt/C catalysts at cell temperature of 50 °C and atmospheric pressure

Table 7.5. Parameters obtained from single cell PEMFC polarization and power density curves of Pt-Pd based catalysts

	Pt/C	Pt-Pd/CNT	Pt-Pd/CNT-C	Pt-Pd/CNT-S
OCV, V*	0.994	0.967	0.933	1.003
Cell voltage @ 50 mAcm^{-2**}, V*	0.774	0.773	0.702	0.821
Cell voltage @ 300 mAcm^{-2**}, V*	0.584	0.621	0.526	0.673
Cell voltage @ 600 mAcm^{-2**}, V*	0.483	0.521	0.438	0.582
Mass activity, mAmg$_{Pt}^{-1}$	38	84	21	51
Maximum power density, mAmg$_{Pt}^{-1}$	640	1104	975	1503

*absolute cell voltages; **cm^2 values correspond to geometric active area of electrode

The polarization curve is dominated by the activation overpotential region (~1 to 100 mAcm^{-2}), the ohmic overpotential region (~100 to 500 mAcm^{-2}) and the mass-transfer overpotential region (>500 mAcm^{-2}). The open circuit voltages (OCVs) of the cells with Pt/C, Pt-Pd/CNT-S, Pt-Pd/CNT and Pt-Pd/CNT-C catalysts were 0.994 V, 1.003 V, 0.967 V and 0.933 V, respectively. As discussed in *Chapter 3, Section 3.3.3*, OCV reflects the overall catalytic potential of the catalyst; a higher OCV indicates lower occurrence of parasitic reactions. The cell with Pt-Pd/CNT-S catalyst demonstrated the highest OCV indicating the best catalytic activity amongst all. The high dispersion achieved in the case of Pt-Pd/CNT-S leads to more number of active catalysis sites (ESA) improving the activity and selectivity resulting in lesser parasitic reactions which are responsible for mixed potential losses and hence render higher OCV [Pethaiah *et al.* 2015, Feng *et al.* 2017]. Focusing in the activation-controlled region (at 50 mAcm^{-2}), the drop in cell voltage follows the order: Pt-Pd/CNT-C (0.230 V)> Pt-C (0.220 V)> Pt-Pd/CNT (0.194 V) > Pt-Pd/CNT-S (0.182 V). Lower cell voltage drop (or higher cell voltage) reveals better ORR catalytic performance. Similar trend in cell voltage was observed in the kinetic (at 300 mAcm^{-2}) and mass (at 600 mAcm^{-2}) controlled regions as well, demonstrating the overall higher performance of the fuel cell with Pt-Pd/CNT-S cathode catalyst. It is noteworthy that both Pt-Pd/CNT-S and Pt-Pd/CNT exhibited better performance than commercial Pt/C catalyst even at lower Pt loading in the catalyst as well as in the electrode. This demonstrates the usefulness of the synthesized Pt-Pd catalyst for effective commercialization of fuel cell by lowering the catalyst cost which almost amounts to 40% of the total fuel cell cost. The lower performance of Pt-Pd/CNT-C catalyst as compared to Pt/C can be attributed to highly agglomerated Pt-Pd NPs hindering their effective utilization in the electrochemical reactions.

The effective Pt utilization in terms of Pt loading can be approximated by mass activity at 0.9 V. In line with previous results, mass activity of Pt-Pd/CNT-S catalyst was 2.21 times, 1.65 times and 4 times higher than that of Pt/C, Pt-Pd/CNT and Pt-Pd/CNT-C catalysts, respectively. At the same time, all

the Pt-Pd based catalysts exhibited better performance than commercial Pt/C catalyst in term of effective Pt utilization. This can be clearly understood from the Pt mass normalized polarization curves of the catalysts as presented in Fig. 7.12. Higher power density which indicates superior Pt utilization was obtained with Pt-Pd based catalysts as compared to the commercial catalysts. Power density reflects the overall compactness of the fuel cell system; a higher power density indicates that a compact system can be realised with a lower Pt loading. The maximum power densities of Pt/C, Pt-Pd/CNT-C, Pt-Pd/CNT and Pt-Pd/CNT-S are 640 $mWmg_{Pt}^{-1}$ 975 $mWmg_{Pt}^{-1}$, 1104 $mWmg_{Pt}^{-1}$ and 1503 $mWmg_{Pt}^{-1}$, respectively, indicating that Pt-Pd/CNT-S has the highest PEMFC performance.
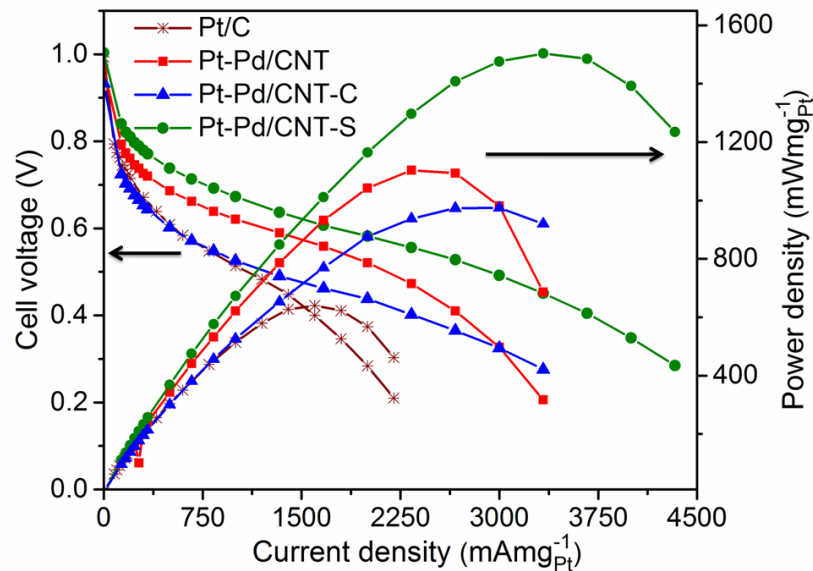
Fig. 7.12. Pt mass normalized polarization and power density curves of Pt-Pd based and Pt/C catalysts

The better fuel cell performance of Pt-Pd/CNT-S catalyst can be attributed to favorable electrochemical properties achieved with SDS assisted route such as high ESA and lower R_c. The single cell performance results fully supported the physico-chemical and electrochemical results (both half cell mode and full cell mode) in ranking the electrocatalysts in their catalytic activity as follows: Pt-Pd/CNT-C< Pt-Pd/CNT< Pt-Pd/CNT-S. These results further confirm the decisive influence of surfactant on the synthesis of the

catalyst NPs in the desired morphology and size which decides its overall ORR catalytic activity in PEMFC. It was found that SDS aided Pt-Pd/CNT-S catalyst favorably enhances the cell performance; whereas, CTAB aided Pt-Pd/CNT-C catalyst depreciates the cell performance.

7.4. Conclusions

In this work, MWCNT supported Pt-Pd composite catalysts were prepared *via* a facile, MW assisted polyol route in presence and absence of surfactant in order to understand the influence of anionic (SDS) and cationic (CTAB) surfactant on physico-chemical properties and ORR performance of the catalyst. It was observed that the surfactant did not affect much the Pt-Pd particle size during synthesis; rather they influenced the aggregation of MWCNT support, which in turn influenced the dispersion of Pt-Pd NPs onto the MWCNT support. The anionic surfactant assisted the disaggregation of MWCNT bundles and homogenous dispersion of Pt-Pd NPs. On the contrary, cationic surfactant was ineffective in disaggregation of MWCNT and led to deposition of agglomerated Pt-Pd NPs on the support. The different levels of dispersion of active NPs of bimetallic Pt-Pd achieved with the two types of surfactants significantly affected the ORR active sites and catalytic activity as evidenced from the electrochemical evaluation. The study demonstrated the efficient synthesis of SDS assisted, Pt-Pd/CNT-S cathode catalyst with superior performance characteristics. Additionally, all Pt-Pd catalysts exhibited better fuel cell performance in terms of effective Pt utilization than the commercial Pt/C catalyst establishing their competence as ORR catalyst in PEMFC. Overall, this study demonstrates that Pt-Pd/CNT-S is an economically viable, promising cathode catalyst in PEMFC which might enhance the scope of PEMFC commercialization due to its high activity, stability and reduced cost as compared to present day catalysts.

Chapter 8

Pt/V-TiO$_2$ and Pt-Pd/MWCNT catalysts: Durability and performance assessment versus commercial Pt/C catalyst

Abstract

The results of investigation on durability and performance characteristics of two selected cathode catalysts, Pt/V-TiO₂ and Pt-Pd/MWCNT are presented in this chapter. Accelerated degradation test (ADT) with potential cycling at 0.2-1.2 V for 6000 cycles in conjunction with cyclic voltammetry (CV), chrono-amperometry (CA), electrochemical impedance spectroscopy (EIS) and fuel cell polarization studies were employed to elucidate the performance and understand the degradation behavior of the catalysts. The study demonstrated enhanced activity and durability of Pt/V-TiO₂ and Pt-Pd/MWCNT catalysts compared to commercial Pt/C catalyst.
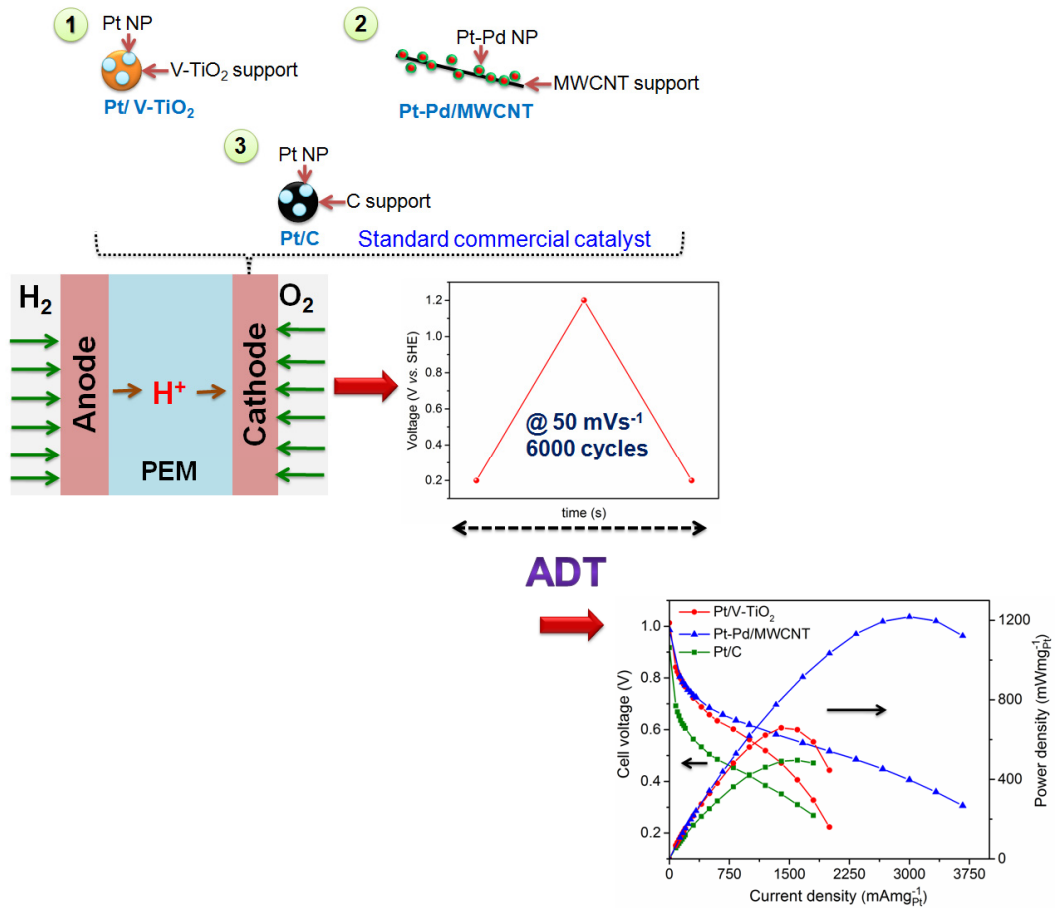
8.1. Introduction

The cathode catalyst in PEMFC gets exposed to highly corrosive conditions emanating from the high electrode potential, low pH and high oxygen and water content which adversely affect its catalytic activity. Thus, cathode catalyst degradation is a major reason for the decline in fuel cell performance over time of usage [Yu *et al.* 2012, Kim *et al.* 2015]. The commonly employed, carbon black supported Pt catalyst suffers severely from poor durability aspects due to carbon corrosion, along with the inevitable agglomeration or dissolution of Pt NPs resulting in decrement of ESA and loss in fuel cell performance [Knights *et al.* 2004, Xie *et al.* 2014, Li *et al.* 2015, Ishiguro *et al.* 2016]. One strategy to reduce performance degradation due to carbon corrosion is to use a more stable support. In this regard, CNTs have recently been proposed as a replacement for traditional carbon black as the support for fuel cell catalysts due to their unique characteristics, including high aspect ratio, high electron conductivity, enhanced mass transport capability and high corrosion resistance [Chen *et al.* 2007, Shao *et al.* 2009, Lv *et al.* 2011]. Similarly, TiO₂ has also been reported as an alternative support material for Pt due to its high corrosion resistance, SMSI and good proton conducting nature; however, poor electrical conductivity limits its applications [Zhang *et al.* 2014, Du *et al.* 2016, Elezovic *et al.* 2016]. Doping of TiO₂ with suitable elements has been an effective approach to achieve high electrical conductivity which improves ORR catalytic activity [Kim *et al.* 2014, Shahgaldi *et al.* 2015, Dhanasekaran *et al.* 2016, Dhanasekaran *et al.* 2016].

In addition to the intrinsic support materials characteristics, durability is also highly dependent on the employed catalytic metals [Shao *et al.* 2007, Zhou *et al.* 2010].Towards this, Pt-M (M = transition element) bi-metallic/alloy systems have been extensively investigated and proved effective demonstrating higher stability against dissolution than the state of the art pure Pt catalysts [Jung *et al.* 2014, Wang *et al.* 2015]. Among the various Pt-M based catalysts, Pt–Pd systems have attracted particular attention because Pd is stable in acidic solutions, less expensive than Pt, and the combination of Pt with Pd would not

only enhance the catalytic performance but the durability of the Pt-based catalysts [Zhang *et al.* 2013, Wang *et al.* 2014, Wang *et al.* 2015].

Most of the studies, which address the durability characteristics of catalysts report electrochemical results performed in a half, cell mode with acidic liquid electrolytes. However, such durability assessments cannot provide the true representation of the actual performance of the catalyst in a working fuel cell. The durability is influenced not only by the intrinsic catalyst characteristics but also by the nature of the catalyst-electrolyte interface where the electrochemical reactions occur which is highly dependent on the fuel cell operating conditions. For a reliable assessment of the performance and durability of the catalyst, it is necessary to evaluate the key performance factors under working PEMFC conditions. *In-situ* electrochemical techniques that can directly characterize the catalyst in the MEA of a PEMFC under operation are the most appropriate methods. Thus, such *in-situ* investigations in full cell mode are of prime importance for further development of PEMFC technology. Additionally, *in-situ* techniques offer non-destructive, on the spot and quick health assessment of the catalyst, which is significant in the adoption of useful strategies to achieve enhanced fuel cell performance.

Accelerated durability test (ADT) is generally employed to evaluate cathode catalyst durability in PEMFC and it provides valuable insights into ORR performance and degradation mechanisms. ADT is typically composed of a fast and suitable aging procedure which is used in conjunction with some measure of performance and/or extent of degradation, such as ESA measurement by cyclic voltammetry (CV), being the most common [Hicks *et al.* 2006, Yuan *et al.* 2011, Saleh *et al.* 2012, Ishiguro *et al.* 2016]. *In-situ* electrochemical ADT-based degradation studies for PEMFC cathode catalysts have been largely limited to evaluation of changes in ESA and polarization characteristics [Zhou *et al.* 2010, Saleh *et al.* 2013, O'Rian *et al.* 2014, Saleh *et al.* 2014]. Such investigations are mainly related to catalyst characteristics and do not directly reveal catalyst-electrolyte interface properties which are critical for a better understanding of degradation behavior. Hence, additional *in-situ*

electrochemical analysis aimed at monitoring catalyst-electrolyte interface is required for understanding the durability and degradation behavior of the catalyst. *In-situ* electrochemical impedance spectroscopy (EIS) has been quite useful towards this, *i.e.* for characterizing the interfacial electrical properties [Saleh *et al.* 2013, O'Rian *et al.* 2014, Saleh *et al.* 2014]. EIS investigations have been very valuable for degradation studies of carbon supported Pt catalyst [Jia *et al.* 2001, Saleh *et al.* 2012, Saleh *et al.* 2014, Shaneeth *et al.* 2016]; however, such investigations have not been extended to TiO₂ supported systems. Also, retention of catalytic activity is a significant facet of durability investigation and hence, needs to be evaluated for selection of a suitable catalyst. For this, *in-situ* chrono-amperometric (CA) measurements in the kinetically controlled potential regime can represent the activity and stability of the cathode catalyst well, and hence, can serve as an effective tool for activity evaluation in durability studies. In view of the above, *in-situ* degradation evaluation through CV, EIS, CA and fuel cell polarization done before and after ADT would be an effective procedure to capture the absolute durability and degradation behavior of cathode catalyst in PEMFC.

Based on the results presented in the previous chapters of this thesis, V-doped TiO₂ supported Pt NPs (Pt/V-TiO₂) and MWCNT supported Pt-Pd bimetallic NPs (Pt-Pd/MWCNT) have been selected for evaluation of durability characteristics. When compared to un-doped TiO₂ supported catalyst, V-doped TiO₂ supported catalyst exhibited better PEMFC performance (results in *Chapter 4*). Similarly, among the MWCNT supported Pt-Pd catalysts prepared through surfactant assisted route, Pt-Pd/CNT-S, prepared though SDS assisted route exhibited higher performance for PEMFC application (results in *Chapter 7*). Thus, these two catalysts were selected for further studies on their durability aspects. Here, the studies performed on performance and durability characteristics of Pt/V-TiO₂ and Pt-Pd/CNT-S catalysts in comparison with the commercial Pt/C cathode catalyst in PEMFC under operation is presented. ADT in conjunction with i*n-situ* CV, CA, EIS and fuel cell polarization studies performed before and after ADT was employed to elucidate the practical

performance and understand the degradation behavior of the above three catalysts. In addition, we propose and demonstrate for the first time, the effectiveness of employing a combination of *in-situ* techniques of CV, CA, EIS and fuel cell polarization with ADT to evaluate durability and degradation behavior of cathode catalysts.

8.2. Experimental
8.2.1. Materials

The materials used for electrode preparation, MEA fabrication and single cell PEMFC assembly remains the same as detailed under *Chapter 2, Section 2.1* and *Section 2.4.1*.

8.2.2. Synthesis of Pt/V-TiO₂ and Pt-Pd/MWCNT catalysts

Pt/V-TiO$_2$ catalyst (with 20 wt. % Pt) was synthesized in-house. For this, V doped TiO$_2$ support was first prepared through acid catalyzed sol-gel route, and then Pt deposition on this support was achieved adopting a MW assisted, modified chemical reduction route as detailed in *Chapter 2, Section 2.2.2*. Pt-Pd bi-metallic catalyst (20 wt. % of Pt-Pd, Pt:Pd atomic ratio 1:1) supported on MWCNT was synthesized in the presence of SDS surfactant by MW assisted, polyol reduction route as detailed in *Chapter 2, Section 2.2.5*. The commercial Pt/C catalyst (20 wt. % Pt) was procured from Alfa Aesar.

8.2.3. Materials Characterization

Characterization methods employed include FESEM, water contact angle measurements and UPS. The details of all these methods are given in *Chapter 2, Section 2.3*.

8.2.4. Fabrication of MEA and assembly of single cell PEMFC

MEA for single cell fuel cell was prepared using Nafion® membrane and catalyst ink coated PTFE sintered carbon paper. The procedures for MEA fabrication and single cell assembly are detailed in *Chapter 2, Section 2.4.1.4* and *Section 2.4.1.5*, respectively. The metal (Pt/Pt-Pd) loading at the electrodes (anode and cathode) in MEA was 0.5 mgcm^{-2}.

8.2.5. Accelerated durability test (ADT) and in-situ electrochemical procedures for evaluation of activity, durability and cell performance with cathode catalysts

All the electrochemical experiments were carried out *in-situ* in a single cell PEMFC at room temperature and atmospheric pressure unless otherwise mentioned. The catalytic activity, stability and fuel cell performance of the employed catalysts were evaluated before and after subjecting them to ADT to have a meaningful comparison.

The ADT and *in-situ* electrochemical procedures to assess the activity, durability and cell performance of the cathode catalyst consisted of the following steps, performed in sequence:

i.   The performance of the catalyst was evaluated through polarization and power density curves obtained with a fuel cell test station at the cell temperature of 50 °C.

ii. The activity of catalyst towards ORR was evaluated through chrono-amperometric (CA) measurements at cell voltage (E_{cell}) of 0.9 V held over a period of 3600 s.

iii. The activity of catalyst towards ORR was also evaluated through electrochemical impedance spectroscopy (EIS) experiments performed by applying ac amplitude of 10 mV over the frequency range 10^{-1} to 10^{5} Hz at E_{cell} of 0.9 V.

iv. ESA of catalyst was evaluated using CV by cycling the cathode at 20 mVs^{-1} between 0 to 1.2 V *vs*. SHE.

v.   The health assessment of catalyst was also carried out using EIS measurements by applying ac amplitude of 10 mV over the frequency range 10^{-1} to 10^{5} Hz at dc bias potential of 0.5 V *vs*. SHE.

vi. The long-term durability performance of the catalyst was evaluated through ADT by potential cycling of the cathode between 0.2 to 1.2 V *vs*. SHE for 6000 cycles [Shaneeth *et al.* 2016].

All the electrochemical experiments except CV and EIS at dc bias of 0.5 V were performed with pure, O_2 and humidified H_2 gases fed at cathode and anode, respectively. For CV and EIS at dc bias of 0.5 V experiments, pure, N_2 and humidified H_2 gases were fed at cathode and anode, respectively.

8.3. Results and discussion

The essential characteristics of the studied catalytic systems are as follows. Pt/V-TiO₂ catalyst consists of Pt NPs (3.2 nm) deposited on anatase phase TiO₂, with 4.8 mole% of V dopant (*Chapter 4*). Bi-metallic Pt-Pd/CNT-S catalyst in 1:1 Pt:Pd atomic ratio has Pt-Pd NPs (4.0 nm) supported on MWCNT (*Chapter 7*). The bi-metallic Pt-Pd/CNT-S catalyst is designated as Pt-Pd/MWCNT in this chapter for easy reference. The commercial Pt/C catalyst has Pt NPs (3.4 nm) supported on carbon black (Vulcan XC-72).

8.3.1. Electrochemical evaluation of activity and durability of catalysts for ORR before and after ADT

For fuel cell applications, it is crucial that the catalysts exhibit long term durability with sufficient activity under working load cycles in the highly corrosive environment. In order to assess the durability and changes in the activity of the catalyst, ADT is generally employed, which is practically feasible and less time-consuming than the real-time durability test. In this study, ADT was performed by potential cycling of cathode between 0.2 V to 1.2 V *vs*. SHE using a scan rate of 50 mVs⁻¹ for 6000 cycles under working fuel cell conditions. The conditions of ADT are chosen such that the catalyst is subjected to continuous, repetitive oxidation/reduction cycles and the catalyst surface along with the support material is exposed to severe corrosion, which are the well-known factors that contribute towards fuel cell performance degradation in the longer run [Kongkanand *et al*. 2006, Xie *et al*. 2014]. Table 8.1 summarizes the electrochemical parameters that are generated pertaining to durability investigations of Pt/V-TiO₂, Pt-Pd/MWCNT and Pt/C catalysts. The performance analyses with respect to each of these parameters are detailed further in subsequent sections.

Table 8.1. Electrochemical parameters of Pt/V-TiO$_2$, Pt-Pd/MWCNT and Pt/C catalysts before and after ADT

Parameters	Pt/V-TiO$_2$		Pt-Pd/MWCNT		Pt/C	
	Before ADT	After ADT	Before ADT	After ADT	Before ADT	After ADT
ESA^a, m^{2}g^{-1}	60	51	110	67	104	52
j^b, mAcm^{-2*}	1.3	4.3	2.4	1.9	0.7	0.3
R$_{ct}$ ^{c}	17.7	8.0	7.4	13.5	29.2	35.9

^{a}from CV; ^{b}from CA plots at E$_{cell}$ of 0.9 V and at t=3600 s; ^{c}from EIS spectra at E$_{cell}$ of 0.9 V; *cm^2 values correspond to geometric active area of electrode

8.3.1.1. CV analyses

It is widely accepted that the loss in ESA of the catalyst with ageing is a major factor that contributes towards performance degradation of PEMFC [Shao *et al.* 2006, Shao *et al.* 2007, Debe 2012]. The CV curves showing hydrogen adsorption/desorption region of Pt/V-TiO$_2$, Pt-Pd/MWCNT and Pt/C catalysts before and after ADT are presented in Fig. 8.1 (a) and (b), respectively. The ESA of the catalysts were obtained by measuring the columbic charge for hydrogen desorption after correcting for double layer charge contribution of the cathodes [Song *et al.* 2011] and the values are included in Table 8.1. ESA depends on the size of metal NPs dispersed onto the support materials; smaller the dispersed particles, higher the ESA, and with similar particle size, much variation in ESA is not expected. However, it is observed that even with similar metal crystallite size (3-4 nm), ESA of Pt/V-TiO$_2$ is lower than that of carbon based catalysts (Pt-Pd/MWCNT and Pt/C) before ADT. This probably arises from the variation in electrical properties of the substrate materials. V-TiO$_2$ has lower electrical conductivity compared to carbon supports and hence, in the case of Pt/V-TiO$_2$ catalyst, the poor electrical contact of Pt NPs onto semi-conducting V-TiO$_2$ surface results in under-estimated catalyst's surface area. On the other hand, with carbon-based supports much better electrical contact of Pt NPs exist with the support favoring more accurate estimation of catalyst surface area. After ADT, it is seen that the

hydrogen desorption peaks (0.0–0.3 V *vs.* SHE) in the CV of carbon-based catalyst is greatly suppressed, indicating significant loss in ESA. However, for Pt/V-TiO$_2$ catalyst, no significant suppression of these peaks is observed, indicating only a marginal loss in ESA after ADT. On completion of 6000 ADT cycles, Pt/V-TiO$_2$ and Pt-Pd/MWCNT retained 85% and 61% of its initial ESA, respectively, while Pt/C retained only 50%. Thus, the loss rate in ESA per cycle for both Pt/V-TiO$_2$ (0.0015 m^{2}g^{-1}) and Pt-Pd/MWCNT (0.0072 m^{2}g^{-1}) is less compared to that for Pt/C (0.0087 m^{2}g^{-1}). These results indicate that Pt/V-TiO$_2$ is better than carbon-based systems in terms of retention of ESA by a factor of 4.8 and 5.8 times with respect to Pt-Pd/MWCNT and Pt/C, respectively under the same testing conditions [He *et al.* 2011].
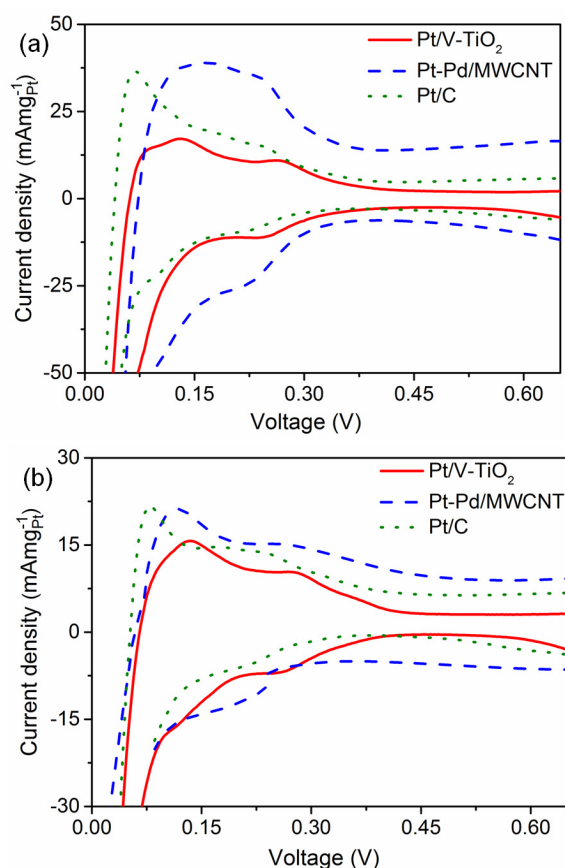
Fig. 8.1. CV curves of the catalysts, (a) before, and (b) after ADT

Among the carbon-based supports, MWCNT-supported catalyst showed better retention of ESA compared to commercial catalyst. For both the carbon-based systems, the lowering of ESA is attributed to the corrosion of sp^2

carbon support material as well as migration of Pt NPs and their agglomeration on the surface of support [Shao *et al.* 2008, Zhang *et al.* 2014]. The higher durability of Pt/V-TiO$_2$ can be attributed to the better corrosion resistance of the V-TiO$_2$ support material and the anchoring effect provided by V-TiO$_2$ surface to the deposited Pt NPs which resists their migration [Kim *et al.* 2016]. The higher stability of V-TiO$_2$ support as compared to carbon-based supports was also evidenced from the FESEM imaging of the catalyst coated electrodes before and after ADT and are shown in Fig. 8.2. Pt/V-TiO$_2$ electrode showed globular aggregates of catalyst particles before ADT [Fig. 8.2 (a1)] which are retained post-potential cycling tests without any significant growth of the particles [Fig. 8.2 (a2)] demonstrating retention of structural integrity of the V-TiO$_2$ support after ADT. However, in the case of both carbon-based supports, coalescence of support particles to form a sheet structure [Fig. 8.2 (b2), (c2)] was observed along with particle growth indicating loss in structural integrity of the supports following potential ageing tests. Coalescence can originate from subsequent corrosion, collision and melting of carbon-based supports during degradation tests as a result of cycling voltage from low to higher potential range. These changes in the supports are bound to adversely affect the supported metal NPs which would also undergo a similar agglomeration due to migration and coalescence of particles on support after potential cycling tests leading to larger particles and reduced surface area as evidenced from ESA analysis. Attempts to carry out further XRD and HRTEM analyses in order to confirm the changes in size of the Pt NPs after ADT proved unsuccessful in view of the extremely low quantity of catalyst material present on the surface of small electrode of 1 cm^2 with metal loading level of 0.5 mgcm^{-2}. Also, collection of the catalyst particles from electrodes is exceedingly difficult due to the delaminated electrodes. In fact, this further highlights the significance of this study to discern changes in the performance of the fuel cell with non-destructive *in-situ* electrochemical measurements without the assistance of post-mortem physical analyses. It is worth mentioning here that, though MWCNT-supported catalysts showed higher corrosion

resistance in terms of retained ESA after ADT as compared to commercial Pt/C catalyst, both the carbon-supported catalysts follow a similar degradation pathway. Hence, it is inferred that with an alternate carbon-based support, it is possible to improve the corrosion resistance of support, but it might be difficult to avoid corrosion totally.
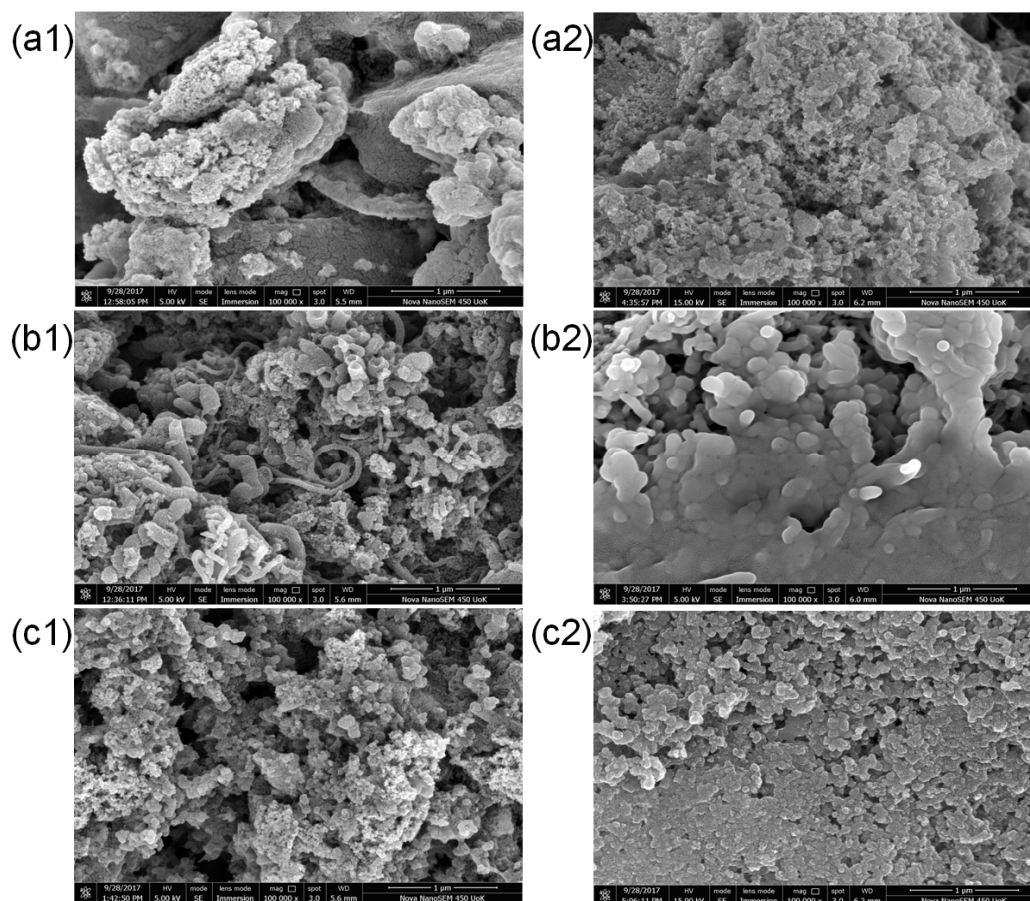
Fig. 8.2. FESEM images of (a1, a2) Pt/V-TiO₂ before and after ADT, respectively, (b1, b2) Pt-Pd/MWCNT before and after ADT, respectively, and (c1, c2) Pt/C before and after ADT, respectively

8.3.1.2. CA and EIS analyses

To compare the activity of the catalysts after ADT, CA tests were carried out at cell voltage of 0.9 V so that the kinetic aspects of the catalysts are captured. The results obtained are included in Table 8.1. Fig. 8.3 (a) and (b) show the current density *vs.* time plots for catalysts before and after ADT, respectively. It is interesting to note that 1.3 and 2.3 times loss in current

density was observed after ADT in the case of Pt-Pd/MWCNT and Pt/C, respectively; whereas, 3.3 times increase was observed in the case of Pt/V-TiO$_2$. The decrease in activity for carbon-based catalysts, reflected as lower current density, can be attributed to the corrosion and collapse of carbon support under fuel cell working conditions, which leads to agglomeration of the active Pt NPs and even their detachment from the support. This explains the loss in ESA for carbon-based catalysts after ADT as observed from CV studies. However, the lower current degradation rate after 3600 s of measurement for Pt-Pd/MWCNT (20.8%) catalyst as compared to Pt/C (57.1%) indicated higher stability of MWCNT support as compared to traditional carbon-black support. On the contrary, the increase in the current density indicating enhanced performance of Pt/V-TiO$_2$ after ADT was contrary to expectation.
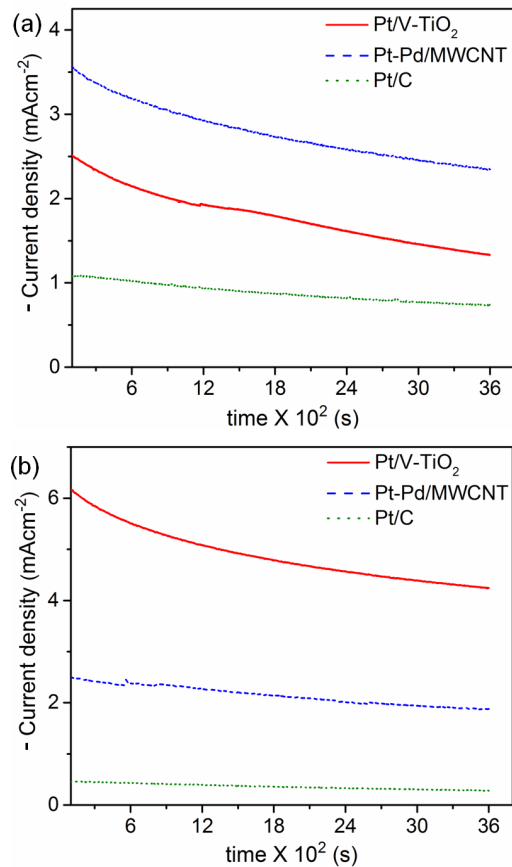
Fig. 8.3. Current density *vs.* time plots for catalysts (a) before ADT, and (b) after ADT

To further understand the changes in the catalytic activity after ADT, EIS studies were performed to evaluate the charge transport properties of the cathode catalysts. Fig. 8.4 (a) and (b) show Nyquist plots of catalysts at 0.9 V before and after ADT, respectively. The high frequency intercept on the real impedance axis of the plot is ascribed to the total ohmic resistance, R_c of the single cell [Iranzo *et al.* 2010]. The diameter of semi-circle on the Nyquist plot represents charge transfer resistance, R_{ct} of the oxygen reduction occurring at cathode [Yang *et al.* 2015]. Smaller diameter of the semi-circle is indicative of lower R_{ct} and hence, faster interfacial oxygen kinetics. The derived parameters from EIS spectra are included in Table 8.1. After performing ADT, increase in diameter of the semi-circle (or R_{ct}) was observed for Pt-Pd/MWCNT and Pt/C indicating a decrease of its catalytic activity after the test; this observation is in agreement with ESA and CA results explained earlier. However, Pt-Pd/MWCNT exhibited lower R_{ct} as compared to Pt/C (13.5 Ω *vs.* 35.9 Ω) following ADT indicating higher activity of bi-metallic MWCNT supported catalysts over commercial catalyst. On the contrary, a significant decrease in R_{ct} was observed for Pt/V-TiO₂ after ADT, indicating an increase in catalytic activity with faster interfacial kinetics, concordant with the CA results. The increased ORR kinetics indicates the availability of more triphase boundaries (TPBs, Pt NPs covered by a thin ionomer film through which oxygen can diffuse) formed in the case of Pt/V-TiO₂ catalyst, that are available for ORR [Park *et al.* 2011]. Generally, formation of more numbers of TPBs are reflected as higher ESA due to more numbers of Pt active sites. However, ESA accounts only for the Pt sites and does not take into consideration of other important aspect of TPBs *i.e.* changes in ionic conductivity at the interface. Since the loss in ESA of Pt NPs after ADT was only marginal (15%), the catalyst indicated excellent retention of Pt active sites which are part of TPBs. Hence, the further increase in the activity will be dependent on the efficient utilization of the retained Pt active sites in favorable formation of TPBs. Thus, it was of interest to investigate the changes in ionic conductivity of the MEA during cycling. It is noteworthy that the presence of water molecules at the interface aids in efficient

proton conduction or enhances ionic conductivity. Thus, the hydrophilic property of the catalyst layer plays an important role in deciding the activity of the material.
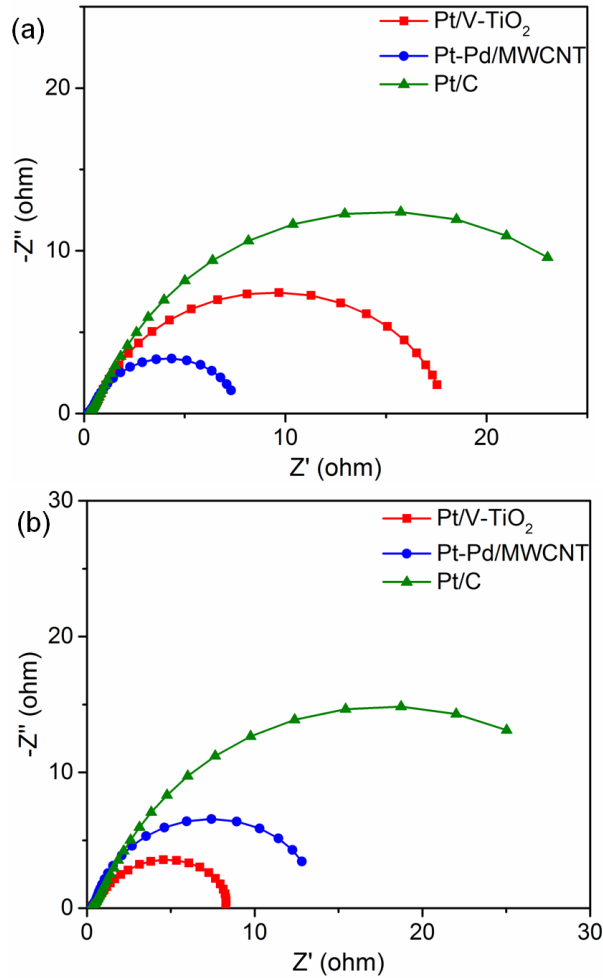
Fig. 8.4. Nyquist plots of catalysts at E_{cell} of 0.9 V: (a) before ADT, and (b) after ADT

Hydrophilic nature of the catalysts were investigated in terms of contact angle subtended by water droplet on the catalyst-coated electrode employed in MEA of fuel cell, and Fig. 8.5 presents the observations made. The relatively more hydrophilic nature of Pt/V-TiO$_2$ layer compared to Pt-Pd/MWCNT and Pt/C layer is evident from its lower water contact angle (140º vs. 149º and 146º). The better hydrophilic nature naturally leads to more efficient humidification of MEA and reduces the membrane drying out which occurs during long term operations, and hence, result in improved proton conductivity

as well as lower ohmic resistance in actual operation [Chaisubanan *et al.* 2016]. Thus, TiO_2 which can improve the hydrophilic properties of the catalyst layer in fuel cells can function as a better support material compared to carbon.
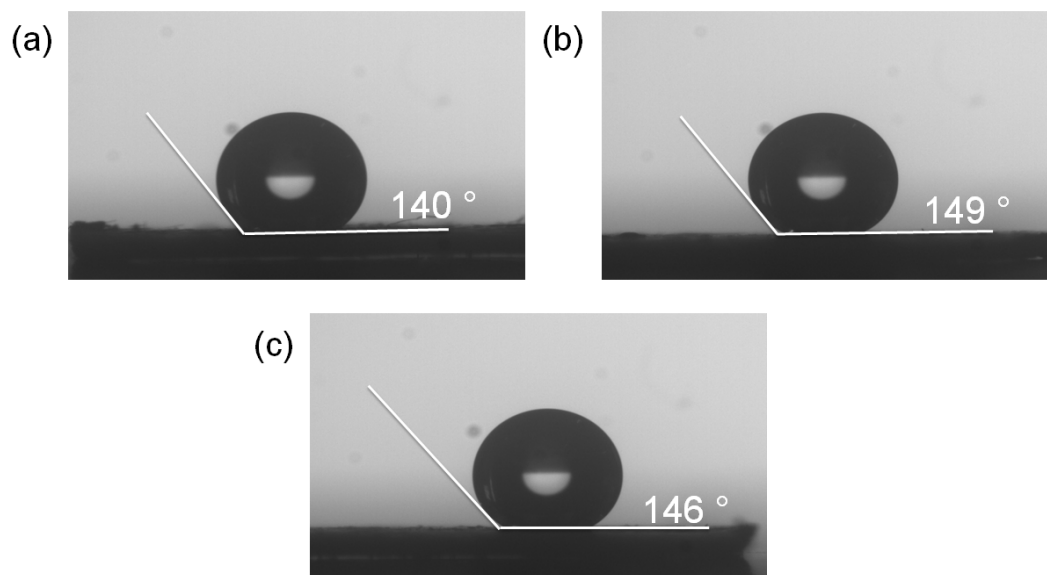
Fig. 8.5. Water contact angle measurements of (a) Pt/V-TiO₂, (b) Pt-Pd/MWCNT, and (c) Pt/C catalyst coated carbon paper employed in MEAs for fuel cell evaluation

The above observations are further supported by the impedance studies carried out for Pt/V-TiO₂, Pt-Pd/MWCNT and Pt/C catalysts before and after ADT with pure, humidified H_2 and N_2 gases fed at the anode and cathode compartments, respectively at dc bias potential of 0.5 V *vs*. SHE. The dc bias potential of 0.5 V was carefully chosen from CV plots of the catalysts shown in Fig. 8.1, which falls in the double charge layer region of the studied catalysts and is devoid of any Faradic processes. If the dc bias potential is set at a region where Faradic processes such as hydrogen adsorption/desorption (0.0-0.3 V) or Pt oxide formation and reduction (0.7- 1.2 V) occur, an increase in capacitance would be observed which might not reflect the actual interface condition [Easton *et al.* 2005]. Also, since the hydrogen electrode has negligible impedance relative to the nitrogen bathed electrode, it is assumed that the variations pertaining to hydrogen electrode are quite negligible. Hence, the

impedance spectra obtained can provide a true representation of the cathode catalyst layer interface characteristics.
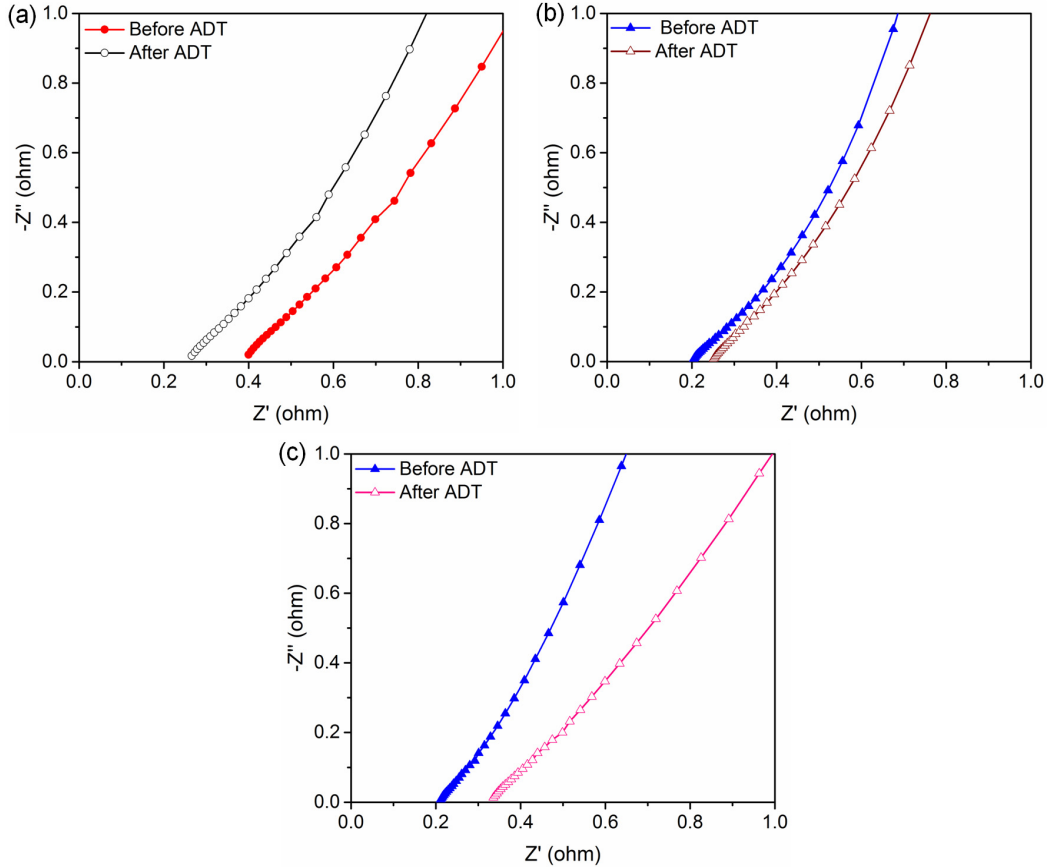
Fig. 8.6. Nyquist plots at dc bias potential of +0.5 V of: (a) Pt/V-TiO$_2$, (b) Pt-Pd/MWCNT, and (c) Pt/C catalysts

Fig. 8.6 (a), (b) and (c) show high frequency region Nyquist plots for Pt/V-TiO$_2$, Pt-Pd/MWCNT and Pt/C catalysts, respectively, before and after ADT. The high frequency intercept represents the total internal resistance of the cell which is dominated by ionic resistance of the membrane [Shaneeth *et al.* 2016]. It is observed that the high frequency intercept decreases for Pt/V-TiO$_2$ catalyst [0.27 Ω *vs.* 0.40 Ω, Fig. 8.6 (a)] after ADT, whereas it increases in the case of carbon-based catalysts [Fig. 8.6 (b) and (c)], showing increase in cell resistance. However, among the two carbon-based catalysts, Pt-Pd/MWCNT exhibited lower increase in cell resistance [0.25 Ω *vs.* 0.20 Ω, Fig. 8.6 (b)] as compared to Pt/C catalyst [0.34 Ω *vs.* 0.21 Ω, Fig. 8.6 (c)] indicating better

corrosion resistance. The respective capacitance plots, presented in Fig. 8.7, can be more useful to estimate the changes in ionic resistance/ionic conductivity. The high frequency slope of the curve with Pt/V-TiO$_2$ catalyst is markedly steeper as compared to before ADT, indicating enhanced proton conductivity [Lefebvre *et al.* 1999]. On the contrary, in the case of Pt-Pd/MWCNT and Pt/C catalyst, the curve in the high frequency region has a lower slope after ADT indicating decrease in proton conductivity.
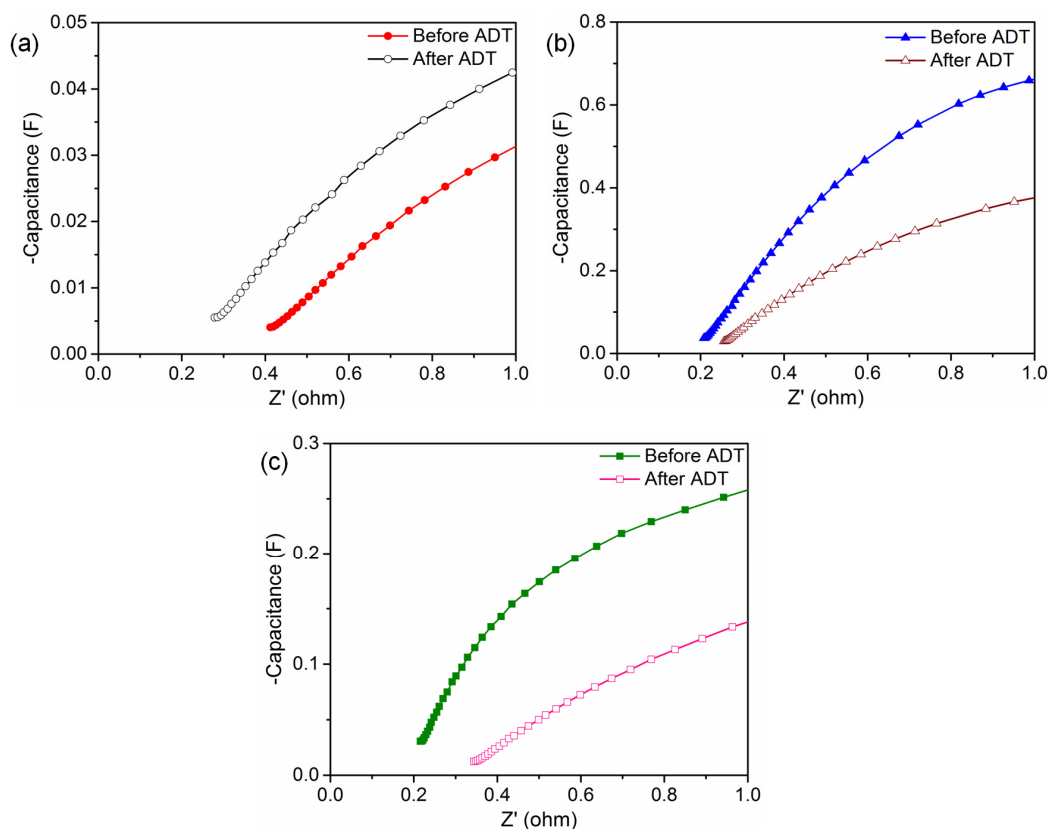
Fig. 8.7. Capacitance plots of (a) Pt/V-TiO$_2$, (b) Pt-Pd/MWCNT, and (c) Pt/C catalysts in the high frequency region, before and after ADT

Another useful information discerned from capacitance plot is limiting capacitance which is proportional to active surface area of the catalyst (area provided by Pt NPs and support material together) [Jia *et al.* 2001]. Thus, a higher limiting capacitance normally means that a larger fraction of the catalyst layer is being utilized. In the case of Pt/V-TiO$_2$ catalyst, a slight increase in limiting capacitance was observed after ADT [ca. 0.03 F *vs*. ca. 0.04 F from

Fig. 8.7 (a)], which can be attributed to enhanced catalyst utilization with increase in ionic conductivity. Conversely, significant reduction in limiting capacitance as a result of ADT was observed in the case of Pt-Pd/MWCNT [ca. 0.37 F *vs*. ca. 0.67 F from Fig. 8.7 (b)] and Pt/C [ca. 0.13 F *vs*. ca. 0.25 F from Fig. 8.7 (c)] indicating reduction in catalyst utilization and activity. This reduction also is indicative of the corrosion of carbon-support which adversely brings down both the active surface area and ESA [Saleh *et al*. 2012]. However, with higher catalyst surface area, MWCNT demonstrated 2.8 times higher corrosion resistance than Pt/C catalyst. The continued corrosion leads to electronic/ionic isolation of parts of the catalyst layer and consequent increase in electronic resistance, which is an undesirable situation for long term durability of PEMFC. The above observations also rationally prove V-TiO$_2$ as a better, corrosion resistant support for Pt as compared to carbon.

8.3.1.3. Single cell polarization analyses

The final performance comparison of the catalysts was done through polarization and power density curves as shown in Fig. 8.8 and the derived parameters are given in Table 8.2. In the activation controlled region (lower current density region <100 mAcm^{-2}) the performance of the cell is largely controlled by the sluggish ORR kinetics. The highest voltage in the activation controlled region (at 50 mAcm^{-2}, Table 8.2) was obtained with Pt-Pd/MWCNT catalyst demonstrating the best fuel cell performance before ADT followed by Pt/V-TiO$_2$ and Pt/C catalysts [Fig. 8.8 (a), Table 8.2]. However, after ADT, considerable reduction in fuel cell performance was observed with carbon support-based catalyst which got reflected as lower cell voltage (over-potential loss) [Fig. 8.8 (b), Table 8.2], and the catalytic activity follows the order Pt/V-TiO$_2$> Pt-Pd/MWCNT> Pt/C. The activity loss at low current region dominated by ohmic losses (at 300 mAcm^{-2}, Table 8.2) can be attributed to the increase of: (i) resistance to ion flow in the electrolyte, and (ii) resistance to electron transfer through the electrically isolated parts of catalyst layer on carbon corrosion [Jung *et al*. 2014], which happen on repeated cycling, as demonstrated by the increase in ohmic/ionic resistance of the cell through EIS

investigations. The decrease in activity at the high current density region (mass transfer limit region, >500 mAcm^{-2}, Fig. 8.8 (b) Table 8.2) is due to the agglomeration and/or loss of Pt NPs induced by the carbon corrosion [Jung *et al.* 2012], which is supported by the observation of decrease in ESA and limiting capacitance. It is to be noted that during fuel cell operation, carbon support corrosion can be accelerated by promotion catalysis of Pt at high potentials prevalent at the cathode which would further adversely affect fuel cell performance [Roen *et al.* 2004, Siroma *et al.* 2005]. The maximum power density with Pt-Pd/MWCNT and Pt/C catalysts also got decreased by 19.1% (from 451 mWcm^{-2} to 365 mWcm^{-2}) and 22.5% after ADT (from 320 mWcm^{-2} to 248 mWcm^{-2}), respectively indicating loss in Pt utilization. Still, bi-metallic Pt-Pd/MWCNT exhibited better performance than the commercial catalyst.
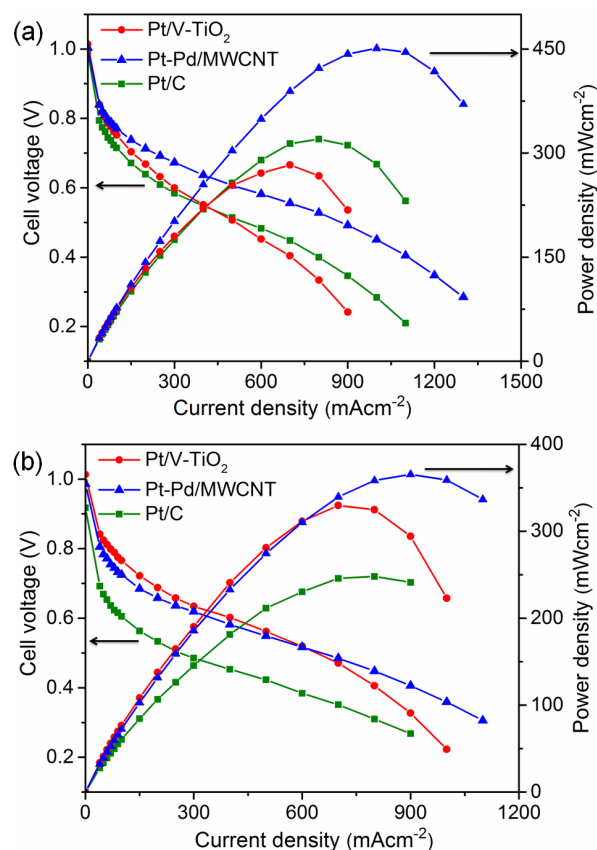
Fig. 8.8. Polarization and power density curves of PEMFC with Pt/V-TiO₂, Pt-Pd/MWCNT and Pt/C catalysts (a) before ADT, and (b) after ADT

Table 8.2. Electrochemical parameters of catalysts derived from polarization and power density curves before and after ADT

Parameters	Pt/V-TiO$_2$		Pt-Pd/MWCNT		Pt/C	
	Before ADT	After ADT	Before ADT	After ADT	Before ADT	After ADT
Voltage @ 50 mAcm^{-2*},V	0.817	0.824	0.821	0.784	0.774	0.669
Voltage @ 300 mAcm^{-2*}, V	0.600	0.632	0.673	0.619	0.584	0.485
Voltage @ 600 mAcm^{-2*}, V	0.452	0.519	0.582	0.517	0.483	0.384
Mass activity @ 0.9 V, mAmg$_{Pt}^{-1}$	52	52	84	57	38	6
Peak Power density mWcm^{-2*}	566	660	1503	1217	640	496
Peak Power density mWmg$_{Pt}^{-1}$	283	330	451	365	320	248

*cm^2 values correspond to geometric active area of electrode

An opposite trend in fuel cell performance after ADT was observed with Pt/V-TiO₂ catalyst, in line with the previous results from CV, EIS and CA. An increase in fuel cell performance was observed, as shown in Fig. 8.8 (b) and Table 8.2, with a higher cell voltage after ADT. This observation supports the earlier explanation of increase in ionic conductivity of the MEA as a major factor responsible for performance enhancement. This suggests that with Pt/V-TiO₂, a conducive environment is prevalent which promotes the formation of a more active three phase interface for ORR performance minimizing the number of less active sites at the Pt surface during the ADT cycles limiting the loss in ESA to 15% only. It was also interesting to observe a significant increase in fuel cell performance specifically in the mass transport region after ADT (Table 8.2). Generally, decrease in performance is significant in mass transport region after ageing due to the degradation of catalyst layer which hinders efficient supply of oxygen to catalytic sites [Liu *et al.* 2017, Zhang *et al.* 2017]. Thus,

the rate of oxygen supply to the Pt catalyst is an important factor that determines the ORR kinetics in the cathode [Lim *et al.* 2010]. The increased performance observed in the case of Pt/V-TiO$_2$ indicates that the supply rate of oxygen to the Pt catalyst was high enough to nullify the over-potential loss at the cathode; and hence, leads to an enhanced cell performance. Since TiO$_2$ has the ability to store oxygen [Schubert *et al.* 2001], it might provide additional oxygen to Pt, especially when oxygen concentration is low in the high current density region. This could also be a factor contributing to increase in the power density of fuel cell with Pt/V-TiO$_2$ catalyst by 16.6% after ADT (from 283 mWcm^{-2} to 330 mWcm^{-2}) in the high current density region (700 mAcm^{-2}). It is also noted here that even though increase in cell performance after ADT was observed with Pt/V-TiO$_2$ catalyst, the highest power density was obtained with Pt-Pd/MWCNT catalyst which reflects its maximum Pt utilization.

Effective Pt utilization is an important aspect and deciding parameter for successful commercialization of PEMFC. Hence, it becomes significant to compare the performance of the different catalytic systems in terms of absolute Pt loading to comment on their performance characteristics. In view of this, the performance comparison of the catalysts was also done through Pt loading normalized polarization and power density curves as shown in Fig. 8.9 and the derived parameters are given in Table 8.2. The Pt loading normalized curves both before and after ADT exhibited better performance by Pt-Pd/MWCNT catalyst which surpassed both Pt/V-TiO$_2$ and Pt/C indicating higher Pt utilization. Hence, in terms of effective Pt utilization expressed by both mass activity and power density, the performance of the catalysts ranks as follows: Pt-Pd/MWCNT> Pt/V-TiO$_2$> Pt/C.

In order to understand the enhanced performance of both Pt/V-TiO$_2$ and Pt-Pd/MWCNT catalyst as compared to commercial catalyst, it was of interest to investigate their surface electrical properties which might have tuned the intrinsic catalytic activity of active Pt sites. Surface electrical properties are critical attributes in deciding the activity and durability of the catalyst. UPS investigation was employed for this and the results are presented in Fig. 8.10. A

232

considerable reduction in the valence band intensity was observed with Pt/V-TiO$_2$ and Pt-Pd/MWCNT catalysts as compared to the Pt/C catalyst [Fig. 8.10 (a)]. This reduction indicates significant electrical transitions between supports and metals which are responsible for tuning intrinsic catalytic activity of Pt active sites.
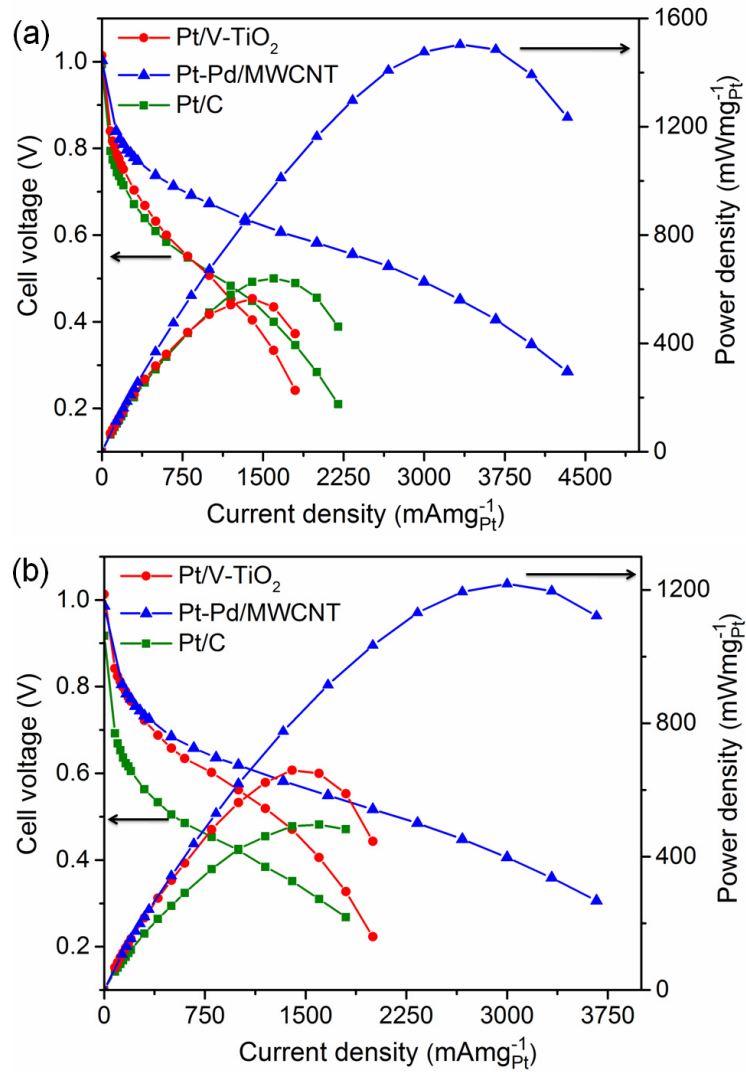
Fig. 8.9. Pt loading normalized polarization and power density curves of PEMFC with Pt/V-TiO$_2$, Pt-Pd/MWCNT and Pt/C catalysts (a) before ADT, and (b) after ADT

From the UPS spectra, valence band maximum (E$_{VB}$) was estimated using the intercept on the abscissa obtained by extrapolating the low binding energy edge to the baseline. Fig. 8.10 (b) shows the zoomed in view of the low binding

energy edges in the UPS spectra shown in (a). E_{VB} was found to be in the order: Pt/C (3.6 eV) > Pt/V-TiO$_2$ (1.9 eV) > Pt-Pd/MWCNT (0.5 eV). E_{VB} represents the highest level of occupancy of 5d electrons of Pt and hence, can be clearly taken as a representation of 5d band vacancy. Lower value of E_{VB} indicates higher Pt 5d band vacancy and lower activation energy for interaction with oxygen during ORR resulting in a facile and faster reaction [Mukerjee *et al.* 1998, Toda *et al.* 1999]. TiO$_2$ supported catalyst showed lower E_{VB} value compared to Pt/C, suggesting stronger metal-support interactions for these catalysts which are responsible for stronger anchoring effect of Pt NPs onto V-TiO$_2$ support leading to higher durability characteristics of the catalyst [Kim *et al.* 2016]. However, Pt-Pd/MWCNT showed the lowest E_{VB} demonstrating higher capability for facile and faster ORR. The lowered E_{VB} in Pt-Pd/MWCNT is attributed to the simultaneous occurrence of both metal-metal (due to electronegativity difference between Pt and Pd metals) [Lu *et al.* 2014, Khan *et al.* 2015] and metal-support interactions (electron transfer from electron rich MWCNT support to metals) [Lopes *et al.* 2008, Khan *et al.* 2015] which favorably enhances Pt activity and durability.
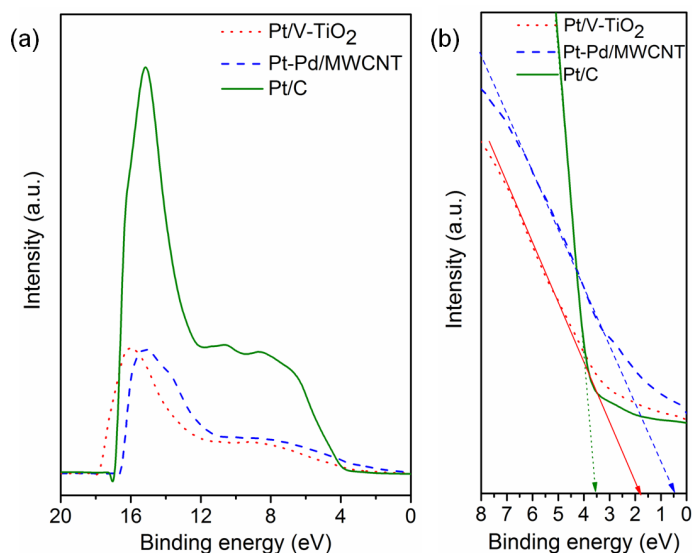
Fig. 8.10. (a) UPS spectra covering the complete binding energy region, and (b) magnified view of the valence band edges of Pt/V-TiO$_2$, Pt-Pd/MWCNT, and Pt/C catalysts

From the electrochemical results, it can be concluded that the ADT along with *in-situ* electrochemical analyses employed in this study before and after ADT are suitable to evaluate activity, durability and performance of cathode catalyst in PEMFC. The results demonstrated that with 6000 ADT cycles, notable degradation in performance occurs for carbon-based catalysts. However, no degradation or activity loss due to durability issues crop up for Pt/V-TiO$_2$ catalyst under the same ADT evaluation and in fact, enhanced performance is achieved after ADT. Durability of Pt/V-TiO$_2$ catalyst beyond 6000 ADT cycles is an area to be explored further.

8.4. Demonstration of applicability of Pt-Pd/MWCNT in PEMFC

Polarization and power density curves showcased Pt-Pd/MWCNT as the most cost-effective catalyst due to its superior performance characteristics in terms of effective Pt utilization as compared to Pt/V-TiO$_2$ and Pt/C catalysts. Hence, it was of interest to demonstrate its applicability at cathode in PEMFC. In this regard, three sets of MEA for the assembly of stack was fabricated with Nafion$^®$ 115 membrane sandwiched between anode and cathode. Anode was made with PTFE sintered carbon paper with commercial Pt/C catalyst with metal loading level of 0.5 mg$_{Pt}$cm^{-2}. Similarly, cathode was made with PTFE sintered carbon paper with Pt-Pd/MWCNT catalyst with metal (Pt+Pd) loading level of 0.5 mg$_{Pt+Pd}$cm^{-2}. The prepared electrodes were hot-pressed with a pre-treated Nafion$^®$ 115 membrane at 125 °C for 600 s to make MEA with an active geometrical area of 1 cm^2. PEMFC stack was assembled with series connection of three sets of MEA which were individually sandwiched between two graphite composite bipolar plates with parallel flow field channels which were finally placed in between two gold plated, Cu terminal plates. The preparation of a three cell stack was completed by assembling it with titanium end plates and tie rods and is shown in Fig. 8.11. For derivation of current from the stack, an external load as shown in Fig. 8.12 was fabricated using 15 LEDs in parallel combination (2 V, current rating 180 mAcm^{-2}) on a polycarbonate sheet to form ISRO logo using hand driller and soldering iron.

The stack was operated at ambient conditions (room temperature and atmospheric pressure) with pure H_2 and O_2 gas fed at anode and cathode compartments, respectively. The stack was operated under two different conditions to demonstrate the functioning of the cathode catalyst as shown in Fig. 8.13: (i) OCV condition, where no current is withdrawn from the stack, and (b) loaded condition where external load is connected to the stack.
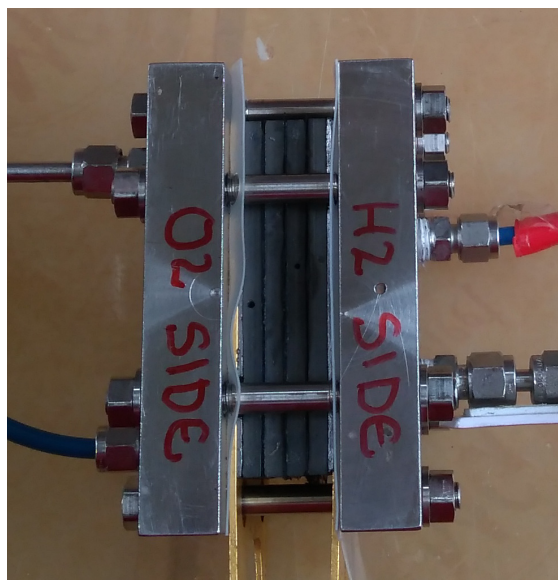
Fig. 8.11. Assembled three cell PEMFC stack

Fig. 8.12. External load

In the OCV condition, the obtained voltage (2.6251 V) corresponds to the combined potential of each cell of the stack when no current is withdrawn

[Fig. 8.13 (a)]. In the loaded condition, the external load withdraws current from the stack and the LEDs glow [Fig. 8.13 (b)] demonstrating the functioning of the Pt-Pd/MWCNT catalyst at cathode in PEMFC. The current is produced by the combined electrochemical reactions at electrodes (anode and cathode) of PEMFC and is decided to a large extent by the cathode catalyst. Hence, the glowing of the LEDs indicates proper functioning Pt-Pd/MWCNT catalyst in PEMFC. In the loaded condition, the decrease in the voltage of the stack to 2.0644 V is sacrificial loss to withdraw useful current from the stack. This demonstration plausibly establishes Pt-Pd/MWCNT as a potential cathode catalyst for wide scale PEMFC applications.
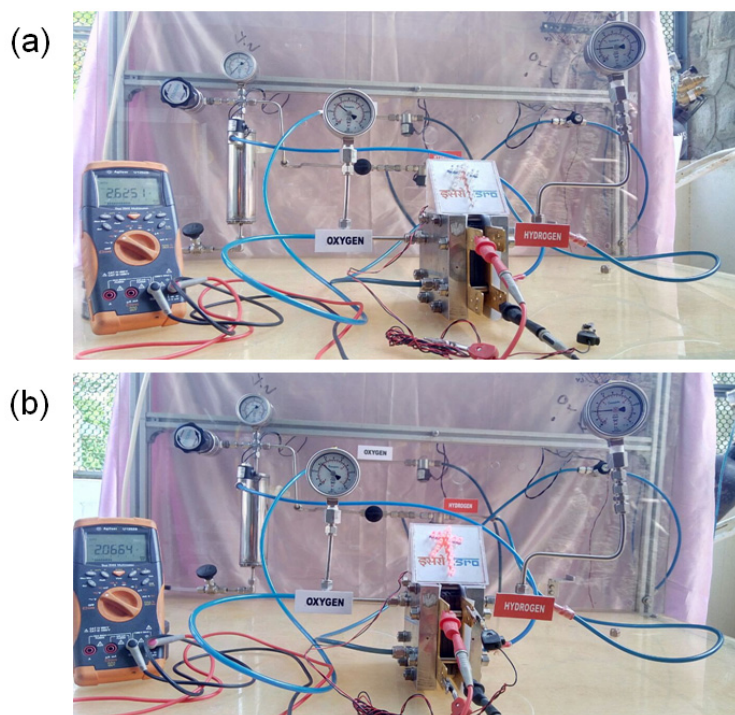
Fig. 8.13. Demonstration of applicability of Pt-Pd/MWCNT at cathode of PEMFC under (a) OCV condition, and (b) loaded condition

8.5. Conclusions

Activity and durability of Pt/V-TiO₂, Pt-Pd/MWCNT and Pt/C cathode catalysts have been investigated in this study through *in-situ* electrochemical techniques under working fuel cell conditions performed before and after an accelerated degradation cycling test. Simple *in-situ* electrochemical testing

methods such as CV, CA, EIS and polarization assessment are used in conjunction with ageing test involving potential cycling to assess performance and durability. Significant changes in ESA, current density, ionic conductivity and polarization behavior of the catalysts were observed after ADT and the results showed that both Pt/V-TiO$_2$ and Pt-Pd/MWCNT exhibited better activity and durability than Pt/C catalyst. The electrochemical analyses revealed prominent influence of support on durability characteristics. The results demonstrated higher stability of both MWCNT and V-TiO$_2$ supports as compared to traditional carbon black supported commercial Pt/C catalyst. Though better durability was obtained with MWCNT supported catalyst as compared to Pt/C the carbon corrosion could not be avoided. In such a scenario, V-TiO$_2$ supported catalyst emerged as the most suitable catalyst to achieve better long term PEMFC performance. However, in terms of effective Pt utilization or per unit Pt activity, superior performance was obtained with Pt-Pd/MWCNT catalyst which was attributed to stronger metal-metal and metal-support interactions which favorably modifies intrinsic Pt catalytic activity. It is demonstrated here that the changes with CV, CA, EIS and polarization response over time can be used to clearly identify the change in activity that occur with time and the degradation behavior. Hence, these simple, time-efficient and reliable *in-situ* electrochemical procedures can also be widely used along with ageing tests for screening new and existing cathode catalysts for PEMFC. This study also demonstrates practical applicability of Pt-Pd/MWCNT in a PEMFC three cell stack establishing its suitability for wide scale PEMFC applications. Moreover, the study showed better performance of Pt/V-TiO$_2$ and Pt-Pd/MWCNT catalysts as compared to commercial Pt/C catalyst making them prospective candidates to be considered for long term PEMFC applications.

Chapter 9

Summary and Future Perspectives

The study presented in this chapter summarizes the important findings and inferences derived from this thesis together with concluding remarks and future scope of work.
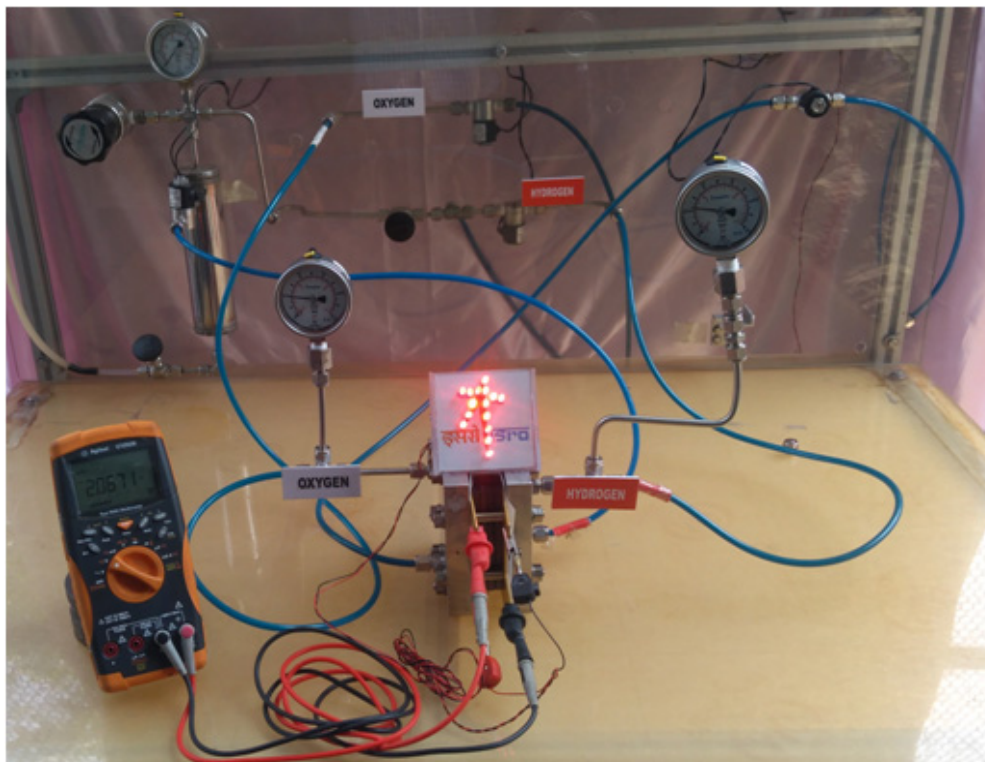
9.1. Summary

PEMFC technology is rapidly emerging as a viable and sustainable energy source that can cater to efficient and green energy requirements of the society due to its inherent advantages such as quick start-up, shut-down cycle, low temperature operation (< 100 °C), high efficiency (60-70%), feasibility of continuous operation and near zero emission. Currently, the commercial application of PEMFC is limited by the activity and durability of cathode catalyst for ORR. Also, the sluggish ORR kinetics occurring at the cathode necessitates a substantially higher Pt metal loading at the cathode compared to the anode, and contributes to increasing the cost further. The commercially available, Pt NPs supported on carbon black (Pt/C), is the most commonly employed cathode catalyst for PEMFC; but it suffers from limitations including insufficient activity and instability due to carbon corrosion, Pt dissolution and agglomeration during harsh operating conditions. To overcome these drawbacks, relatively higher Pt content is required at the cathode which further adds to the cost. Hence, the development of more efficient and durable electrocatalysts with lower cost is crucial for commercial application of PEMFCs. Studies undertaken to improve the activity and stability of cathode catalysts for ORR in PEMFCs are reported in this thesis. The promising nano-structured Pt based cathode catalysts for PEMFC with improved activity and durability have potential for wide scale commercialization of fuel cell.

There were three different classes of Pt based catalysts investigated to achieve improved activity and durability towards ORR in PEMFC *viz.* (i) Metal-oxide (non-carbonaceous) supported Pt catalysts, (ii) Carbonaceous materials supported Pt catalysts and (iii) bi-metallic Pt based catalysts. Under the metal-oxide supported Pt based catalysts, TiO_2 was employed as alternative support to traditional carbon black in commercial Pt/C catalyst to achieve better corrosion resistance. With TiO_2 based Pt cathode catalysts, two avenues were explored to achieve enhanced fuel cell performance. These included investigations on effect of synthesis medium pH and influence of V doping of TiO_2 host matrix on ORR activity. Pt-TiO_2 nanocomposite catalysts in different Pt:Ti atomic ratios (1:1, 2:1 and 3:1) were synthesized in acidic (pH < 3) and basic (pH > 10) medium for ORR in PEMFCs (*Chapter 3*). The pH of

synthesis medium significantly influenced both physico-chemical and catalytic properties of Pt-TiO$_2$. Pt-TiO$_2$ prepared in acidic medium exhibited smaller crystallite size, higher specific surface area and more non-stoichiometric titania with higher electrical conductivity as compared to that prepared in basic medium. The ORR performance from fuel cell polarisation curves showed that Pt-TiO$_2$ catalysts synthesized in acidic medium performed better than those prepared in basic medium. Among the catalysts with varying Pt:Ti atomic ratios, performance decreased in the order 3:1 > 2:1 > 1:1. Among all, Pt:Ti 3:1-A was found to exhibit better fuel cell performance as ORR catalyst (power density-530 mWcm^{-2}; mass acitiviy-123 mAmg$_{Pt}^{-1}$) compared to commercial Pt/C catalyst (power density-440 mWcm^{-2}; mass acitiviy-87 mAmg$_{Pt}^{-1}$), under identical conditions. It was concluded that the favourable conditions of synthesis of Pt-TiO$_2$ catalyst achieved in acidic medium contribute to its enhanced properties.

TiO$_2$ supported catalysts without doping (Pt/TiO$_2$) and with V-doping (Pt/V-TiO$_2$) were synthesized by an easy and efficient route combining sol-gel and MW assisted, modified chemical reduction method (*Chapter 4*). A series of dopant concentration (1-25 mole%) was studied and the optimum was obtained with 5 mole%. As compared to un-doped TiO$_2$ support, V-TiO$_2$ showed lower band gap (1.05 eV *vs.* 2.85 eV) and higher electrical conductivity (5.6 x 10^{-3} Scm^{-1} *vs.* 2.3 x 10^{-3} Scm^{-1}) establishing V as an efficient dopant for electrochemical applications. Both Pt/TiO$_2$ and Pt/V-TiO$_2$ were evaluated *in-situ* as ORR/cathode catalyst in PEMFC and performance was compared with the commercial Pt/C catalyst. It was found that Pt/V-TiO$_2$ showed lower polarization losses and higher voltage in activation region (0.817 V *vs.* 0.732 V, 0.774 V at 50 mAcm^{-2}) than Pt/TiO$_2$ and Pt/C, exhibiting better ORR performance. This study demonstrated V-TiO$_2$ as a promising support for Pt catalyst to attain high cathode performance in PEMFC.

In the class of carbonaceous materials based Pt catalysts, two different approaches were made to enhance fuel cell performance. First, studies were carried out to select the most suitable reduction conditions to achieve high performing Pt/CNT catalysts. CNT supported Pt catalysts were prepared *via* a simple and facile, modified chemical reduction route using a mixture of NaBH$_4$ and EG as the reducing

agent (*Chapter 5*). Two different heating methods, CH and MW irradiation, were adopted to understand their effect on the properties and catalytic activities of Pt/CNT catalyst. The Pt/CNT catalysts were evaluated *in-situ* as ORR catalyst in PEMFC and performance was compared with commercial Pt/C catalyst. The results showed deposition of smaller Pt NPs (2.7 nm *vs.* 3.8 nm) with uniform distribution and higher SSA (57.9 m^2g^{-1} *vs.* 41.4 m^2g^{-1}) for Pt/CNT-MWH compared to Pt/CNT-CH. *In-situ* electrochemical characterization studies revealed higher ESA (70 $m^2mg_{Pt}^{-1}$ *vs.* 48 $m^2mg_{Pt}^{-1}$), lower charge transfer resistance (14 Ω *vs.* 22 Ω), higher cell voltage (0.838 V *vs.* 0.780 V at 50 $mAcm^{-2}$) and higher peak power density (365 $mWcm^{-2}$ *vs.* 270 $mWcm^{-2}$) compared to the cathode with Pt/CNT-CH. Pt/CNT-MWH also exhibited better performance (power density-365 $mWcm^{-2}$; mass acitiviy-60 $mAmg_{Pt}^{-1}$) as compared to commercial Pt/C catalyst (power density-320 $mWcm^{-2}$; mass acitiviy-38 $mAmg_{Pt}^{-1}$). This study demonstrated the viability of MW assisted, metal particle deposition as a simple, yet effective method to prepare high performing Pt/CNT catalyst for ORR in PEMFC.

In the second approach, the influence of different carbon nano-forms was investigated to select the most suitable support for Pt to achieve better ORR activity and durability. Pt supported on various carbon nano-forms (Pt/CB, Pt/SWCNT, Pt/MWCNT and Pt/G) were synthesized by a facile, single step, MW assisted, modified chemical reduction route (*Chapter 6*). The study showed that the different carbon supports not significantly affect the Pt particle size during synthesis, but lead to different amount of defective sites in the carbon framework which influenced both the availability of active metal nano-catalysts and metal-support interaction. *In-situ* electrochemical investigations revealed that the different carbon supports influenced both ORR catalytic activity and stability of the catalyst. This study revealed MWCNT as the most suitable carbon support for Pt catalyst, exhibiting high activity (mass acitiviy-60 $mAmg_{Pt}^{-1}$) and stability (current degradation rate of 6%) for ORR in PEMFC.

Under the class of bi-metallic cathode catalyst class, Pt-Pd supported on MWCNT was explored. In this study, influence of two surfactant, SDS and CTAB on ORR activity and durability was investigated to attain high performing Pt-Pd catalysts

with lower Pt content. Pt-Pd/CNT catalysts were prepared through MW assisted, polyol route in presence of SDS (Pt-Pd/CNT-S) or CTAB (Pt-Pd/CNT-C) and their performance was compared with Pt-Pd/CNT prepared in an identical way without any surfactant. The study showed the prominent influence of the type of surfactant in disaggregation of MWCNT bundles and the dispersion of Pt-Pd NPs on MWCNT support, which in turn controlled their catalytic activity for ORR. *In-situ* electrochemical characterization studies showed improved catalytic activity of Pt-Pd/CNT-S (ESA- 110 $m^2mg_{Pt}^{-1}$, R_{ct}- 7.5 Ω) compared to Pt-Pd/CNT-C (ESA- 29 $m^2mg_{Pt}^{-1}$, R_{ct}- 38.4 Ω) and Pt-Pd/CNT (ESA- 83 $m^2mg_{Pt}^{-1}$, R_{ct}- 12.7 Ω), demonstrating SDS as an efficient disperser for MWCNT. A comparison of their fuel cell performance was also made with commercial Pt/C catalyst. Higher fuel cell performance (power density-451 $mWcm^{-2}$; mass acitiviy- 84 $mAmg_{Pt}^{-1}$) was achieved with Pt-Pd/CNT-S having less Pt content (~12 wt. %) than the commercial Pt/C (20 wt.%) catalyst (power density-320 $mWcm^{-2}$; mass acitiviy-38 $mAmg_{Pt}^{-1}$) demonstrating that it is a viable cathode catalyst candidate for PEMFC that can help its wider commercialization.

In the last part of the thesis, in-depth comparative studies were carried out on durability and performance characteristics of screened Pt/V-TiO$_2$ and Pt-Pd/MWCNT catalysts along with commercial Pt/C catalyst (*Chapter 8*). A combination of simple, but effective, *in-situ* electrochemical procedures comprising of CV, CA, EIS and polarization measurements were conducted before and after ADT with potential cycling at 0.2-1.2 V for 6000 cycles, to assess the degradation behaviour of the catalysts. Both the carbon based catalysts showed lowered cell performance after ADT. However, Pt-Pd/MWCNT showed higher voltage (0.784 V *vs.* 0.669 V at 50 $mAcm^{-2}$) as compared to Pt/C exhibiting better ORR activity and durability. On the contrary, with Pt/V-TiO$_2$ catalyst an unexpected trend of increase in cell performance was observed after cycling tests. The improved performance of Pt/V-TiO$_2$ catalyst is attributed to high corrosion resistance, anchoring effect and increased ionic conductivity achieved with V-TiO$_2$ support as compared to carbon based supports. In terms of effective Pt utilization even after ADT, superior performance was obtained with Pt-Pd/MWCNT catalyst (mass acitiviy-57 $mAmg_{Pt}^{-1}$, peak power density- 1217

mWmg$_{Pt}$$^{-1}$) which was ascribed to stronger metal-metal and metal-support interactions which favorably modifies intrinsic Pt catalytic activity. This study also demonstrated practical applicability of Pt-Pd/MWCNT in a PEMFC three cell stack establishing its potential for wide scale PEMFC applications. Moreover, the study showed better fuel cell performance of Pt/V-TiO$_2$ (660 mWmg$_{Pt}$$^{-1}$; mass acitiviy-52 mAmg$_{Pt}$$^{-1}$) and Pt-Pd/MWCNT (1217 mWmg$_{Pt}$$^{-1}$; mass acitiviy-57 mAmg$_{Pt}$$^{-1}$) catalysts as compared to commercial Pt/C catalyst (496 mWmg$_{Pt}$$^{-1}$; mass activity- 6 mAmg$_{Pt}$$^{-1}$) making them prospective candidate to be considered for long term PEMFC applications.

This thesis presented a comprehensive approach to the development of promising Pt based cathode catalysts for PEMFC. This involved synthesis, characterization and *in-situ* performance evaluation of the proposed Pt based catalytic systems. To summarize briefly, the catalysts synthesized and investigated in this thesis demonstrated better PEMFC performance than the commercial Pt/C catalyst. The study revealed Pt/V-TiO$_2$ and Pt-Pd/MWCNT catalysts as highly promising, cost effective and durable cathode catalysts for PEMFC.

9.2. Future perspectives

The future perspectives of this research work are:

i. Scale up of the experiments conducted by single MEA in this study to stack experiments under typical PEMFC conditions.

ii. Evaluation of PEMFC performance with the present catalyst systems with lower Pt loading level (0.05-0.3 mg$_{Pt}$cm^{-2}) in order to reduce the amount of Pt per kW of fuel cell to achieve the much needed cost benefit to attain DOE target of $ 35 per kW.

iii. Modeling of EIS spectra with present catalyst systems for quantitative estimation of ionic conductivity of membrane and monitoring its changes during PEMFC operation.

iv. The present study revealed the influence of various carbon nano-forms as support for Pt on PEMFC performance. Further, investigations can be extended onto

nitrogen doping of carbon support materials which have been reported to change the nucleation and growth behavior of supported catalyst NPs.

v. The present study showed promising influence of V-TiO$_2$, MWCNT support and Pt-Pd bi-metallic NPs on fuel cell performance. Hence, investigations can be extended on the exploration of hybrid Pt-Pd/V-TiO$_2$ and Pt-Pd/V-TiO$_2$/MWCNT catalysts for ORR in PEMFC.

vi. Investigation of the present catalyst systems for different electrochemical reactions in other types of fuel cells such as DMFC, PAFC and Borohydride Fuel Cell.

References

Abràmoff M. D., Magalhães P. J. and Ram S. J. (2004). "Image processing with ImageJ." *Biophotonics International*, 11 (7): 36-42.

Ahmadi M. H., Mohammadi A., Pourfayaz F., Mehrpooya M., Bidi M., Valero A. and Uson S. (2016). "Thermodynamic analysis and optimization of a waste heat recovery system for proton exchange membrane fuel cell using transcritical carbon dioxide cycle and cold energy of liquefied natural gas." *Journal of Natural Gas Science and Engineering*, 34: 428-438.

Alayoglu S., Nilekar A. U., Mavrikakis M. and Eichhorn B. (2008). "Ru–Pt core–shell nanoparticles for preferential oxidation of carbon monoxide in hydrogen." *Nature Materials*, 7 (4): 333-338.

Anandha Ganesh P. and Jeyakumar D. (2017). "Nano-Porous Electro-Catalyst with Textured Surface Active Pd-Pt Islands for Efficient Methanol Tolerant Oxygen Reduction Reaction." *Chemistry Select*, 2 (25): 7544-7552.

Antolini E. (2007). "Platinum-based ternary catalysts for low temperature fuel cells: part I. Preparation methods and structural characteristics." *Applied Catalysis B: Environmental*, 74 (3): 324-336.

Antolini E. (2009). "Carbon supports for low-temperature fuel cell catalysts." *Applied Catalysis B: Environmental*, 88 (1): 1-24.

Antolini E. (2012). "Graphene as a new carbon support for low-temperature fuel cell catalysts." *Applied Catalysis B: Environmental*, 123: 52-68.

Antolini E., Salgado J. R. C., da Silva R. M. and Gonzalez E. R. (2007). "Preparation of carbon supported binary Pt–M alloy catalysts (M = first row transition metals) by low/medium temperature methods." *Materials Chemistry and Physics*, 101 (2–3): 395-403.

Antolini E., Salgado J. R. C. and Gonzalez E. R. (2006). "The stability of Pt–M (M = first row transition metal) alloy catalysts and its effect on the activity in low temperature fuel cells: A literature review and tests on a Pt–Co catalyst." *Journal of Power Sources*, 160 (2): 957-968.

Arbiol J., Cerda J., Dezanneau G., Cirera A., Peiro F., Cornet A. and Morante J. R. (2002). "Effects of Nb doping on the TiO2 anatase-to-rutile phase transition." *Journal of Applied Physics*, 92 (2): 853-861.

Aruna S. T., Tirosh S. and Zaban A. (2000). "Nanosize rutile titania particle synthesis a hydrothermal method without mineralizers." *Journal of Materials Chemistry*, 10 (10): 2388-2391.

Asgharinezhad M., Eshaghi A. and Arab A. (2016). "Fabrication and characterization of optical and electrical properties of vanadium doped titanium dioxide nanostructured thin film." *Optik-International Journal for Light and Electron Optics*, 127 (19): 8130-8134.

Bagotskii V. S., Tarasevich M. R. and Filinovskii V. Y. (1969). "Calculation of the

References

kinetic parameters of conjugated reactions of oxygen and hydrogen peroxide." *Elektrokhimiya*, 5: 1218.

Bagotsky V. S. (2012). *Fuel cells: Problems and Solutions*, John Wiley & Sons.

Bai Y., Park I. S., Lee S. J., Bae T. S., Watari F., Uo M. and Lee M. H. (2011). "Aqueous dispersion of surfactant-modified multiwalled carbon nanotubes and their application as an antibacterial agent." *Carbon*, 49 (11): 3663-3671.

Baker R. T. K., Prestridge E. B. and Garten R. L. (1979). "Electron microscopy of supported metal particles: I. Behavior of Pt on titanium oxide, aluminum oxide, silicon oxide, and carbon." *Journal of Catalysis*, 56 (3): 390-406.

Balbuena P. B., Altomare D., Vadlamani N., Bingi S., Agapito L. A. and Seminario J. M. (2004). "Adsorption of O, OH, and H2O on Pt-based bimetallic clusters alloyed with Co, Cr, and Ni." *The Journal of Physical Chemistry A*, 108 (30): 6378-6384.

Barathi P. and Senthil Kumar A. (2013). "Electrochemical conversion of unreactive pyrene to highly redox-active 1, 2-quinone derivatives on a carbon nanotube-modified gold electrode surface and its selective hydrogen peroxide sensing." *Langmuir*, 29 (34): 10617-10623.

Barbir F. (2012). *PEM fuel cells: Theory and Practice*, Academic Press.

Bartholomew R. F. and Frankl D. R. (1969). "Electrical properties of some titanium oxides." *Physical Review*, 187 (3): 828.

Bauer A., Chevallier L., Hui R., Cavaliere S., Zhang J., Jones D. and Rozière J. (2012). "Synthesis and characterization of Nb-TiO 2 mesoporous microsphere and nanofiber supported Pt catalysts for high temperature PEM fuel cells." *Electrochimica Acta*, 77: 1-7.

Bauer A., Lee K., Song C., Xie Y., Zhang J. and Hui R. (2010). "Pt nanoparticles deposited on TiO2 based nanofibers: Electrochemical stability and oxygen reduction activity." *Journal of Power Sources*, 195 (10): 3105-3110.

Bavykin D. V., Friedrich J. M. and Walsh F. C. (2006). "Protonated titanates and TiO2 nanostructured materials: synthesis, properties, and applications." *Advanced Materials*, 18 (21): 2807-2824.

Beard B. C. and Ross P. N. (1986). "Characterization of a Titanium-Promoted Supported Platinum Electrocatalyst." *Journal of The Electrochemical Society*, 133 (9): 1839-1845.

Beranek R. and Kisch H. (2008). "Tuning the optical and photoelectrochemical properties of surface-modified TiO 2." *Photochemical & Photobiological Sciences*, 7 (1): 40-48.

Bessel C. A., Laubernds K., Rodriguez N. M. and Baker R. T. K. (2001). "Graphite nanofibers as an electrode for fuel cell applications." *The Journal of Physical Chemistry B*, 105 (6): 1115-1118.

Bezerra C. W. B., Zhang L., Liu H., Lee K., Marques A. L. B., Marques E. P., Wang H. and Zhang J. (2007). "A review of heat-treatment effects on activity and stability

of PEM fuel cell catalysts for oxygen reduction reaction." *Journal of Power Sources*, 173 (2): 891-908.

Biloul A., Coowar F., Contamin O., Scarbeck G., Savy M., Van den Ham D., Riga J. and Verbist J. J. (1990). "Oxygen reduction in acid media on supported iron naphthalocyanine: effect of isomer configuration and pyrolysis." *Journal of Electroanalytical Chemistry and Interfacial Electrochemistry*, 289 (1-2): 189-201.

Bonakdarpour A., Löbel R., Atanasoski R. T., Vernstrom G. D., Schmoeckel A. K., Debe M. K. and Dahn J. R. (2006). "Dissolution of Transition Metals in Combinatorially Sputtered Pt1− x− y M x M y′(M, M′= Co, Ni, Mn, Fe) PEMFC Electrocatalysts." *Journal of the Electrochemical Society*, 153 (10): A1835-A1846.

Cai Z.-x., Liu C.-c., Wu G.-h., Chen X.-m. and Chen X. (2014). "Green synthesis of Pt-on-Pd bimetallic nanodendrites on graphene via in situ reduction, and their enhanced electrocatalytic activity for methanol oxidation." *Electrochimica Acta*, 127: 377-383.

Carmo M., Paganin V. A., Rosolen J. M. and Gonzalez E. R. (2005). "Alternative supports for the preparation of catalysts for low-temperature fuel cells: the use of carbon nanotubes." *Journal of Power Sources*, 142 (1–2): 169-176.

Celorrio V., Flórez-Montaño J., Moliner R., Pastor E. and Lázaro M. J. (2014). "Fuel cell performance of Pt electrocatalysts supported on carbon nanocoils." *International Journal of Hydrogen Energy*, 39 (10): 5371-5377.

Cerri I., Nagami T., Davies J., Mormiche C., Vecoven A. and Hayden B. (2013). "Innovative catalyst supports to address fuel cell stack durability." *International Journal of Hydrogen Energy*, 38 (1): 640-645.

Chaisubanan N., Pruksathorn K., Vergnes H., Senocq F. and Hunsom M. (2016). "Stability of TiO2 Promoted PtCo/C Catalyst for Oxygen Reduction Reaction." *International Journal of Electrochemical Science*, 11 (2): 1012-1028.

Chandran R. and Dharmalingam S. (2014). "Facile Synthesis and Characterization of PtCu Core–Shell and Alloy Nanoparticles." *Journal of Nanoscience and Nanotechnology*, 14 (9): 6957-6964.

Che G., Lakshmi B. B., Fisher E. R. and Martin C. R. (1998). "Carbon nanotubule membranes for electrochemical energy storage and production." *Nature*, 393 (6683): 346-349.

Chen G., Bare S. R. and Mallouk T. E. (2002). "Development of supported bifunctional electrocatalysts for unitized regenerative fuel cells." *Journal of the Electrochemical Society*, 149 (8): A1092-A1099.

Chen J., Jiang C., Yang X., Feng L., Gallogly E. B. and Wang R. (2011). "Studies on how to obtain the best catalytic activity of Pt/C catalyst by three reduction routes for methanol electro-oxidation." *Electrochemistry Communications*, 13 (4): 314-316.

Chen Q., Cao Z., Du G., Kuang Q., Huang J., Xie Z. and Zheng L. (2017). "Excavated octahedral Pt-Co alloy nanocrystals built with ultrathin nanosheets as superior multifunctional electrocatalysts for energy conversion applications." *Nano Energy*, 39: 582-589.

References

Chen Y., Yang J., Yang Y., Peng Z., Li J., Mei T., Wang J., Hao M., Chen Y. and Xiong W. (2015). "A facile strategy to synthesize three-dimensional Pd@ Pt core–shell nanoflowers supported on graphene nanosheets as enhanced nanoelectrocatalysts for methanol oxidation." *Chemical Communications*, 51 (52): 10490-10493.

Chen Z., Deng W., Wang X. and Yan Y. (2007). "Durability and activity study of single-walled, double-walled and multi-walled carbon nanotubes supported Pt catalyst for PEMFCs." *ECS Transactions*, 11 (1): 1289-1299.

Chen Z., Waje M., Li W. and Yan Y. (2007). "Supportless Pt and PtPd Nanotubes as Electrocatalysts for Oxygen-Reduction Reactions." *Angewandte Chemie International Edition*, 46 (22): 4060-4063.

Chevallier L., Bauer A., Cavaliere S., Hui R., Rozière J. and Jones D. J. (2012). "Mesoporous nanostructured Nb-doped titanium dioxide microsphere catalyst supports for PEM fuel cell electrodes." *ACS applied materials & interfaces*, 4 (3): 1752-1759.

Chhina H., Campbell S. and Kesler O. (2009). "Ex situ and in situ stability of platinum supported on niobium-doped titania for PEMFCs." *Journal of the Electrochemical Society*, 156 (10): B1232-B1237.

Choi K.-H., Jang Y., Chung D. Y., Seo P., Jun S. W., Lee J. E., Oh M. H., Shokouhimehr M., Jung N. and Yoo S. J. (2016). "A simple synthesis of urchin-like Pt–Ni bimetallic nanostructures as enhanced electrocatalysts for the oxygen reduction reaction." *Chemical Communications*, 52 (3): 597-600.

Choi W., Termin A. and Hoffmann M. R. (1994). "Effects of Metal-Ion Dopants on the Photocatalytic Reactivity of Quantum-Sized TiO2 Particles." *Angewandte Chemie International Edition in English*, 33 (10): 1091-1092.

Christoforidis K. C. and Fernández-García M. (2016). "Photoactivity and charge trapping sites in copper and vanadium doped anatase TiO 2 nano-materials." *Catalysis Science & Technology*, 6 (4): 1094-1105.

Chu Y.-Y., Wang Z.-B., Jiang Z.-Z., Gu D.-M. and Yin G.-P. (2012). "Facile synthesis of hollow spherical sandwich PtPd/C catalyst by electrostatic self-assembly in polyol solution for methanol electrooxidation." *Journal of Power Sources*, 203: 17-25.

Colón-Mercado H. R. and Popov B. N. (2006). "Stability of platinum based alloy cathode catalysts in PEM fuel cells." *Journal of Power Sources*, 155 (2): 253-263.

Couper A. M., Pletcher D. and Walsh F. C. (1990). "Electrode materials for electrosynthesis." *Chemical Reviews*, 90 (5): 837-865.

Cui Z., Feng L., Liu C. and Xing W. (2011). "Pt nanoparticles supported on WO 3/C hybrid materials and their electrocatalytic activity for methanol electro-oxidation." *Journal of Power Sources*, 196 (5): 2621-2626.

Damjanovic A., Genshaw M. A. and Bockris J. O. M. (1966). "Distinction between intermediates produced in main and side electrodic reactions." *The Journal of Chemical Physics*, 45 (11): 4057-4059.

Daş E., Gürsel S. A., Şanli L. I. and Yurtcan A. B. (2016). "Comparison of two different catalyst preparation methods for graphene nanoplatelets supported platinum catalysts." *International Journal of Hydrogen Energy*, 41 (23): 9755-9761.

Das N., Eckert H., Hu H., Wachs I. E., Walzer J. F. and Feher F. J. (1993). "Bonding states of surface vanadium (V) oxide phases on silica: structural characterization by vanadium-51 NMR and Raman spectroscopy." *The Journal of Physical Chemistry*, 97 (31): 8240-8243.

De Volder M. F. L., Tawfick S. H., Baughman R. H. and Hart A. J. (2013). "Carbon nanotubes: present and future commercial applications." *Science*, 339 (6119): 535-539.

Debe M. K. (2012). "Electrocatalyst approaches and challenges for automotive fuel cells." *Nature*, 486 (7401): 43.

Debe M. K. (2012). "Electrocatalyst approaches and challenges for automotive fuel cells." *Nature*, 486 (7401): 43-51.

Dhanasekaran P., Selvaganesh S. V. and Bhat S. D. (2016). "Nitrogen and carbon doped titanium oxide as an alternative and durable electrocatalyst support in polymer electrolyte fuel cells." *Journal of Power Sources*, 304: 360-372.

Dhanasekaran P., Selvaganesh S. V. and Bhat S. D. (2016). "A nitrogen and cobalt co-doped titanium dioxide framework as a stable catalyst support for polymer electrolyte fuel cells." *RSC Advances*, 6 (91): 88736-88750.

Ding E., More K. L. and He T. (2008). "Preparation and characterization of carbon-supported PtTi alloy electrocatalysts." *Journal of Power Sources*, 175 (2): 794-799.

Divya P. and Ramaprabhu S. (2016). "Investigation of Electrocatalytic Activity of Pt–Y Alloy Nanoparticles Dispersed on Nitrogen Doped Graphene for Proton Exchange Membrane Fuel Cell." *Journal of Nanoscience and Nanotechnology*, 16 (9): 9642-9650.

Dobrzańska-Danikiewicz A. D., Łukowiec D. and Wolany W. "Comparative analysis of the structure of nanocomposites consisting of MWCNTs and Pt or Re nanoparticles." *Carbon*, 31: 31.

Dresselhaus M. S. and Eklund P. C. (2000). "Phonons in carbon nanotubes." *Advances in Physics*, 49 (6): 705-814.

Du C. Y., Zhao T. S. and Yang W. W. (2007). "Effect of methanol crossover on the cathode behavior of a DMFC: A half-cell investigation." *Electrochimica Acta*, 52 (16): 5266-5271.

Du L., Shao Y., Sun J., Yin G., Liu J. and Wang Y. (2016). "Advanced catalyst supports for PEM fuel cell cathodes." *Nano Energy*, 29: 314-322.

Du Q., Wu J. and Yang H. (2013). "Pt@ Nb-TiO2 catalyst membranes fabricated by electrospinning and atomic layer deposition." *ACS Catalysis*, 4 (1): 144-151.

Du S., Lu Y., Malladi S. K., Xu Q. and Steinberger-Wilckens R. (2014). "A simple approach for PtNi-MWCNT hybrid nanostructures as high performance electrocatalysts for the oxygen reduction reaction." *Journal of Materials Chemistry A*,

References

2 (3): 692-698.

Duan H. and Xu C. (2015). "Nanoporous PtPd alloy electrocatalysts with high activity and stability toward oxygen reduction reaction." *Electrochimica Acta*, 152: 417-424.

Duan W. H., Wang Q. and Collins F. (2011). "Dispersion of carbon nanotubes with SDS surfactants: a study from a binding energy perspective." *Chemical Science*, 2 (7): 1407-1413.

Dubau L., Durst J., Maillard F., Guétaz L., Chatenet M., André J. and Rossinot E. (2011). "Further insights into the durability of Pt 3 Co/C electrocatalysts: Formation of "hollow" Pt nanoparticles induced by the Kirkendall effect." *Electrochimica Acta*, 56 (28): 10658-10667.

Dudin P. V., Unwin P. R. and Macpherson J. V. (2010). "Electrochemical nucleation and growth of gold nanoparticles on single-walled carbon nanotubes: New mechanistic insights." *The Journal of Physical Chemistry C*, 114 (31): 13241-13248.

Easton E. B. and Pickup P. G. (2005). "An electrochemical impedance spectroscopy study of fuel cell electrodes." *Electrochimica Acta*, 50 (12): 2469-2474.

El-Deeb H. and Bron M. (2015). "Electrochemical Dealloying of PtCu/CNT Electrocatalysts Synthesized by NaBH 4-Assisted Polyol-Reduction: Influence of Preparation Parameters on Oxygen Reduction Activity." *Electrochimica Acta*, 164: 315-322.

Elen K., Capon B., De Dobbelaere C., Dewulf D., Peys N., Detavernier C., Hardy A. and Van Bael M. K. (2014). "Transparent conducting oxide films of group V doped titania prepared by aqueous chemical solution deposition." *Thin Solid Films*, 555: 33-38.

Elezović N. R., Babić B. M., Gajić-Krstajić L., Radmilović V., Krstajić N. V. and Vračar L. J. (2010). "Synthesis, characterization and electrocatalytical behavior of Nb–TiO2/Pt nanocatalyst for oxygen reduction reaction." *Journal of Power Sources*, 195 (13): 3961-3968.

Elezović N. R., Babić B. M., Gajić-Krstajić L., Radmilović V., Krstajić N. V. and Vračar L. J. (2010). "Synthesis, characterization and electrocatalytical behavior of Nb–TiO 2/Pt nanocatalyst for oxygen reduction reaction." *Journal of Power Sources*, 195 (13): 3961-3968.

Elezović N. R., Babić B. M., Radmilović V. R., Gojković S. L., Krstajić N. V. and Vračar L. M. (2008). "Pt/C doped by MoO x as the electrocatalyst for oxygen reduction and methanol oxidation." *Journal of Power Sources*, 175 (1): 250-255.

Elezovic N. R., Babic B. M., Radmilovic V. R., Vracar L. M. and Krstajic N. V. (2009). "Synthesis and characterization of MoO x-Pt/C and TiO x-Pt/C nano-catalysts for oxygen reduction." *Electrochimica Acta*, 54 (9): 2404-2409.

Elezovic N. R., Radmilovic V. R. and Krstajic N. V. (2016). "Platinum nanocatalysts on metal oxide based supports for low temperature fuel cell applications." *RSC Advances*, 6 (8): 6788-6801.

Esfahani R. A. M., Videla A. H. A. M., Vankova S. and Specchia S. (2015). "Stable

and methanol tolerant Pt/TiOx-C electrocatalysts for the oxygen reduction reaction." *International Journal of Hydrogen Energy*, 40 (42): 14529-14539.

Fang B., Chaudhari N. K., Kim M.-S., Kim J. H. and Yu J.-S. (2009). "Homogeneous deposition of platinum nanoparticles on carbon black for proton exchange membrane fuel cell." *Journal of the American Chemical Society*, 131 (42): 15330-15338.

Farsinezhad S., Sharma H. and Shankar K. (2015). "Interfacial band alignment for photocatalytic charge separation in TiO_2 nanotube arrays coated with CuPt nanoparticles." *Physical Chemistry Chemical Physics*, 17 (44): 29723-29733.

Feng Y., Liu H. and Yang J. (2017). "A selective electrocatalyst–based direct methanol fuel cell operated at high concentrations of methanol." *Science Advances*, 3 (6): e1700580.

Fernández J. L., Walsh D. A. and Bard A. J. (2005). "Thermodynamic guidelines for the design of bimetallic catalysts for oxygen electroreduction and rapid screening by scanning electrochemical microscopy. M-Co (M: Pd, Ag, Au)." *Journal of the American Chemical Society*, 127 (1): 357-365.

Fovet Y., Gal J.-Y. and Toumelin-Chemla F. (2001). "Influence of pH and fluoride concentration on titanium passivating layer: stability of titanium dioxide." *Talanta*, 53 (5): 1053-1063.

Fujigaya T. and Nakashima N. (2013). "Fuel Cell Electrocatalyst Using Polybenzimidazole-Modified Carbon Nanotubes As Support Materials." *Advanced Materials*, 25 (12): 1666-1681.

Galema S. A. (1997). "Microwave chemistry." *Chemical Society Reviews*, 26 (3): 233-238.

Gamez A., Richard D. and Gallezot P. (1999). "In Resume des Journees d'Etude Piles a Combustible." *Paris, France*: 401.

Ganesh I., Gupta A. K., Kumar P. P., Sekhar P. S. C., Radha K., Padmanabham G. and Sundararajan G. (2012). "Preparation and characterization of Co-doped TiO 2 materials for solar light induced current and photocatalytic applications." *Materials Chemistry and Physics*, 135 (1): 220-234.

Ganesh P. A. and Jeyakumar D. (2014). "One pot aqueous synthesis of nanoporous Au 85 Pt 15 material with surface bound Pt islands: an efficient methanol tolerant ORR catalyst." *Nanoscale*, 6 (21): 13012-13021.

Gangeri M., Perathoner S. and Centi G. (2006). "Synthesis and performances of carbon-supported noble metal nanoclusters as electrodes for polymer electrolyte membrane fuel cells." *Inorganica Chimica Acta*, 359 (15): 4828-4832.

Gao B., Zhang Y., Zhang J., Kong J. and Liu Z. (2008). "Systematic comparison of the Raman spectra of metallic and semiconducting SWNTs." *The Journal of Physical Chemistry C*, 112 (22): 8319-8323.

García B. L., Fuentes R. and Weidner J. W. (2007). "Low-Temperature Synthesis of a PtRu∕Nb0. 1Ti0. 9O2 Electrocatalyst for Methanol Oxidation." *Electrochemical and Solid-State Letters*, 10 (7): B108-B110.

References

Gasteiger H. A., Kocha S. S., Sompalli B. and Wagner F. T. (2005). "Activity benchmarks and requirements for Pt, Pt-alloy, and non-Pt oxygen reduction catalysts for PEMFCs." *Applied Catalysis B: Environmental*, 56 (1–2): 9-35.

Gasteiger H. A. and Marković N. M. (2009). "Just a Dream—or Future Reality?" *Science*, 324 (5923): 48-49.

Gebauer C., Hoffmann D., Jusys Z. and Behm R. J. (2016). "Novel, Highly Conductive Pt/TiO2 Thin-Film Model Catalyst Electrodes: The Role of Metal–Support Interactions." *ChemElectroChem*, 3 (10): 1553-1563.

Golikand A. N., Lohrasbi E. and Asgari M. (2010). "Enhancing the durability of multi-walled carbon nanotube supported by Pt and Pt–Pd nanoparticles in gas diffusion electrodes." *International Journal of Hydrogen Energy*, 35 (17): 9233-9240.

Gopal M., Chan W. J. M. and De Jonghe L. C. (1997). "Room temperature synthesis of crystalline metal oxides." *Journal of Materials Science*, 32 (22): 6001-6008.

Graves J. E., Pletcher D., Clarke R. L. and Walsh F. C. (1991). "The electrochemistry of Magnéli phase titanium oxide ceramic electrodes Part I. The deposition and properties of metal coatings." *Journal of Applied Electrochemistry*, 21 (10): 848-857.

Grolleau C., Coutanceau C., Pierre F. and Leger J. M. (2010). "Optimization of a surfactant free polyol method for the synthesis of platinum–cobalt electrocatalysts using Taguchi design of experiments." *Journal of Power Sources*, 195 (6): 1569-1576.

Gruver G. A. (1978). "The corrosion of carbon black in phosphoric acid." *Journal of the Electrochemical Society*, 125 (10): 1719-1720.

Guo J., Sun G., Shiguo S., Shiyou Y., Weiqian Y., Jing Q., Yushan Y. and Qin X. (2007). "Polyol-synthesized PtRu/C and PtRu black for direct methanol fuel cells." *Journal of Power Sources*, 168 (2): 299-306.

Gupta C., Maheshwari P. H. and Dhakate S. R. (2016). "Development of multiwalled carbon nanotubes platinum nanocomposite as efficient PEM fuel cell catalyst." *Materials for Renewable and Sustainable Energy*, 5 (1): 2.

Gupta C., Maheshwari P. H., Sachdev D., Sahu A. K. and Dhakate S. R. (2016). "Highly purified CNTs: an exceedingly efficient catalyst support for PEM fuel cell." *RSC Advances*, 6 (38): 32258-32271.

Gustavsson M., Ekström H., Hanarp P., Eurenius L., Lindbergh G., Olsson E. and Kasemo B. (2007). "Thin film Pt/TiO 2 catalysts for the polymer electrolyte fuel cell." *Journal of Power Sources*, 163 (2): 671-678.

Güvenatam B., Fıçıcılar B., Bayrakçeken A. and Eroğlu İ. (2012). "Hollow core mesoporous shell carbon supported Pt electrocatalysts with high Pt loading for PEMFCs." *International Journal of Hydrogen Energy*, 37 (2): 1865-1874.

Hamann C. H., Hamnett A. and Vielstich W. (1998). "Electrochemistry. 1998." *Wiley-VCH*.

Hameed R. M. A., Amin R. S., El-Khatib K. M. and Fetohi A. E. (2016). "Preparation and characterization of Pt–CeO 2/C and Pt–TiO 2/C electrocatalysts with improved

254

electrocatalytic activity for methanol oxidation." *Applied Surface Science*, 367: 382-390.

Hayden B. E., Malevich D. V. and Pletcher D. (2001). "Electrode coatings from sprayed titanium dioxide nanoparticles–behaviour in NaOH solutions." *Electrochemistry Communications*, 3 (8): 390-394.

He D., Mu S. and Pan M. (2011). "Perfluorosulfonic acid-functionalized Pt/carbon nanotube catalysts with enhanced stability and performance for use in proton exchange membrane fuel cells." *Carbon*, 49 (1): 82-88.

He L., Franzen H. F. and Johnson D. C. (1996). "Synthesis and characterization of Pt-Ti4O7 microelectrode arrays." *Journal of Applied Electrochemistry*, 26 (8): 785-793.

He Z., Chen J., Liu D., Tang H., Deng W. and Kuang Y. (2004). "Deposition and electrocatalytic properties of platinum nanoparticals on carbon nanotubes for methanol electrooxidation." *Materials Chemistry and Physics*, 85 (2): 396-401.

Herrera J. E., Balzano L., Pompeo F. and Resasco D. E. (2003). "Raman characterization of single-walled nanotubes of various diameters obtained by catalytic disproportionation of CO." *Journal of Nanoscience and Nanotechnology*, 3 (1-2): 133-138.

Hicks M., Pierpont D., Turner P. and Watschke T. (2006). "Accelerated testing and lifetime modeling for the development of durable fuel cell MEAs." *ECS Transactions*, 1 (8): 229-237.

Ho V. T. T., Pan C.-J., Rick J., Su W.-N. and Hwang B.-J. (2011). "Nanostructured Ti0. 7Mo0. 3O2 support enhances electron transfer to Pt: high-performance catalyst for oxygen reduction reaction." *Journal of the American Chemical Society*, 133 (30): 11716-11724.

Horsley J. A. (1979). "A molecular orbital study of strong metal-support interaction between platinum and titanium dioxide." *Journal of the American Chemical Society*, 101 (11): 2870-2874.

Hsieh B.-J., Tsai M.-C., Pan C.-J., Su W.-N., Rick J., Lee J.-F., Yang Y.-W. and Hwang B.-J. (2017). "Platinum loaded on dual-doped TiO2 as an active and durable oxygen reduction reaction catalyst." *NPG Asia Materials*, 9 (7): e403.

Hsieh C.-T., Lin J.-Y. and Wei J.-L. (2009). "Deposition and electrochemical activity of Pt-based bimetallic nanocatalysts on carbon nanotube electrodes." *International Journal of Hydrogen Energy*, 34 (2): 685-693.

Hsieh C.-T., Liu Y.-Y., Chen W.-Y. and Hsieh Y.-H. (2011). "Electrochemical activity and durability of Pt–Sn alloys on carbon-based electrodes prepared by microwave-assisted synthesis." *International Journal of Hydrogen Energy*, 36 (24): 15766-15774.

Hsieh C.-T., Liu Y.-Y., Cheng Y.-S. and Chen W.-Y. (2011). "Microwave-assisted synthesis and pulse electrodeposition of palladium nanocatalysts on carbon nanotube-based electrodes." *Electrochimica Acta*, 56 (18): 6336-6344.

Hsieh S. H., Hsu M. C., Liu W. L. and Chen W. J. (2013). "Study of Pt catalyst on

References

graphene and its application to fuel cell." *Applied Surface Science*, 277: 223-230.

Hu S., Li F., Fan Z. and Chang C.-C. (2011). "Enhanced photocatalytic activity and stability of nano-scaled TiO 2 co-doped with N and Fe." *Applied Surface Science*, 258 (1): 182-188.

Huang M., Dong G., Wu C. and Guan L. (2014). "Preparation of highly dispersed Pt nanoparticles supported on single-walled carbon nanotubes by a microwave-assisted polyol method and their remarkably catalytic activity." *International Journal of Hydrogen Energy*, 39 (9): 4266-4273.

Huang S.-Y., Ganesan P., Park S. and Popov B. N. (2009). "Development of a Titanium Dioxide-Supported Platinum Catalyst with Ultrahigh Stability for Polymer Electrolyte Membrane Fuel Cell Applications." *Journal of the American Chemical Society*, 131 (39): 13898-13899.

Huang X., Zhao Z., Cao L., Chen Y., Zhu E., Lin Z., Li M., Yan A., Zettl A. and Wang Y. M. (2015). "High-performance transition metal–doped Pt3Ni octahedra for oxygen reduction reaction." *Science*, 348 (6240): 1230-1234.

Hussain S., Erikson H., Kongi N., Merisalu M., Rähn M., Sammelselg V., Maia G. and Tammeveski K. (2017). "Platinum Particles Electrochemically Deposited on Multiwalled Carbon Nanotubes for Oxygen Reduction Reaction in Acid Media." *Journal of The Electrochemical Society*, 164 (9): F1014-F1021.

Hwang S. J., Kim S.-K., Lee J.-G., Lee S.-C., Jang J. H., Kim P., Lim T.-H., Sung Y.-E. and Yoo S. J. (2012). "Role of Electronic Perturbation in Stability and Activity of Pt-Based Alloy Nanocatalysts for Oxygen Reduction." *Journal of the American Chemical Society*, 134 (48): 19508-19511.

Iketani K., Sun R.-D., Toki M., Hirota K. and Yamaguchi O. (2004). "Sol–gel-derived $V_xTi_{1-x}O_2$ films and their photocatalytic activities under visible light irradiation." *Materials Science and Engineering: B*, 108 (3): 187-193.

Inoue M., Akamaru S., Taguchi A. and Abe T. (2008). "Physical and electrochemical properties of Pt–Ru/C samples prepared on various carbon supports by using the barrel sputtering system." *Vacuum*, 83 (3): 658-663.

Ioroi T., Siroma Z., Fujiwara N., Yamazaki S.-i. and Yasuda K. (2005). "Sub-stoichiometric titanium oxide-supported platinum electrocatalyst for polymer electrolyte fuel cells." *Electrochemistry Communications*, 7 (2): 183-188.

Iranzo A., Muñoz M., López E., Pino J. and Rosa F. (2010). "Experimental fuel cell performance analysis under different operating conditions and bipolar plate designs." I*nternational Journal of Hydrogen Energy*, 35 (20): 11437-11447.

Ishiguro N., Kityakarn S., Sekizawa O., Uruga T., Matsui H., Taguchi M., Nagasawa K., Yokoyama T. and Tada M. (2016). "Kinetics and Mechanism of Redox Processes of Pt/C and Pt3Co/C Cathode Electrocatalysts in a Polymer Electrolyte Fuel Cell during an Accelerated Durability Test." *The Journal of Physical Chemistry C*, 120 (35): 19642-19651.

Jafri R. I., Rajalakshmi N., Dhathathreyan K. S. and Ramaprabhu S. (2015). "Nitrogen doped graphene prepared by hydrothermal and thermal solid state methods

as catalyst supports for fuel cell." *International Journal of Hydrogen Energy*, 40 (12): 4337-4348.

Jafri R. I., Rajalakshmi N. and Ramaprabhu S. (2010). "Nitrogen doped graphene nanoplatelets as catalyst support for oxygen reduction reaction in proton exchange membrane fuel cell." *Journal of Materials Chemistry*, 20 (34): 7114-7117.

Jaiswal R., Patel N., Kothari D. C. and Miotello A. (2012). "Improved visible light photocatalytic activity of TiO 2 co-doped with Vanadium and Nitrogen." *Applied Catalysis B: Environmental*, 126: 47-54.

Jalan V. and Taylor E. J. (1983). "Importance of interatomic spacing in catalytic reduction of oxygen in phosphoric acid." *Journal of the Electrochemical Society*, 130 (11): 2299-2302.

Jha N., Jafri R. I., Rajalakshmi N. and Ramaprabhu S. (2011). "Graphene-multi walled carbon nanotube hybrid electrocatalyst support material for direct methanol fuel cell." *International Journal of Hydrogen Energy*, 36 (12): 7284-7290.

Jia N., Martin R. B., Qi Z., Lefebvre M. C. and Pickup P. G. (2001). "Modification of carbon supported catalysts to improve performance in gas diffusion electrodes." *Electrochimica Acta*, 46 (18): 2863-2869.

Jiang L., Colmenares L., Jusys Z., Sun G. Q. and Behm R. J. (2007). "Ethanol electrooxidation on novel carbon supported Pt/SnO x/C catalysts with varied Pt: Sn ratio." *Electrochimica Acta*, 53 (2): 377-389.

Jiang L., Sun G., Sun S., Liu J., Tang S., Li H., Zhou B. and Xin Q. (2005). "Structure and chemical composition of supported Pt–Sn electrocatalysts for ethanol oxidation." *Electrochimica Acta*, 50 (27): 5384-5389.

Jiang Z. and Jiang Z.-J. (2011). *Carbon Nanotubes Supported Metal Nanoparticles for the Applications in Proton Exchange Membrane Fuel Cells (PEMFCs)*. Carbon Nanotubes - Growth and Applications. D. M. Naraghi. Rijeka, InTech**:** Ch. 24.

Jung J.-H., Cha M.-S. and Kim J.-B. (2012). "Optimization of nafion ionomer content using synthesized Pt/carbon nanofibers catalyst in polymer electrolyte membrane fuel cell." *Journal of Nanoscience and Nanotechnology*, 12 (7): 5412-5417.

Jung J. H., Park H. J., Kim J. and Hur S. H. (2014). "Highly durable Pt/graphene oxide and Pt/C hybrid catalyst for polymer electrolyte membrane fuel cell." *Journal of Power Sources*, 248: 1156-1162.

Jung N., Chung D. Y., Ryu J., Yoo S. J. and Sung Y.-E. (2014). "Pt-based nanoarchitecture and catalyst design for fuel cell applications." *Nano Today*, 9 (4): 433-456.

Kallala M., Sanchez C. and Cabane B. (1992). "SAXS study of gelation and precipitation in titanium-based systems." *Journal of Non-Crystalline Solids*, 147: 189-193.

Kang S. H., Jeon T.-Y., Kim H.-S., Sung Y.-E. and Smyrl W. H. (2008). "Effect of annealing PtNi nanophases on extended TiO2 nanotubes for the electrochemical oxygen reduction reaction." *Journal of the Electrochemical Society*, 155 (10): B1058-

References

B1065.

Kang S. H., Sung Y.-E. and Smyrl W. H. (2008). "The effectiveness of sputtered PtCo catalysts on TiO2 nanotube arrays for the oxygen reduction reaction." *Journal of the Electrochemical Society*, 155 (11): B1128-B1135.

Karthikeyan N., Vinayan B. P., Rajesh M., Balaji K., Subramani A. K. and Ramaprabhu S. (2015). "Highly durable platinum based cathode electrocatalysts for PEMFC Application using oxygen and nitrogen functional groups attached nanocarbon supports." *Fuel Cells*, 15 (2): 278-287.

Khan M., Yousaf A. B., Chen M., Wei C., Wu X., Huang N., Qi Z. and Li L. (2015). "Mixed-phase Pd–Pt bimetallic alloy on graphene oxide with high activity for electrocatalytic applications." *Journal of Power Sources*, 282: 520-528.

Khodakov A., Olthof B., Bell A. T. and Iglesia E. (1999). "Structure and catalytic properties of supported vanadium oxides: support effects on oxidative dehydrogenation reactions." *Journal of Catalysis*, 181 (2): 205-216.

Kil K. C., Hong S.-G., Park J. O., Pak C., Chang H. and Paik U. (2014). "The use of MWCNT to enhance oxygen reduction reaction and adhesion strength between catalyst layer and gas diffusion layer in polymer electrolyte membrane fuel cell." *International Journal of Hydrogen Energy*, 39 (30): 17481-17486.

Kim D.-Y., Han S.-B., Lee Y.-W. and Park K.-W. (2013). "Core–shell nanostructure supported Pt catalyst with improved electrocatalytic stability in oxygen reduction reaction." *Materials Chemistry and Physics*, 137 (3): 704-708.

Kim J.-H., Chang S. and Kim Y.-T. (2014). "Compressive strain as the main origin of enhanced oxygen reduction reaction activity for Pt electrocatalysts on chromium-doped titania support." *Applied Catalysis B: Environmental*, 158: 112-118.

Kim J.-H., Kwon G., Lim H., Zhu C., You H. and Kim Y.-T. (2016). "Effects of transition metal doping in Pt/M-TiO 2 (M= V, Cr, and Nb) on oxygen reduction reaction activity." *Journal of Power Sources*, 320: 188-195.

Kim J. H., Kwon G., Chun H. and Kim Y. T. (2014). "Enhancement of Activity and Durability through Cr Doping of TiO2 Supports in Pt Electrocatalysts for Oxygen Reduction Reactions." *ChemCatChem*, 6 (11): 3239-3245.

Kim O.-H., Cho Y.-H., Jeon T.-Y., Kim J. W., Cho Y.-H. and Sung Y.-E. (2015). "Realization of Both High-Performance and Enhanced Durability of Fuel Cells: Pt-Exoskeleton Structure Electrocatalysts." *ACS applied materials & interfaces*, 7 (25): 14053-14063.

Kim P., Joo J. B., Kim W., Kim J., Song I. K. and Yi J. (2006). "NaBH 4-assisted ethylene glycol reduction for preparation of carbon-supported Pt catalyst for methanol electro-oxidation." *Journal of Power Sources*, 160 (2): 987-990.

Kim S. J., Park Y. J., Ra E. J., Kim K. K., An K. H., Lee Y. H., Choi J. Y., Park C. H., Doo S. K. and Park M. H. (2007). "Defect-induced loading of Pt nanoparticles on carbon nanotubes." *Applied Physics Letters*, 90 (2): 023114.

Kim T. W., Park I. S. and Ryoo R. (2003). "A synthetic route to ordered mesoporous

carbon materials with graphitic pore walls." *Angewandte Chemie*, 115 (36): 4511-4515.

Kinoshita K. (1990). "Particle size effects for oxygen reduction on highly dispersed platinum in acid electrolytes." *Journal of the Electrochemical Society*, 137 (3): 845-848.

Klosek S. and Raftery D. (2001). "Visible light driven V-doped TiO2 photocatalyst and its photooxidation of ethanol." *The Journal of Physical Chemistry B*, 105 (14): 2815-2819.

Knights S. D., Colbow K. M., St-Pierre J. and Wilkinson D. P. (2004). "Aging mechanisms and lifetime of PEFC and DMFC." *Journal of power sources*, 127 (1): 127-134.

Knupp S. L., Li W., Paschos O., Murray T. M., Snyder J. and Haldar P. (2008). "The effect of experimental parameters on the synthesis of carbon nanotube/nanofiber supported platinum by polyol processing techniques." *Carbon*, 46 (10): 1276-1284.

Koh B. S., hun Yoo J., Kim J. H. and Yi S.-C. (2016). "Platinum catalysts on KOH-treated multi-walled carbon nanotubes for PEM fuel cell nano sized dense structured electrodes." *Journal of Ceramic Processing Research*, 17 (4): 332-337.

Kongkanand A., Kuwabata S., Girishkumar G. and Kamat P. (2006). "Single-wall carbon nanotubes supported platinum nanoparticles with improved electrocatalytic activity for oxygen reduction reaction." *Langmuir*, 22 (5): 2392-2396.

Krstajic N. V., Vracar L. M., Radmilovic V. R., Neophytides S. G., Labou M., Jaksic J. M., Tunold R., Falaras P. and Jaksic M. M. (2007). "Advances in interactive supported electrocatalysts for hydrogen and oxygen electrode reactions." *Surface Science*, 601 (9): 1949-1966.

Kumar A. and Ramani V. (2014). "Strong metal–support interactions enhance the activity and durability of platinum supported on tantalum-modified titanium dioxide electrocatalysts." *ACS Catalysis*, 4 (5): 1516-1525.

Kundu P., Nethravathi C., Deshpande P. A., Rajamathi M., Madras G. and Ravishankar N. (2011). "Ultrafast microwave-assisted route to surfactant-free ultrafine Pt nanoparticles on graphene: synergistic co-reduction mechanism and high catalytic activity." *Chemistry of Materials*, 23 (11): 2772-2780.

Landmann M., Rauls E. and Schmidt W. G. (2012). "The electronic structure and optical response of rutile, anatase and brookite TiO 2." *Journal of Physics: Condensed Matter*, 24 (19): 195503.

Larminie J., Dicks A. and McDonald M. S. (2003). *Fuel cell systems explained*, J. Wiley Chichester, UK.

Lebègue E., Baranton S. and Coutanceau C. (2011). "Polyol synthesis of nanosized Pt/C electrocatalysts assisted by pulse microwave activation." *Journal of Power Sources*, 196 (3): 920-927.

Lee C.-L., Chiou H.-P., Wu S.-C. and Wu C.-C. (2010). "Alloy ratio effect of Pd/Pt nanoparticles on carbon nanotubes for catalysing methanol-tolerant oxygen

reduction." *Electrochimica Acta*, 56 (2): 687-692.

Lee C.-L., Huang C.-H., Huang K.-L., Tsai Y.-L. and Yang C.-C. (2013). "A comparison of three carbon nanoforms as catalyst supports for the oxygen reduction reaction." *Carbon*, 60: 392-400.

Lee S.-J., Pyun S.-I., Lee S.-K. and Kang S.-J. L. (2008). "Fundamentals of Rotating Disc and Ring–Disc Electrode Techniques and their Applications to Study of the Oxygen Reduction Mechanism at Pt/C Electrode for Fuel Cells." *Israel Journal of Chemistry*, 48 (3-4): 215-228.

Lee S. J., Mukerjee S., McBreen J., Rho Y. W., Kho Y. T. and Lee T. H. (1998). "Effects of Nafion impregnation on performances of PEMFC electrodes." *Electrochimica Acta*, 43 (24): 3693-3701.

Lee W.-J., Alhosan M., Yohe S. L., Macy N. L. and Smyrl W. H. (2008). "Synthesis of Pt/TiO2 nanotube catalysts for cathodic oxygen reduction." *Journal of the Electrochemical Society*, 155 (9): B915-B920.

Lee W.-J., Lim D.-H. and Smyrl W. H. (2013). "Miniature H2/O2 fuel cells using TiO2 nanotube substrates and sputtered Pt catalyst." *Journal of Power Sources*, 240 (0): 612-617.

Lefebvre M. C., Martin R. B. and Pickup P. G. (1999). "Characterization of ionic conductivity profiles within proton exchange membrane fuel cell gas diffusion electrodes by impedance spectroscopy." *Electrochemical and solid-state letters*, 2 (6): 259-261.

Leroux F., Dewar P. J., Intissar M., Ouvrard G. and Nazar L. F. (2002). "Study of the formation of mesoporous titania via a template approach and of subsequent Li insertion." *Journal of Materials Chemistry*, 12 (11): 3245-3253.

Li B., Higgins D. C., Xiao Q., Yang D., Zhng C., Cai M., Chen Z. and Ma J. (2015). "The durability of carbon supported Pt nanowire as novel cathode catalyst for a 1.5 kW PEMFC stack." *Applied Catalysis B: Environmental*, 162: 133-140.

Li F., Gong H., Wang Y., Zhang H., Wang Y., Liu S., Wang S. and Sun C. (2014). "Enhanced activity, durability and anti-poisoning property of Pt/W 18 O 49 for methanol oxidation with a sub-stoichiometric tungsten oxide W 18 O 49 support." *Journal of Materials Chemistry A*, 2 (47): 20154-20163.

Li L., Liu C.-y. and Liu Y. (2009). "Study on activities of vanadium (IV/V) doped TiO 2 (R) nanorods induced by UV and visible light." *Materials Chemistry and Physics*, 113 (2): 551-557.

Li S.-S., Zheng J.-N., Ma X., Hu Y.-Y., Wang A.-J., Chen J.-R. and Feng J.-J. (2014). "Facile synthesis of hierarchical dendritic PtPd nanogarlands supported on reduced graphene oxide with enhanced electrocatalytic properties." *Nanoscale*, 6 (11): 5708-5713.

Li S.-S., Zheng J.-N., Wang A.-J., Tao F.-L., Feng J.-J., Chen J.-R. and Yu H. (2014). "Branched platinum-on-palladium bimetallic heteronanostructures supported on reduced graphene oxide for highly efficient oxygen reduction reaction." *Journal of Power Sources*, 272: 1078-1085.

260

Li W., Liang C., Zhou W., Qiu J., Zhou Z., Sun G. and Xin Q. (2003). "Preparation and characterization of multiwalled carbon nanotube-supported platinum for cathode catalysts of direct methanol fuel cells." *The Journal of Physical Chemistry B*, 107 (26): 6292-6299.

Li X., Liu X., Wang W., Li L. and Lu X. (2014). "High loading Pt nanoparticles on functionalization of carbon nanotubes for fabricating nonenzyme hydrogen peroxide sensor." *Biosensors and Bioelectronics*, 59: 221-226.

Liebhafsky H. A. and Cairns E. J. (1968). "Fuel cells and fuel batteries. Guide to their research and development."

Lim B., Jiang M., Camargo P. H. C., Cho E. C., Tao J., Lu X., Zhu Y. and Xia Y. (2009). "Pd-Pt bimetallic nanodendrites with high activity for oxygen reduction." *Science*, 324 (5932): 1302-1305.

Lim C. and Wang C. Y. (2004). "Effects of hydrophobic polymer content in GDL on power performance of a PEM fuel cell." *Electrochimica Acta*, 49 (24): 4149-4156.

Lim D.-H., Lee W.-D., Choi D.-H. and Lee H.-I. (2010). "Effect of ceria nanoparticles into the Pt/C catalyst as cathode material on the electrocatalytic activity and durability for low-temperature fuel cell." *Applied Catalysis B: Environmental*, 94 (1): 85-96.

Limpattayanate S. and Hunsom M. (2014). "Electrocatalytic activity of Pt–Pd electrocatalysts for the oxygen reduction reaction in proton exchange membrane fuel cells: Effect of supports." *Renewable Energy*, 63: 205-211.

Liu B., Chen H. M., Liu C., Andrews S. C., Hahn C. and Yang P. (2013). "Large-scale synthesis of transition-metal-doped TiO2 nanowires with controllable overpotential." *Journal of the American Chemical Society*, 135 (27): 9995-9998.

Liu B. and Zhao X. (2017). "The synergetic effect of V and Fe-co-doping in TiO 2 studied from the DFT+ U first-principle calculation." *Applied Surface Science*, 399: 654-662.

Liu H., George M. G., Messerschmidt M., Zeis R., Kramer D., Scholta J. and Bazylak A. (2017). "Accelerated Degradation of Polymer Electrolyte Membrane Fuel Cell Gas Diffusion Layers I. Methodology and Surface Characterization." *Journal of The Electrochemical Society*, 164 (7): F695-F703.

Liu M., Zhang R. and Chen W. (2014). "Graphene-supported nanoelectrocatalysts for fuel cells: synthesis, properties, and applications." *Chemical Reviews*, 114 (10): 5117-5160.

Liu S., Wang J., Zeng J., Ou J., Li Z., Liu X. and Yang S. (2010). ""Green" electrochemical synthesis of Pt/graphene sheet nanocomposite film and its electrocatalytic property." *Journal of Power Sources*, 195 (15): 4628-4633.

Liu X., Wu X. and Scott K. (2014). "Study of niobium and tantalum doped titania-supported Pt electrocatalysts for methanol oxidation and oxygen reduction reactions." *Catalysis Science & Technology*, 4 (11): 3891-3898.

Liu Z.-r., Wang B.-l., Lei Z. H. U., Yang J.-p. and Li X.-a. (2012). "Preparation of graphene-supported Pt-Co nanoparticles and their use in oxygen reduction reactions."

References

New Carbon Materials, 27 (4): 250-257.

Liu Z., Gan L. M., Hong L., Chen W. and Lee J. Y. (2005). "Carbon-supported Pt nanoparticles as catalysts for proton exchange membrane fuel cells." *Journal of Power Sources*, 139 (1): 73-78.

Liu Z., Ling X. Y., Su X. and Lee J. Y. (2004). "Carbon-supported Pt and PtRu nanoparticles as catalysts for a direct methanol fuel cell." *The Journal of Physical Chemistry B*, 108 (24): 8234-8240.

Long J. W., Stroud R. M., Swider-Lyons K. E. and Rolison D. R. (2000). "How to make electrocatalysts more active for direct methanol oxidation avoid PtRu bimetallic alloys!" *The Journal of Physical Chemistry B*, 104 (42): 9772-9776.

Long N. V., Yang Y., Minh Thi C., Minh N. V., Cao Y. and Nogami M. (2013). "The development of mixture, alloy, and core-shell nanocatalysts with nanomaterial supports for energy conversion in low-temperature fuel cells." *Nano Energy*, 2 (5): 636-676.

Long N. V., Yang Y., Thi C. M., Van Minh N., Cao Y. and Nogami M. (2013). "The development of mixture, alloy, and core-shell nanocatalysts with nanomaterial supports for energy conversion in low-temperature fuel cells." *Nano Energy*, 2 (5): 636-676.

Lopes T., Antolini E. and Gonzalez E. R. (2008). "Carbon supported Pt–Pd alloy as an ethanol tolerant oxygen reduction electrocatalyst for direct ethanol fuel cells." *international journal of hydrogen energy*, 33 (20): 5563-5570.

López T., Gómez R., Pecci G., Reyes P., Bokhimi X. and Novaro O. (1999). "Effect of pH on the incorporation of platinum into the lattice of sol–gel titania phases." *Materials Letters*, 40 (2): 59-65.

Lu Q., Yang B., Zhuang L. and Lu J. (2005). "Anodic activation of PtRu/C catalysts for methanol oxidation." *The Journal of Physical Chemistry B*, 109 (5): 1715-1722.

Lu Y., Jiang Y. and Chen W. (2014). "Graphene nanosheet-tailored PtPd concave nanocubes with enhanced electrocatalytic activity and durability for methanol oxidation." *Nanoscale*, 6 (6): 3309-3315.

Lv H., Cheng N., Mu S. and Pan M. (2011). "Heat-treated multi-walled carbon nanotubes as durable supports for PEM fuel cell catalysts." *Electrochimica Acta*, 58: 736-742.

Lv H., Li D., Strmcnik D., Paulikas A. P., Markovic N. M. and Stamenkovic V. R. (2016). "Recent advances in the design of tailored nanomaterials for efficient oxygen reduction reaction." *Nano Energy*, 29: 149-165.

Maass S., Finsterwalder F., Frank G., Hartmann R. and Merten C. (2008). "Carbon support oxidation in PEM fuel cell cathodes." *Journal of Power Sources*, 176 (2): 444-451.

Macak J. M., Barczuk P. J., Tsuchiya H., Nowakowska M. Z., Ghicov A., Chojak M., Bauer S., Virtanen S., Kulesza P. J. and Schmuki P. (2005). "Self-organized nanotubular TiO 2 matrix as support for dispersed Pt/Ru nanoparticles: enhancement

of the electrocatalytic oxidation of methanol." *Electrochemistry Communications*, 7 (12): 1417-1422.

Maghsodi A., Hoseini M. R. M., Mobarakeh M. D., Kheirmand M., Samiee L., Shoghi F. and Kameli M. (2011). "Exploration of bimetallic Pt-Pd/C nanoparticles as an electrocatalyst for oxygen reduction reaction." *Applied Surface Science*, 257 (15): 6353-6357.

Maiyalagan T., Viswanathan B. and Varadaraju U. V. (2005). "Nitrogen containing carbon nanotubes as supports for Pt–Alternate anodes for fuel cell applications." *Electrochemistry Communications*, 7 (9): 905-912.

Malheiro A. R., Perez J. and Villullas H. M. (2009). "Well-Alloyed PtFe∕ C Nanocatalysts of Controlled Composition and Same Particle Size: Oxygen Reduction and Methanol Tolerance." *Journal of the Electrochemical Society*, 156 (1): B51-B58.

Malheiro A. R., Perez J. and Villullas H. M. (2010). "Surface structure and electronic properties of Pt–Fe/C nanocatalysts and their relation with catalytic activity for oxygen reduction." *Journal of Power Sources*, 195 (10): 3111-3118.

Manikandan M., Vedarajan R., Kodiyath R., Abe H., Ueda S., Dakshnamoorthy A., Rajalakshmi N., Dhathathreyan K. S. and Ramesh G. V. (2016). "Pt Decorated Free-Standing TiO2 Nanotube Arrays: Highly Active and Durable Electrocatalyst for Oxygen Reduction and Methanol Oxidation Reactions." *Journal of Nanoscience and Nanotechnology*, 16 (8): 8269-8278.

Markovic N. M., Schmidt T. J., Stamenkovic V. and Ross P. N. (2001). "Oxygen reduction reaction on Pt and Pt bimetallic surfaces: a selective review." *FUEL CELLS-WEINHEIM-*, 1 (2): 105-116.

Mass J., Bhattacharya P. and Katiyar R. S. (2003). "Effect of high substrate temperature on Al-doped ZnO thin films grown by pulsed laser deposition." *Materials Science and Engineering: B*, 103 (1): 9-15.

Mawhinney D. B., Naumenko V., Kuznetsova A., Yates J. T., Liu J. and Smalley R. E. (2000). "Infrared spectral evidence for the etching of carbon nanotubes: ozone oxidation at 298 K." *Journal of the American Chemical Society*, 122 (10): 2383-2384.

Mayrhofer K. J. J., Hartl K., Juhart V. and Arenz M. (2009). "Degradation of carbon-supported Pt bimetallic nanoparticles by surface segregation." *Journal of the American Chemical Society*, 131 (45): 16348-16349.

McBreen J., Olender H., Srinivasan S. and Kordesch K. V. (1981). "Carbon supports for phosphoric acid fuel cell electrocatalysts: alternative materials and methods of evaluation." *Journal of Applied Electrochemistry*, 11 (6): 787-796.

McCreery R. L. (2008). "Advanced carbon electrode materials for molecular electrochemistry." *Chem. Rev*, 108 (7): 2646-2687.

Mei H., Sheng Q., Li Y., Chen J. and Wu H. (2015). "Effects of different carbon matrix on the Pt0. 55Co0. 45 catalysts using for the cathode of proton exchange membrane fuel cell." *Journal of Nanoscience and Nanotechnology*, 15 (6): 4510-4515.

References

Mentus S. V. (2005). "Electrochemical response of a composite Pt/TiO2 layer formed potentiodynamically on titanium surfaces." *Electrochimica Acta*, 50 (18): 3609-3615.

Min M.-k., Cho J., Cho K. and Kim H. (2000). "Particle size and alloying effects of Pt-based alloy catalysts for fuel cell applications." *Electrochimica Acta*, 45 (25): 4211-4217.

Moreira J., Del Angel P., Ocampo A. L., Sebastian P. J., Montoya J. A. and Castellanos R. H. (2004). "Synthesis, characterization and application of a Pd/Vulcan and Pd/C catalyst in a PEM fuel cell." *International Journal of Hydrogen Energy*, 29 (9): 915-920.

Morris D., Dou Y., Rebane J., Mitchell C. E. J., Egdell R. G., Law D. S. L., Vittadini A. and Casarin M. (2000). "Photoemission and STM study of the electronic structure of Nb-doped TiO 2." *Physical Review B*, 61 (20): 13445.

Mukerjee S. and McBreen J. (1998). "Effect of particle size on the electrocatalysis by carbon-supported Pt electrocatalysts: an in situ XAS investigation." *Journal of Electroanalytical Chemistry*, 448 (2): 163-171.

Mukerjee S. and Srinivasan S. (1993). "Enhanced electrocatalysis of oxygen reduction on platinum alloys in proton exchange membrane fuel cells." *Journal of Electroanalytical Chemistry*, 357 (1–2): 201-224.

Mukerjee S., Srinivasan S., Soriaga M. P. and McBreen J. (1995). "Effect of preparation conditions of Pt alloys on their electronic, structural, and electrocatalytic activities for oxygen reduction-XRD, XAS, and electrochemical studies." *The Journal of Physical Chemistry*, 99 (13): 4577-4589.

Mukerjee S., Srinivasan S., Soriaga M. P. and McBreen J. (1995). "Role of structural and electronic properties of Pt and Pt alloys on electrocatalysis of oxygen reduction an in situ XANES and EXAFS investigation." *Journal of the Electrochemical Society*, 142 (5): 1409-1422.

Mustain W. E. and Prakash J. (2007). "Kinetics and mechanism for the oxygen reduction reaction on polycrystalline cobalt–palladium electrocatalysts in acid media." *Journal of Power Sources*, 170 (1): 28-37.

Myers D. (1990). *Surfaces, interfaces and colloids*, Wiley-Vch New York etc.

Nam K.-W., Song J., Oh K.-H., Choo M.-J., Park H., Park J.-K. and Choi J. W. (2012). "Monodispersed PtCo nanoparticles on hexadecyltrimethylammonium bromide treated graphene as an effective oxygen reduction reaction catalyst for proton exchange membrane fuel cells." *Carbon*, 50 (10): 3739-3747.

Nilekar A. U., Xu Y., Zhang J., Vukmirovic M. B., Sasaki K., Adzic R. R. and Mavrikakis M. (2007). "Bimetallic and ternary alloys for improved oxygen reduction catalysis." *Topics in Catalysis*, 46 (3-4): 276-284.

Nørskov J. K., Rossmeisl J., Logadottir A., Lindqvist L., Kitchin J. R., Bligaard T. and Jonsson H. (2004). "Origin of the overpotential for oxygen reduction at a fuel-cell cathode." *The Journal of Physical Chemistry B*, 108 (46): 17886-17892.

Novikova K., Kuriganova A., Leontyev I., Gerasimova E., Maslova O., Rakhmatullin

A., Smirnova N. and Dobrovolsky Y. "Influence of Carbon Support on Catalytic Layer Performance of Proton Exchange Membrane Fuel Cells." *Electrocatalysis*: 1-9 (2017).

Novikova K., Kuriganova A., Leontyev I., Gerasimova E., Maslova O., Rakhmatullin A., Smirnova N. and Dobrovolsky Y. (2017). "Influence of Carbon Support on Catalytic Layer Performance of Proton Exchange Membrane Fuel Cells." *Electrocatalysis*: 1-9.

Novoselov K. S. A., Geim A. K., Morozov S., Jiang D., Katsnelson M., Grigorieva I., Dubonos S. and Firsov A. (2005). "Two-dimensional gas of massless Dirac fermions in graphene." *Nature*, 438 (7065): 197-200.

O'Hayre R., Cha S.-W., Prinz F. B. and Colella W. (2016). *Fuel cell fundamentals*, John Wiley & Sons.

O'Hayre R., Cha S. W., Colella W. and Prinz F. B. (2006). "Fuel Cell Fundamentals, John Wiley & Sons." *Inc, New Jersey*: 3-305.

O'Rian O. R., Saleh F. S. and Easton E. B. (2014). "Application of the transmission line EIS model to fuel cell catalyst layer durability." *ECS Transactions*, 61 (23): 25-32.

Ohsaka T., Izumi F. and Fujiki Y. (1978). "Raman spectrum of anatase, TiO2." *Journal of Raman Spectroscopy*, 7 (6): 321-324.

Okada T. and Kaneko M. (2008). *Molecular catalysts for energy conversion*, Springer Science & Business Media.

Okamoto M., Fujigaya T. and Nakashima N. (2009). "Design of an Assembly of Poly (benzimidazole), Carbon Nanotubes, and Pt Nanoparticles for a Fuel-Cell Electrocatalyst with an Ideal Interfacial Nanostructure." *Small*, 5 (6): 735-740.

Oztuna F. E. S., Barim S. B., Bozbag S. E., Yu H., Aindow M., Unal U. and Erkey C. (2017). "Graphene Aerogel Supported Pt Electrocatalysts for Oxygen Reduction Reaction by Supercritical Deposition." *Electrochimica Acta*, 250: 174-184.

Padmavathi R. and Sangeetha D. (2013). "Synthesis and characterization of electrospun carbon nanofiber supported Pt catalyst for fuel cells." *Electrochimica Acta*, 112: 1-13.

Pankove J. I. (1971). "Optical Processes in Semiconductors Prentice-Hall." *New Jersey*, 92.

Panomsuwan G., Saito N. and Ishizaki T. (2016). "Electrocatalytic oxygen reduction on nitrogen-doped carbon nanoparticles derived from cyano-aromatic molecules via a solution plasma approach." *Carbon*, 98: 411-420.

Park K.-W., Ahn K.-S., Nah Y.-C., Choi J.-H. and Sung Y.-E. (2003). "Electrocatalytic enhancement of methanol oxidation at Pt-WO x nanophase electrodes and in-situ observation of hydrogen spillover using electrochromism." *The Journal of Physical Chemistry B*, 107 (18): 4352-4355.

Park K.-W. and Seol K.-S. (2007). "Nb-TiO$_2$ supported Pt cathode catalyst for polymer electrolyte membrane fuel cells." *Electrochemistry Communications*, 9 (9):

References

2256-2260.

Park K.-W., Sung Y.-E., Han S., Yun Y. and Hyeon T. (2004). "Origin of the enhanced catalytic activity of carbon nanocoil-supported PtRu alloy electrocatalysts." *The Journal of Physical Chemistry B*, 108 (3): 939-944.

Park S., Shao Y., Wan H., Rieke P. C., Viswanathan V. V., Towne S. A., Saraf L. V., Liu J., Lin Y. and Wang Y. (2011). "Design of graphene sheets-supported Pt catalyst layer in PEM fuel cells." *Electrochemistry Communications*, 13 (3): 258-261.

Parker J. C. and Siegel R. W. (1990). "Raman microprobe study of nanophase TiO2 and oxidation-induced spectral changes." *Journal of Materials Research*, 5 (06): 1246-1252.

Passalacqua E., Lufrano F., Squadrito G., Patti A. and Giorgi L. (2001). "Nafion content in the catalyst layer of polymer electrolyte fuel cells: effects on structure and performance." *Electrochimica Acta*, 46 (6): 799-805.

Paulus U. A., Wokaun A., Scherer G. G., Schmidt T. J., Stamenkovic V., Radmilovic V., Markovic N. M. and Ross P. N. (2002). "Oxygen reduction on carbon-supported Pt-Ni and Pt-Co alloy catalysts." *The Journal of Physical Chemistry B*, 106 (16): 4181-4191.

Paulus U. A., Wokaun A., Scherer G. G., Schmidt T. J., Stamenkovic V., Radmilovic V., Markovic N. M. and Ross P. N. (2002). "Oxygen Reduction on Carbon-Supported Pt−Ni and Pt−Co Alloy Catalysts." *The Journal of Physical Chemistry B*, 106 (16): 4181-4191.

Pethaiah S. S., Ulaganathan M., Ramalinga Viswanathan M. and Chan S. H. (2015). "Fabrication and electrochemical characterization of Pt-Pd impregnated nanocomposite polymer electrolyte membranes for high concentration DMFCs." *RSC Advances*, 5 (2): 981-987.

Peuckert M., Yoneda T., Dalla Betta R. A. and Boudart M. (1986). "Oxygen reduction on small supported platinum particles." *Journal of the Electrochemical Society*, 133 (5): 944-947.

Picher M., Anglaret E., Arenal R. and Jourdain V. (2011). "Processes controlling the diameter distribution of single-walled carbon nanotubes during catalytic chemical vapor deposition." *ACS Nano*, 5 (3): 2118-2125.

Pinchuk O. A., Dundar F., Ata A. and Wynne K. J. (2012). "Improved thermal stability, properties, and electrocatalytic activity of sol-gel silica modified carbon supported Pt catalysts." *International Journal of Hydrogen Energy*, 37 (3): 2111-2120.

Pourbaix M. (1974). "Atlas of electrochemical equilibria in aqueous solutions."

Pozio A., De Francesco M., Cemmi A., Cardellini F. and Giorgi L. (2002). "Comparison of high surface Pt/C catalysts by cyclic voltammetry." *Journal of Power Sources*, 105 (1): 13-19.

Pullamsetty A., Subbiah M. and Sundara R. (2015). "Platinum on boron doped graphene as cathode electrocatalyst for proton exchange membrane fuel cells."

International Journal of Hydrogen Energy, 40 (32): 10251-10261.

Pullamsetty A. and Sundara R. (2016). "Investigation of catalytic activity towards oxygen reduction reaction of Pt dispersed on boron doped graphene in acid medium." *Journal of Colloid and Interface Science*, 479: 260-270.

Qu L., Liu Y., Baek J.-B. and Dai L. (2010). "Nitrogen-doped graphene as efficient metal-free electrocatalyst for oxygen reduction in fuel cells." *ACS Nano*, 4 (3): 1321-1326.

Raghuveer V. and Viswanathan B. (2005). "Synthesis, characterization and electrochemical studies of Ti-incorporated tungsten trioxides as platinum support for methanol oxidation." *Journal of Power Sources*, 144 (1): 1-10.

Rajalakshmi N., Lakshmi N. and Dhathathreyan K. S. (2008). "Nano titanium oxide catalyst support for proton exchange membrane fuel cells." *International Journal of Hydrogen Energy*, 33 (24): 7521-7526.

Ralph T. R. and Hogarth M. P. (2002). "Catalysis for low temperature fuel cells." *Platinum Metals Review*, 46 (3): 117-135.

Rausch J., Zhuang R.-C. and Mäder E. (2010). "Surfactant assisted dispersion of functionalized multi-walled carbon nanotubes in aqueous media." *Composites Part A: Applied Science and Manufacturing*, 41 (9): 1038-1046.

Ren F., Li H., Wang Y. and Yang J. (2015). "Enhanced photocatalytic oxidation of propylene over V-doped TiO 2 photocatalyst: reaction mechanism between V 5+ and single-electron-trapped oxygen vacancy." *Applied Catalysis B: Environmental*, 176: 160-172.

Roen L. M., Paik C. H. and Jarvi T. D. (2004). "Electrocatalytic corrosion of carbon support in PEMFC cathodes." *Electrochemical and Solid-State Letters*, 7 (1): A19-A22.

Rončević I. Š., Grubač Z. and Metikoš-Huković M. (2014). "Electrodeposition of hydroxyapatite coating on AZ91D alloy for biodegradable implant application." *Int. J. Electrochem. Sci*, 9: 5907-5923.

Rosado G., Verde Y., Valenzuela-Muñiz A. M., Barbosa R., Yoshida M. M. and Escobar B. (2016). "Catalytic activity of Pt-Ni nanoparticles supported on multi-walled carbon nanotubes for the oxygen reduction reaction." *International Journal of Hydrogen Energy*, 41 (48): 23260-23271.

Roy A. K. and Hsieh C.-T. (2013). "Pulse microwave-assisted synthesis of Pt nanoparticles onto carbon nanotubes as electrocatalysts for proton exchange membrane fuel cells." *Electrochimica Acta*, 87: 63-72.

Ruan M., Sun X., Zhang Y. and Xu W. (2014). "Regeneration and Enhanced Catalytic Activity of Pt/C Electrocatalysts." *ACS Catalysis*, 5 (1): 233-240.

Rüdorff W. and Luginsland H. H. (1964). "Studies of Ternary Oxides of the Transition Metals. II. The Systems of TiO2-NbO2 and TiO2-TiTaO4." *Z. anorg. allg. Chem*, 334: 125-141.

Ruiz-Camacho B., Martínez-González J. H., González-Huerta R. G. and Tufiño-

References

Velázquez M. (2014). "Kinetic study of oxygen reduction reaction and PEM fuel cell performance of Pt/TiO2-C electrocatalyst." *International Journal of Hydrogen Energy*, 39 (29): 16731-16739.

Saito R., Fujita M., Dresselhaus G. and Dresselhaus u. M. S. (1992). "Electronic structure of chiral graphene tubules." *Applied Physics Letters*, 60 (18): 2204-2206.

Saleh F. S. and Easton E. B. (2012). "Diagnosing degradation within PEM fuel cell catalyst layers using electrochemical impedance spectroscopy." *Journal of The Electrochemical Society*, 159 (5): B546-B553.

Saleh F. S. and Easton E. B. (2013). "Determining electrochemically active surface area in PEM fuel cell electrodes with electrochemical impedance spectroscopy and its application to catalyst durability." *Electrochimica Acta*, 114: 278-284.

Saleh F. S. and Easton E. B. (2014). "Assessment of the ethanol oxidation activity and durability of Pt catalysts with or without a carbon support using Electrochemical Impedance Spectroscopy." *Journal of Power Sources*, 246: 392-401.

Salgado J. R. C., Alcaide F., Álvarez G., Calvillo L., Lázaro M. J. and Pastor E. (2010). "Pt–Ru electrocatalysts supported on ordered mesoporous carbon for direct methanol fuel cell." *Journal of Power Sources*, 195 (13): 4022-4029.

Samet L., Nasseur J. B., Chtourou R., March K. and Stephan O. (2013). "Heat treatment effect on the physical properties of cobalt doped TiO 2 sol–gel materials." *Materials Characterization*, 85: 1-12.

Sasaki K., Noda Z., Tsukatsune T., Kanda K., Takabatake Y., Nagamatsu Y., Daio T., Lyth S. M. and Hayashi A. (2014). "Alternative Oxide-Supported PEFC Electrocatalysts." *ECS Transactions*, 64 (3): 221-227.

Schimmoeller B., Schulz H., Ritter A., Reitzmann A., Kraushaar-Czarnetzki B., Baiker A. and Pratsinis S. E. (2008). "Structure of flame-made vanadia/titania and catalytic behavior in the partial oxidation of o-xylene." *Journal of Catalysis*, 256 (1): 74-83.

Schonvogel D., Hülstede J., Wagner P., Kruusenberg I., Tammeveski K., Dyck A., Agert C. and Wark M. (2017). "Stability of Pt Nanoparticles on Alternative Carbon Supports for Oxygen Reduction Reaction." *Journal of The Electrochemical Society*, 164 (9): F995-F1004.

Schubert M. M., Hackenberg S., Van Veen A. C., Muhler M., Plzak V. and Behm R. J. (2001). "CO oxidation over supported gold catalysts—"Inert" and "active" support materials and their role for the oxygen supply during reaction." *Journal of Catalysis*, 197 (1): 113-122.

Serp P., Corrias M. and Kalck P. (2003). "Carbon nanotubes and nanofibers in catalysis." *Applied Catalysis A: General*, 253 (2): 337-358.

Shahgaldi S. and Hamelin J. (2015). "The effect of low platinum loading on the efficiency of PEMFC's electrocatalysts supported on TiO 2–Nb, and SnO 2–Nb: An experimental comparison between active and stable conditions." *Energy Conversion and Management*, 103: 681-690.

Shaijumon M. M., Ramaprabhu S. and Rajalakshmi N. (2006). "Platinum/multiwalled carbon nanotubes-platinum/carbon composites as electrocatalysts for oxygen reduction reaction in proton exchange membrane fuel cell." *Applied Physics Letters*, 88 (25): 253105-253105.

Shanahan P. V., Xu L., Liang C., Waje M., Dai S. and Yan Y. S. (2008). "Graphitic mesoporous carbon as a durable fuel cell catalyst support." *Journal of Power Sources*, 185 (1): 423-427.

Shaneeth M., Basu S. and Aravamuthan S. (2016). "PEM fuel cell cathode catalyst layer durability: An electrochemical spectroscopic investigation." *Chemical Engineering Science*, 154: 72-80.

Shao M., Chang Q., Dodelet J.-P. and Chenitz R. (2016). "Recent advances in electrocatalysts for oxygen reduction reaction." *Chem. Rev*, 116 (6): 3594-3657.

Shao Y., Kou R., Wang J., Viswanathan V. V., Kwak J. H., Liu J., Wang Y. and Lin Y. (2008). "The influence of the electrochemical stressing (potential step and potential-static holding) on the degradation of polymer electrolyte membrane fuel cell electrocatalysts." *Journal of Power Sources*, 185 (1): 280-286.

Shao Y., Liu J., Wang Y. and Lin Y. (2009). "Novel catalyst support materials for PEM fuel cells: current status and future prospects." *Journal of Materials Chemistry*, 19 (1): 46-59.

Shao Y., Yin G. and Gao Y. (2007). "Understanding and approaches for the durability issues of Pt-based catalysts for PEM fuel cell." *Journal of Power Sources*, 171 (2): 558-566.

Shao Y., Yin G., Gao Y. and Shi P. (2006). "Durability Study of Pt∕C and Pt∕CNTs Catalysts under Simulated PEM Fuel Cell Conditions." *Journal of the Electrochemical Society*, 153 (6): A1093-A1097.

Shao Y., Zhang S., Wang C., Nie Z., Liu J., Wang Y. and Lin Y. (2010). "Highly durable graphene nanoplatelets supported Pt nanocatalysts for oxygen reduction." *Journal of Power Sources*, 195 (15): 4600-4605.

Sharma S. and Pollet B. G. (2012). "Support materials for PEMFC and DMFC electrocatalysts—A review." *Journal of Power Sources*, 208 (0): 96-119.

Sharma S. and Pollet B. G. (2012). "Support materials for PEMFC and DMFC electrocatalysts—a review." *Journal of Power Sources*, 208: 96-119.

Shim J., Lee C.-R., Lee H.-K., Lee J.-S. and Cairns E. J. (2001). "Electrochemical characteristics of Pt–WO3/C and Pt–TiO2/C electrocatalysts in a polymer electrolyte fuel cell." *Journal of Power Sources*, 102 (1–2): 172-177.

Shopova-Gospodinova D., Jeurgens L. P. H., Welzel U., Bauermann L. P., Hoffmann R. C. and Bill J. (2012). "Synthesis of V-doped TiO 2 films by chemical bath deposition and the effect of post-annealing on their properties." *Thin Solid Films*, 520 (18): 5928-5935.

Simonsen M. and Søgaard E. (2010). "Sol–gel reactions of titanium alkoxides and water: influence of pH and alkoxy group on cluster formation and properties of the

References

resulting products." *Journal of Sol-Gel Science and Technology*, 53 (3): 485-497.

Siracusano S., Stassi A., Modica E., Baglio V. and Aricò A. S. (2013). "Preparation and characterisation of Ti oxide based catalyst supports for low temperature fuel cells." *International Journal of Hydrogen Energy*, 38 (26): 11600-11608.

Siroma Z., Ishii K., Yasuda K., Miyazaki Y., Inaba M. and Tasaka A. (2005). "Imaging of highly oriented pyrolytic graphite corrosion accelerated by Pt particles." *Electrochemistry Communications*, 7 (11): 1153-1156.

Smitha B., Sridhar S. and Khan A. A. (2005). "Solid polymer electrolyte membranes for fuel cell applications—a review." *Journal of Membrane Science*, 259 (1): 10-26.

Sode A., Li W., Yang Y., Wong P. C., Gyenge E., Mitchell K. A. R. and Bizzotto D. (2006). "Electrochemical formation of a Pt/Zn alloy and its use as a catalyst for oxygen reduction reaction in fuel cells." *The Journal of Physical Chemistry B*, 110 (17): 8715-8722.

Song S., Liu J., Shi J., Liu H., Maragou V., Wang Y. and Tsiakaras P. (2011). "The effect of microwave operation parameters on the electrochemical performance of Pt/C catalysts." *Applied Catalysis B: Environmental*, 103 (3–4): 287-293.

Stamatin S. N., Borghei M., Dhiman R., Andersen S. M., Ruiz V., Kauppinen E. and Skou E. M. (2015). "Activity and stability studies of platinized multi-walled carbon nanotubes as fuel cell electrocatalysts." *Applied Catalysis B: Environmental*, 162: 289-299.

Stamenković V., Schmidt T. J., Ross P. N. and Marković N. M. (2003). "Surface segregation effects in electrocatalysis: kinetics of oxygen reduction reaction on polycrystalline Pt3Ni alloy surfaces." *Journal of Electroanalytical Chemistry*, 554–555 (0): 191-199.

Stamenkovic V. R., Mun B. S., Arenz M., Mayrhofer K. J. J., Lucas C. A., Wang G., Ross P. N. and Markovic N. M. (2007). "Trends in electrocatalysis on extended and nanoscale Pt-bimetallic alloy surfaces." *Nature materials*, 6 (3): 241-247.

Stamenkovic V. R., Mun B. S., Mayrhofer K. J. J., Ross P. N. and Markovic N. M. (2006). "Effect of Surface Composition on Electronic Structure, Stability, and Electrocatalytic Properties of Pt-Transition Metal Alloys: Pt-Skin versus Pt-Skeleton Surfaces." *Journal of the American Chemical Society*, 128 (27): 8813-8819.

Steigerwalt E. S., Deluga G. A., Cliffel D. E. and Lukehart C. M. (2001). "A Pt-Ru/graphitic carbon nanofiber nanocomposite exhibiting high relative performance as a direct-methanol fuel cell anode catalyst." *The Journal of Physical Chemistry B*, 105 (34): 8097-8101.

Steigerwalt E. S., Deluga G. A. and Lukehart C. M. (2002). "Pt-Ru/carbon fiber nanocomposites: Synthesis, characterization, and performance as anode catalysts of direct methanol fuel cells. A search for exceptional performance." *The Journal of Physical Chemistry B*, 106 (4): 760-766.

Stonehart P. (1984). "Carbon substrates for phosphoric acid fuel cell cathodes." *Carbon*, 22 (4): 423-431.

270

Takabatake Y., Noda Z., Lyth S. M., Hayashi A. and Sasaki K. (2014). "Cycle durability of metal oxide supports for PEFC electrocatalysts." *International Journal of Hydrogen Energy*, 39 (10): 5074-5082.

Tamizhmani G., Dodelet J. P. and Guay D. (1996). "Crystallite Size Effects of Carbon-Supported Platinum on Oxygen Reduction in Liquid Acids." *Journal of The Electrochemical Society*, 143 (1): 18-23.

Tammeveski K., Tenno T., Rosental A., Talonen P., Johansson L. S. and Niinistö L. (1999). "The Reduction of Oxygen on Pt-TiO2 Coated Ti Electrodes in Alkaline Solution." *Journal of the Electrochemical Society*, 146 (2): 669-676.

Tang H., Prasad K., Sanjines R., Schmid P. E. and Levy F. (1994). "Electrical and optical properties of TiO2 anatase thin films." *Journal of applied Physics*, 75 (4): 2042-2047.

Tang Y., Zhang H., Zhong H., Xu T. and Jin H. (2011). "Carbon-supported Pd–Pt cathode electrocatalysts for proton exchange membrane fuel cells." *Journal of Power Sources*, 196 (7): 3523-3529.

Tarasevich M. R., Sadkowski A. and Yeager E. (1983). *Oxygen electrochemistry*. Comprehensive treatise of electrochemistry, Springer**:** 301-398.

Tasis D., Tagmatarchis N., Bianco A. and Prato M. (2006). "Chemistry of carbon nanotubes." *Chemical reviews*, 106 (3): 1105-1136.

Thanasilp S. and Hunsom M. (2011). "Effect of Pt: Pd atomic ratio in Pt–Pd/C electrocatalyst-coated membrane on the electrocatalytic activity of ORR in PEM fuel cells." *Renewable Energy*, 36 (6): 1795-1801.

Tkalya E. E., Ghislandi M., de With G. and Koning C. E. (2012). "The use of surfactants for dispersing carbon nanotubes and graphene to make conductive nanocomposites." *Current Opinion in Colloid & Interface Science*, 17 (4): 225-232.

Toda T., Igarashi H., Uchida H. and Watanabe M. (1999). "Enhancement of the electroreduction of oxygen on Pt alloys with Fe, Ni, and Co." *Journal of The Electrochemical Society*, 146 (10): 3750-3756.

Tsujiko A., Itoh H., Kisumi T., Shiga A., Murakoshi K. and Nakato Y. (2002). "Observation of cathodic photocurrents at nanocrystalline TiO2 film electrodes, caused by enhanced oxygen reduction in alkaline solutions." *The Journal of Physical Chemistry B*, 106 (23): 5878-5885.

Vaisman L., Wagner H. D. and Marom G. (2006). "The role of surfactants in dispersion of carbon nanotubes." *Advances in colloid and interface science*, 128: 37-46.

Valenzuela-Muñíz A. M., Alonso-Nuñez G., Miki-Yoshida M., Botte G. G. and Verde-Gómez Y. (2013). "High electroactivity performance in Pt/MWCNT and PtNi/MWCNT electrocatalysts." *International Journal of Hydrogen Energy*, 38 (28): 12640-12647.

Van der Vliet D., Wang C., Debe M., Atanasoski R., Markovic N. M. and Stamenkovic V. R. (2011). "Platinum-alloy nanostructured thin film catalysts for the

References

oxygen reduction reaction." *Electrochimica Acta*, 56 (24): 8695-8699.

Vedrine J. C., Dufaux M., Naccache C. and Imelik B. (1978). "X-ray photoelectron spectroscopy study of Pd and Pt ions in type Y-zeolite. Electron transfer between metal aggregates and the support as evidenced by X-ray photoelectron spectroscopy and electron spin resonance." *Journal of the Chemical Society, Faraday Transactions 1: Physical Chemistry in Condensed Phases*, 74: 440-449.

Venezia A. M., Duca D., Floriano M. A., Deganello G. and Rossi A. (1992). "XPS study of pumice-supported palladium and platinum catalysts." *Surface and Interface Analysis*, 19 (1-12): 543-547.

Vinayan B. P., Jafri R. I., Nagar R., Rajalakshmi N., Sethupathi K. and Ramaprabhu S. (2012). "Catalytic activity of platinum–cobalt alloy nanoparticles decorated functionalized multiwalled carbon nanotubes for oxygen reduction reaction in PEMFC." *International Journal of Hydrogen Energy*, 37 (1): 412-421.

Vinayan B. P. and Ramaprabhu S. (2013). "Platinum–TM (TM= Fe, Co) alloy nanoparticles dispersed nitrogen doped (reduced graphene oxide-multiwalled carbon nanotube) hybrid structure cathode electrocatalysts for high performance PEMFC applications." *Nanoscale*, 5 (11): 5109-5118.

von Kraemer S., Wikander K., Lindbergh G., Lundblad A. and Palmqvist A. E. C. (2008). "Evaluation of TiO2 as catalyst support in Pt-TiO2/C composite cathodes for the proton exchange membrane fuel cell." *Journal of Power Sources*, 180 (1): 185-190.

Vracar L. M., Sepa D. B. and Damjanovic A. (1986). "Palladium Electrode in Oxygen-Saturated Aqueous Solutions: Reduction of Oxygen in the Activation-Controlled Region." *Journal of the Electrochemical Society*, 133 (9): 1835-1839.

Wang C., Hou Y., Kim J. and Sun S. (2007). "A general strategy for synthesizing FePt nanowires and nanorods." *Angewandte Chemie International Edition*, 46 (33): 6333-6335.

Wang H. (2009). "Dispersing carbon nanotubes using surfactants." *Current Opinion in Colloid & Interface Science*, 14 (5): 364-371.

Wang H., Yuan X.-Z. and Li H. (2011). *PEM fuel cell diagnostic tools*, CRC press.

Wang M., Guo D.-j. and Li H.-l. (2005). "High activity of novel Pd/TiO 2 nanotube catalysts for methanol electro-oxidation." *Journal of Solid State Chemistry*, 178 (6): 1996-2000.

Wang S., Bai L. N., Sun H. M., Jiang Q. and Lian J. S. (2013). "Structure and photocatalytic property of Mo-doped TiO 2 nanoparticles." *Powder technology*, 244: 9-15.

Wang X., Li W., Chen Z., Waje M. and Yan Y. (2006). "Durability investigation of carbon nanotube as catalyst support for proton exchange membrane fuel cell." *Journal of Power Sources*, 158 (1): 154-159.

Wang X., Vara M., Luo M., Huang H., Ruditskiy A., Park J., Bao S., Liu J., Howe J.

and Chi M. (2015). "Pd@ Pt core–shell concave decahedra: a class of catalysts for the oxygen reduction reaction with enhanced activity and durability." *Journal of the American Chemical Society*, 137 (47): 15036-15042.

Wang Y.-J., Wilkinson D. P., Neburchilov V., Song C., Guest A. and Zhang J. (2014). "Ta and Nb co-doped TiO 2 and its carbon-hybrid materials for supporting Pt–Pd alloy electrocatalysts for PEM fuel cell oxygen reduction reaction." *Journal of Materials Chemistry A*, 2 (32): 12681-12685.

Wang Y.-J., Zhao N., Fang B., Li H., Bi X. T. and Wang H. (2015). "Carbon-supported Pt-based alloy electrocatalysts for the oxygen reduction reaction in polymer electrolyte membrane fuel cells: particle size, shape, and composition manipulation and their impact to activity." *Chemical Reviews*, 115 (9): 3433-3467.

Wang Z. B., Yin G. P. and Shi P. F. (2005). "Stable Pt–Ru∕C Catalysts Prepared from New Precursors by Thermal Reduction for Direct Methanol Fuel Cell." *Journal of the Electrochemical Society*, 152 (12): A2406-A2412.

Winjobi O., Zhang Z., Liang C. and Li W. (2010). "Carbon nanotube supported platinum–palladium nanoparticles for formic acid oxidation." *Electrochimica Acta*, 55 (13): 4217-4221.

Wroblowa H. S. and Razumney G. (1976). "Electroreduction of oxygen: A new mechanistic criterion." *Journal of Electroanalytical Chemistry and Interfacial Electrochemistry*, 69 (2): 195-201.

Wu G. and Xu B.-Q. (2007). "Carbon nanotube supported Pt electrodes for methanol oxidation: A comparison between multi- and single-walled carbon nanotubes." *Journal of Power Sources*, 174 (1): 148-158.

Wu H., Wexler D. and Liu H. (2012). "Pt–Ni/C catalysts using different carbon supports for the cathode of the proton exchange membrane fuel cell (PEMFC)." *Materials Chemistry and Physics*, 136 (2): 845-849.

Wu X.-F., Chen Y.-F., Yoon J.-M. and Yu Y.-T. (2010). "Fabrication and properties of flower-shaped Pt@TiO2 core–shell nanoparticles." *Materials Letters*, 64 (20): 2208-2210.

Xie T., Jung W., Kim T., Ganesan P. and Popov B. N. (2014). "Development of highly active and durable hybrid cathode catalysts for polymer electrolyte membrane fuel cells." *Journal of The Electrochemical Society*, 161 (14): F1489-F1501.

Xie X., Xue Y., Li L., Chen S., Nie Y., Ding W. and Wei Z. (2014). "Surface Al leached Ti 3 AlC 2 as a substitute for carbon for use as a catalyst support in a harsh corrosive electrochemical system." *Nanoscale*, 6 (19): 11035-11040.

Xie Z. and Holdcroft S. (2004). "Polarization-dependent mass transport parameters for orr in perfluorosulfonic acid ionomer membranes: an EIS study using microelectrodes." *Journal of Electroanalytical Chemistry*, 568: 247-260.

Xiong L. and Manthiram A. (2004). "Synthesis and characterization of methanol tolerant Pt/TiOx/C nanocomposites for oxygen reduction in direct methanol fuel Cells." *Electrochimica Acta*, 49 (24): 4163-4170.

References

Xiong L. and Manthiram A. (2005). "Effect of atomic ordering on the catalytic activity of carbon supported PtM (M= Fe, Co, Ni, and Cu) alloys for oxygen reduction in PEMFCs." *Journal of the Electrochemical Society*, 152 (4): A697-A703.

Xiong L., More K. L. and He T. (2010). "Syntheses, characterization, and catalytic oxygen electroreduction activities of carbon-supported PtW nanoparticle catalysts." *Journal of Power Sources*, 195 (9): 2570-2578.

Xiong X., Chen W., Wang W., Li J. and Chen S. (2017). "Pt-Pd nanodendrites as oxygen reduction catalyst in polymer-electrolyte-membrane fuel cell." *International Journal of Hydrogen Energy*, 42 (40): 25234-25243.

Xu J., Ao Y., Chen M., Fu D. and Yuan C. (2010). "Photocatalytic activity of vanadium-doped titania–activated carbon composite film under visible light." *Thin Solid Films*, 518 (15): 4170-4174.

Yan Z., Wei W., Xie J., Meng S., Lü X. and Zhu J. (2013). "An ion exchange route to produce WO_3 nanobars as Pt electrocatalyst promoter for oxygen reduction reaction." *Journal of Power Sources*, 222: 218-224.

Yang H. N., Lee D. C., Park K. W. and Kim W. J. (2015). "Platinum–boron doped graphene intercalated by carbon black for cathode catalyst in proton exchange membrane fuel cell." *Energy*, 89: 500-510.

Yang X., Ma F., Li K., Guo Y., Hu J., Li W., Huo M. and Guo Y. (2010). "Mixed phase titania nanocomposite codoped with metallic silver and vanadium oxide: new efficient photocatalyst for dye degradation." *Journal of Hazardous Materials*, 175 (1): 429-438.

Yano H., Song J. M., Uchida H. and Watanabe M. (2008). "Temperature dependence of oxygen reduction activity at carbon-supported Pt x Co (X= 1, 2, and 3) alloy catalysts prepared by the nanocapsule method." *The Journal of Physical Chemistry C*, 112 (22): 8372-8380.

Yoshii K., Yamaji K., Tsuda T., Matsumoto H., Sato T., Izumi R., Torimoto T. and Kuwabata S. (2016). "Highly durable Pt nanoparticle-supported carbon catalysts for the oxygen reduction reaction tailored by using an ionic liquid thin layer." *Journal of Materials Chemistry A*, 4 (31): 12152-12157.

You D. J., Pak C., Jin S.-A., Lee K. H., Kwon K., Choi K. H., Heo P. W., Jang H., Kim J. Y. and Kim J. M. (2016). "Heterogeneous Electrocatalyst of Palladium-Cobalt-Phosphorus on Carbon Support for Oxygen Reduction Reaction in High Temperature Proton Exchange Membrane Fuel Cells." *Journal of Nanoscience and Nanotechnology*, 16 (5): 4357-4361.

Yu P., Pemberton M. and Plasse P. (2005). "PtCo/C cathode catalyst for improved durability in PEMFCs." *Journal of Power Sources*, 144 (1): 11-20.

Yu S., Lou Q., Han K., Wang Z. and Zhu H. (2012). "Synthesis and electrocatalytic performance of MWCNT-supported Ag@ Pt core–shell nanoparticles for ORR." *International Journal of Hydrogen Energy*, 37 (18): 13365-13370.

Yu Y., Li H., Wang H., Yuan X.-Z., Wang G. and Pan M. (2012). "A review on performance degradation of proton exchange membrane fuel cells during startup and

274

shutdown processes: Causes, consequences, and mitigation strategies." *Journal of Power Sources*, 205: 10-23.

Yuan X.-Z., Li H., Zhang S., Martin J. and Wang H. (2011). "A review of polymer electrolyte membrane fuel cell durability test protocols." *Journal of Power Sources*, 196 (22): 9107-9116.

Zaidi S. M. J. (2009). *Research trends in polymer electrolyte membranes for PEMFC*. Polymer membranes for fuel cells, Springer**:** 7-25.

Zapata-Fernández J. R., Gochi-Ponce Y., Salazar-Gastélum M. I., Reynoso-Soto E. A., Paraguay-Delgado F., Lin S. W. and Félix-Navarro R. M. (2017). "Ultrasonic-assisted galvanic displacement synthesis of Pt–Pd/MWCNT for enhanced oxygen reduction reaction: Effect of Pt concentration." *International Journal of Hydrogen Energy*, 42 (15): 9806-9815.

Zhang C., Yu H., Fu L., Xiao Y., Gao Y., Li Y., Zeng Y., Jia J., Yi B. and Shao Z. (2015). "An Oriented Ultrathin Catalyst Layer Derived from High Conductive TiO2 Nanotube for Polymer Electrolyte Membrane Fuel Cell." *Electrochimica Acta*, 153 (0): 361-369.

Zhang J., Tang Y., Song C., Zhang J. and Wang H. (2006). "PEM fuel cell open circuit voltage (OCV) in the temperature range of 23 C to 120 C." *Journal of power sources*, 163 (1): 532-537.

Zhang J., Vukmirovic M. B., Sasaki K., Nilekar A. U., Mavrikakis M. and Adzic R. R. (2005). "Mixed-metal Pt monolayer electrocatalysts for enhanced oxygen reduction kinetics." *Journal of the American Chemical Society*, 127 (36): 12480-12481.

Zhang L., Chang Q., Chen H. and Shao M. (2016). "Recent advances in palladium-based electrocatalysts for fuel cell reactions and hydrogen evolution reaction." *Nano Energy*, 29: 198-219.

Zhang L., Mi M., Li B. and Dong Y. (2013). "Modification of activated carbon by means of microwave heating and its effects on the pore texture and surface chemistry." *Res. J. Appl. Sci. Eng. Technol*, 5 (5): 1836-1840.

Zhang M., Su L. and Mao L. (2006). "Surfactant functionalization of carbon nanotubes (CNTs) for layer-by-layer assembling of CNT multi-layer films and fabrication of gold nanoparticle/CNT nanohybrid." *Carbon*, 44 (2): 276-283.

Zhang W., Wang M., Chen J., Romeo T., Harris A. T. and Minett A. I. (2013). "Localized growth of Pt on Pd as a bimetallic electrocatalyst with enhanced catalytic activity and durability for proton exchange membrane fuel cell." *Electrochemistry Communications*, 34: 73-76.

Zhang W. F., He Y. L., Zhang M. S., Yin Z. and Chen Q. (2000). "Raman scattering study on anatase TiO 2 nanocrystals." *Journal of Physics D: Applied Physics*, 33 (8): 912.

Zhang X., Yang Y., Guo L. and Liu H. (2017). "Effects of carbon corrosion on mass transfer losses in proton exchange membrane fuel cells." *International Journal of Hydrogen Energy*, 42 (7): 4699-4705.

References

Zhang Y., Zang J., Dong L., Cheng X., Zhao Y. and Wang Y. (2014). "A Ti-coated nano-SiC supported platinum electrocatalyst for improved activity and durability in direct methanol fuel cells." *Journal of Materials Chemistry A*, 2 (26): 10146-10153.

Zhang Z., Liu J., Gu J., Su L. and Cheng L. (2014). "An overview of metal oxide materials as electrocatalysts and supports for polymer electrolyte fuel cells." *Energy & Environmental Science*, 7 (8): 2535-2558.

Zhang Z., Sun T., Chen C., Xiao F., Gong Z. and Wang S. (2014). "Bifunctional nanocatalyst based on three-dimensional carbon nanotube–graphene hydrogel supported pd nanoparticles: one-pot synthesis and its catalytic properties." *ACS Applied Materials & Interfaces*, 6 (23): 21035-21040.

Zheng J.-N., He L.-L., Chen F.-Y., Wang A.-J., Xue M.-W. and Feng J.-J. (2014). "Simple one-pot synthesis of platinum-palladium nanoflowers with enhanced catalytic activity and methanol-tolerance for oxygen reduction in acid media." *Electrochimica Acta*, 137: 431-438.

Zhou Y., Neyerlin K., Olson T. S., Pylypenko S., Bult J., Dinh H. N., Gennett T., Shao Z. and O'Hayre R. (2010). "Enhancement of Pt and Pt-alloy fuel cell catalyst activity and durability via nitrogen-modified carbon supports." *Energy & Environmental Science*, 3 (10): 1437-1446.

Zhou Y., Yang J., Zhu C., Du D., Cheng X., Yen C. H., Wai C. M. and Lin Y. (2016). "Newly Designed Graphene Cellular Monolith Functionalized with Hollow Pt-M (M= Ni, Co) Nanoparticles as the Electrocatalyst for Oxygen Reduction Reaction." *ACS Applied Materials & Interfaces*, 8 (39): 25863-25874.

Zhou Z.-M., Shao Z.-G., Qin X.-P., Chen X.-G., Wei Z.-D. and Yi B.-L. (2010). "Durability study of Pt–Pd/C as PEMFC cathode catalyst." *international journal of hydrogen energy*, 35 (4): 1719-1726.

Zhu J., Xiao M., Zhao X., Liu C., Ge J. and Xing W. (2015). "Strongly coupled Pt nanotubes/N-doped graphene as highly active and durable electrocatalysts for oxygen reduction reaction." *Nano Energy*, 13: 318-326.

List of Publications

a) Publications in International Journals

1. **Abha Bharti,** Gouri Cheruvally, Shaneeth Muliankeezhu, "Microwave assisted, facile synthesis of Pt/CNT catalyst for proton exchange membrane fuel cell application", **International Journal of Hydrogen Energy,** 42 (2017) 11622-11631.

2. **Abha Bharti,** Gouri Cheruvally, 'Influence of various carbon nano-forms as supports for Pt catalyst on proton exchange membrane fuel cell performance', **Journal of Power Sources,** 360 (2017) 196-205.

3. **Abha Bharti**, Gouri Cheruvally, "V-doped TiO_2 supported Pt as a promising oxygen reduction reaction catalyst: Synthesis, characterization and in-situ evaluation in proton exchange membrane fuel cell", **Journal of Power Sources**, 363 (2017) 413-421.

4. **Abha Bharti,** Shaneeth Muliankeezhu, Gouri Cheruvally, 'Pt/TiO_2 Nanocomposites as Catalysts for Proton Exchange Membrane Fuel Cell: Prominent Effects of Synthesis Medium pH', **Journal of Nanoscience and Nanotechnology**, 2017,doi:10.1166/jnn.2017.14336.

5. **Abha Bharti,** Gouri Cheruvally, "Performance and durability characteristics of Pt/V-TiO_2 and Pt/C as cathode catalysts in proton exchange membrane fuel cell", **(Communicated).**

6. **Abha Bharti**, Gouri Cheruvally, "Surfactant assisted synthesis of Pt-Pd/MWCNT and evaluation as cathode catalyst for proton exchange membrane fuel cell", **(Communicated).**

b) Papers presented in conferences and seminars

1. **Abha Bharti**, Gouri. C, "In-situ diagnosis of proton exchange membrane fuel cell performance with Pt/TiO_2 cathode catalyst", 7th European Fuel Cell Technology & Applications Conference- Piero Lunghi Conference, December 12-15 (**2017**) Naples, Italy.

2. **Abha Bharti**, "Biomimetic transition metal based complexes for onboard hydrogen generation for PEM fuel cell application", National Competition for Research Scholars on Hydrogen Energy and Related Advanced Materials -HEAM SCIENTIST-2017, March 16-17 (**2017**) Thiruvananthapuram, India.

3. **Abha Bharti**, Gouri. C, "Investigation on Pt supported on various carbon nano-forms as cathode catalyst for PEM fuel Cell", Annual Technical Meeting of Materials Research Society of India-Trivandrum Chapter, January 27 (**2017**) Thiruvananthapuram, India.

4. **Abha Bharti**, Shaneeth. M, Gouri. C, "Simple and facile one pot synthesis of Pt supported on MWCNT as an ORR catalyst for PEM fuel cells", International Conference on Nanoscience and Nanotechnology for Energy Applications, June 27-29 (**2016**) Chennai, India.

5. **Abha Bharti**, Shaneeth. M, Gouri. C, "Hydroxide Reduction- An aspect of oxygen reduction reaction in PEM fuel cells", A National Seminar on Hydrogen Energy and Other Renewable Energy Sources-HEAM SCIENTIST-2014, November 17-18 (**2014**) Thiruvananthapuram, India.

6. **Abha Bharti**, Shaneeth M., Gouri. C, "Proton Exchange Membrane Fuel cells: Oxygen Reduction Reaction and Efficiency Enhancements", International Conference on Advances in Chemical Engineering & Technology, October 16-18 (**2014**) Kollam, India.

7. **Abha Bharti**, Shaneeth. M, Gouri. C,"Oxygen Reduction Reaction in PEM fuel cells: Study on catalytic activities of Pt, 20%Pt-C, 55%Pt-C and Pt-Co", International Conference on Electrochemical Science & Technology, August 7-9 (**2014**) Bangalore, India.

8. **Abha Bharti**, Shaneeth. M, Gouri. C, "Study on catalytic activities of Pt, 20%Pt-C, 55%Pt-C and Pt-Co", National Conference on Materials Science and Technology, July 10-12, (**2013**) Thiruvanathapuram, India.

List of Awards

1. **HEAM SCHOLAR-2017 Award** at "National Competition for Research Scholars on Hydrogen Energy and Related Advanced Materials-HEAM SCIENTIST-2017", March 16-17 (**2017**) Thiruvananthapuram, India.

2. **Best Oral Paper Presentation Award** for the paper "Investigation on Pt supported on various carbon nano-forms as cathode catalyst for PEM fuel Cell", Annual Technical Meeting of Materials Research Society of India-Trivandrum Chapter, January 27 (**2017**) Thiruvananthapuram, India.

3. **Best Oral Paper Presentation Award** for the paper "Simple and facile one pot synthesis of Pt supported on MWCNT as an ORR catalyst for PEM fuel cells", International Conference on Nanoscience and Nanotechnology for Energy Applications, June 27-29 (**2016**) Chennai, India.

4. **Best Oral Paper Presentation Award** for the paper "Hydroxide Reduction-An aspect of oxygen reduction reaction in PEM fuel cells", A National Seminar on Hydrogen Energy and Other Renewable Energy Sources-HEAM SCIENTIST-2014, November 17-18 (**2014**) Thiruvananthapuram, India.

Bio-Data

Abha Bharti

Senior Research Fellow
Propellants, Polymers, Chemicals & Materials Entity,
Vikram Sarabhai Space Centre,
Thiruvananthapuram 695021
Kerala, India.
Phone No. : +91-8606400934; +91-9871233827
Email Id   : bharti.abha@gmail.com

I.   Personal Information:

Father's Name   : Ashok Kumar
Birth Date   : 6th June 1989
Gender   : Female
Marital Status   : Single
Languages Known   : Hindi, English & Malayalam
Nationality   : Indian

II.   Education:

Secondary (X)   : ICSE, Don Bosco Academy, Patna, Bihar, India, 2005, (78.33%).

Senior Secondary (XII)   : CBSE, Kendriya Vidyalaya, Patna, Bihar, India, 2007, (79.80%).

Bachelor of Life Science : University of Delhi, New Delhi, India 2010, (74.29%).

Master of Chemistry   : University of Delhi, New Delhi, India 2012, (72.28%)

Ph.D. in Chemistry   : Cochin University of Science and Technology, Cochin, Kerala, India, 2013-Cont. (CGPA- 9.0/10)
Thesis titled "Studies on Pt based cathode catalysts for proton exchange membrane fuel cell".

III. Research Interests:

Nanomaterials and nanocomposites for energy application; PEM fuel cells; Water electrolyzer; Lithium ion batteries; Supercapacitors; Solar cells; Onboard hydrogen production; Hydrogen storage materials; Hydrogen economy

IV. Research Experience:

Catalyst synthesis and characterization, Catalyst ink, electrode and MEA preparation, Single cell fuel cell assembly and health verification, *In-situ* performance evaluation (activity and durability) through electrochemical techniques

2013-Cont. : ISRO Research Fellow,
Vikram Sarabhai Space Centre,
Thiruvananthapuram, Kerala, India.

V. Scholarship/Fellowship:

- Jeans & Ashit Ganguly Education Scholarship for the year 2011-12 (MSc. Chemistry, University of Delhi)
- Indian Space Research Organization Fellowship for Ph. D. research (2013-Cont.).

VI. Research publications, Conferences/workshop and Awards

a) *Publications in International Journals*

1. **Abha Bharti,** Shaneeth Muliankeezhu, Gouri Cheruvally, "*Pt/TiO₂ Nanocomposites as Catalysts for Proton Exchange Membrane Fuel Cell: Prominent Effects of Synthesis Medium pH*", **Journal of Nanoscience and Nanotechnology**, 2017,doi:10.1166/jnn.2017.14336

2. **Abha Bharti,** Gouri Cheruvally, Shaneeth Muliankeezhu, "*Microwave assisted, facile synthesis of Pt/CNT catalyst for proton exchange membrane fuel cell application*", **International Journal Of Hydrogen Energy,** 42 (2017) 11622-11631.

3. **Abha Bharti,** Gouri Cheruvally, "*Influence of various carbon nano-forms as supports for Pt catalyst on proton exchange membrane fuel cell performance*", **Journal of Power Sources,** 360 (2017) 196-205.

4. **Abha Bharti,** Gouri Cheruvally, "*V-doped TiO₂ supported Pt as a promising oxygen reduction reaction catalyst: Synthesis, characterization*

and in-situ evaluation in proton exchange membrane fuel cell", **Journal of Power Sources**, 363 (2017) 413-421.

b) Conferences/ Workshop:

1. Oral presentation on *"In-situ diagnosis of proton exchange membrane fuel cell performance with Pt/TiO₂ cathode catalyst"*, at 7th European Fuel Cell Technology & Applications Conference- Piero Lunghi Conference, Naples, Italy, 2017

2. Oral presentation at National Competition for Research Scholars on Hydrogen Energy and Related Advanced Materials-HEAM SCIENTIST-2017, Kerala University, Thiruvananthapuram, India, 2017.

3. Oral presentation on *"Investigation on Pt supported on various carbon nano-forms as cathode catalyst for PEM fuel Cell"*, at Annual Technical Meeting of Materials Research Society of India-Trivandrum Chapter, Thiruvananthapuram, India, 2017

4. Oral presentation on *"Simple and facile one pot synthesis of Pt supported on MWCNT as an ORR catalyst for PEM fuel cells"*, at International Conference on Nanoscience and Nanotechnology for Energy Applications, Sathyabama University, Chennai, India, 2016

5. National Workshop on Recent Trends in X-Ray Diffraction Techniques, Sathyabama University, Chennai, India, 2014.

6. Oral presentation on *"Hydroxide Reduction- An aspect of oxygen reduction reaction in PEM fuel cells"*, at A National level meet of Young Scientists of Hydrogen Energy and Other Renewable Energy Sources, Kerala University, Thiruvananthapuram, India, 2014

7. Oral presentation on *"Proton Exchange Membrane Fuel cells: Oxygen Reduction Reaction and Efficiency Enhancements"*, at International Conference on Advances in Chemical Engineering & Technology, TKMCE, Kollam, India, 2014.

8. Oral presentation on "Oxygen Reduction Reaction in PEM fuel cells: Study on catalytic activities of Pt, 20%Pt-C, 55%Pt-C and Pt-Co", at International Conference on Electrochemical Science & Technology, IISc, Bangalore, India, 2014.

9. National Conference on Materials Science & Technology, IIST, Thiruvananthapuram, India, 2014.

10. National workshop on Characterization of advanced materials, Thiruvananthapuram, India, 2013.

11. Oral presentation on "*Study on catalytic activities of Pt, 20%Pt-C, 55%Pt-C and Pt-Co*", at National Conference on Materials Science and Technology, IIST, Thiruvananthapuram, India, 2013.

c) *Awards:*

1. **HEAM SCHOLAR-2017** at "National Competition for Research Scholars on Hydrogen Energy and Related Advanced Materials-HEAM SCIENTIST-2017", Kerala University, Thiruvananthapuram (2017).

2. **Best Oral Paper Presentation Award** at "Annual Technical Meeting of Materials Research Society of India-Trivandrum Chapter", Thiruvananthapuram (2017).

3. **Best Oral Paper Presentation Award** at "International Conference on Nanoscience and Nanotechnology for Energy Applications", Sathyabama University, Chennai (2016).

4. **Best Oral Paper Presentation Award** at "A National meet of Young Scientists of Hydrogen Energy and Other Renewable Energy Sources", Kerala University, Thiruvananthapuram (2014)

This bio-data is a true and accurate declaration of my activities and accomplishments. I certify that the information furnished in this bio-data is true to the best of my knowledge and belief.

Place: Thiruvananthapuram, Kerala   **Abha Bharti**

Date: 21/12/2017